

PAVEMENT AND GEOTECHNICAL ENGINEERING FOR TRANSPORTATION

Edited by

Baoshan Huang, Ph.D., P.E.,

Benjamin F. Bowers,

Guo-Xiong Mei, Ph.D., Si-Hai Luo, Ph.D.,

and Zhongjie Zhang, Ph.D.



GEO-
INSTITUTE

GEOTECHNICAL PRACTICE PUBLICATION NO. 8

PAVEMENT AND GEOTECHNICAL ENGINEERING FOR TRANSPORTATION

PROCEEDINGS OF SESSIONS OF THE FIRST INTERNATIONAL SYMPOSIUM ON
PAVEMENT AND GEOTECHNICAL ENGINEERING FOR TRANSPORTATION
INFRASTRUCTURE

June 5–7, 2011
Nanchang, Jiangxi Province, China

SPONSORED BY
Nanchang Hangkong University
Association of Chinese Infrastructure Professionals, China
The Geo-Institute of the American Society of Civil Engineers

EDITED BY
Baoshan Huang, Ph.D., P.E.
Benjamin F. Bowers, Ph.D.
Guo-Xiong Mei, Ph.D.
Si-Hai Luo, Ph.D.
Zhongjie Zhang, Ph.D.

ASCE



Published by the American Society of Civil Engineers

Library of Congress Cataloging-in-Publication Data

International Symposium on Pavement and Geotechnical Engineering for Transportation Infrastructure (1st : 2011 : Nanchang, China)

Pavement and geotechnical engineering for transportation : proceedings of sessions of the First International Symposium on Pavement and Geotechnical Engineering for Transportation Infrastructure, June 5-7, 2011, Nanchang, Jiangxi Province, China ; sponsored by Nanchang Hangkong University ; Association of Chinese Infrastructure Professionals, China ; The Geo-Institute of the American Society of Civil Engineers ; edited by Baoshan Huang, Benjamin F. Bowers, Guoxiong Mei, Si-Hai Luo, Zhongjie "Doc" Zhang.

pages cm. -- (Geotechnical practice publication ; No. 8)

Includes bibliographical references and index.

ISBN 978-0-7844-1281-7 (pbk.) -- ISBN 978-0-7844-7780-9 (e-book)

1. Roads--Design and construction--Congresses. 2. Engineering geology--Congresses. I. Huang, Baoshan. II. Bowers, Benjamin F. III. Mei, Guoxiong. IV. Luo, Si-Hai. V. Zhang, Zhongjie VI. Nanchang hang kong da xue. VII. Association of Chinese Infrastructure Professionals (China) VIII. American Society of Civil Engineers. Geo-Institute. IX. Title.

TE5.I475 2013

625.8--dc23

2013000488

American Society of Civil Engineers
1801 Alexander Bell Drive
Reston, Virginia, 20191-4400

www.pubs.asce.org

Any statements expressed in these materials are those of the individual authors and do not necessarily represent the views of ASCE, which takes no responsibility for any statement made herein. No reference made in this publication to any specific method, product, process, or service constitutes or implies an endorsement, recommendation, or warranty thereof by ASCE. The materials are for general information only and do not represent a standard of ASCE, nor are they intended as a reference in purchase specifications, contracts, regulations, statutes, or any other legal document. ASCE makes no representation or warranty of any kind, whether express or implied, concerning the accuracy, completeness, suitability, or utility of any information, apparatus, product, or process discussed in this publication, and assumes no liability therefore. This information should not be used without first securing competent advice with respect to its suitability for any general or specific application. Anyone utilizing this information assumes all liability arising from such use, including but not limited to infringement of any patent or patents.

ASCE and American Society of Civil Engineers—Registered in U.S. Patent and Trademark Office.

Photocopies and reprints. You can obtain instant permission to photocopy ASCE publications by using ASCE's online permission service (<http://pubs.asce.org/permissions/requests/>). Requests for 100 copies or more should be submitted to the Reprints Department, Publications Division, ASCE, (address above); email: permissions@asce.org. A reprint order form can be found at <http://pubs.asce.org/support/reprints/>.

Copyright © 2013 by the American Society of Civil Engineers.
All Rights Reserved.

ISBN 978-0-7844-1281-7 (paper)

ISBN 978-0-7844-7780-9 (e-book)

Manufactured in the United States of America.

Preface

Pavement and Geotechnical Engineering for Transportation selects 20 papers that represent the latest developments in the application of soil, rock, and paving materials to the study and application of geomechanics and transportation geotechnology.

Many of the selected papers were presented at the 1st International Symposium on Pavement and Geotechnical Engineering for Transportation Infrastructure sponsored by the Nanchang Hangkong University and the International Association of Chinese Infrastructure Professionals (IACIP) in co-operation with ASCE, which occurred from June 5–7, 2011 in Nanchang, Jiangxi Province, China. The papers were selected based on their relevance to the geotechnical and transportation geotechnology.

Presented within the *Pavement and Geotechnical Engineering for Transportation* Geotechnical Practice Publication (GPP) are papers that examine the use of waste in pavement structures, thus attracting one of the many sustainable elements of pavement design. Studies of the pavement structure beginning with the inclusion of chemical additives in soil subgrade, the use of geogrid reinforcement in unpaved and paved roads, to the surface roughness of asphalt mixtures and the freeze-thaw performance of concrete are reported. Also showcased herein are mathematical models that simulate various geotechnical problems. Various soil types are evaluated and discussed for common problems and design inputs used in practice such as slope failure, consolidation, and embankment behavior. An early warning system for subway construction is also exhibited.

One or more reviewers along with the editors evaluated each paper published in this ASCE Geotechnical Practice Publication. All published papers are eligible for discussion in the *Journal of Geotechnical and Geoenvironmental Engineering* and the *Journal of Materials in Civil Engineering*, and are eligible for ASCE awards.

The editors would like to thank Mr. Ken Fishman and the Geo-Institute for their vast assistance with this publication. Due thanks is also given to Ms. Donna Dickert from ASCE publications. Appreciation is given to those who helped assist in the editing duties of this publication. Without their assistance this publication would not be possible.

Jason Moore, University of Tennessee, USA

Jie Han, University of Kansas, USA

Qiao Dong, University of Tennessee, USA

Sheng Zhao, University of Tennessee, USA

Zhongjie “Doc” Zhang, Louisiana Department of Transportation, USA

We would like to acknowledge the peer reviewers who spent their time and efforts in ensuring the exceptional quality of the papers presented within this GPP. Without their contributions this publication would not be possible.

Angel Palomino, University of Tennessee, USA
Edwin Burdette, University of Tennessee, USA
Eric Drumm, University of Tennessee, USA
Feng Chen, Soilvision Systems, Ltd, Canada
Gang Zuo, Consultant, USA
Haifang Wen, Washington State University, USA
Hao Wu, Central South University, China
Jie Han, University of Kansas, USA
Jie Huang, University of Texas-San Antonio, USA
John L. Daniels, University of North Carolina at Charlotte, USA
Juanyu “Jenny” Liu, University of Alaska-Fairbanks, USA
Khalid Alshibli, University of Tennessee, USA
Lianyang Zhang, University of Arizona, USA
Ningyuan Li, Ministry of Transportation of Ontario, Canada
Mingjiang Tao, Worcester Polytechnic Institute, USA
Qiming Chen, Louisiana Transportation Research Center, USA
Qiao Dong, University of Tennessee, USA
Qing Lu, University of South Florida, USA
Shihui Shen, Washington State University, USA
Xin Chen, Maryland Department of Transportation, USA
Xingwei Chen, Louisiana Department of Transportation and Development, USA
Xiong Yu, Case Western Reserve University, USA
Xiong Zhang, University of Alaska-Fairbanks, USA
Zhongjie “Doc” Zhang, Louisiana Department of Transportation, USA
Zhong Wu, Louisiana State University, USA

Contents

Structural Performance of Thin Asphalt Pavement Under Accelerated Pavement Testing	1
Zhong Wu	
Performance Measures and Evaluation of Asphalt Pavements Using the Internal Roughness Index	19
Ningyuan Li, Renjie Qin, and Zhaohui Liu	
Design of Planar Geosynthetic-Improved Unpaved and Paved Roads	31
Jie Han	
Investigation of Moisture Content-Induced Variations in Unbound Aggregates' Resilient Modulus Through Suction Stress Concept	42
Mingjiang Tao, Zhongjie Zhang, Qiming Chen, and Hong Guo	
Laboratory Evaluation on the Mechanical Properties of Asphalt Concrete Incorporating Industrial Waste	53
Qiao Dong and Baoshan Huang	
The Relationship Between Freeze-Thaw Resistance and Pore Structure of Concrete	60
Shanshan Jin, Jinxi Zhang, and Baoshan Huang	
Additives for Soil-Cement Stabilization	68
Benjamin F. Bowers, John L. Daniels, Shaogang Lei, and Nicholas J. DeBlasis	
Tube Suction Test for Evaluating Moisture Susceptibility Resulting from Calcium Chloride	76
Shaogang Lei, John L. Daniels, and Benjamin F. Bowers	
Critical Load of Subsoil Considering Poisson's Ratio	83
Chuang Yu, Xiaoqing Cai, and Liangliang Tang	
Heat Transfer Capacity of Heat Exchanger Piles in Soft Clay	88
Chuang Yu, Xiaoqing Cai, and Linyou Pan	
An Empirical Study on the Estimation of Soil Properties of Loess Ground After Dynamic Compaction	93
Si-hai Luo, Yang Wang, Xiao-qing Pang, and Tong-fa Deng	

Theoretical Background of Axis-Radiate Infinite Element with Its Applications in Foundation Analysis	102
Hongyang Xie, Yang Huang, and Jinquan Yin	
Influence of Features of Natural Soft Clay on Embankment Behavior	111
Jian-Hua Wang, Minna Karstunen, and Zhen-Yu Yin	
Influence of Fracture Filling on Mechanical Behavior of Loess	117
Mingjing Jiang, Haijun Hu, Jianbing Peng, and Xinxin Wang	
One-Dimensional Consolidation of Soft Ground with Impeded Boundaries Under Depth-Dependent Ramp Load	127
Jia-cai Liu and Qiang Ma	
Remote Monitoring and Early Warning System for Subway Construction	135
Mingyang Wang, Junhua Xiao, and Xiaoli Rong	
Research on the Influence of the Rotation of Principle Axis of Stress to the Constitutive Relation Soil	142
Yuan-xue Liu, Zhong-you Li, and Yu Zhang	
Settlement Analysis of Embedded Foundation Resting on Elastic Soil	154
Guoxiong Mei and Meijuan Xu	
Study on Mechanism of Expansive Soil Slope Failure and Numerical Simulation	162
Ting-hao Lu, Jun-hua Wu, Song Yang, and Guo-xiong Mei	
Time Effect on Bearing Capacity of Jacked Piles Using the Back-Analysis Method	175
Tong-fa Deng, Zhong-fang Zhao, and Yong Gui	

Author List

Bowers, Benjamin F., 68, 76

Cai, Xiaoqing, 83, 88

Chen, Qiming, 42

Daniels, John L., 68, 76

DeBlasis, Nicholas J., 68

Deng, Tong-Fa, 93, 175

Dong, Qiao, 53

Gui, Yong, 175

Guo, Hong, 42

Han, Jie, 31

Hu, Haijun, 117

Huang, Baoshan, 53, 60

Huang, Yang, 102

Jiang, Mingjing, 117

Jin, Shanshan, 60

Karstunen, Minna, 111

Lei, Shaogang, 68, 76

Li, Ningyuan, 19

Li, Zhong-You, 142

Liu, Jia-Cai, 127

Liu, Yuan-Xue, 142

Liu, Zhaohui, 19

Lu, Ting-Hao, 162

Ma, Qiang, 127

Mei, Guoxiong, 154

Mei, Guo-Xiong, 162

Pan, Linyou, 88

Pang, Xiao-Qing, 93

Peng, Jianbing, 117

Qin, Renjie, 19

Rong, Xiaoli, 135

Tang, Liangliang, 83

Tao, Mingjiang, 42

Wang, Jian-Hua, 111

Wang, Mingyang, 135

Wang, Xinxin, 117

Wang, Yang, 93

Wu, Jun-Hua, 162

Wu, Zhong, 1

Xiao, Junhua, 135

Xie, Hongyang, 102

Xu, Meijuan, 154

Yang, Song, 162

Yin, Jinqun, 102

Yin, Zhen-Yu, 111

Yu, Chuang, 83, 88

Zhang, Jinxi, 60

Zhang, Yu, 142

Zhang, Zhongjie, 42

Zhao, Zhong-Fang, 175

This page intentionally left blank

STRUCTURAL PERFORMANCE OF THIN ASPHALT PAVEMENT UNDER ACCELERATED PAVEMENT TESTING

Zhong Wu¹

¹ Accelerated Pavement Research Program Manager, Louisiana Transportation Research Center, 4101 Gourrier Ave, Baton Rouge, LA 70808. zhongwu@ltrc.lsu.edu. Tel: (225) 767-9163, Fax (225) 767-9108.

ABSTRACT: Three thin asphalt pavement sections containing different chemically stabilized base and subbase materials were tested under the accelerated pavement testing (APT) at the Louisiana Accelerated Pavement Research Facility. Each pavement section consisted of different base and subbase materials, but having a common configuration of layer thicknesses. APT results generally indicated that both stabilized Blended Calcium Sulfate (BCS) bases outperformed a foamed asphalt treated base by a significantly large margin while a cement-treated soil subbase layer proved to have better load bearing capacity than a lime-treated soil layer. The structural performance of test sections was further analyzed using the non destructive test results and instrumentation measured pavement responses. The newly developed Mechanistic-Empirical Pavement Design Guide (M-E PDG) software was also used in predicting the rutting development on tested sections. Finally, a simple rut depth prediction model, which relates flexible pavement rutting development to the in-situ surface deflection characteristics, was proposed.

KEY WORDS: Thin asphalt pavement, rutting, stabilized base, treated soil, accelerated loading, NDT, instrumentation

INTRODUCTION

The Louisiana Pavement Research Facility (PRF) is an outdoor, full-scale accelerated pavement testing laboratory located on a six-acre site in Port Allen, Louisiana. It has space available for the construction of ten full-scale test pavement lanes, each having a size of 65-m (215-ft) long by 4-m (13-ft) wide. Traffic loading is provided by a machine called the Accelerated Loading Facility (ALF). The ALF device is a 33-m (100 ft) long accelerated loading device originally developed in Australia. The ALF wheel assembly models one half of a single axle with dual tires and the load is adjustable from 43.4 kN (9,750 lb) to 84.4 kN (18,950 lb) per load application. With a computer-controlled load trolley, the weight and movement of traffic is simulated repetitively in one direction at a speed of 16.8 km/hr (10.5 mph).

Therefore, Louisiana PRF provides an ideal accelerated pavement testing (APT) facility to evaluate the structural performance of various base and subbase materials investigated by the Louisiana Transportation Research Center (LTRC) (Mcmanis 2003, Zhang and Tao 2006, Wu, Zhang, and King 2011, and Metcalf et al 2001).

OBJECTIVES AND SCOPES

The main objective of this study was to evaluate the structural performance of thin asphalt pavements containing different chemically stabilized base and subbase materials under accelerated loading. The scopes included accelerated pavement testing (APT), in situ pavement instrumentation, non destructive testing (NDT), surface distress survey and surface rutting prediction.

PAVEMENT STRUCTURE AND INSTRUMENTATION LAYOUT

Three full-scale flexible pavement test sections were constructed at the PRF over a silty-soil embankment using normal highway construction equipment. Figure 1 presents the pavement structure and in situ instrumentation layouts of test sections. Each section had a 50.8-mm (2-in.) hot mix asphalt (HMA) top layer, a 216-mm (8.5-in) base and a 305-mm (12-in) subbase layer. Note that such a pavement thickness configuration is typically used for a low volume road in Louisiana except that an 88.9-mm (3.5-in) HMA layer is often used.

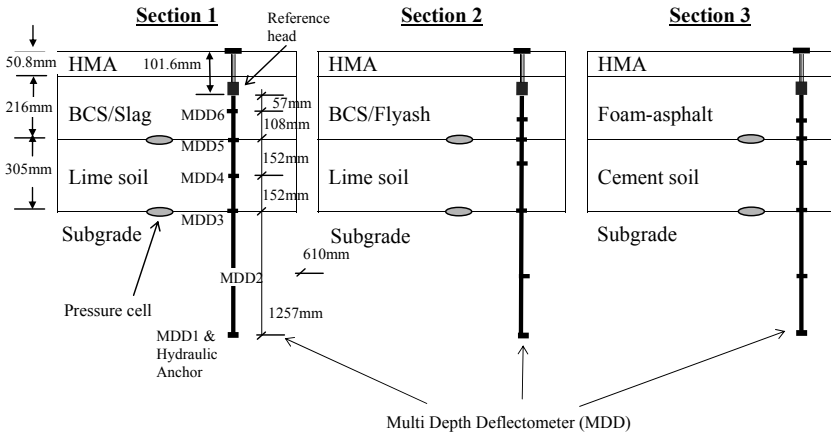


FIG. 1. Pavement Structures of ALF Test Lanes

As shown in Figure 1, two earth pressure cells were embedded at two vertical depths on each test section directly under the centerline: the bottom of base layer and the top

of subgrade. In addition, one multi-depth deflectometer (MDD) was installed 1.4-m (4.5-ft) away from the pressure cell location on each test section. The installation of the MDDs was accomplished through a surface drilling operation after the construction (Wu, Zhang, and King 2011). Each MDD consisted of six potentiometers (MDD1-MDD6) for measuring load-induced plastic and elastic deformations at each of selected vertical depths (Figure 1).

MATERIALS

HMA Mixture

The HMA mixture used was a 19-mm Superpave mixture designed at a gyration number of 100. The aggregate blend consisted of 45.4 percent #67 coarse granite aggregate, 17.1 percent #11 crushed siliceous limestone, 10.3 percent coarse sand, 12.9 percent crushed gravel and 14.3 percent reclaimed asphalt pavement (RAP). The optimum asphalt binder content was 4.4 percent including 3.7 percent PG 76-22 virgin binder (elastomeric polymer-modified) and 0.7 percent recycled binder (from RAP). Other design information is summarized in Table 1.

Base Materials

Base materials considered in this APT experiment include two stabilized BCS and one foamed asphalt treated mixture. BCS is Blended Calcium Sulfate, a by-product material from hydrogen fluoride production. A large amount of BCS material is available in Louisiana as well as in other states (Zhang and Tao 2003). The major engineering concern for using raw BCS as a pavement base material is its moisture susceptibility. Water entering in a raw BCS base can cause both short-term construction and long-term durability problems due to dilation. To improve its water resistance, raw BCS was stabilized with different stabilization agents (lime, cement, flyash, and furnace slag) in a laboratory study at LTRC (Zhang and Tao 2003). Laboratory results indicated that a grade 120 Granulated Ground Blast Furnace Slag stabilized BCS (hereafter termed as BCS/Slag) showed a significant improvement over the raw BCS in terms of both water resistance and strength. In order to verify the laboratory findings, two stabilized BCS materials were included in this APT experiment. Specifically, a 10 percent by volume slag stabilized BCS base was used in section 1 and a 15 percent fly ash stabilized BCS base (hereafter termed as BCS/Flyash) was placed in section 2 (Figure 1). The gradation and other general design material properties of the two stabilized BCS materials are presented in Table 1.

The foamed asphalt base on section 3 was designed based on the standard Wirtgen Cold Recycling Manual (Wirtgen Cold Recycling Manual 1998). This mixture contained 48.6 percent RAP, 48.6 percent recycled soil cement and 2.8 percent PG 58-22 asphalt binder. A water injection rate of 3.0 percent was used in the foaming process with the binder temperature at 170°C. More design information of the foamed asphalt base can be found in Table 1.

Subbase and Subgrade Materials

The subbase layer for both sections 1 and 2 was an in-place lime treated soil (10 percent by volume), whereas an in-place cement treated soil subbase was used in section 3 (8 percent by volume). A silty clay soil, classified as A-6 type, was used in both cement and lime treated layers as well as in the embankment subgrade. The last column in Table 1 presents the basic soil properties.

While the use of 10 percent lime by volume to treat wet subgrade soils during the construction may be considered as a common practice in Louisiana, the selection of 8 percent cement by volume to treat the A-6 soil in this study was based on a design criterion of a minimum unconfined compressive strength of 1.03-Mpa (150-psi).

TABLE 1 General Design Properties and Gradations

Mixture Name	HMA	BCS/Slag Base		BCS/Flyash		Foam Asphalt Base		Subgrade Soil	
Binder type	PG 76-22	Dry unit weight, kN/m ³	15.9	Dry unit weight, kN/m ³	15.4	Binder type	PG 58-22	Dry unit weight, kN/m ³	17.1(107.5 pcf)
Design binder content, %	4.4	Moisture (%)	14.3	Moisture (%)	18.0	Design binder content, %	2.8	W _{opt} ⁽³⁾ (%)	18.5
Design air voids, %	4.0	UCS ⁽¹⁾ -Dry, MPa	5.1	UCS-Dry, MPa	0.14	Design air voids, %	20.3	LL ⁽⁴⁾ (%)	31
								PI ⁽⁵⁾	12
VMA, %	13.8	UCS-Wet, MPa	5.6	UCS-Wet, MPa	--	ITS ⁽²⁾ -Dry (kPa)	322.2	Clay (%)	23.5
								Silt (%)	60.3
VFA, %	71.0	%GGBFS, by volume	10	%Flyash, by volume	15	ITS-Wet (kPa)	256.6	Classification	CL-ML A-6
Sieve Size	Gradation (% passing)								
50 mm	100	100		100		100			
37.5 mm	100	98.9		98.0		100			
25 mm	100	95.3		94.8		100			
19 mm	97	91.0		90.2		95.0			
12.5 mm	83	76.3		82.8		82.6			
9.5 mm	73	69.0		78.6		71.5			
4.75 mm	49	54.0		70.8		51.6		100 (No. 4)	
2.36 mm	33	41.0		63.9		38.2		No. 8	
2.00 mm								97.3 (No.10)	
1.18 mm	24	34.5		61.0		28.8		No. 16	
0.6 mm	18	31.5		58.6		21.4		No. 30	
0.425 mm								96.6 (No.40)	
0.3 mm	10	29.3		56.7		15.4		No. 50	
0.15 mm	5.7	27.8		55.4		12.2		No. 100	
0.075 mm	4.6	26.9		54.4		10.2		91 (No. 200)	

⁽¹⁾UCS – Unconfined compressive strength; ⁽²⁾ITS – Indirect tensile strength; ⁽³⁾W_{opt} – optimum water content

⁽⁴⁾LL – liquid limit; ⁽⁵⁾PI – plastic index

Laboratory Resilient Modulus Test (Repeated Load Triaxial Test)

The resilient modulus test was performed on the base and subbase materials according to the AASHTO T-307-99 test method (AASHTO 2003). Details of the resilient modulus testing have been reported elsewhere (Mohammad et al 2006). The constitutive soil model, recommended by the NCHRP project 1-37A for the use in the new Mechanistic-Empirical (M-E) Pavement Design Guide (NCHRP 2004), has the following form:

$$\frac{M_r}{P_a} = k_1 \left(\frac{\theta}{P_a} \right)^{k_2} \left(\frac{\tau_{oct}}{P_a} + 1 \right)^{k_3} \tag{1}$$

where

M_r = resilient modulus

θ = bulk stress = $\sigma_1 + \sigma_2 + \sigma_3$

σ_1 = major principal stress

σ_2 = intermediate principal stress = σ_3

σ_3 = minor principal stress/ confining pressure

$$\tau_{oct} = \frac{1}{3} \sqrt{(\sigma_1 - \sigma_2)^2 + (\sigma_1 - \sigma_3)^2 + (\sigma_2 - \sigma_3)^2}$$

P_a = normalizing stress (atmospheric pressure) = 14.7 psi (101.35 kPa), and

k_1, k_2, k_3 = material constants.

The measured resilient moduli and corresponding bulk and deviator stresses were input to Eq.1 to determine the coefficients k_1, k_2 and k_3 . The coefficients for the base and the subgrade materials predicted by regression analysis are summarized in Table 2. The last column in Table 2 also shows the typical resilient modulus (M_r) values for each material tested.

TABLE 2 Resilient Modulus Input for the M-E Pavement Design Guide

Material	k_1	k_2	k_3	M_r (Mpa)
Subgrade soil	692	0.30	-3.04	38 ^(a)
Lime-treated soil	1445	0.23	-2.92	138 ^(a)
Cement-treated soil	6761	0.64	-1.79	408 ^(a)
BCS-Slag	8114	0.27	-0.08	850 ^(b)
BCS-Flyash	5950	0.22	-0.30	605 ^(b)
Foamed asphalt (50%RAP & 50% Soil cement)	2200	0.38	-0.56	195 ^(b)

Note: ^(a) M_r measured at 13.8-kPa (2-psi) confining pressure and 41.4-kPa (6-psi) deviator stress;

^(b) M_r measured at 34.5-kPa (5-psi) confining pressure and 103.5-kPa (15-psi) deviator stress;

Among the coefficients, k_1 is proportional to Young’s modulus (NCHRP 2004) and has been considered as the best indicator of the stiffness characteristics of the base

and subgrade layers by many researchers (Kim et al 2000, Park and Fernando 1998). Thus, by referring to those k_1 and typical M_r values in Table 2, laboratory resilient modulus test results indicate the following: (1) the lime-treated soil has improved stiffness characteristics over the untreated subgrade soil; (2) the cement-treated soil is significantly stiffer than the lime-treated soil; (3) BCS/Slag material is stiffer than BCS/Flyash; (4) both BCS materials have much higher k_1 values than that of the foamed-asphalt mixture; (5) since the k_1 value for the foam asphalt is considerably smaller than that of the cement-treated soil, this may have resulted an inverted structure for section 3 (i.e. a layer with a higher modulus is laid below a layer with a lower modulus in a pavement structure).

APT LOADING AND FIELD MEASUREMENTS

The ALF dual tires used for this study were the MICHELIN radial 11R22.5 tires, inflated to 723-kPa (105-psi) cold. The starting load was 43.4-kN (9,750-lb). After 175,000 repetitions, the load was increased to 53.6 kN (12,050 lb). Note that traffic wanders, 190 mm (7.5 in.) at each side of the centerline, were considered in this experiment. At the end of 225,000 repetitions, loading on section 3 was stopped due to excessive rutting developed on the pavement surface. According to the fourth power relationship, 225,000 ALF repetitions is equivalent to about 400,000 ESALs. Testing was conducted under a natural, unconfined, southern Louisiana highway environment.

The field instrumentation data (pressure cells and MDDs) were collected approximately at every 8,500 ALF load repetitions NDT tests, including DYNAFLECT and falling weight deflectometer (FWD), as well as the rutting and cracking survey were performed at the end of each 25,000 load repetitions. The DYNAFLECT used in this study is a trailer mounted device which induces a dynamic load of 4.45 kN (1,000 lb) at a frequency of 8 Hz on the pavement and measures the resulting deflections by using five geophones spaced under the trailer at approximately 300 mm (1 ft) intervals from the application of the load. A Dynatest 8002 model FWD device was used with nine sensors spaced at 0, 200, 300, 450, 600, 900, 1,200, 1,500 and 1,800 mm (0, 8, 12, 18, 24, 36, 48, 60 and 72 in.), respectively.

DISCUSSION OF TEST RESULTS

Instrumentation Results

Pressure Cells

Table 3 presents a statistical summary of measured vertical compressive stresses from the two pressure cells installed at each test section subjected to moving loads. As stated earlier, data was collected roughly at every 8,500 load repetitions. As shown in Table 3, the average vertical stresses under “43.4-kN load” contained the vertical stressed measured from 0 to 175,000 ALF load repetitions, while those “under 53.6-kN load” were taken between 175,000 and 225,000 load passes. The coefficient of variation (COV) in Table 3 indicates the variation of pavement

responses (vertical compressive stresses) due to both effects of seasonal variation and trafficking-induced material deterioration.

TABLE 3 Results of the measured vertical compressive stresses

Test Section No.	Vertical Compressive Stress (kPa)				% Change due to load increase of 24%		
	Under 43.4 kN		Under 53.6 kN		@bottom of base	@top of subgrade	
	@bottom of base	@top of subgrade	@bottom of base	@top of subgrade			
1	Avg	5.9	3.5	6.0	4.3	1.2	24.8
	Std	0.8	0.5	0.5	0.2		
	COV	13%	14%	0.9%	0.5%		
2	Avg	34.5	12.0	N/a*	17.0	N/a	42.2
	Std	3.5	1.2		1.1		
	COV	10%	10%		0.6%		
3	Avg	70.4	2.6	85.2	5.3	21.0	100.4
	Std	8.6	0.5	1.6	0.4		
	COV	12%	19%	0.2%	0.8%		

* Data not available.

In general, stiffer base has better load spreading capability. As shown in Table 3, under a dual tire load of 43.4-kN, the average vertical compressive stresses at the bottom of the base layer were 5.9-, 34.5-, and 70.4- kPa for sections 1, 2, and 3, respectively; whereas, those values on the top of a subgrade were 3.5, 12.0 and 2.6-kPa, respectively. In terms of the load carrying capability, this implies that the stiff BCS/Slag material in section 1 could provide a significantly larger load spreading angle as compared to those of the other two base materials. In addition, the BCS/Flyash base in section 2 also distributed the load in a larger angle than the foam asphalt base in section 3. The highest average vertical stress at the bottom of the foam asphalt base layer in section 3 indicates that this layer would have always been in a state of high compression under the ALF wheel loading, as compared to the two other base courses in this study. On the other hand, section 3 received the smallest average vertical stresses on the top of its subgrade. By referring to pavement structures shown in Figure 1, this indicates that the cement-treated subbase used in this section performed significantly better and can provide a higher level of protection to the subgrade than the lime-treated soil layers used in other two sections, as it spreads a high pressure of 70.4 kPa at its top to a very low pressure of 2.6 kPa at its bottom.

As the load increased from 43.4-kN to 53.6-kN, the measured vertical compressive stresses increased correspondingly. However, as shown in the last two columns of Table 3, higher percentages of stress increase were found on the top of subgrade. This observation implies that a heavier truck would have a deeper influence zone and could cause more damage to a subgrade than a lighter truck does.

MDD Results

MDD measures both elastic and plastic deformations. Figure 2 shows a plot of typical elastic deflection profile obtained in this study. Figure 2 indicates that, in general, section 1 developed the smallest elastic deformations at all depths among the

three sections evaluated, followed by section 2 and section 3, which is consistent with the pressure cell measured stress results.

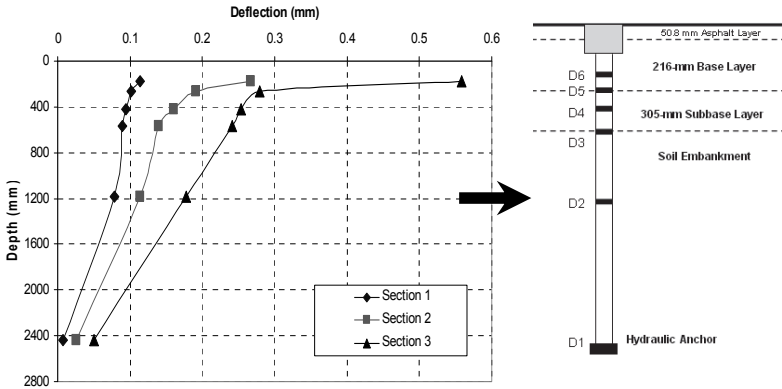
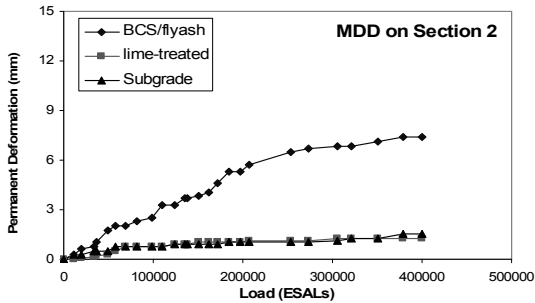


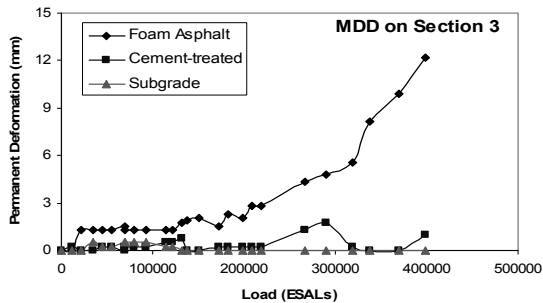
FIG. 2. Typical MDD elastic deflection profiles

On the other hand, the plastic deformation measured from MDD can be used to calculate the permanent deformation developed within each pavement structural layer. In this experiment, noticeable permanent deformations were observed on both sections 2 and 3. However, very limited plastic deformation was obtained on section 1 after 225,000 ALF passes. Figure 3 presents the MDD measured permanent deformation development curves for three pavement layers at sections 2 and 3.

Figure 3(a) indicates that a significant amount of permanent deformation was developed on the BCS/Flyash layer of section 2, with a similar small amount of permanent deformation (about 1.5 mm at the end of 400,000 ESAL repetitions) developed on both the lime-treated subbase and the subgrade. The permanent deformation data obtained on section 3 was slightly more noisy than those on section 2. As shown in Figure 3(b), a large amount of permanent deformation was also observed on the base layer (foam asphalt) of section 3, especially after 200,000 EALS repetitions. However, the permanent deformations developed on both the cement-treated subbase and the subgrade of section 3 were negligible. This observation appears to agree well with the vertical compressive stress results described above. Due to the high strength and high load carrying capability of the cement-treated subbase, only very small vertical compressive stress was developed on the top of the subgrade in section 3, which caused negligible permanent deformation to be developed in this layer.



(a)



(b)

FIG. 3. (a) Plastic deformation at section 2; (b) Plastic deformation at section 3

The primary difference between the permanent deformation development curves for the BCS/Flyash and foam-asphalt bases lies in the permanent deformation increasing rate. After 200,000 ESAL repetitions, the permanent deformation rate started to increase rapidly, indicating a rapid deterioration of the material in the vicinity of the MDD location. A preliminary investigation on section 3 revealed that such failure could be attributed to the moisture (Table 3). Laboratory Asphalt Pavement Analyzer (APA) test results (Wu, Zhang, and King 2011) revealed that the average APA rut depth for the foam-asphalt base under a wet condition (samples were submerged into water) was ten times higher than that tested in a dry condition, indicating this material is fairly water-sensitive. Since rain water is believed to have entered into the pavement through the edge of MDD surface cap, this could be the reason for the rapid deterioration of foam-asphalt base materials near the MDD location. A trench investigation will be performed at this location.

DYNAFLECT and FWD Test Results

Kinchen and Temple (1980) developed a Dynaflect-deflection based approach for structural evaluation of flexible pavements in Louisiana. In that approach, a structure

number and subgrade resilient modulus of existing pavement structures can be determined using a nomograph chart method based on a temperature-corrected Dynaflect center deflection and a spreadability value (more details may be referred to the reference).

The spreadability, Sp , is the average deflection in percent of the central deflection. It is defined as follows (Park and Fernando 1998):

$$Sp = \frac{D_0 + D_{300} + D_{600} + D_{900} + D_{1200}}{5 \times D_0} \times 100 \text{ percent} \quad (2)$$

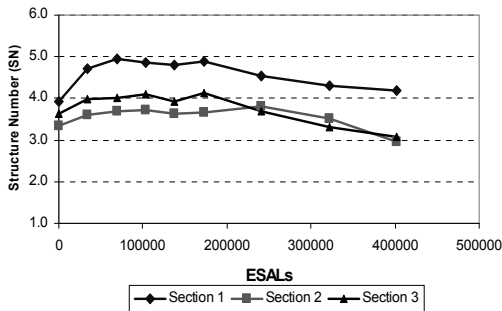
Where: D_{300} , D_{600} , D_{900} , and D_{1200} = deflections measured at 300-mm (12-in), 600-mm (24-in), 900-mm (36-in) and 1200-mm (48-in) from the center of the applied load.

Figure 4(a) presents the average structure number (SN) values predicted from DYNAFLECT test results for the three test sections evaluated under different loading passes (in ESAL values). As expected, the SN values for all three test sections generally showed a decreasing trend with the increase of the load repetitions and deterioration of pavement structures. The initial increase in SN values (before approximately 50,000 load repetitions) indicates an overall strength gain on test sections. Such overall pavement strength gain may be attributed to the post-compaction of pavement layers under wheel loading and the strength increases in those chemically stabilized base and treated subbase layers due to curing. Section 1, with a BCS/Slag base layer and lime soil sub-base, possessed the highest SN values among the three sections tested, with an initial high SN value of 5.0 and an ending value of 4.2 after 400,000 ESAL repetitions. By comparing sections 1 and 2's pavement structures, the SN results indicate that the 216-mm BCS/Slag base in section 1 generally possesses a 1.0 higher SN value than the corresponding BCS/flyash base in section 2. If the layer coefficient for BCS/flyash base was assumed to be 0.20, this would result in a layer coefficient value of 0.31 for the BCS/Slag base materials. Prior to 200,000 ESALs loading, section 3 possessed a 0.5 higher SN value than section 2. However, after 200,000 ESAL repetitions, section 3 deteriorated faster than section 2 and resulted in a similar SN value for both sections at the end of 400,000 ESALs loading. The SN change in section 3 is thought primarily due to the strength decrease for the foam asphalt base material, as showed by its rapidly increasing permanent deformation development curve in Figure 3(b).

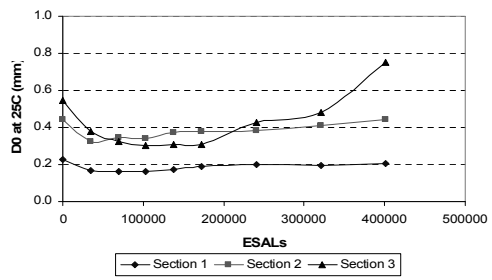
Figure 4(b) presents the average FWD center deflection (D_0) test results for the three test sections evaluated. The deflection was first normalized to a 40-kN load level and then temperature-corrected to 25 °C based on a procedure developed under the Long Term Pavement Performance (LTPP) program (Lukanen, Strubstad, and Briggs 2000). The center deflection measured directly under the FWD loading plate is used as an indicator of the composite stiffness of a pavement structure. A higher surface deflection indicates a smaller composite stiffness for a pavement structure. Similar to the SN values, the initial decrease in the center deflection is due to the post-compaction of pavement layers and the curing of base and subbase materials. Figure 4(b) shows that the center deflections of section 1 were much lower than both sections 2 and 3, but the values for sections 2 and 3 were generally similar at the beginning and then departed from each other with a higher deflection increasing rate

on section 3 (foam asphalt base pavement). This observation is generally consistent with the DYNAFLECT structure number results, which indicates that in terms of overall loading capacity, section 1 is the strongest, followed by section 2 and section 3.

Figure 4(c) presents the average spreadability (Sp) values for the three test sections evaluated. The Sp -values were calculated using Eq.2 based on FWD deflection basin results. Since a Sp -value represents an average response (or deflection) among different pavement layers relative to the overall pavement response (or $D0$) under a FWD load, it can be viewed as an indicator of the flexibility of a pavement structure. Pavement structures that had similar $D0$ values under a same FWD load would have different Sp -values because of different flexibility. High Sp -value indicates low flexibility for a pavement. In general, Figure 4(c) indicates that section 1 is more rigid than section 2, and section 2 is relatively more rigid than section 3. As the load repetitions increased, the Sp -values showed a decreasing tendency, which indicates the deterioration of a pavement structure. However, as shown in Figure 4(c), the decreasing trend in the Sp -value does not necessarily match exactly with the increasing trend for the $D0$ -value as shown in Figure 4(b).



(a)



(b)

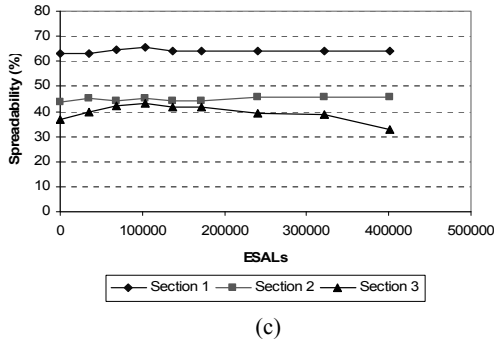


FIG. 4. (a) Dynaflect structure number results; (b) FWD center deflections; (c) FWD spreadability

Observed Pavement Distresses

The major distresses observed on the three APT test sections were permanent deformations (or rutting) at pavement surfaces. No visible cracks were found on either section 1 or 2. However, at one location on section 3, primarily due to a severe rutted surface, some localized cracks were also developed correspondingly at this location after 400,000 ESAL load repetitions.

Figure 5 presents the average rut depths versus the number of load repetitions for the three test sections. At the end of 400,000 ESAL loads, section 3 with a foamed asphalt base and cement-treated soil subbase developed the highest average rut depth, followed by section 2 with a BCS/Flyash base and lime-treated subbase. As expected, section 1 with BCS/Slag base received the smallest rut depths among test sections. It can be noticed from Figure 5 that section 3 (the foam asphalt base section) had a sudden increase in the rutting depth. Such drastic increase in the rate of rutting may be explained by the stress-dependence of pavement base materials using the Shakedown theory (Sharp and Booker 1984). When continuously increasing the stress level and passing the threshold stress of the base material, it will first go to plastic creep stage and eventually to a stage of incremental collapse, as evidenced in Figure 5 by the drastic increase in rutting rate on section 3.

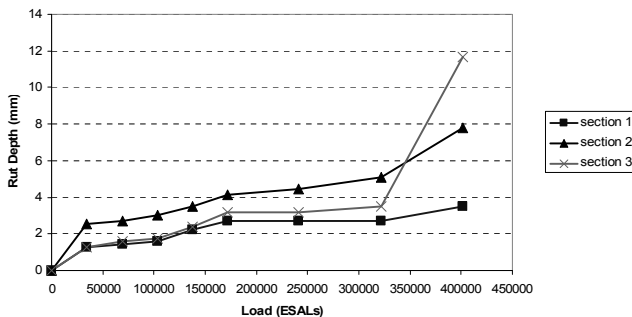


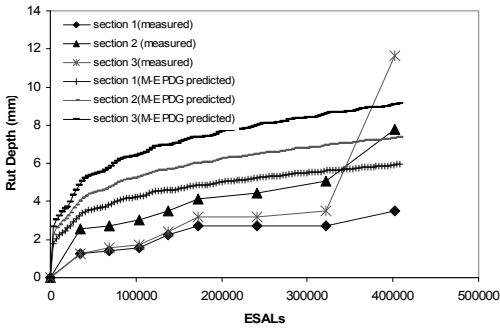
FIGURE 5 Average measured rut depths

Permanent Deformation Analysis Using the New M-E Pavement Design Guide (NCHRP 2004)

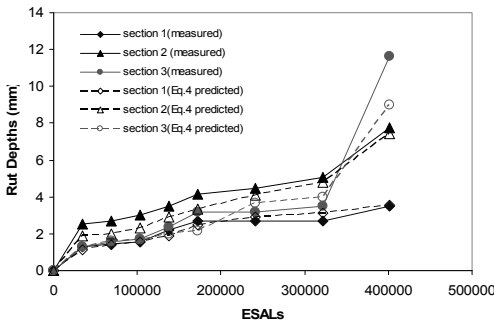
The Mechanistic-Empirical Pavement Design Guide (M-E PDG) software Version 0.900, developed under NCHRP projects 1-37A and 1-40D, was used to predict the permanent deformation development on the three test sections evaluated. A conventional flexible pavement cross-section similar to the ones shown in Figure 1 was used in the analysis. The structure is a four-layer pavement system with a single 50-mm thick asphalt concrete layer, a 216-mm thick stabilized base layer, a 305-mm thick treated soil subbase layer, and an infinite subgrade. In general, the laboratory resilient modulus test information (Table 2) was used as the design inputs for the permanent deformation development analysis. As pointed out in the M-E PDG software, the use of Level 1 input (k_1 , k_2 , k_3 values) for the base, subbase and subgrade layers is not recommended at this time because Level 1 inputs utilized the stress dependent finite element method, which has not been calibrated with distress. Therefore, Level 2 inputs were chosen for all pavement layers (other than the asphalt layer) based on the laboratory resilient modulus test results, whereas the Level 3 input was selected for the asphalt concrete layer for simplicity. The initial two-way average annual daily truck traffic (AADTT) was assumed to be 234 vehicles with 50 percent of trucks in the design direction and 95 percent of trucks in the design lane. The vehicle classification file was modified to only include 18,000 lbs single axle trucks with an axle configuration similar to the ALF load machine. Such traffic input would result in a total number of 407,000 cumulative heavy trucks (or 18,000-lbs ESAL) at the end of 10-year design life, which is close to the total ESAL repetitions in the ALF testing. In addition, the 10-year design life was chosen based on a scale factor of 10, with respect to the 1-year loading period for the APT test of this study. The environmental file was generated from the Baton Rouge weather station database included in the MEPDG software. The design reliability was set to be 90 percent.

Figure 6(a) presents the total predicted rut depths for the three test sections evaluated. In general, the M-E PDG software seems to be able to correctly rank the three test sections in terms of their overall performance in rut resistance, that is,

section 1 performed better than section 2, and section 2 was better than section 3. As compared with the average measured rut depths in those three sections, however, the M-E PDG software generally over-predicted the rut depths on all three sections before 300,000 ESAL repetitions. At the end of 400,000 ESAL repetitions, it underestimated the rut depths in section 3, and over-predicted them in sections 1 and 2. Investigating those output files from the M-E PDG software revealed that the M-E PDG software generally under-estimated the rut depths developed in the base layers in sections 2 and 3, but over-predicted rutting in the subbase and subgrade layers (refers to Figure 3). The results from this exercise suggested that the rutting models used in the M-E PDG software need to be calibrated and customized before they can be implemented for use in a local state pavement conditions, such as in Louisiana.



(a)



(b)

FIG. 6. (a) M-E PDG predicted rut depths; (b) Equation 4 predicted rut depths

Rutting Prediction Model

It is well-understood that the FWD center deflection represents a dynamic response of pavement structure due to an applied load and is indicative of composite pavement stiffness of the pavement structure. On the other hand, surface rut depths are the accumulated permanent deformation from all pavement layers, caused by the repeated traffic load applications. Theoretically speaking, FWD center deflection and surface rut depths are two different physical parameters measured for the pavement structure under the investigation. However, both these parameters would change simultaneously due to the traffic loading and the environmental effect over the time, as shown in figures 4 and 5. Therefore, empirically speaking, they may be correlated to each other based upon a damage accumulation point of view.

Ullidtz proposed a simple damage model based on Miner's law to characterize the pavement deterioration. The simple damage model uses the following equation (Ullidtz 2005):

$$Damage = A \times MN^\alpha \times \left(\frac{resp}{resp_{ref}} \right)^\beta \times \left(\frac{E}{E_i} \right)^\gamma \quad (3)$$

Where

MN = 1 million load applications,

$resp$ = pavement response (e.g. stress or strain),

$resp_{ref}$ = reference response.

E = modulus,

E_i = initial modulus, and

A, α, β, γ = model constants.

The advantage of using Eq. 3 in predicting the damage is that it can be used incrementally with the time hardening procedure (Ullidtz 2005). That means when the response or modulus changed with the changes in the load level, environmental conditions, or gradual deterioration of pavement layers due to loading, the new damage level with an increment load, dMN , should be determined from the present level of damage load repetitions and the present level of response and modulus values during the increment. The new damage level will then be input recursively to the next increment (Ullidtz 2005).

In this study, the central deflection, D_0 , under 40 kN load was chosen as the pavement response parameter in Eq. 3. Instead of using the modulus (E), the spreadability (Sp) was selected. As indicated from previous discussion, the combination of the center deflection (D_0) and a Sp -value forms a unique signature for a pavement structure under a certain load. This is based on an assumption that if two different pavement structures have the same set of D_0 and Sp -values, they will behave similarly in rutting development under traffic. Based on this assumption, a deflection-based regression model for rutting prediction was developed with FWD data collected at every 25,000 passes on each of eight stations from the three test sections. The total number of data points used in the regression analysis was 212. The resulting model parameters are given below with a R^2 value of 0.89:

$$Rut\ Depth(mm) = 5.08mm \times MN^{0.1663} \times \left(\frac{D_0}{0.3mm} \right)^{2.1433} \times \left(\frac{S_p}{80\%} \right)^{3.5293} \quad (4)$$

Eq. 4 was then used to predict the average rut depths developed at each test section. Figure 6(b) presents the prediction results. The predicted rut depth was calculated using the average FWD deflection data collected at the eight tested stations at every rut measurement cycle. As shown in Figure 6(b), the predicted rut depths using Eq. 4 appear to be matched fairly well with the measured ones for all three sections.

The above model is deemed to have important practical application. With the measured FWD deflection results and projected future traffic volumes, the future rut depth can be easily estimated. In addition, this model can be directly implemented into an M-E based pavement design procedure, since both D_0 and S_p can be estimated from elastic multi-layer pavement software for predicting rutting. The seasonal variation on the elastic characteristic of pavement materials can also be reflected through the D_0 and S_p calculation, and this model can be used incrementally with the time hardening procedure.

The major disadvantage of the proposed model is that it can not be used to predict the rut depths for individual layers of a pavement structure. In addition, although the FWD basin parameters and surface ruts were highly related in this study, variations in pavement structure and environmental effects limit the current developed rutting model applicable only for local test conditions and for the pavement sections tested. Therefore, this model needs to be further verified for different pavement structures as well as different loading and environmental conditions. Furthermore, structural normalization of deflection basin parameters is theoretically possible. Kim et al. (Kim et al 2000) proposed a structural correction procedure that normalizes those deflection basin parameter values to a standard pavement structure. A similar structural normalization procedure can be developed for the D_0 and S_p values used in the proposed rutting prediction model. More research will be performed by authors with regard to the structural normalization.

SUMMARY AND CONCLUSIONS

Three asphalt pavement test sections were instrumented and tested under accelerated loading. Non destructive deflection data and instrumentation results, collected for the duration of the accelerated loading test, were employed in the pavement structural performance analysis. The following observations and conclusions may be drawn from this study:

- Field performance measurements indicate that the BCS/Slag base material performed significantly better than its counterpart material - BCS/Flyash. This was evidenced by all measurement results obtained: low MDD measured permanent deformation, low vertical compressive stress, high structure number, small FWD center deflection and surface rutting. On the other hand, both stabilized BCS bases seemed to perform better than foam asphalt treated

base designed for this study. However, a further trench investigation is needed to confirm this observation.

- The cement-treated subbase possessed higher load-induced structural capacity than the lime-treated subbase in terms of higher resilient modulus, greater load carrying capability, and smaller permanent deformation.
- It was observed that a heavier load caused higher percent increase of vertical stresses on top of the subgrade than on top of the subbase base. Therefore, by using the cement-treated subbase with greater load carrying capability in a low-volume pavement structure, the permanent deformation developed in the subgrade due to overload traffics may be greatly reduced.
- The rutting analysis using the M-E PDG software indicates that it generally overestimated the rut depths developed in the three test sections of this study.
- A simple rutting prediction model was proposed. The proposed model, which relates flexible pavement rutting development to the in-situ surface deflection characteristics, has a potential to be directly utilized in a mechanistic-empirical pavement design and analysis. On the other hand, this model needs to be further verified for different pavement structures as well as different loading and environmental conditions.

ACKNOWLEDGMENTS

This study was supported by the Louisiana Transportation Research Center and the Louisiana Department of Transportation and Development. The author would like to express thanks to all those who provided valuable help in this study.

REFERENCES

- ASSHTO T 307 (2003). "Determining the Resilient Modulus of Soils and Aggregate Materials, *American Association of State Highway and Transportation Officials*, 2003.
- Kim, Y.R., Ranjithan, S.R., Troxler, J.D., and Xu, B. (2000). *Assessing Pavement Layer Condition Using Deflection Data*. Final Report, NCHRP Project 10-48. North Carolina State University, Raleigh, 2000.
- Kinchen, R.W. and Temple, W.H. (1980). *Asphalt concrete overlays of rigid and flexible pavements*. Report No. FHWA/LA-80/147, Louisiana Department of Transportation and Development, Baton Rouge, 1980.
- Lukanen, E.O., Stubstad, R., and Briggs, R. (2000). *Temperature Predictions and Adjustment Factors for Asphalt Pavement*. Publication FHWA-RD-98-085, FHWA, 2000.
- Mcmanis, K. (2003). *Identification and Stabilization Methods for Problematic Silt Soils: A Laboratory Evaluation of Modification and Stabilization Additives*. Final Report No. FHWA/LA-02/371, Louisiana Transportation Research Center, Baton Rouge, LA., 2003.

- Metcalf, J.B., Roberts, F.L., Rasoulilian, M., Romanoschi, S., Li, Y., and Djakfar, L. (2001). *Construction and Comparison of Louisiana's Conventional and Alternative Base Courses Under Accelerated Loading*. Final Report No. FHWA/LA-00/347, Louisiana Transportation Research Center, Baton Rouge, 2001.
- Mohammad, L.N., Herath, A., Rasoulilian, M., and Zhang, Z. (2006). Laboratory Evaluation of Untreated and Treated Pavement Base Materials: Repeated Load Permanent Deformation Test. In *Transportation Research Record: Journal of the Transportation Research Board, No. 1967*, TRB, National Research Council, Washington, D.C., 2006, pp. 78-88.
- National Cooperative Highway Research Program (NCHRP) (2004). *Guide for Mechanistic-Empirical Design of New and Rehabilitated Pavement Structures, Part 2*, Design Inputs, National cooperative highway research program (NCHRP), NCHRP 1-37A, Final Report, March 2004.
- Park, S.W., and Fernando, E.G. (1998). Sensitivity Analysis of Stress-Dependent and Plastic Behavior for loading Zoning. *Proceedings of the 5th International Conference on the Bearing Capacity of Roads and Airfields, Vol. 2*, Trondheim, Norway, 1998, pp. 627-636.
- Sharp, R. and Booker, J. (1984). Shakedown of pavements under moving surface loads. *Journal of Transportation Engineering*, ASCE, 1984, 110(1), 1-14
- Ullidtz, P. (2005). Simple Model for Pavement Damage. In *Transportation Research Record: Journal of the Transportation Research Board, No. 1905*, TRB, National Research Council, Washington, D.C., 2005, pp. 128-137.
- Wirtgen Cold Recycling Manual* (1998). Wirtgen GmbH, Hohner Straße 2, D-5357 Windhagen, 1998.
- Wu, Z., Zhang, Z., and King, B. (2011). *Accelerated Loading Evaluation of Stabilized BCS Materials in Pavement Performance*, Final Report No. FHWA/LA-09/474, Louisiana Transportation Research Center, Baton Rouge, 2011.
- Zhang, Z. and Tao, M. (2006). *Stability of Calcium Sulfate Base Course in a Wet Environment*. Final Report No. FHWA/LA-06/419, Louisiana Transportation Research Center, Baton Rouge, 2006

PERFORMANCE MEASURES AND EVALUATION OF ASPHALT PAVEMENTS USING THE INTERNAL ROUGHNESS INDEX

Ningyuan Li¹, Renjie Qin² and Zhaohui Liu³

¹ Adjunct Professor, Changsha University of Science & Technology and Senior Engineer, Ministry of Transportation of Ontario, 1201 Wilson Avenue, Ontario, Canada, M3M 1J8; Li.Ningyuan@ontario.ca
^{2&3} Professors, School of Transportation Engineering, Changsha University of Science & Technology, 45 Chiling Road, Tianxin District, Changsha, Hunan, China 410001; rjqin@126.com

ABSTRACT: International Roughness Index (IRI) has become a well-recognised tool and standard measurement of pavement riding quality. The IRI is also used by many road agencies as an end-result specification for newly constructed asphalt concrete pavements. As the IRI is a geographically transferable, repeatable, auditable, and time-stable means, it has been largely considered as a measure suitable for evaluating pavement performance evaluation. This paper describes analysis of IRI measurements provided by several contractors using different IRI measuring devices conducted on 12 representative pavement sections in Canada. Furthermore, the influence of different devices on IRI measurement is carried out through statistical analysis.

INTRODUCTION

Roughness measurement in terms of International Roughness Index (IRI) has become the primary parameter used to measure pavement surface condition. The American Society for Materials and Testing (ASTM E1777-96) assigns roughness the highest priority among performance related data for pavement management both at the project and at the network levels (ASTM 1996). Thus, the most important factor in characterizing the serviceability of a pavement is the riding quality or roughness of the traveled surface.

This paper describes calibration and verification techniques used to obtain reproducible and time-stable IRI measurements supplied by different equipment providers. As part of the objectives, this study addresses statistical analyses of IRI values measured on a calibration circuit, which is composed of 12 sections with four different pavement types in Ontario, Canada. Impact analysis of pavement profiles measured by various devices on pavement condition evaluation in terms of IRI value is presented, with some examples.

In recent years, some American states and Canadian provinces have used IRI in their business plan as well as an objective measure of their pavement network conditions

(Ashraf and Jurgens 2000). One of the key performance evaluation indices applied to highway system condition or serviceability is to use IRI measurement. Table 1 is a summary of the average IRI values measured on state or provincial highway networks, including national highway, freeway, primary and secondary highways, and local road networks.

TABLE 1. Comparisons of Average IRI among Highway Jurisdictions

DOT Name	Average IRI (mm/m)					
	NHS	Freeway	Primary Highway	Secondary Highway	Primary & Secondary	Local
CANADA						
Alberta	1.58		1.61	1.26	1.45	
British Columbia	1.53		1.60	1.95		
Manitoba	1.93		2.32	2.50		
New Brunswick	1.72		2.24	3.36		
Ontario		1.29	1.60	1.93		2.27
Quebec	2.25	1.75	2.69	2.97		
Saskatchewan	1.8		1.9	2.6		
USA	NHS	Interstate	Primary Highway	Secondary Highway	Primary & Secondary	Local
Montana	1.33	1.22	1.47	1.83		
Idaho	1.39		1.59			
Washington	1.28	1.21	1.48	1.81		
Oregon	1.89		2.03	2.46		
Minnesota	1.41	1.13	1.61	1.87		
Alaska	1.86		2.28	2.39		
North Dakota	1.43	1.09	1.43	1.56		
Utah	1.29		1.49	1.89	1.98	
Colorado	1.82	1.56			2.13	
Nevada	1.90	1.64			2.09	
Kansas*	1.27	1.26			1.38	2.76
Pennsylvania	1.75	1.39	2.07	3.35		
Iowa*	1.61		1.97			
Wisconsin*	1.87	1.72	2.0	2.29		

As summarized in (ASTM 1994), the methods and devices developed to qualify pavement roughness over the past few decades are divided into three basic categories: a) profile measuring devices - used directly to obtain pavement profile data; b) response measuring devices - which measures from the movement over a pavement surface and c) subjective ratings. Many highway agencies that have historically gathered roughness measurements using response type devices are converting their

existing data into IRI through the use of correlation techniques (Gillespie 1980). Because of its consistency in pavement performance evaluation, an IRI database can be used to develop rehabilitation and maintenance (R&M) priority strategies at the network level. The main advantages of IRI are time-stability, transferability, and readily measurable by almost all-existing profile measuring devices.

IRI measurement at network level has become a routine practice for many road agencies in recent years. At the network level, roughness is measured on an annual or biennial basis as part of pavement evaluation that is critical to formulating maintenance and rehabilitation priorities. On the other hand, IRI measurement at the project level is required primarily for accepting or price adjusting a paving contractor's product. Therefore, there is a need to standardize the pavement roughness evaluation protocol both at the project and at network levels.

By its definition, IRI is a summary statistic representing an aggregation of the profile elevation data. When it is used as an end-result specification for newly constructed asphalt concrete pavements, a relatively long base length (i.e., 100 m) would ensure the overall quality of the pavement, and a relatively short base length (i.e., 10 m) would identify very short sections of high roughness levels that would otherwise go undetected. IRI may be applied to measurement of all pavement types: exposed concrete, composite, asphalt concrete or surface-treated pavements. Thus, given an IRI parameter and relative information, a highway agency can objectively assess how the condition of its pavement network responds to the pavement investments including maintenance and rehabilitation (M&R) program and budget plan.

SCOPE AND OBJECTIVES

This study aims to analyze the influence of different factors on IRI data collected by different profilers from different test sections in Canada and proposed several recommendations for IRI measurement. In addition, analysis of IRI measurements collected by various measuring devices is presented. More specifically, the study addresses the following technical issues on IRI measurements and their impacts on pavement performance evaluation:

- a) Review of the IRI profiles measured on the calibration circuit, including pavement structures, section length and IRI measuring devices used for raw data collection and data process. If IRI measurements are done by different roughness contractors in subsequent years, it is essential to ensure that a consistent IRI measuring protocol be established which encompasses variability in measuring devices, operation procedures and calibration methods.
- b) Comparison of IRI values measured on different test sections, ranging from 10 to 150 meters in length. The 150-meter long base length would ensure assessment of the overall quality of pavement and the relative short base length distance would identify the localized areas of rough pavement that would otherwise go undetected.
- c) The influence of pavement type and wheelpath on IRI measurements based on the IRI measurements and other information collected at the IRI calibration circuit.

CALIBRATION OF PAVEMENT ROUGHNESS IRI MEASUREMENTS

The measurement of IRI using Dipstick on each pavement section in the calibration circuit is illustrated in Figure 1. Collection of pavement surface profile data of the wheelpaths is conducted in a continuous, closed loop fashion (i.e., up one wheelpath, cross over, down the other wheelpath and cross over to the starting point) using the Dipstick at 300 mm spacing.

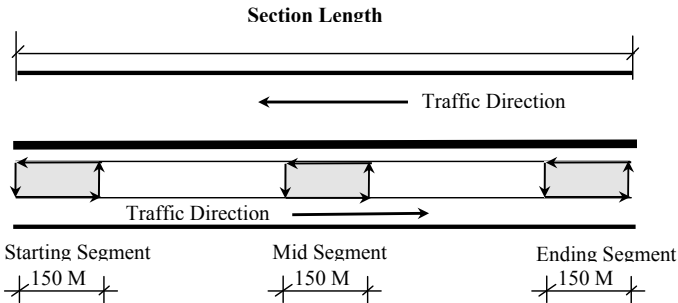


FIG. 1. A Sketch showing the segments for IRI Measurement on a section

All measurements within a pavement section were taken at three different subsections of equal length, i.e., 150 meters at the starting segment (or sub-section), 150 meters in the middle segment and 150 meters at the ending segment of the section, as shown in Figure 1. The total length of the 72 pavement longitudinal profiles measured on the 12 pavement sections was 10,800 meters (2 paths \times 150 meters \times 3 segments \times 12 sections). For the Dipstick profiler, results of IRI measurements on the calibration circuit were required to report at least the following key elements:

- Average IRI for every 10 meters, 50 meters and 150 meters (the entire length) of each pavement segment measured along the inner wheelpath, the outer wheelpath and the average of the two paths;
- Average IRI of the three pavement segments measured, which will be used to represent the mean IRI value of an entire pavement.
- Error or correction used to adjust the measurements in order to close the loop measured on each pavement segment;

Device B, C and D are all laser-based high precision profilometers and they all meet the requirements of ASTM Standard E950, with a precision of 0.35 mm a vertical resolution of 0.05 mm, and ability to perform longitudinal sampling at 25 mm when travelling at 80-100 km per hour. All of the road profilers are non-contact sensor based IRI measuring systems that record pavement profiles. The comparison of differences between IRI measurements did not include an assessment of accuracy or bias.

Precision accelerometers measure the vertical motion of the vehicle-to-road displacement for compilation of longitudinal profile. Modern profilometers use the

latest computer technology, non-contact sensors (ultra-sonic, infrared or laser), and accelerometers to accurately and quickly measure the longitudinal profile of a road. All measurements are independent of variation in vehicle weight, speed, temperature, wind or pavement colour and texture. The profile data points were averaged and recalculated at 304.8 mm intervals to obtain the 1057 points required in E950 to calculate the precision and bias. All of the individual IRI measuring devices are efficient, highly accurate with professional data collection and delivery capabilities. These devices are easy to use, and have superior resolution and repeatability. On-board computers provide automatic calculation of roughness statistics such as IRI and RN (Ride Number). They are capable of detecting all wavelengths that affect the ride quality.

Roughness measured by response-type devices, such as Device E defined in the study, are dependent on the system dynamics and operating procedures including vehicle characteristics (suspension, spring/damper, tire stiffness, etc.), the travel speed and other operating factors. Output from Device E measuring system gives RMSVA, which is converted into Riding Comfort Index (RCI) and then converted into IRI through regression equation between the two indices.

TABLE 2. Basic Parameters of the Profiling Devices Used at the Calibration Circuit

Device	Type of Device	Key Parameters	Description
A	Digital Incremental Dipstick	300 mm sampling and recording intervals, manual	Capable of measuring longitudinal profiles (as a series of elevation points) at sampling rate less than 250 mm and precision of less than 0.5 mm. Class 1 Device
B, C, D	Laser - based High Precision Road Profilometers	< 150 mm sampling interval Operating speed: 80 km/hr 1.65 - 1.670 m wheelpaths	The profile sensors are mounted in the front of vehicle spaced at 1.67m. One of the devices has been used by LTPP-North Atlantic Regional Office for LTPP Testing sites. Class 2 Device.
E	Response Type Measuring Systems	< 300 mm sampling interval, 80 km/hr operating speed	Measure a vehicle's response travelling on the profile or measure / surface distortion relative to reference platform moved along the road. Class 3 Device.

During May 2000, five different profilers including the Dipstick were used to measure IRI profiles on the twelve (12) selected pavement sections comprising the calibration circuit. Those used for roughness measurements at the calibration circuit included the Dipstick, response-type measuring systems, and profile-based measuring devices. The purpose of the comparison was to evaluate and select a contractor for doing the entire network pavement roughness IRI measurements on the basis of individual vendor's IRI measurement results as comparing with that measured by Class I Dipstick IRI measuring device. The calibration circuit was used to compare the IRI values measured on the same pavements but with different devices. These individual devices

are denoted in this paper as Device A, B, C, D and E, respectively. The basic parameters of the five individual IRI measuring devices are summarized in Table 2.

COMPARISON OF THE IRI VALUES MEASUREMENTS

Figure 2 shows the average IRI value measured on both inner and outer wheelpaths of each pavement section in the calibration circuit by the 4 devices. Among the 12 pavement sections measured, the IRI values calculated by the four different measuring devices are comparable or close to each other except for Section 7 and 10. It should be noted that both Section 7A and 7B are PCC pavements and Section 10 is a surface-treated pavement. Based on this figure, it leads a conclusion that Device E is not suitable for use in measuring IRI of rigid pavements. The tined texture of this pavement type results in additional pseudo-excitation of the accelerometer resulting in fictitiously high RMSVA values. A similar result occurs on surface-treated pavements with their coarse macro-texture.

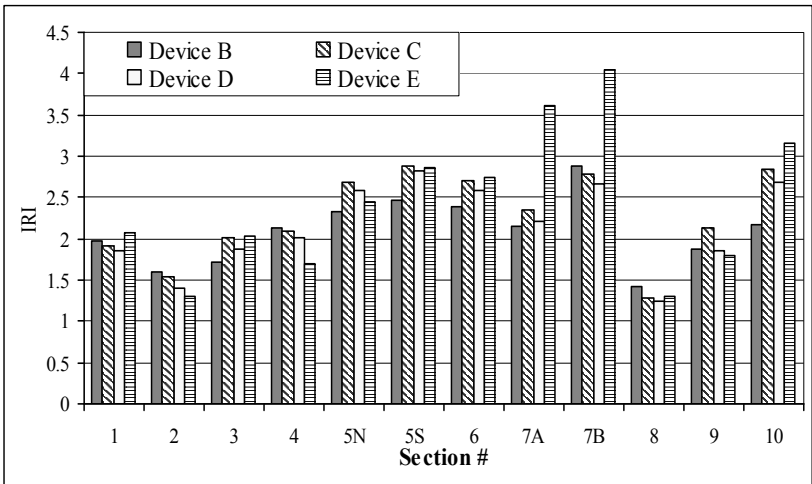


FIG. 2. Comparison of Average IRI Measured by Four Different Devices

Considering the time-consuming nature of the operation and associated costs, the Dipstick device was required to measure only three segments on each pavement section: the starting segment, the middle segment and the ending segment of the section, with each segment being 150 - meter long. IRI measurements on each segment are recorded in every 10, 50 and 150 meters. All measuring devices except the Dipstick were used to measure the whole pavement section with similar summary reporting intervals.

Figure 3 shows the differences of the average IRI measured along the outer wheelpath on three segments of the pavement sections profiled by the three different types of

measuring devices. By comparing with each other, it is obvious that Device B measurements are closer to the measurements from Dipstick although both Device B and C are laser based high precision profilometers. Regression analysis was conducted to examine their individual relationships and statistical parameters based on IRI measurements performed by the three measuring devices.

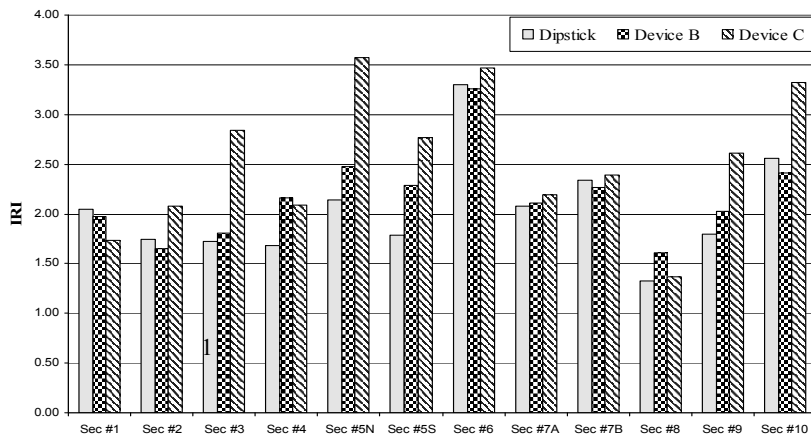


FIG. 3. Comparison of Average IRI Measured by Three Different Measuring Devices

As shown in Figure 4, a good linear relationship exists between Dipstick measurement and Device B, while the relationship between Dipstick and Device C turns less linear relationship (Figure 5) with several scattered measurements. The figure compares the average IRI measurements obtained from all 12 sections of the circuit by the three IRI measuring systems. The higher R square value from the regression between the IRI measurements from the Dipstick and Device B indicates that 80 percent of measurements performed by these two devices can be explained or converted by using the regression equation. It is clear that calibration produces more consistent results if it is done on an individual wheelpath basis. Both Device B and C have good correlations with Dipstick based on the IRI measurements from the outer (or right) wheelpath.

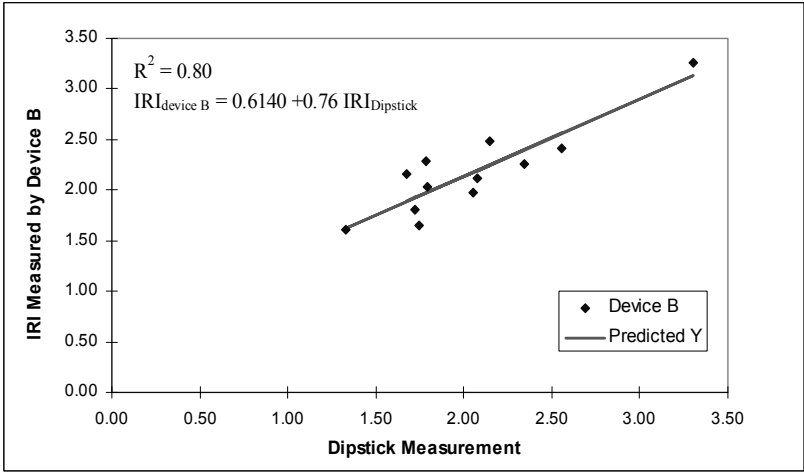


FIG. 4. Regression Between IRI Measurements by Dipstick Versus Device B.

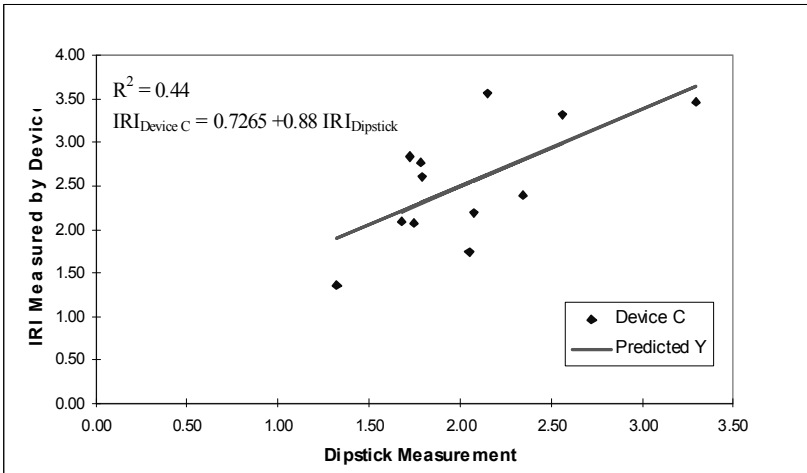


FIG. 5. Regression Between IRI Measurements by Dipstick and Device C

A specific study issue was the correlation between IRI values measured on the outer wheelpath of each individual pavement segments by Dipstick and the two sensor based IRI measuring devices. A high correlation between the two devices would provide a mechanism of transforming IRI values measured from one to another for network level monitoring. The results show that the Device B can reproduce the Dipstick-IRI with a high level of confidence. The R square value indicates that 80 percent of the predicted are explained by this equation. Device C results indicated a lower level of confidence when compared to the Dipstick. The overall mean IRI values of the three segments obtained for all sections by the three IRI-measuring systems were 2.04, 2.17 and 2.54 m/km, respectively for the Dipstick and Device B and C. The differences between the overall means were highly statistically-significant judging by a paired t-test.

FACTORS INFLUENCING IRI MEASUREMENTS

Effect of Segment Length on IRI Measurement

Given a pavement section, is there a cost-effective approach to ranking or assigning an IRI value for the pavement without measuring the entire length of the section. This will have a significant meaning to any highway agency that would otherwise save substantial amount of time and resources in performing annual IRI data collection.

Table 3 shows an example comparing the average IRI values measured by Device B along the whole section with that measured along the three segments within the section. For each section, the Table 3 gives the average IRI values measured along the inner wheelpath and outer wheelpath separately. It is apparent that the averaged IRI of the 3 segments within a section is different from the average IRI measured on the whole length of the same section, ranging from 1.15 m/km to 0.76 m/km in absolute value measured on the inner wheelpath, and 1.09 m/km to 0.86 m/km on the outer wheelpath.

TABLE 3. Impact of Measuring Length on IRI Values (m/km)

Section	Section Length	Average IRI of the 3 Segments Versus Entire the Section along Inner Wheelpath			Average IRI of the 3 Segments Versus Entire the Section Along Outer Wheelpath		
		Segment	Section	Difference	Segments	Section	Difference
1	1.428	2.18	2.15	0.03	1.98	2.19	-0.21
2	1.300	1.35	1.75	-0.40	1.65	2.04	-0.39
3	2.400	1.64	1.17	0.47	1.81	1.63	0.18
4	2.410	1.37	2.52	-1.15	2.16	3.25	-1.09
5 N	1.036	2.37	2.14	0.23	2.48	2.17	0.31
5 S	1.036	2.27	2.21	0.06	2.29	2.56	-0.27
6	1.424	2.35	2.52	-0.17	3.25	2.39	0.86
7A	1.800	1.99	2.29	-0.30	2.11	2.33	-0.22
7B	1.540	2.23	1.47	0.76	2.26	2.77	-0.51
8	1.516	1.14	1.70	-0.56	1.61	1.74	-0.13
9	1.480	1.68	1.35	0.33	2.03	1.85	0.18
10	1.040	2.19	2.01	0.18	2.41	1.94	0.47
Average	1.53	1.90	1.94	-0.04	2.17	2.24	-0.07

Table 3 also indicates that if we consider the 12 sections as a small network within

18.3 km of roads in total, the average IRI is 1.90 measured on 5.4 km of the total segments while the average IRI is 1.94 measured on the total 18.3 km of the pavement sections. The difference is 0.04 m/km, which is only a 2 percent difference of the IRI value measured on the whole network. A similar conclusion can be drawn from comparisons of the IRI measurements performed by Device C. Since the Dipstick did not measure the entire length, there is no data available for comparing IRI measurements performed by Dipstick along partial (segments) and the entire section.

Influence of Wheel Path or Profile location

For the purpose of calibrating various measuring devices, it is recommended that IRI profiles measured on either inner or outer wheelpath be used. In addition, a study was conducted to analyze the profile data IRI measured on the same wheelpath in opposite directions which may differ in spectral frequencies. This study was recommended that correlation between averaged measurements over the two wheelpaths and for two directions (of the same wheelpath) be tested separately.

TABLE 4. Impact of Measuring Length on IRI Values

Section	Device A		Device B		Device C	
	Middle of wheelpaths	Outer wheelpath	Inner wheelpath	Outer wheelpath	Inner wheelpath	Outer wheelpath
1	2.59	2.05	2.18	1.98	2.23	1.74
2	1.68	1.74	1.35	1.65	1.63	2.07
3	1.59	1.72	1.64	1.81	1.64	2.84
4	1.57	1.68	1.37	2.16	1.69	2.09
5 N	1.91	2.14	2.37	2.48	2.09	3.57
5 S	2.14	1.79	2.27	2.29	2.41	2.77
6	2.21	3.30	2.35	3.25	2.19	3.47
7A	1.98	2.07	1.99	2.11	2.12	2.19
7B	2.39	2.34	2.23	2.26	2.40	2.39
8	1.18	1.33	1.14	1.61	1.20	1.37
9	1.91	1.79	1.68	2.03	1.72	2.61
10	2.14	2.56	2.19	2.41	2.39	3.32
Average	1.94	2.04	1.90	2.17	1.98	2.53

Table 4 shows a summary of the IRI profiles measured on both inner and outer wheelpaths by device B and device C, plus the IRI profiles measured by device A on outer wheelpath and the profile between the two paths using Dipstick. The IRI differences between the left, the middle and the right paths measured by Devices A, B and C are significant for some individual sections (e.g., Section 2, Section 4 and Section 10). However, the average IRI summarised for the all sections are not significant except for the last column (IRI measured along outer wheelpath of the all sections measured by Device C). Overall, Table 4 indicates that the right wheelpath was rougher than the left.

In view of Table 4, concrete pavements (Section 7A and 7B) have significant

influence on the IRI measurements performed by Device E, as against the IRI measurements performed by other three devices. The surface-treated pavement (Section 10) has also shown a certain degree of difference but not significant between the IRI measured performed by Device B and E.

The output can be processed to give IRI at various distance intervals (e.g., 50, 100, 150m, etc.) or raw profile elevation data at various sampling intervals (e.g., 300 mm). The 50 m interval IRI was used to check the uniformity of roughness over the calibration sections. The 150 m interval IRI (mean for each calibration section) was used to correlate with Dipstick results.

CONCLUSIONS

Based on observations of the IRI measurements conducted on the 12 complete pavement sections at the calibration circuit, the differences of IRI values measured on a pavement section with different devices may negatively affect monitoring of pavement performance trends on a network level and a project level. The IRI measuring systems can not be used interchangeably and must be calibrated to match the existing historical roughness measurement scale.

The use of IRI by a highway agency has several advantages, including normalized, reproducible and time stable roughness measurements and enable highway agencies to solicit IRI measurement services for obtaining actual pavement profiles for both network level and project-level work. Based on the data analysis conducted in this study, it is recommended that road agencies design and implement regular annual programs for calibrating roughness devices as a mandatory practice in standardizing their roughness databases. In order to ensure a consistent and transferable network-wide roughness database, it is important to establish a rigorous approach to calibrating IRI measurements especially when different measuring devices are used each year. Some of the major findings to date can be summarized as follows:

- a) A linear relationship between the Dipstick and the laser based IRI measuring systems exists with high confidence level. The best correlation was found for single wheelpath in one direction. Averaging IRI values over the two wheelpaths produced relatively lower but acceptable correlation.
- b) There were systematic differences between IRI measurements provided by different measuring devices. The average overall difference in IRI obtained for the 12 pavement sections ranged from 0.01 to 1.0 m/km. The systems cannot be used interchangeably without proper calibration and Q.A. protocol being established.
- c) The study showed that individual measuring devices have correlation differences when compared with the Dipstick measured IRI, due to mechanical and electronic variations between devices because of measurement errors and mechanical variations.
- d) Although IRI measurement speed was not discussed in this paper, it is suggested that a correlation be used to normalize the IRI output to the standard speed. If measurements can not be taken at standard speed due to road geometric or traffic and safety related constraints, a functional relationship

between IRI measured at standard speed versus IRI measured at another speed should be established for calibration purpose.

REFERENCES

- American Society of Testing and Materials. Standard Guide for Prioritization of Data Needs for Pavement Management, *ASTM Book of Standards*. Vol.04.03. Designation E 1777-96, 1996.
- American Society of Testing and Materials. Measuring the Longitudinal Profile of Traveled Surfaces with an Accelerometer Established Inertial Profiling Reference. *ASTM Book of Standards*. Vol. 04.03. Designation E 950-94, 1994.
- Ashraf, M and R. Jurgens, Uses and Comparison of IRI with Other Jurisdictions, Document Reported by Alberta Infrastructure Transportation and Civil Engineering Division, Alberta Government, June 8, 2000.
- Gillepsie, T.D., Sayers, M, and Segel, L. Calibration of Response Type Road Roughness Measuring Systems, *National Cooperative Highway Research Program Report #228*. Transportation Research Board, National Research Council, Washington, D. C., 1980.

DESIGN OF PLANAR GEOSYNTHETIC-IMPROVED UNPAVED AND PAVED ROADS

Jie Han¹

¹ Professor, Department of Civil, Environmental, and Architectural Engineering, the University of Kansas, Lawrence, KS 66045, USA

ABSTRACT: Geosynthetics (geotextile, geogrid, geocell, geocomposite, and geomembrane) have been increasingly used for the construction of roadways to reduce required base thickness and/or prolong pavement life. The improvement of pavement performance is achieved by geosynthetics through separation, filtration, drainage, reinforcement, and/or containment. This paper summarizes the methods commonly used in the United States to design planar geosynthetic-improved unpaved and paved roads when geotextile, geogrid, or geocomposite is used for separation, drainage, and/or reinforcement.

INTRODUCTION

Geosynthetics (geotextile, geogrid, geocell, geocomposite, and geomembrane) have been increasingly used for the construction of roadways to reduce required base thickness and prolong pavement life. Their functions in the roadway applications include separation, drainage, reinforcement, and/or containment. Nonwoven and woven geotextiles have apparent advantages for separation between fine-grained subgrade and coarse-grained base courses. Geocomposites, formed by a geonet and a geotextile, can provide a drainage path to remove water entering the roadway system. Geogrid, a planar reinforcement, and geocell, a three-dimensional reinforcement can interact with base course materials and provide lateral confinement to minimize rut depths and the chance of fatigue failure. Geomembranes are mostly used as barriers for moisture-sensitive soils, such as expansive soils, to prevent water from entering the roadway system.

Geosynthetics for roadway applications include unpaved roads, paved roads, and railroads. Unpaved roads (i.e., without a pavement surface) are commonly constructed as local, low volume roads and temporary construction platforms. AASHTO (1993) defined low volume roads as those expected to carry traffic loads for less than 100,000 ESALs (Equivalent Single Axial Loads). Paved roads include flexible (asphalt) and rigid (concrete) pavements. However, geosynthetics have been

used as reinforcement mostly for flexible pavements and used as separation and drainage for both flexible and rigid pavements. The research and application of geosynthetics for railroads in the United States are limited; therefore, no further discussion will be presented herein. Geomembranes have been placed vertically, horizontally, or in a combination around expansive soil to prevent water intrusion into the expansive soil. This application has been used in limited locations due to the nature of the problems. A technical book by Steinberg (1998) may be sought on this application; therefore, no further discussion will be provided in this paper. Geocells, as three-dimensional geosynthetics, have been increasingly researched and used in the past few years. The recent advances in the use of geocells for unpaved and paved roads can be found in the publications, for example, Han et al. (2011), Pokharel et al. (2011), Acharya (2012), and Yang et al. (2012). The objective of this paper is to summarize the methods commonly used in the United States to design planar geosynthetic-improved unpaved and paved roads when geotextile, geogrid, or geocomposite is used for separation, drainage, and/or reinforcement.

DESIGN OF GEOSYNTHETICS FOR SEPARATION

When granular bases are used above fine-grained subgrade, fine particles in the subgrade may migrate into base courses and continue moving up to the roadway surface under wheel loading. The loss of fine particles in the subgrade would weaken its support for the pavement structure and create space for base courses to settle in so that ruts form on the surface. On the other hand, when granular particles are directly in contact with the subgrade, they would penetrate or sink into the subgrade, especially for a soft subgrade, under wheel loading. Both mechanisms would cause the intermixing of base and subgrade, which deteriorate the quality of the base courses and eventually affect the performance of the roadway. To avoid these problems, a nonwoven or woven geotextile can be used as a separator between the base and the subgrade.

To ensure the geotextile functions as a separator, it must first survive construction. The serviceability of the geotextile during the construction depends on the subgrade condition, quality of base material, and construction equipment. AASHTO M288-96 defines three classes of geotextile products based on their serviceability during the construction as presented in Table 1. For separation of subgrade soil with soaked CBR > 3 or undrained shear strength > 90 kPa, which is a typical roadway construction condition, Class 2 geotextile should be used. When the subgrade soil has a CBR of 1 to 3 or undrained shear strength of 30 to 90kPa, reinforcement of the subgrade is needed. As a result, Class 1 geotextile or geogrid should be used. The design of geosynthetics for subgrade improvement or base reinforcement will be discussed later. The required properties of Class 2 geotextiles are provided in Table 2. The required properties of other classes can be found in the AASHTO M288-96 Specifications. These strength values ensure the geotextile would not be damaged during the construction thus affecting its effectiveness as a separator. Geotextiles typically have large tolerable tensile strain before rupture. Strains less or more than 50% have been used to define the strength requirements of geotextiles. Details of these test methods can be found in ASTM standards. Permittivity is a parameter to

evaluate the rate of water flow through the geotextile perpendicular to the plane of the geotextile. This parameter becomes important when there is a requirement for filtration. AOS stands for apparent opening size of geotextile. This parameter is important for the geotextile to retain fine particles as one of the important functions of the separator but still provide enough drainage for water through the geotextile. UV stability is a parameter to ensure the long-term stability of the geotextile exposed to UV. Typically, geotextile products would reduce their strengths after exposed to UV. The minimum requirements for the above parameters for a geotextile used as a separator are provided as follows: Class 2 geotextile, permittivity = 0.02 s^{-1} , AOS = 0.60 mm, and 50% retained strength after 500 hours of exposure to UV.

TABLE 1. Classifications of Geotextiles in AASHTO M288-96 Specifications

Class	Description
Class 1	For severe or harsh survivability conditions where there is a greater potential for geotextile damage
Class 2	For typical survivability conditions; this is the default classification to be used in the absence of site specific information
Class 3	For mild survivability conditions

TABLE 2. AASHTO M288-96 Class 2 Geotextile Property Requirements

	Test methods	Units	$\epsilon < 50\%$	$\epsilon \geq 50\%$
Grab strength	ASTM D4632	N	1100	700
Sewn seam strength	ASTM D4632	N	990	630
Tear strength	ASTM D4533	N	400	250
Puncture strength	ASTM D4833	N	400	250
Burst strength	ASTM D3786	kPa	2700	1300
Permittivity	ASTM D4491	s^{-1}		
AOS	ASTM D4751	mm	Based on geotextile applications	
UV stability	ASTM D4355	%		

ϵ = strain of geotextile

DESIGN OF GEOSYNTHETICS FOR DRAINAGE

It is well known that water is detrimental to performance and life of roadways at least in the following ways: (1) softening subgrade, (2) intermixing subgrade and base, (3) causing expansion in expansive soil, (4) causing freezing and thaw problems in fine-grained soils in winter and spring, (5) stripping of hot-mix asphalt, and (6) erosion of concrete pavement foundations. Removal of water would minimize damage, maintain performance, and prolong life of roadways. The benefits of good drainage have been recognized in roadway design including the 1993 AASHTO Design Guide. Drainable aggregate layers have been successfully used in rigid and flexible pavements. AASHTO (1993) defined the quality of pavement drainage from excellent (two hours) to very poor (does not drain) based on the time for water to be

removed within the pavement system. However, to provide enough drainage capacity necessary for good to excellent drainage, a thick drainable base (typically 10 to 30 cm thick) is needed. FHWA (1992) recommended that a drainable base should have a minimum permeability of approximately 300 m/day, which can remove water from the roadway system within a few hours (i.e., an excellent drainage defined by AASHTO).

Geocomposites, formed by a drainable core (commonly a geonet) wrapped around by a nonwoven geotextile layer, have a higher drainage capacity than an aggregate layer. Therefore, a thin geocomposite can serve equally or better than a thick aggregate layer. The geocomposite drain can be placed between the subgrade and the base to shorten the drainage path for the base. Since the geocomposite drain is highly permeable, the effective drainage distance for the water to leave the pavement system is the thickness of the base course rather than the width of the road lane. This shortened drainage distance significantly reduces the time to drain. The geocomposite drain can also be placed between a concrete pavement and a subgrade or a frost susceptible soil and a subgrade.

To provide equivalent drainage capacity to a 10-cm free-draining base layer with a transmissivity (i.e., permeability multiplied by the thickness) of approximately 30 to 100 m²/day, the required transmissivity for a geocomposite drain is approximately 90 to 300 m²/day due to unconfined, partially filled flow within the drainage layer (Giroud et al., 2000; Christopher and Zhao, 2001). In addition, the geocomposite drain should have enough crush resistance to withstand construction and compaction loading from 480 kPa beneath the base course to as high as 1,450 kPa beneath the asphalt layer, which is higher than the stress on the geocomposite drain during trafficking (Christopher and Zhao, 2001).

The 50% percent drained approach recommended by FHWA (1992) can be used to determine the time to drain as follows:

$$t = T_{50} \cdot m \cdot 24 \quad (1)$$

where t = time to drain in hours; T_{50} = time factor; and m = “m” factor. The time factor, T_{50} , can be determined from Figure 1 based on the slope factor, S_1 , which depends on the resultant slope, S_R , length, L_R , and thickness, h , of the drainage layer:

$$S_1 = \frac{L_R S_R}{h} \quad (2)$$

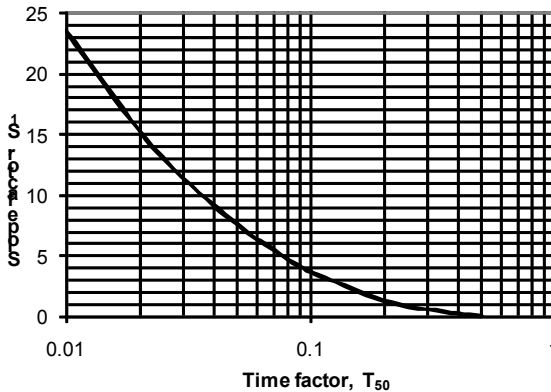


FIG. 1. Time Factor for 50 Percent Drainage (FHWA, 1992)

If the geocomposite drain is placed directly underneath the pavement and above the subgrade, the drainage only happens in the geocomposite. The design parameters, S_R , L_R , and h refer to the geocomposite drain. The slope and length of the drainage layer, S_R and L_R , are equal to the slope and the width of the pavement section. h is equal to the thickness of the composite drain. However, if the geocomposite drain is placed between the base and the subgrade, the time to drain includes the time needed for water to drain through the base and the geocomposite. The time needed for water to drain through the base can be calculated using $S_R = 1$ and L_R and h both equal to the thickness of the geocomposite. The time for water to drain through the geocomposite drain is the same as that for the geocomposite directly underneath the pavement.

The “m” factor can be determined by the following equation:

$$m = \frac{N_0 L_R^2}{kh} = \frac{N_0 L_R^2}{\psi} \tag{3}$$

where N_0 = effective porosity of the drainage layer; k = permeability of the drainage layer; ψ = transmissivity of the drainage layer. The effective porosity is the ratio of the volume of the drainable water in the material to the total volume of the material.

In order for the geocomposite drain to be effective in a long term, the nonwoven geotextile around the drainage core should meet the requirements for filtration. AASHTO (1991) recommended the following requirements: (1) for soil with less than 50% passing the No. 200 sieve, AOS \geq No. 30 sieve and (2) for soil with more than 50% passing the No. 200 sieve, AOS \geq No. 50 sieve.

DESIGN OF GEOSYNTHETICS FOR REINFORCEMENT IN UNPAVED ROADS

Design of geosynthetics for subgrade improvement for unpaved roads has been based on the concepts of local bearing capacity failure and an increase of bearing capacity by the use of geosynthetics. A tensioned membrane effect is sometimes considered in the design; however, its effect is minimal unless an excessive rut depth is allowed. Geogrids and woven geotextiles have been mostly used for improvement of soft subgrade with CBR less than 3 (Berg et al., 2000). For extremely soft subgrade (i.e., $CBR < 1$ and undrained shear strength less than 30 kPa), geogrid should be used with a nonwoven geotextile to provide separation. The design methods developed so far are empirical or semi-empirical and have been used for many projects.

A comprehensive design method proposed by Giroud and Han (2004a and 2004b) as follows can be used for unreinforced and geotextile or geogrid-unpaved roads. In this method, a stress distribution method is used to estimate the stress at the interface between the base and the subgrade based on Burmister's two-layer solution. This model considers the variation of the stress distribution angle with the number of traffic passes based on the laboratory test data obtained by Gabr (2001). The decrease of the stress distribution angle can be explained as the deterioration of the base quality. The bearing capacity failure (assuming 75 mm rut depth) happens when the stress distribution angle decreases to a certain value and the stress at the interface exceeds the strength of the subgrade. The inclusion of the geosynthetic at the interface can slow down the deterioration rate of the base quality and increase the bearing capacity of the subgrade so that the life of the unpaved road is extended. Giroud and Han (2004a) correlated this deterioration rate to the aperture stability modulus for two specific biaxial geogrid products for geogrid-reinforced unpaved roads. Webster (1992) and Collin et al. (1996) also found that the aperture stability modulus of a geogrid was shown to give good correlation with the measured performance of paved roads. Measurement of the aperture stability modulus is presented in a draft test method by Kinney (2000). Giroud and Noiray (1981) suggested that the bearing capacity factors for the failure of unreinforced and geotextile-reinforced roads are 3.14 and 5.14, respectively. Considering the rough interface between the geogrid with stones and the subgrade, the bearing capacity factor of 5.71 was suggested by Giroud and Han (2004a) for a geogrid-reinforced road.

Considering all the above factors, a formula for estimating the required base thickness was developed by Giroud and Han (2004a) as follows:

$$h = \frac{0.868 + (0.661 - 1.006J^2) \left(\frac{r}{h}\right)^{1.5} \log N}{1 + 0.204[R_E - 1]} \left[\sqrt{\frac{P}{\pi r^2}} - 1 \right] r \quad (4)$$

$$\left[\sqrt{\frac{s}{f_s}} \left[1 - 0.9 \exp\left(-\left(\frac{r}{h}\right)^2\right) \right] N_c f_c CBR_{sg}} \right]$$

where h = required base course thickness (m); P = wheel load (kN); N = number of passes of axle; J = aperture stability modulus of geogrid (with $J = 0$ for unreinforced and geotextile-reinforced unpaved roads); r = radius of equivalent tire contact area; R_E = limited modulus ratio of base course to subgrade soil; s = allowable rut depth (mm); f_s = factor equal to 75 mm; N_c = bearing capacity factor. For unreinforced unpaved roads, $J = 0$ and $N_c = 3.14$. For geotextile-reinforced unpaved roads, $J = 0$ and $N_c = 5.14$. For geogrid-reinforced unpaved roads, $J > 0$ and $N_c = 5.71$. f_c = factor equal to 30 kPa; $CBR_{sg} = CBR$ of the subgrade soil.

Based on field data, Giroud and Han (2004a) suggested that the modulus ratio of base course to subgrade should be limited to 5.0 as follows:

$$R_E = \min\left(\frac{E_{bc}}{E_{sg}}, 5.0\right) = \min\left(\frac{3.48 CBR_{bc}^{0.3}}{CBR_{sg}}, 5.0\right) \quad (5)$$

where E_{bc} = moduli of base course, which can be estimated by $E_{bc} = f_{EBC} CBR_{bc}^{0.3}$, $f_{EBC} = 36$ MPa; E_{sg} = modulus of subgrade, which can be estimated by $E_{sg} = f_{ESG} CBR_{sg}$, $f_{ESG} = 10.35$ MPa; CBR_{bc} = CBR of base course; and CBR_{sg} = CBR of subgrade.

The required base thickness can be solved using Equation (4) by iterations.

DESIGN OF GEOSYNTHETICS FOR REINFORCEMENT IN PAVED ROADS

Design of geosynthetics for paved roads (commonly referred as base reinforcement) has been conducted by modifying the AASHTO 1993 Design Guide including the benefits of geosynthetics. Two common design parameters, Traffic Benefit Ratio (TBR) and Layer Coefficient Ratio (LCR), have been proposed to consider the benefits of geosynthetics. The purposes of geosynthetics used as base reinforcement are to reduce the required base thickness and prolong pavement life. In the past few years, great efforts have been made to develop a mechanistic-based design method for this application. However, no such method has been adopted by AASHTO, FHWA, or geosynthetic industry. Base reinforcement has been used for low to medium strength subgrade of CBR up to 8 with noticeable benefits to different degrees. Very few states consider the use of geosynthetics for base reinforcement as standard practice. A number of agencies are or have considered their use on an experimental basis. However, the majority of states have not used geosynthetics for base reinforcement. The main reasons for the states not to use this technology are (1) the lack of information regarding whether there is a cost benefit for this technology and (2) the lack of an acceptable design method.

In the AASHTO 1993 Design Guide, the number of 18-kip (80 kN) equivalent single axle (ESAL) load applications is used to define the number of the equivalent traffics based on standard highway truck axle loads and can be estimated by

$$\log_{10}(W_{18}) = Z_R S_0 + 9.36 \log_{10}(SN+1) - 0.20 + \frac{\log_{10} \left[\frac{\Delta PSI}{4.2-1.5} \right]}{0.40 + \frac{1094}{(SN+1)^{5.19}}} + 2.32 \log_{10}(M_R) - 8.07 \quad (6)$$

where W_{18} = predicted number of 18-kip equivalent single axle load applications (ESALs); Z_R = standard normal deviate (dimensionless); S_0 = combined standard error of the traffic prediction and performance prediction (dimensionless), 0.45 commonly used; ΔPSI = difference between the initial design serviceability index, p_0 , and the design terminal serviceability index, p_t (dimensionless); and M_R = resilient modulus (psi).

The serviceability index, ΔPSI , is defined as the difference between the initial serviceability and the terminal serviceability, i.e.,

$$\Delta PSI = p_0 - p_t \quad (7)$$

where p_0 = initial serviceability (use 4.2 for flexible pavements based on the AASHTO Road Test); p_t = terminal serviceability (use 2.5 or higher for major highways, 2.0 for highways with lesser traffic volume, and less than 2.0 for minor highways).

Based on Equation (6), the number of ESALs also depends on the resilient moduli of pavement structural layers (surface, base, subbase, and subgrade), which define the elastic response of each layer under repeated loading. The resilient modulus can be measured using a dynamic triaxial test apparatus. The resilient modulus of a fine-grained subgrade with a soaked CBR of 10 or less can be estimated using the following correlation:

$$M_R (\text{psi}) = 1500 CBR_{sg} \quad (8)$$

Because Equation (6) was developed based on English units, the resilient modulus of a pavement layer should be expressed in English units.

A structural number is defined in the AASHTO 1993 Design Guide to represent the capacity of the pavement structure in addition to the subgrade, which is expressed as

$$SN = a_1 D_1 + a_2 D_2 m_2 + a_3 D_3 m_3 \quad (9)$$

where a_1, a_2, a_3 = layer coefficients representative of surface, base, and subbase courses, respectively, which can be found in the AASHTO 1993 Guide; D_1, D_2, D_3 = actual thicknesses (in inches) of surface, base, and subbase layers, respectively; and m_2, m_3 = drainage coefficients for base and subbase layers, respectively, which are provided in AASHTO (1993).

As discussed earlier, the geocomposite drain can be used to improve the quality of drainage so that a higher drainage coefficient can be used to prolong the life of the pavement and/or reduce the thickness of the base.

For practical and economic considerations, the AASHTO 1993 Design Guide recommended the minimum thickness requirements for the asphalt concrete and the aggregate base based on the level of traffic.

Two empirical methods are available to consider the effects of the geosynthetic reinforcement for paved roads: (1) the Traffic Benefit Ratio (TBR) method and (2) the Layer Coefficient Ratio (LCR) method. Both methods modify the AASHTO 1993 Design Guide.

In the TBR method, TBR is introduced and defined as: the ratio of the number of cycles necessary to reach a given rut depth for a test section containing reinforcement divided by the number of cycles necessary to reach this same rut depth for an unreinforced section with the same section thickness and subgrade properties. Laboratory and field test results show that the TBR values for geotextiles and geogrids range from 1.5 to 10 and 1.5 to 70, respectively (Berg et al., 2000; Han et al., 2011). Typically, a TBR value of 2 to 6 has been used in the design. The TBR value can be used to calculate the extended pavement life as follows:

$$W_{18(\text{reinforced})} = TBR \cdot W_{18} \quad (10)$$

where $W_{18(\text{reinforced})}$ = extended pavement life in ESALs with the use of geosynthetic reinforcement and W_{18} = pavement life in ESALs without the use of geosynthetic reinforcement, which can be determined from Equation (6).

Instead of prolonging the pavement life, the geosynthetic can also be used to reduce the required thickness of the base course. The following reduced traffics should be used in Equation (6) to estimate the required structural number and then in Equation (9) to determine the required thickness of the base course in the reinforced section:

$$W'_{18} = W_{18} / TBR \quad (11)$$

where W'_{18} = reduced traffics in ESALs used for the calculation of the required thickness of the base course in the reinforced section.

Alternatively, the reduced thickness of the base course in the geogrid-reinforced section can be determined based on the following adjusted structural number considering the LCR value (Zhao and Foxworthy, 1999):

$$SN_{\text{reinforced}} = a_1 D_1 + LCR a_2 D_2 m_2 + a_3 D_3 m_3 \quad (12)$$

The LCR value can be estimated based on subgrade CBR, which is provided in Zhao and Foxworthy (1999).

CONCLUSIONS

This paper summarizes the methods commonly used in the United States for the design of planar geosynthetic-improved unpaved and paved roads considering the functions of geosynthetics as separation, drainage, and/or reinforcement. Most of the design methods are empirical or semi-empirical and were developed based on

laboratory and/or field studies. The benefits of geosynthetics used in unpaved and paved roads are considered in the design methods, which result in the reduced thickness of base course and/or the prolonged life of the roadway.

REFERENCES

- AASHTO (1991). *Report on Task Force 25, Joint Committee Report of AASHTO-AGCARTBA*, American Association of State, Highway, and Transportation Officials, Washington, D.C., Dec.
- AASHTO (1993). *AASHTO Guide for Design of Pavement Structures*, 589 p.
- Acharya, B. (2011). *Experimental Study of Geocell-reinforced Flexible Pavements with Recycled Asphalt Pavement (RAP) Bases under Cyclic Loads*. MS thesis, the University of Kansas.
- Berg, R.R., Christopher, B.R., and Perkins, S.W. (2000). *Geosynthetic Reinforcement of the Aggregate Base/Subbase Courses of Flexible Pavement Structures – GMA White Paper II*, Geosynthetic Materials Association, Roseville, MN, USA, 176p.
- Burmister, D.M. (1958). "Evaluation of pavement systems of the WASHO road test by layered systems method." *Bulletin 177*, Highway Research Board, 26-54.
- Christopher, B.C. and Zhao, A. (2001). *Design Manual for Roadway Geocomposite Underdrain Systems*. Internal Report, 37p.
- Collin, J.G., Kinney, T.C., and Fu, X. (1996). "Full scale highway load test of flexible pavement systems with geogrid reinforced base courses." *Geosynthetics International*, 3(4), 537-549.
- FHWA (1992). *Demonstration Project 87: Drainage Pavement Systems, Participant Notebook*, Federal Highway Administration, Publication No. FHWA-SA-92-008, Washington, DC.
- Gabr, M. (2001). *Cyclic Plate Loading Tests on Geogrid Reinforced Roads*. Research Report to Tensar Earth Technologies, Inc., NC State University, 43 p.
- Giroud, J.P. and Han, J. (2004a). "Design method for geogrid-reinforced unpaved roads – Part I: theoretical development." *Journal of Geotechnical and Geoenvironmental Engineering*, ASCE, 130(8), 776-786.
- Giroud, J.P. and Han, J. (2004b). "Design method for geogrid-reinforced unpaved roads – Part II: calibration and verification." *Journal of Geotechnical and Geoenvironmental Engineering*, ASCE, 130(8), 787-797.
- Giroud, J.P. and Noiray, L. (1981). "Geotextiles-reinforced unpaved road design." *Journal of Geotechnical Engineering*, ASCE, 107(9), 1233-1253.
- Giroud, J.P., Zhao, A., and Bonaparte, R. (2000). "The myth of hydraulic transmissivity equivalency between geosynthetic and granular liquid collection layers." *Geosynthetics International*, 7(4-6), 381-401.
- Han, J., Pokharel, S.K., Yang, X., Manandhar, C., Leshchinsky, D., Halahmi, I., and Parsons, R.L. (2011). "Performance of geocell-reinforced RAP bases over weak subgrade under full-scale moving wheel loads." *Journal of Materials in Civil Engineering*, ASCE, 23(11), 1525–1534.
- Han, J., Zhang, Y.Z., and Parsons, R.L. (2011). "Experimentally quantifying the influence of geosynthetics on performance of reinforced granular bases." *Journal*

- of Geotechnical Engineering*, Southeast Asian Geotechnical Society, 42(1), 74-83.
- Kinney, T.C. (2000). Standard test method for determining the 'Aperture Stability Modulus' of a geogrid. Shannon & Wilson, Inc., WA. 9p.
- Pokharel, S.K., Han, J., Manandhar, C., Yang, X.M., Leshchinsky, D., Halahmi, I., and Parsons, R.L. (2011). "Accelerated pavement testing of geocell-reinforced unpaved roads over weak subgrade." *Journal of the Transportation Research Board*, No. 2204, *Low-Volume Roads*, Vol. 2, Proceedings of the 10th International Conference on Low-Volume Roads, July 24–27, Lake Buena Vista, Florida, USA, 67-75.
- Steinberg, M. (1998). *Geomembranes and the Control of Expansive Soils in Construction*. McGraw-Hill, 222p.
- Webster, S.L. (1992). *Geogrid Reinforced Base Courses for Flexible Pavements for Light Aircraft: Test Section Construction, Behavior under Traffic, Laboratory Tests, and Design Criteria*, final report, DOT/FAA/RD-92/25, U.S. Department of Transportation and Federal Aviation Administration, 91p.
- Yang, X., Han, J., Pokharel, S.K., Manandhar, C., Parsons, R.L., Leshchinsky, D., and Halahmi, I. (2012). "Accelerated pavement testing of unpaved roads with geocell-reinforced sand bases." *Geotextiles and Geomembranes*, 32, 95-103.
- Zhao, A. and Foxworthy, P.T. (1999). *Geogrid Reinforcement of Flexible Pavements: A Practical Perspective*. Technical Reference GRID-DE-6, Tenax Corporation.

INVESTIGATION OF MOISTURE CONTENT-INDUCED VARIATIONS IN UNBOUND AGGREGATES' RESILIENT MODULOUS THROUGH SUCTION STRESS CONCEPT

Mingjiang Tao¹, Zhongjie Zhang², Qiming Chen³ and Hong Guo⁴

¹Assistant Professor, Department of Civil and Environmental Engineering, Worcester Polytechnic Institute, 100 Institute Rd., Worcester, MA 01609; taomj@wpi.edu.

²Pavement and Geotechnical Research Administrator, Louisiana Transportation Research Center, 4101 Gourrier Avenue, Baton Rouge, LA 70808; doc.zhang@la.gov.

³Research Associate, Louisiana Transportation Research Center, Louisiana State University, 4101 Gourrier Avenue, Baton Rouge, LA 70808; qchen1@lsu.edu.

⁴Graduate student, Department of Civil and Environmental Engineering, Worcester Polytechnic Institute, 100 Institute Rd., Worcester, MA 01609; hguo@wpi.edu; Northwest A&F University, Yangling, Shaanxi, PRC, 712100.

ABSTRACT: The influence of moisture content on unbound aggregates' resilient modulus has been well recognized, but accurate prediction of this influence remains a challenge. With prediction models incorporating matric suction, great improvement has been achieved in understanding and modeling moisture-dependent resilient modulus. Nevertheless, matric suction, in the sense of soil water tension, cannot be measured directly. The actual measured matric suction in geotechnical literature is water potential, which leads to a conceptual inconsistency. In addition, difficulties associated with determining the effective stress parameter χ may limit the general applicability of matric suction-based prediction models in practice. On the basis of suction stress concept, which is lumped macroscopic effect of various interparticle physicochemical forces, a prediction model for resilient modulus is proposed in this paper. The feasibility of such a model has been confirmed and illustrated by laboratory testing results.

INTRODUCTION

Unbound aggregates, such as limestone, gravel, and granite, are often used as pavement structural layers and their resilient modulus, a fundamental engineering property that characterizes their elastic response under traffic loading, has been one of the most important material parameters for pavement design, distress diagnosis,

and pavement rehabilitation (AASHTO 1993; NCHRP I-37A 2004). Resilient modulus depends on multiple factors, including stress state and aggregates' physical properties (density, moisture content, gradation, mineralogy, morphology, etc.) (Lekarp et al. 2000), and moisture content has long been recognized for its important role. For example, Haynes and Yoder (1963) observed a 50% decrease in resilient modulus in gravel as the degree of saturation increased from 70 to 97%. Hicks and Monismith (1971) showed that the resilient modulus decreases steadily as the moisture content increases above its optimum value. Therefore, many research efforts have been spent to establish the correlations between moisture content (or degree of saturation) and resilient modulus for various types of aggregates and soils, which lay the foundation for purely empirical approaches to predict the variation of resilient modulus.

Another way to address the issue is to investigate the influence of moisture content on resilient modulus within the framework of unsaturated soil mechanics principles. The advantage of this approach is to provide a better understanding why and how the variation of moisture content affects the change of resilient modulus in unbound aggregates and soils. For instance, Heath et al. (2004) proposed a mechanistic framework for determining the behavior of unsaturated granular pavement materials with the use of a soil suction model that has three density-independent parameters. Yang et al. (2005) proposed a model that the effect of moisture content is explicitly considered by including a matric suction term (the difference of pore air pressure with pore water pressure in soils) since the correlation between moisture content and matric suction can be determined and called the soil water characteristic curve (SWCC).

Based on the generalized model adopted by Mechanistic-Empirical Pavement Design Guide (MEPDG) (NCHRP I-37A, 2004), Liang et al. (2008) proposed a model to account for the influence of moisture content on resilient modulus by adding a matric suction term to bulk stress. In their study, Bishop's effective stress parameter (χ) was approximated by the equation proposed by Khalili and Khabbaz (1998) that is a function of air entry value (air entry value is the matric suction at which air enters the largest pores of the soil). Experimental studies, however, have suggested the non-uniqueness of $\chi = f(S)$ (Lu and Likos, 2006).

Despite great improvement in understanding and modeling the role of matric suction played in resilient modulus with suction-based prediction models, a problem associated with the approach is related to the testing technique of axis translation procedure (ATP), which is the most commonly used technique in matric-suction controlled laboratory tests for SWCC and other engineering properties. It involves the translation of the pore air pressure (u_a) through artificially increasing the air pressure in which the soil is immersed. Consequently, the pore water pressure (u_w) is translated into the positive pressure range by an equal amount increase, thus preventing cavitation of the water in soil or aggregates. This suppression of cavitation may change soil behavior, compared with field conditions where pore air pressure is under atmospheric conditions and cavitation is allowed, because water tension in soils remains approximately constant following cavitation. In addition, the application of external air pressure may change the curvature of the water meniscus, thus changing the magnitude of suction (Baker and Frydman 2009). Because of the drawbacks

associated with the ATP technique, the complexities associated with the ATP-based tests may also not be warranted for the determination of SWCC and other lab determined engineering properties.

This study attempts to overcome these hurdles by using the concept of suction stress suggested by Lu and Likos (2006) to consider the influence of moisture content on resilient modulus. The potential advantages of the suction stress concept include theoretical soundness and the ease of implementation. The effect of moisture content can be described in term of the influence of suction stress on resilient modulus or other engineering properties. As a function of moisture content or degree of saturation, suction stress can be readily approximated with moisture content measured in the field.

SUCTION STRESS CONCEPT

The suction stress by Lu and Likos (2006) is on the basis of a micromechanical interparticle force consideration and Terzaghi's classical effective stress concept. It is a macroscopic reflection of collective effect among van der Waals forces, electrical double-layer forces, cementation forces, surface tension forces, and forces arising from negative pore water pressure that act at soil particles. According to Lu and Likos's definition, suction stress can be expressed as:

$$\sigma'_s = \sigma_{pc} + \sigma_{cap} + \chi(u_a - u_w) - \sigma_{c0} \quad (1)$$

where σ'_s is suction stress; σ_{pc} is stress attributable to physicochemical forces; σ_{cap} is capillary stress arising from surface tension; χ is effective stress parameter; and σ_{c0} is apparent tensile stress at the saturated state. With combined suction stress and net normal stress, the effective stress (or intergranular stress) in unsaturated soils due to all known physical stresses can be completely defined as (Lu and Likos 2006):

$$\sigma_c = \sigma' = \sigma_t - u_a + \sigma'_s + \sigma_{c0} = \sigma_t - u_a + \sigma_s \quad (2)$$

where σ_t is the stress due to the applied load; σ_c or σ' is the effective (intergranular) stress; and $\sigma_s = \sigma'_s + \sigma_{c0}$ is uncorrected suction stress. Lu and Likos also defined the correlation of suction stress with matric suction as suction stress characteristic curve (SSCC) and proposed a testing procedure to determine such curves

The concept of SSCC is expanded by this research to include the correlation of suction stress with moisture content or degree of saturation due to the existence of SWCC. The new SSCC can be determined by conducting simple moisture-content controlled tests, as illustrated in Figure 1, which is the modification to that recommended by Lu and Likos [i.e., SSCC here is presented in form of $\sigma'_s(w)$, while it is presented as a function of matric suction in Lu and Likos's paper (2006), and unconsolidated undrained (UU) triaxial tests (i.e., moisture-content-controlled tests) instead that matric-suction-controlled triaxial tests were used]. These modifications were based on the consideration that the moisture-content-controlled laboratory shear strength test can significantly simplify the procedures to obtain SSCC (Lu and Likos 2006) and still keep the theoretical soundness of approach. By describing the SSCC in

the form of $\sigma'_s(w)$, the potential for implementation of any suction stress-based prediction model can also be significantly enhanced because moisture content is much easier to monitor than matric suction does in the field.

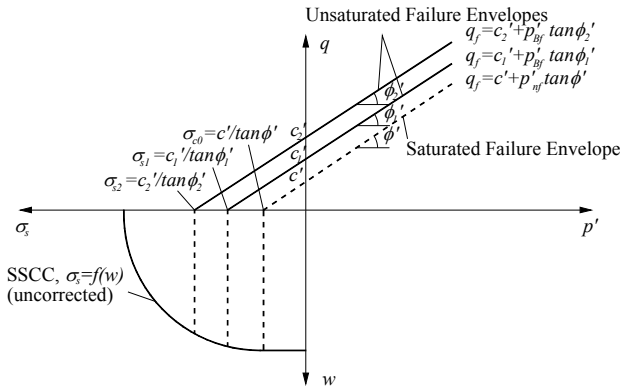


FIG. 1. Laboratory testing procedure to determine SSCC [adapted from Lu and Likos (2006)]

OBJECTIVE AND SCOPE

This paper aims to investigate the feasibility of applying the suction stress concept as a function moisture content to consider its influence on resilient modulus of unbound aggregates. Conventional unconsolidated undrained (UU) triaxial tests were conducted on Mexican limestone to determine the relationship between suction stress and moisture content (i.e., SSCC) and their corresponding resilient moduli were determined using repeated load triaxial (RLT) tests at different moisture contents.

MATERIAL AND LABORATORY TESTS

Physical Property Tests

Basic physical properties of Mexican limestone, including specific gravity, gradation analysis, plasticity index (PI), and moisture–density relationship, were determined in accordance with their respective ASTM specifications. The moisture–density relationship determined from the Proctor compaction test provides the information of optimum moisture content and maximum dry unit weight that was used in preparing samples for UU and RLT tests.

UU Tests

Unconsolidated undrained triaxial tests were conducted on samples with the same maximum dry unit weight at three different moisture contents (optimum-3%, optimum, and optimum+1.2%). UU samples were 150 mm by 300 mm (6 in. by 12

in.) and compacted by using a vibratory compactor and a 152 mm by 330 mm (6 in. by 13 in.) split mold. Two membranes were used to prevent any damage from coarse particles, and a vacuum was used to achieve a good contact between the membranes and the mold during sample preparation.

Three UU tests were performed for each moisture content level at confining pressures of 5, 10, and 15 kPa to generate a failure line. To derive the uncorrected suction stress (σ_s), the methodology proposed by Lu and Likos (2006) was generally followed except that a deviatoric stress–mean stress space ($q - p$) was used and gravimetric moisture content was used as an independent variable. With the uncorrected suction stress at each moisture content determined from the corresponding failure envelope, SSCC was then generated from these derived suction stresses.

Repeated Load Triaxial (RLT) Tests

Repeated load triaxial tests were performed in accordance with AASHTO T307-99 (2003). RLT tests were conducted on samples with the maximum dry unit weight at optimum-3%, optimum, and optimum +1.2% moisture contents. Duplicate samples were tested for each moisture content case.

TEST RESULT, ANALYSIS, AND DISCUSSION

Basic Physical Properties

Mexican limestone has a specific gravity of 2.54, with moisture absorption of 5.7% and nonplastic fines. The basic physical properties of Mexican limestone are summarized in Table 1.

TABLE 1. Physical properties of Mexican limestone

C_u^a	C_c^b	F_{200}^{200} (%) ^c	Max. dry unit weight (kN/m ³)	Optimum moisture content (%)	USCS /AASHTO ^d
55.61	0.64	12.0	20.3	8.8	GW- GM/A-1-b

^a C_u = coefficient of uniformity; ^b C_c = coefficient of curvature; ^c F_{200} = percent of fines (passing through No. 200 sieve); and ^dUSCS (unified soil classification system); AASHTO (American Association of State Highway Official soil classification system).

UU Test results and SSCC

UU test results shown in Figure 2 were obtained from samples with the maximum dry unit weight (20.3 kN/m³) at moisture contents of 5.8 (optimum-3%), 8.8 (optimum), and 10.0 (optimum+1.2%). The deviatoric stress ($q = \sigma_1 - \sigma_3$) and mean stress [$p = 1/3 (\sigma_1 + 2\sigma_3)$] in Figure 2 are the peak point values. The influence of moisture content or matric suction on shear strength of unsaturated Mexican

limestone is manifested by the increased apparent cohesion (the intercept term in regression equations) with the decrease of moisture content.

By following the methodology illustrated in Figure 1, uncorrected suction stress is readily determined from the regression equations in Figure 2 ($\sigma_s = \text{intercept} / \text{gradient}$) and tabulated in Table 2. With these derived suction stresses, the UU test results in Figure 2 is re-plotted in deviatoric stress q – effective mean stress p' space in Figure 3 ($p' = p + \sigma_s$, where, σ_s is uncorrected suction stress with its value listed in Table 2). It is apparent that all different failure envelopes in Figure 2 now collapse into a unique failure line when suction stress is included. This result provides further evidence from a coarse-grained soil in support of the validity of the true effective stress and suction stress concept, while only test results on fine-grained soils were examined to validate suction stress concept in Lu and Likos' paper.

The derived suction stress values at different moisture contents are also used to generate a SSCC as shown in Figure 4 with the conceptual SSCC proposed by Lu and Likos (2006) superimposed. The measured suction stress values appear to follow the general trend of the conceptual SSCC although a rightward exponent decay curve is used for the ease of calculating suction stresses at other moisture contents. It should also be noted that although the portion of SSCC at lower moisture contents is undefined in this study, it is of little consequence to unbound aggregates' behavior in pavement structures since such low moisture levels are less likely to be encountered under field conditions.

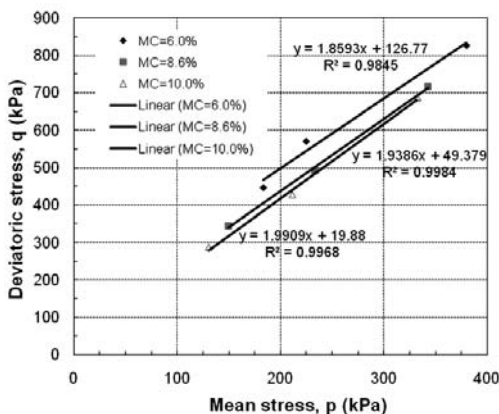


FIG. 2. Deviatoric stress vs. mean stress at peak points from UU tests

TABLE 2. Uncorrected suction stress derived from UU test results

Moisture content (%)	Uncorrected suction stress σ_s (kPa)
6.0	68.2
8.6	25.5
10.0	10.0

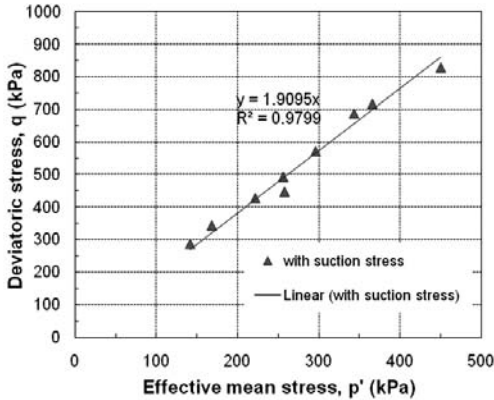


FIG. 3. Deviatoric stress vs. effective mean stress at peak points from UU tests

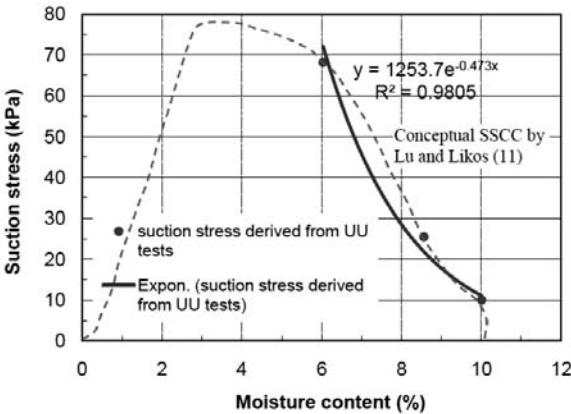


FIG. 4. Suction stress characteristic curve (SSCC) derived from UU tests

Resilient Modulus Model Incorporating Suction Stress

The appreciable influence of moisture content on resilient modulus of Mexican limestone is manifested in Figure 5 (only part of testing results included for clarity). It shows that trier sample has larger resilient modulus, this is mainly because of its higher strength due to the suction stress. These results suggest the importance of taking moisture content into account in order to realistically characterize pavement materials' behavior in field conditions.

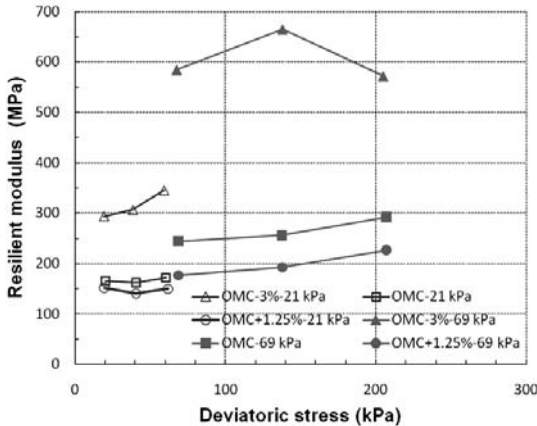


FIG. 5. Influence of moisture content and deviatoric stress on resilient modulus

A prediction model with the capacity of considering moisture-dependence of resilient modulus is proposed here, which is based on the generalized model adopted by MEPDG (3):

$$M_r = k_1 P_a \left(\frac{\theta + 3\sigma_s}{P_a} \right)^{k_2} \left(\frac{\tau_{oct}}{P_a} + 1 \right)^{k_3} \quad (3)$$

Where, σ_s is uncorrected suction stress; and other variables are the same as those defined previously. A coefficient of 3 in the suction stress term is used to be consistent with summation nature of the bulk stress.

The model in Eq. (3) resembles that proposed by Liang et al. (2008), but the concept behind the added term [σ_s herein vs. $\chi\psi_m$ in the model by Liang et al. (2008)] is significantly different. Physicochemical interparticle forces may not be relevant for Mexican limestone under investigation here. Nevertheless, suction stress has the capacity of not only reflecting the effect of negative pore water pressure and surface tension, but also the contributions from other physicochemical interparticle forces. These other physicochemical interparticle forces are expected to play more important roles in fine-grained soils (e.g., subgrade silt or clay soils). Another major difference between the model proposed in this study and that by Liang et al (2008) is the procedure to determine the added term: conventional UU tests are used to derive the suction stress while SWCC determination is required to obtain matric suction and Bishop's effective stress parameter in the model by Liang et al. (2008).

The Excel built-in solver was used for obtaining prediction model parameters (k_1 , k_2 , and k_3). When the generalized model with total stress approach (i.e., ignoring suction stress) is used, the coefficient of correlation between the measured and model predicted resilient modulus is so poor ($R^2 = -0.70$) that the samples cannot be considered as the same sample group. The modified prediction model with the inclusion of suction stress term yields a much improved prediction with a coefficient

of correlation of 0.85. The measured vs. predicted resilient modulus from the generalized model as well as those from the proposed model in this study is illustrated in Figure 6. The regression parameters (k_1 , k_2 , and k_3) and the corresponding coefficient of correlation are summarized in Table 3. It should be pointed out that the regression parameters from the model without suction stress are listed only for comparison purposes and should not be used for any prediction due to the very poor correlation. The coefficient of correlation from the prediction model with suction stress may be limited by the variability in resilient modulus measurements that has been noted by Heath et al. (2004). Nevertheless, the feasibility of using the suction stress concept in predicting moisture-dependent resilient modulus is confirmed by the improved correlation for Mexican limestone.

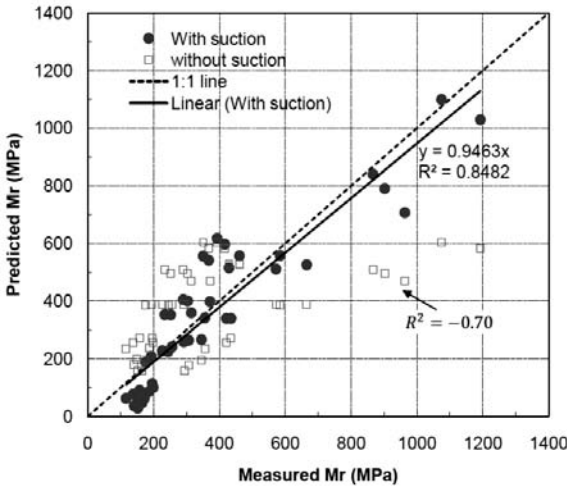


FIG. 6. Comparison of measured and predicted resilient modulus

TABLE 3. Model regression parameters and corresponding coefficient of correlation

Soil	Prediction model	k_1	k_2	k_3	R^2
Mexican limestone	Without suction stress	2045.5	0.87	-0.88	-0.70
	With suction stress	249.8	2.18	-1.55	0.85

CONCLUSIONS

This study implements the concept of suction stress suggested by Lu and Likos in considering the impact of moisture content on the resilient modulus of unbound aggregates. The proposed prediction model using suction stress as one of

independent parameters has been confirmed by experimental results on Mexican limestone. Compared to previous matric suction based prediction models, the suction-stress based prediction model has the following advantages:

- As demonstrated in this study, the suction stress-based model eliminates the conceptual inconsistency of potential and stress. It also avoids difficulties associated with determining the effective stress parameter χ .
- As a function of moisture content, SSCC bridges the easily measured moisture content with fundamental mechanical property–suction stress that directly relates to pavement material performance under traffic and environmental loading. With SSCC determined from simple water-content-controlled laboratory shear strength tests, suction-stress based models can readily be used by practitioners.

Although only the resilient modulus is investigated using the concept of suction stress in this study, the approach can be used to investigate the impact of moisture content on other engineering properties of various geo-materials. With the combination of theoretical rigor and the ease of implementation, suction stress-based models are expected to assist engineers realistically predicting moisture-related engineering property variation in the field.

REFERENCES

- AASHTO, 1993. *Guide for design of pavement structures*, Washington, D.C.
- AASHTO T 307-99, 2003. *Standard method of test for determining the resilient modulus of soils and aggregates*, Washington, D.C.
- Baker, R., and Frydman, S., 2009. "Unsaturated soil mechanics critical review of physical foundations." *Engineering Geology*, 106: 26–39.
- Haynes, J. G., and Yoder, E. J., 1963. "Effects of repeated loading on gravel and crushed stone base course materials used in the AASHO Road Test." *Hwy. Res. Rec.* 39.
- Heath, A. C., Pestana, J. M., Harvey, J. T., and Bejerano, M. O., 2004. "Normalizing behavior of unsaturated granular pavement materials." *Journal of Geotechnical and Geoenvironmental Engineering*, 130(9): 896–904.
- Hicks, R. G., and Monismith, C. L., 1971. "Factors influencing the resilient properties of granular materials." *Hwy. Res. Rec.* 345: 15–31.
- Khalili, N., and Khabbaz, M. H., 1998. "A unique relationship for χ for the determination of the shear strength of unsaturated soils." *Geotechnique*, 48(2): 1–7.
- Lekarp, F., Isacsson, U., and Dawson, A., 2000. "State of the art I: resilient response of unbound aggregates." *Journal of Transportation Engineering*, ASCE, 126(1): 66–75.
- Liang, R., Rabab'ah, S., Khasawneh, M., 2008. "Predicting moisture-dependent resilient modulus of cohesive soils using soil suction concept." *Journal of Transportation Engineering*, ASCE, 134(1): 34–40.

- Lu, N., and Likos, W., 2006. "Suction stress characteristic curve for unsaturated soils." *Journal of Geotechnical and Geoenvironmental Engineering*, ASCE, 132(2): 131–142.
- NCHRP 1-37A, 2004. "Guide for mechanistic-empirical design of new and rehabilitation pavement structures, Final Report, Part 2, Design Inputs." *National Cooperative Highway Research Program* (NCHRP), Washington, D.C.
- Yang, R. R., Huang, W. H., and Tai, Y. T., 2005. "Variation of resilient modulus with soil suction for compacted subgrade soils." *Transportation Research Record*, 1913, Transportation Research Board, Washington, D.C., 99–106.

LABORATORY EVALUATION ON THE MECHANICAL PROPERTIES OF ASPHALT CONCRETE INCORPORATING INDUSTRIAL WASTE

Qiao Dong¹ and Baoshan Huang²

¹Key Laboratory of Road Structure and Material of Ministry of Transport, Changsha University of Science and Technology, Changsha, China

Post-doctoral Research Associate, University of Tennessee, Knoxville, TN, 37996; qdong2@utk.edu

²Professor, Changsha University of Science and Technology, Changsha, China

Associate Professor, University of Tennessee, Knoxville, TN, 37996; bhuang@utk.edu

ABSTRACT: Laboratory tests were conducted to evaluate the feasibility of incorporating an industrial waste material (i.e. fine sand from automobile manufacturing) into pavement material. In this study, the fine materials were added into hot mix asphalt mixture as mineral fillers to replace agriculture lime. Test results indicated that the waste fines can be used in the asphalt mixture. Adding a certain amount (up to 45% by weight) of the waste sand improved the asphalt mastic's resistance to deformation. The dynamic modulus and indirect tensile strength of the mixture were improved by adding a specific amount of "filler" while the flow numbers were slightly reduced. 2.5% "filler" content was recommended for a dense-graded HMA surface mixture.

INTRODUCTION

USA generates around 7.6 billion tons of industrial wastes each year. Around 97% is wastewater managed by surface impoundments and the remainder (228 million tons) is usually managed by landfills, waste piles, and land application units. (EPA, 1999) With the large demand of managing the wastes and increasing environmental awareness, many research activities have been conducted on recycling industrial wastes.

Highway construction and maintenance consume large amounts of asphalt concrete every year. Incorporating industrial wastes into pavement asphalt concrete is a potentially promising method to recycle industrial wastes. Some researches on incorporating waste materials in asphalt mixtures have been published Su et al. (2002) evaluated the performance of asphalt concrete using recycled glass as fine aggregate and found that the skid resistance of asphalt concrete was improved. Tuncan et al. (2003) evaluated the effects of waste plastic, crumb rubber and petroleum contaminated soil on asphalt concrete. Karasahin et al. (2005) used marble dust as mineral filler in asphalt concrete. Huang et al. (2007) reported the successful application of recycled wastes including include waste glass, steel slag, tires and

plastics in asphalt pavement in UK.

This presented study investigated the feasibility of adding an industrial waste material into hot mix asphalt (HMA) mixtures as mineral filler by a series of laboratory tests. Dynamic shear rheology (DSR) tests, dynamic modulus tests, flow number tests and indirect tensile strength (IDT) tests were conducted to evaluate the mechanical properties of the asphalt mastic and HMA mixture.

PROPERTIES OF INDUSTRIAL WASTES

The waste materials are fine particles from the dust collection system of the Federal Mogul during the manufacturing of brake shoes from the automotive industry. Hereafter, the material is referred as BS filler (brake shoes filler). The Federal Mogul generates more than 2,300 tons of this type of waste materials every year. Visual observation of the material indicated that it contains mostly very fine ($<0.075\text{mm}$) dark grey powder and around 10% metal chips (slightly larger). Four major components for the materials are: steel shards (10-15%), graphite (20%), phenolic resins (20%), and barium sulfate (10%). For the four major components for BS filler, the steel chips should not have any negative effects on HMA. The existence of graphite may change the electric conductivity and viscoelastic characteristics of asphalt mastic. The phenolic resin is a thermal setting material. Due to chemical similarity, the phenolic resin should be compatible with asphalt binder. The effect of barium sulfate on asphalt mastic and mixtures need to be evaluated through laboratory testing.

BS filler exhibits similar properties with mineral filler. FIG. 1 shows the BS filler and agriculture lime (pulverized limestone widely used in Tennessee) which is a pulverized limestone and is widely used in Tennessee as mineral filler for asphalt mixtures. The BS filler was sieved and mixed at the ratio of $W_{\text{passing No. 16}}: W_{\text{passing No. 30}}: W_{\text{passing No. 50}}: W_{\text{passing No. 200}} = 3:2:25:70$ to produce the standard “mineral filler” that met the gradation requirement of ASTM D 242. The Specific gravity of the “filler” was 2.886 determined according to ASTM C 128-07.

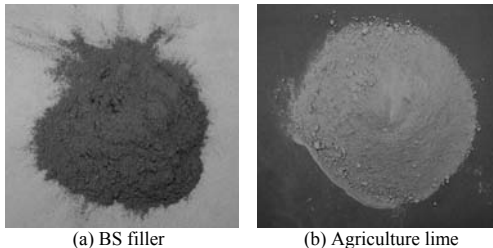


FIG. 1. Comparison of BS filler and agriculture lime

PREPARATION OF MATERIALS

Asphalt Mastic

Asphalt binder and different amount of BS filler (0%, 15%, 30% and 45% by volume) were heated in an oven to 165°C and hand-mixed to produce asphalt mastic samples.

HMA Mixture

As shown in Table 1, different amounts of “filler” (0%, 2.5%, 5% and 7.5% by weight) were added into a typical Tennessee Department of Transportation (TDOT) dense grade mixture (D-mix) to replace part of the agriculture lime. D-mix is designed by the Marshall method and used as the surface layer. The original proportion of “D-mix” is $W_{Gravel} : W_{No.10} : W_{Sand} : W_{Lime} = 55:10:25:10$. The PG 64-22 asphalt binder, which is most frequently used in Tennessee, was chosen in the study. The asphalt content of the mixture was 5.8%. The maximum specific gravity (G_{mm}) of the 0% and 7.5% group were 2.403 and 2.405 respectively; thus, 2.404 was used as the G_{mm} for all the mixtures. Bulk specific gravity (G_{mb}) was controlled at 2.309 so that the air voids were 4.0%. A Superpave Gyrotory machine was utilized to make 150mm diameter specimens. Then, specimens were cored and cut for testing.

TABLE 1. Gradation (Passing percent) of Aggregates and the Mixture

Sieve size	Gravel	No. 10 Soft screenings	Natural Sand	Ag. Lime	Waste Fines	Joint Mixture Formula				Design Range
						0%	2.5%	5%	7.5%	
5/8"	100	100	100	100	100	100	100	100	100	100
1/2"	92	100	100	100	100	96	96	96	96	95-100
3/8"	59	100	100	100	100	80	80	80	80	80-93
#4	18	93	97	99	0	57	57	57	57	54-76
#8	11	68	82	93	0	45	46	46	46	35-57
#30	4	26	45	57	0	23	24	25	26	17-29
#50	2	16	19	36	0	12	13	14	16	10-18
#100	1	9	6	27	0	5.9	6.7	7.4	8.1	3-10
#200	0	5	2	13	0	3	3	3	3	0-6.5

TEST METHODS

Dynamic Shear Modulus Test of Asphalt Mastic

Dynamic Shear modulus tests evaluated the viscoelastic properties of asphalt mastic at different temperature and loading rates. The tests were conducted by a Dynamic Shear Rheometer (DSR) at three different temperatures: 15°C, 25°C and 40°C. Small plates (Ø 8mm) were used. Details of the DSR testing can be found in ASTM D7175.

Dynamic Modulus Test

Dynamic modulus measures mixture’s strain response characteristics as a function of loading rate and temperature. It is a primary material property input in the AASHTO Mechanistic-Empirical Design Guide for flexible pavements. According to NCHRP Report 547 (Witczak, 2005), a Simple Performance Tester (SPT) was utilized to conduct the test on cylindrical specimens (Ø100mm *150mm H) at three temperatures: 5 °C, 20 °C and 40 °C. At each temperature, the load frequencies were: 25 Hz, 20 Hz, 10 Hz, 5 Hz, 2 Hz, 1 Hz, 0.5 Hz, 0.2 Hz, 0.1 Hz. A haversine dynamic loading was applied for 10 cycles at each frequency. The dynamic modulus (E^*) for each test condition was determined using the average stress amplitude and the average recoverable axial strain over the last six loading cycles.

Flow Number Test

The flow number measures the mixture's resistance to permanent deformation at high temperature. The test temperature was 54.4°C. According to NCHRP 547 (10), a stress was applied on cylindrical specimens (Ø100mm *150mm H) in a haversine waveform with a wavelength of 0.1 s followed by a rest period of 0.9 s by using a SPT. The typical relationship between permanent strain and the load cycles can be generally divided into three zones: primary, secondary, and tertiary. The permanent deformations accumulate rapidly again in the tertiary zone. "Flow number" is the cycle number at which tertiary flow starts and is an indication of the deformation failure of specimens.

Indirect Tensile Test

Indirect Tensile (IDT) test was conducted to determine the tensile strength and strain at failure of the mixtures to evaluate their resistance to cracking at intermediate temperature. The test temperature was 25°C. Consistent with ASTM D 6931, test specimens (Ø150mm *50mm H) were loaded on their lateral surface to failure at a 50 mm/min deformation rate using an 810 Material Testing System (MTS). The maximum tensile strength is calculated by the following equation.

$$S_t = \frac{2P}{\pi bD} \quad (2)$$

Where, S_t = maximum indirect tensile strength;

P = failure load at first crack;

b, D = thickness and diameter of the specimen.

DISCUSSION OF EXPERIMENT RESULTS

Effect of "filler" on Viscoelastic Property of Asphalt Mastics

Master curves of asphalt mastics with different "filler" contents were obtained through the DSR test. The data at temperatures higher than 25°C were forced to lie in the lower region of the normalized frequency while the data at temperatures lower than 25°C got aligned in the higher region of normalized frequency. The portion of the master curve in the low frequency region describes the rheological behavior of the mastic at higher temperatures, while the other portion of the master curve in the higher frequency region describes the rheological behavior at lower temperatures. As shown in FIG. 2, master curves of all four type binders exhibit similar trends. As the increase of filler content, the complex moduli increased, indicating the overall resistance to high temperature deformation and intermediate temperature distresses were improved by adding fillers.

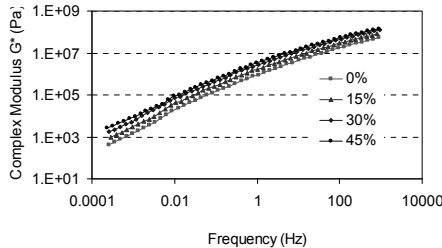


FIG. 2. Master Curves of Binders with Different “Filler” Content

Dynamic Modulus

FIG. 3 shows the dynamic moduli of mixtures of different filler content at 40°C 0.1Hz and 5°C 25Hz. The dynamic moduli at high temperature and low frequency describe the mechanical behavior of mixture at higher temperatures, while low temperature and high frequency describes the rheological behavior at lower temperatures. The dynamic moduli of 2.5% and 7.5% groups are higher than those of 0% and 5% groups at 40°C and 0.1Hz condition while adding filler decrease the dynamic moduli at 5°C 25Hz. Thus, adding BS filler improved the dynamic modulus at high temperature but decreased the dynamic modulus at low temperature. 2.5% content is recommended to avoid loss of dynamic modulus at low temperature.

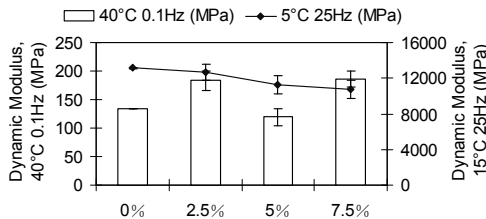


FIG. 3. Dynamic Moduli of Different Mixtures

Flow Number

Flow number test results are shown in FIG. 4. It can be observed that although the flow numbers of the mixture including “fillers” are lower than the control mixture, the flow number of the 2.5% group is higher than other two mixtures and is only slightly lower than the control group, which indicates the mixture still retain relatively higher resistance to permanent deformation.

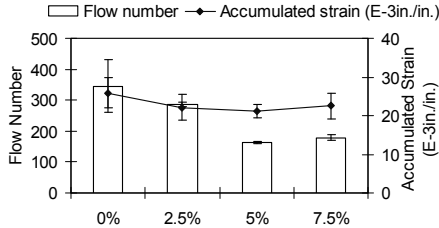


FIG. 4. Flow Number and Accumulated Strain of Different Mixtures

Indirect Tensile Strength

FIG. 5 presents the results from IDT test. It can be seen that indirect tensile strength of 2.5% group achieved the highest value while the strength of 5% and 7.5% groups are lower than that of the control group. Adding 2.5% filler increase the mixture's resistance to fatigue cracking.

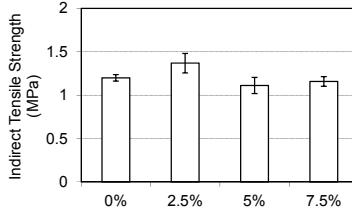


FIG. 5. Indirect Tensile Strength of Different Mixtures

CONCLUSIONS

The applicability of incorporating BS filler into HMA mixture was studied through laboratory tests. Based on the test results, the BS filler can be used in this pavement material and the following conclusions can be drawn:

1. DSR test results indicated that binder's total resistance to permanent deformation increased as the content of BS filler increase up to of 45% by volume.
2. HMA mixture performance test results indicated that the dynamic modulus and indirect tensile strength were improved by adding a specific amount of filler and the 2.5% group reached the peak tensile strength. However, adding filler slightly reduced the flow number and thus the mixture's resistance to permanent deformation failure at high temperature was compromised. 2.5% content is recommended for the TDOT "D-Mix".

ACKNOWLEDGEMENT

The project was supported by Open Fund of Key Laboratory of Road Structure and Material of Ministry of Transport (Changsha University of Science & Technology).

REFERENCES

- Huang, Y., Bird, R. N. and Heidrich, O. (2007). "A review of the use of recycled solid waste materials in asphalt pavements", *Conservation and Recycling*, n 52, 58-73.
- Karaşahina, M., Terzib, S. (2007). "Evaluation of marble waste dust in the mixture of asphaltic concrete", *Construction and Building Materials*, v 21, n 3, 616-620.
- Mustafa Tuncan, Ahmet Tuncan, Altan Cetin, (2003). The use of waste materials in asphalt concrete mixtures, *Waste Management and Research*, v 21 n 2, 83-92.
- Su, N., Chen, J.S. (2002), "Engineering properties of asphalt concrete made with recycled glass", *Conservation and Recycling*, v 35, n 4, 259-274.
- U.S. Environmental Protection Agency, (1999). "Guide for Industrial Waste Management", *EPA Report 530-R-99-001*, Office of Solid Waste and Emergency Response.
- Witczak, M. (2005). "Simple Performance Tests: Summary of Recommended Methods and Database", *NCHRP Report 547*, National Research Council, Washington D.C.

THE RELATIONSHIP BETWEEN FREEZE-THAW RESISTANCE AND PORE STRUCTURE OF CONCRETE

Shanshan Jin¹, Jinxi Zhang², Baoshan Huang³

¹Ph.D., Beijing University of Civil Engineering and Architecture, Beijing, China 100044. E-mail: jinshanshan@bucea.edu.cn

²Ph.D., Beijing Key Laboratory of Traffic Engineering, Beijing University of Technology, Beijing, China 100124. E-mail: zhangjinxi@bjut.edu.cn

³Ph.D, P.E., University of Tennessee, 223 Perkins Hall, Knoxville, TN, 37996; bhuang@utk.edu

Abstract: In order to evaluate and predict the freeze-thaw resistance of concrete according to its pore structure, the freeze-thaw resistance and pore structure of concretes with different mix proportions were investigated in this study. The fractal theory was employed to characterize the pore structure of concrete, and the deterioration of pore structure due to the effect of freezing and thawing was assessed in all the concrete mixtures. The results indicated that: first, the deteriorations of pore structures of ordinary concretes were worse than those of air-entrained concretes; second, the decrement rate of fractal dimension of pore surface is effective to describe the deterioration of pore structure due to the effect of freezing and thawing; third, an evident relationship could be found between the durability factor and the decrement rate of fractal dimension.

INTRODUCTION

The pore structure as an important feature of the concrete has vital influence on its freeze-thaw resistance. Based on the hypothesis of hydrostatic pressure proposed by Powers (1950), there is a direct relationship between the freeze-thaw resistance and the air-void spacing, thus the air-void spacing factor has been assumed as the representative parameter of the pore structure to evaluate the freeze-thaw resistance of concrete. Although, simple relations between the freeze-thaw resistance and the spacing factor have been concluded in many studies (Manns 1970, Pigeon and Malhotra 1995, Gao et al. 2006), there are some controversies on the threshold of spacing factor among those simple conclusions. In addition to the spacing factor, many other parameters associated with the characteristics of pore structure have been proposed to establish the correlation with the freeze-thaw resistance (Maage *et al.* 1985, Pleau *et al.* 1996, Zhao *et al.* 2002, Jerath *et al.* 2007). Especially, the study of Nakamura indicates that freeze-thaw resistance is strongly influenced by the pore-size distribution of concrete (Nakamura 1994). Accordingly, it is necessary to find a more

effective parameter which is able to characterize the pore structure of concrete to evaluate or predict its freeze-thaw resistance.

OBJECTIVES AND SCOPE

The primary objectives of this study are to propose a proper parameter to describe the pore structure of concrete and establish its relationship with the freeze-thaw resistance. In this study, the pore structure and the freeze-thaw resistance of 8 different concrete mixtures were tested. The fractal theory was employed to characterize the pore structure and the correlation between durability factor and fractal dimension was investigated as well.

TEST PROGRAM

Materials

Ordinary Portland cement with 42.5 strength grade was used. Ground granulated blast-furnace slag (GGBS) (2.80 g/cm^3 density and $410 \text{ m}^2/\text{kg}$ specific surface), fly ash (class F, 4.4% fineness), and silica fume (2.1 g/cm^3 density, $24100 \text{ m}^2/\text{kg}$ specific surface and 95.8% SiO_2 content) were used as replacements of cement in various concrete groups. The aggregate consists of coarse aggregate (5~25mm particle size, 0.3% fines content and 0.5% water absorption) and fine aggregate (2.85 fineness modulus and 1.1% fines content). Naphthalene sulfonate water-reducing admixture and rosin-based air-entraining agent were used as additives.

Proportions of mixtures

5 groups of ordinary concrete and 3 groups of air-entrained concrete were considered in this study. The mix proportions are presented in Table 1 and 2 respectively. The slumps of all the mixtures were controlled as $10 \pm 3 \text{ cm}$.

TABLE 1. Mix Proportions of Ordinary Concretes (kg/m^3)

Mixtures	Cement	Fine aggregate	Coarse aggregate	water	Silica fume	Fly ash	GGBS
Control	400	613	1138	200	—	—	—
GGBS	260	613	1138	200	—	—	140
FA	280	613	1138	200	—	120	—
SF	360	613	1138	200	40	—	—
Compound	280	613	1138	200	20	40	60

TABLE 2. Mix Proportions of Air-Entrained Concretes (kg/m³)

Mixtures	Cement	Fine aggregate	Coarse aggregate	water	Air-entraining agent/ % (of cement weight)	Measured air content in fresh concrete
A1	400	613	1138	200	0.09	2.6%
A2	400	613	1138	200	0.15	5.5%
A3	400	613	1138	200	0.35	7.0%

EXPERIMENTAL PROCEDURES

Freezing and thawing test

The “Standard Test Method for Resistance of Concrete to Rapid Freezing and Thawing (T0565-2005)” in the Chinese standard “Test Methods of Cement and Concrete for Highway Engineering (JTG E30-2005)” was adopted for freezing and thawing test. This method is similar to the specification of ASTM C666 which is widely used in the United States.

Pore structure test

Both the mercury intrusion porometers (MIP) and automatic analyzer for air-void characteristic (hereinafter referred as “air-void analyzer”) were employed to investigate the pore structure of the hardened concretes specimens.

The specimens for MIP were fragments of the concrete with the size of 3-5mm which were crushed from original specimens. The range of the pore diameter measured in this study was 3-360000nm. The dimensions of specimens for air-void analyzer were 10cm in both length and width, and 1-2cm in thickness which were cut from the original specimens with the size of 10cm×10cm×40cm. The diameter of the air-voids obtained through the air-void analyzer was in the range of 9.917- 2185.740μm.

METHODOLOGY

In order to find a parameter of pore structure to build a more reliable relationship between freeze-thaw resistance and pore structure than the usual, the fractal theory was adopted to characterize the pore structure. The fractal dimension of pore surface was calculated by the fractal model based on the thermodynamic method which was deduced by Zhang (Zhang *et al.* 1995), and improved by Liu (Liu *et al.* 2004). The formula of the fractal model is shown as follow:

$$\ln\left(\frac{W_n}{r_n^2}\right) = D_s \ln Q'_n + \ln C \quad (1)$$

Where, W_n is the short expression of $\sum_{i=1}^n \bar{P}_i \Delta V_i$; Q'_n is the short expression of $V_n^{1/3}/r_n$; \bar{P}_i is the applied pressure at the i th intrusion of mercury, Pa; ΔV_i is the intrusion volume at the i th intrusion of mercury, m^3 ; n is the times of intrusion of mercury; r_n is the pore radius at the n th intrusion of mercury, m; V_n is the cumulative intrusion volume, m^3 ; C is a constant; D_s is the fractal dimension of pore surface.

According to the Eq. (1), the terms of W_n/r_n^2 and Q'_n can be calculated by the collected data in the MIP. The W_n/r_n^2 term was plotted versus the Q'_n term on log-log coordinates. Through the linear regression, the fractal dimension of pore surface, D_s , can be obtained as the slope of the best fitting line.

It was demonstrated that the fractal model based on the thermodynamic method could represent the complexity of pore structure quantitatively and effectively, and the fractal dimension of pore surface had good correlation with the pore surface area, average pore diameter, median pore diameter and strength (Jin *et al.* 2011).

TEST RESULTS AND DISCUSSION

Freeze-thaw resistance and air-void characteristic of the concrete

The strength, saturation degree, and the air-void spacing are all the important factors influencing the freeze-thaw resistance of concrete. Prior to testing, all the specimens were saturated by immersing in the saturated lime solution for 4 days. Thus, the strength and air-void spacing were considered as the two main influence factors of the freeze-thaw resistance in this study.

The test results of durability factor, strength and spacing factor are summarized in Table 3. It shows that the durability factors of air-entrained concretes were much higher than those of ordinary concretes and the spacing factors of air-entrained concretes were lower than those of ordinary concretes. However, the durability factor did not vary with the spacing factor uniformly, because the strength of the concrete also had remarkable influence on its freeze-thaw resistance. Hence, the freeze-thaw resistance could not be evaluated only by one parameter; both the spacing factor and strength should be considered in the evaluation system.

In addition, the freezing and thawing test is an evolving process. The deterioration of pore structure occurs due to the effect of freezing and thawing, and on the other hand, the deterioration of pore structure influences its freeze-thaw resistance. Thus, the deterioration of pore structure is a vital feature during the freeze-thaw process. In order to establish a reliable relationship between the freeze-thaw resistance and pore structure, it is essential to find a proper parameter which is able to represent multiple factors affecting the freeze-thaw resistance and characterize the deterioration of pore structure during the freezing and thawing process.

TABLE 3. Test Results of Durability Factor, Strength and Air-Void Spacing Factor

Mixtures	Durability factor /%	Strength (Before freezing and thawing) /MPa	Air-void spacing factor / μm
Control	9	47.4	891.8
GGBS	7	48.3	916.8
FA	7	35.0	470.0
SF	15	55.3	830.5
Compound	8	49.6	727.1
A1	79	40.9	439.7
A2	90	36.2	314.7
A3	92	38.9	328.4

Fractal Dimension of Pore Surface before and After Freezing and Thawing

The pore structure before and after freezing and thawing test were determined by MIP. The test data indicated that the pore size distribution changed during the test. In order to quantify the changes, the average pore diameter, the median pore diameter, the total pore surface area and the fractal dimension of pore surface were taken into account. Among these parameters, only fractal dimension of pore surface had a strong variation trend after the freezing and thawing test. The fractal dimensions before and after freezing and thawing test are plotted in Fig. 1. It shows that the fractal dimensions decreased after freezing and thawing test for both ordinary concretes and air-entrained concretes. The fractal dimension of pore surface can reflect the complexity of pore structure: the higher the fractal dimension, the more complex the pore structure. The results shown in Fig. 1 indicate that after freezing and thawing test the pore structure became simpler. This result demonstrates that the fractal dimension can reflect the deterioration of pore structure quantitatively. Meanwhile, it has been illustrated that the strength of mortar increased as the increase of the fractal dimension of pore surface (Jin et al. 2011). Thus, the fractal dimension of pore surface can be used as a representative parameter of the pore structure to reflect the freeze-thaw resistance of concrete.

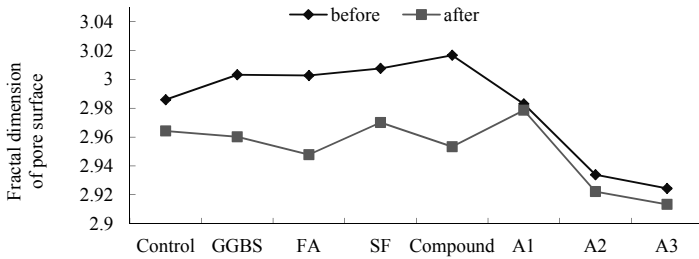


FIG. 1. Fractal Dimensions before and after Freezing and Thawing

Relationship between freeze-thaw resistance and pore structure

It also can be seen from Fig. 1, the decrements of fractal dimensions in ordinary concretes were more remarkable than those in air-entrained concretes. It reveals that the decrement rate of fractal dimension should be an effective index to describe the deterioration of pore structure. The durability factor was plotted versus the decrement rate of fractal dimension in Fig. 2.

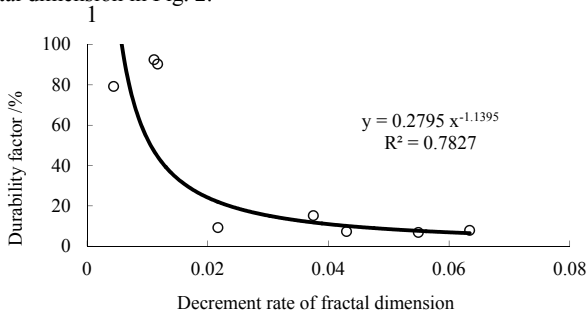


FIG. 2. Durability Factor vs. Decrement Rate of Fractal Dimension

Fig. 2 indicates that there was an apparent inverse relationship between durability factor and the decrement rate of fractal dimension, and the durability factor became larger as the decrement rate of fractal dimension decreasing. Accordingly, it implies that the freeze-thaw resistance can be evaluated and predicted by the fractal dimension. However, more test data are needed to improve the relationship.

CONCLUSIONS

(1) The deterioration of pore structure occurred in all the concrete mixtures in this study due to the effect of freezing and thawing. The results showed that the deterioration in ordinary concretes were worse than those in air-entrained concretes, which indicates that the air-entrained concretes had higher freeze-thaw resistance than ordinary concretes.

- (2) The fractal dimension of pore surface was the only parameter which decreased after the freeze-thaw process. The decrement rate of fractal dimension was validated to be an effective parameter to describe the deterioration of the pore structure of concrete.
- (3) There was a clearly evident relationship between the durability factor and the decrement rate of fractal dimension of pore surface. The relationship can be employed to predict the freeze-thaw resistance of concrete and evaluate the freeze-thaw resistance of existing concrete structure.

REFERENCE

- B. Zhang, S. Li (1995). "Determination of the surface fractal dimension for porous media by mercury porosimetry." *Industrial and Engineering Chemistry Research*, 1995: v 34, n4, p 1383-1386
- Gao, S. Wu, P. Lin, Z. Wu and M. Tang (2006). "The characteristics of air void and freeze-thaw resistance of RCC with fly ash and expansive agent." *Construction and Building Materials*, 2006: v 20, n 8, p 586-590.
- Jin, J. Zhang, C. Chen, W. Chen (2011). "Study on pore fractal characteristic of cement mortar." *Journal of Building Materials*, 2011: v 14, n 1, p 110-115.
- M. Maage, J. Sliper, R. Grasdalen (1985). "Pore structure and porosity in concrete, characterized by mercury porosimetry and microscopy, correlated to freeze-thaw resistance", *Principles and Applications of Pore Structural Characterization*, Proceedings of the RILEM/CNR International Symposium, *J. W. Arrowsmith Ltd*, 1985: p 463-475.
- M. Nakamura, T. Fukushima (1994). Pore Structure and Freeze-Thaw Damage of Fiber Reinforced Cement Boards. *Journal of the Society of Materials Science*, 1994: v 43, n 487, p 382-387
- M. Pigeon and V.M. Malhotra (1995). "Freeze-thaw resistance of roller-compacted high-volume fly ash concrete", *Journal of Materials in Civil Engineering*, 1995, v 7, n 4, p 208-211
- P. Guo Mingyang (2008). "Experimental study on freeze-thaw resistance of road structure cement concrete." Master's thesis of Beijing University of Technology, 2008
- R. Pleau, M. Pigeon, J.L. Laurecot, R. Gagne (1996). "Use of the flow length concept to assess the efficiency of air entrainment with regards to frost durability: Part II – experimental results." *Cemen, Concrete and Aggregates*, 1996: v 18, n 1, p 30-41.
- S. Jerath, N. Hanson (2007). "Effect of fly ash content and aggregate gradation on the durability of concrete pavements." *Journal of Materials in Civil Engineering*, 2007: v 19, n5, p 367-375
- S. Zhang, M. Deng, J. Wu, M. Tang (2008). "Effect of pore structure on the freeze-thaw resistance of concrete." *Journal of Wuhan University of Technology*, 2008: v 30, n 6, p 56-59.
- T.C. Powers (1950). "Air requirement of frost-resistant concrete", *Portland Cement Association -- Research Laboratories -- Bulletin*, 1950: n 33, p 1-19
- W. Manns (1970). "The spacing factor as characteristics for evaluation of the frost-

- resistance of concrete”, *Beton Herstellung Verwend*, 1970: v 20, n 6, p 253-255
- X. Zhao, J. Wei, Y. Huang (2002). “Relationship between pore structure change of concrete and its frost durability degradation.” *Journal of Wuhan University of Technology*, 2002: v 24, n 12, p 14-18.
- Y. Liu, S. Chen, H. Sun (2004). “Characterizing pores in freeze-dried materials by fractal models and fractal dimensions” *Transactions of the CSAE*, 2004: v 20, n 6, p 41-45

ADDITIVES FOR SOIL-CEMENT STABILIZATION

Benjamin F. Bowers¹, John L. Daniels², M. ASCE, P.E., Shaogang Lei³
and Nicholas J. DeBlasis⁴

¹Graduate Student, Department of Civil and Environmental Engineering, University of Tennessee-Knoxville, Knoxville, TN 37996

²Associate Professor, Department of Civil and Environmental Engineering, University of North Carolina at Charlotte, Charlotte, NC 28223, USA

³Associate Professor, Institute of Land Resources, China University of Mining and Technology, Xuzhou, Jiangsu Province, China

⁴Graduate Student, Department of Civil and Environmental Engineering, University of North Carolina at Charlotte, Charlotte, NC 28223, USA

ABSTRACT: Soil-cement stabilization is commonly used in road construction applications when temperatures exceed 10°C. At lower temperatures, cementitious reactions proceed more slowly and strength development remains incomplete. As a component of a larger research effort, this paper reports on the use of sodium chloride (NaCl) and calcium chloride (CaCl₂) for enhancing strength gain at curing temperatures of 2°C and 10°C. The results are mixed depending on the soil, with both increased and decreased unconfined compressive (UC) strength at both temperatures for curing durations of 3 and 7 days. For example, one local soil (Johnston County, NC) mixed with 6% Portland cement and 1.5% sodium chloride (by volume in molding moisture content) resulted in an increase in UC strength from 1748 to 2303 kPa when cured at 10°C for 7 days. Another local soil (Buncombe County, NC) responded negatively to NaCl addition. Clay content and overall composition are postulated as controls on additive efficacy.

INTRODUCTION

Cement is often blended with subgrade soils used in road construction to increase strength and improve overall pavement structure performance. The process begins by mixing specified dosages of Portland cement into the subgrade soil, then wet mixing the soil and cement to the optimum moisture content, followed by roller compaction and curing. Much like concrete, the efficacy of cement modified soil is a function of temperature. As such, this process is typically not used in climates and seasons where the average temperature is less than 10°C. As an alternative, research has suggested that various additives can be used to accelerate strength gain in soil-cement systems under low temperatures (Daniels and Janardhanam 2007, Daniels et al. 2009). The objective of this paper is to provide preliminary data regarding the use of sodium

chloride (NaCl), and to a lesser extent calcium chloride (CaCl₂), as a function of temperature and concentration for three soils.

MATERIALS AND METHODS

The primary material used in this study was soil collected from three locations across North Carolina. Each sample consisted of eight 0.21 m³ (55-gallon) drums of soil. Once obtained, a portion of each sample was returned to the Division of Highway Materials and Tests Unit of the North Carolina Department of Transportation (NCDOT) for classification. Each drum was labeled, securely tightened and closed until needed. Properties of the three soils are provided in Table 1. Soil from each county was mixed with 6% (by weight) Type I Portland cement and tap water, and compacted using a 4" by 4.5" cylindrical mold to approximately one percent wet of optimum. NaCl modification was accomplished by using salt solutions of varying strength (0.5%, 1.0% and 1.5% by volume) as the molding moisture content for modified specimens. A limited number of CaCl₂ modification tests were performed at varying dosages (1-10% by volume) by mixing a CaCl₂ solution into the water required to reach the molding moisture content. A minimum of two replicates was tested for each mixture. The selection of sodium chloride and calcium chloride concentrations was based in part on previous research (Daniels and Janardhanam 2007; Daniels et al. 2009) and was informed by experience with cold weather concreting. For example, the extent to which commercially available additives allow fresh concrete to cure under cold and subfreezing conditions has been investigated under laboratory and field conditions (Korhonen, 2002, 2004). The cement content was not optimized for strength gain but instead selected to reflect current practice in North Carolina. Laboratory-grade sodium chloride was obtained from Fisher Scientific and a 38% calcium chloride solution was used from TETRA Technologies of Houston, Texas.

Table 1: Soil location and selected properties

No.	Location	Liquid Limit	Plasticity Index	% Passing #200 Sieve	AASHTO ID	Optimum Moisture Content (%)	Maximum Dry Unit Weight (kN/m ³)
1	Buncombe, I-40, near Asheville, NC	33	4	32	A-2-4	16	17.4
2	Guilford, I-40, near Greensboro	37	9	46	A-4	14	17.6
3	Johnston, U.S. 70, near Clayton, NC	35	8	40	A-4	18	17.0

After compaction, samples were placed into a re-sealable plastic bag along with a damp sponge, closed, and moved to the curing chamber at either 2°C or 10°C for 3 or 7 days. When a specimen had reached its designated curing duration it was removed from the curing chamber and soaked for 4 hours in a water bath. After soaking, samples were subjected to unconfined compression (UC) testing at a rate of 1.27 mm/min following ASTM D 1633 “Standard Test Methods for Compressive Strength of Molded Soil-Cement Cylinders”.

RESULTS AND DISCUSSION

A plot of sodium chloride dosage versus strength is provided in Figures 1, 2 and 3 for soils from Buncombe, Guilford and Johnston County, respectively. As one would expect, the UC strength is generally increased for longer curing durations (3 vs. 7 days) and warmer temperatures (10°C vs. 2°C). However, some 3-day strength values modestly exceeded their 7-day counterparts, and this is attributed to sample variability and statistical variation. UC strength measurements were made in replicate with the average value plotted in the figures.

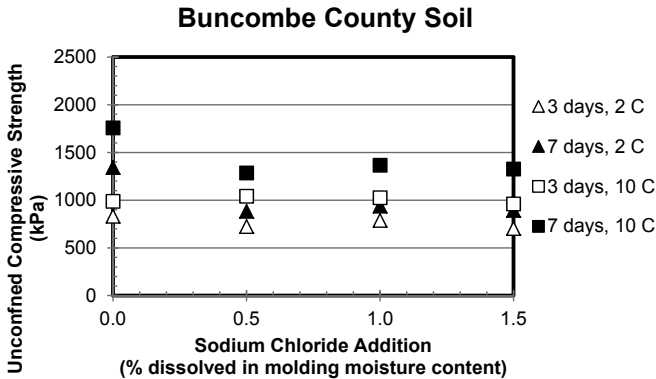


FIG 1. Unconfined compression strength as a function of NaCl addition, Buncombe County soil

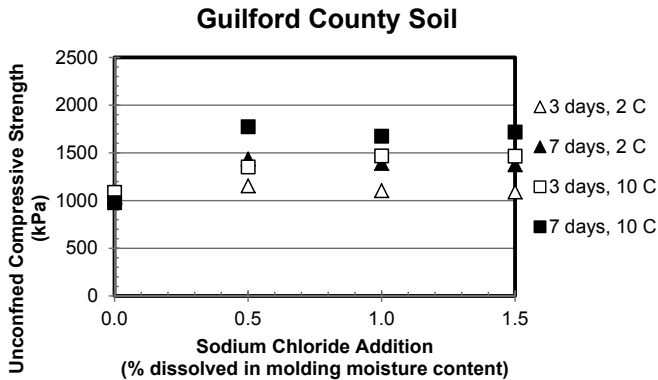


FIG 2. Unconfined compression strength as a function of NaCl addition, Guilford County soil

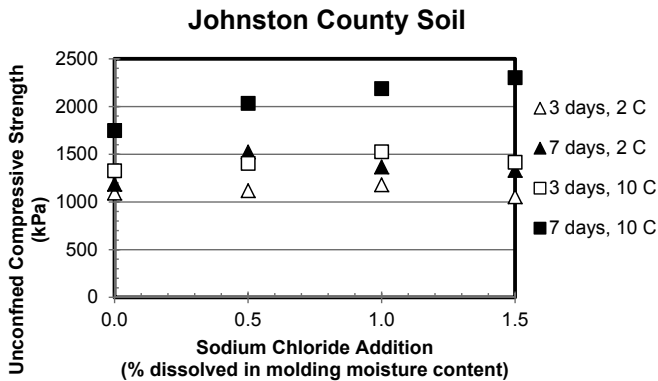


FIG 3. Unconfined compression strength as a function of NaCl addition, Johnston County soil

The addition of NaCl resulted in strength increases for most dosage levels for Guilford and Johnston County soils while decreasing the strength of Buncombe County soil. Guilford County exhibited an optimum NaCl dosage of 0.5% at 7 days. Johnston County soil had different optimum 7 day NaCl dosages based on the curing temperature. At 2°C the optimum NaCl dosage is 0.5%, while at 10°C the optimum tested dosage is 1.5%.

Figures 4, 5, and 6 are representative of varying CaCl_2 dosages in Buncombe, Guilford, and Johnston Counties. Buncombe and Johnston County soils both experienced a loss in unconfined strength at the tested temperatures. Project resources allowed for a more complete data set to be generated for Guilford County, and in all cases the addition of CaCl_2 increased the UC strength as compared to the control. Higher dosages did in some cases lead to strength loss as compared to the maximum strength, occurring at either 2% or 4% CaCl_2 additive. The varying concentrations of CaCl_2 additive in each soil was used in an effort to try to determine if a window of efficacy exist in the additive-soil relationship.

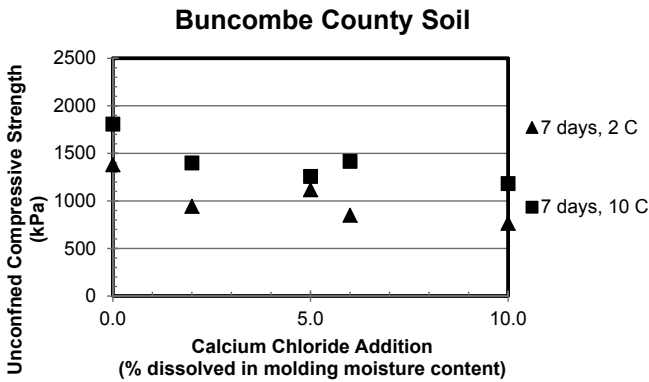


FIG 4. Unconfined compression strength as a function of CaCl_2 addition, Buncombe County Soil

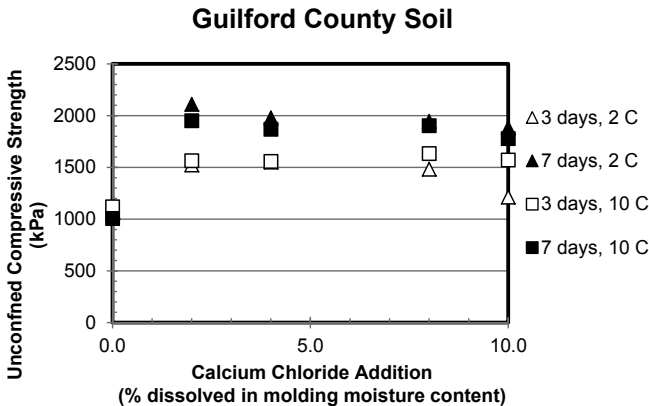


FIG 5. Unconfined compression strength as a function of CaCl_2 addition, Guilford County Soil

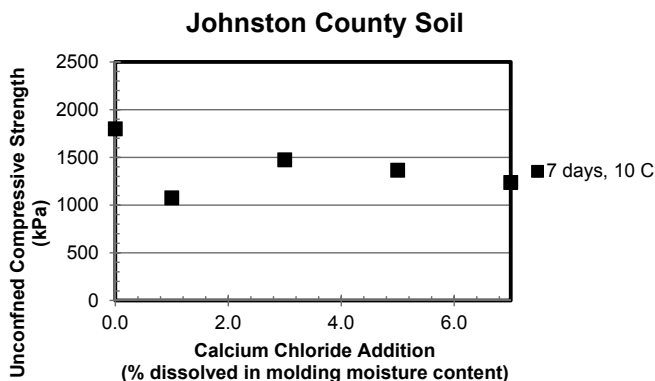
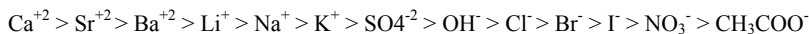


FIG 6. Unconfined compression strength as a function of CaCl₂ addition, Johnston County Soil

The mechanism for strength gain is expected to be the same as that which occurs when set accelerators are added to concrete mixtures. In particular, when a set accelerating admixture is added to a cement mixture such as concrete, the effects are threefold: there is an increase in the rate of hydration of cement, the time of setting of concrete is shortened, and the rate of early strength development is increased (Dodson 1990). The accelerating effect is related mainly to the tricalcium silicate (C3S) phase of the cement-water mixture. The set accelerating potential of the following cations and anions, respectively, are diagrammed in as follows (Ramachandran 1984):



It is not clear why NaCl addition resulted in strength decreases for Buncombe County soil and CaCl₂ addition only accounts for increases in strength in Guilford County soil, considering that there are reports of CaCl₂-soil modification resulting uniformly in strength increases (Uppot et al. 2007, 2008, Rollings et al. 2002). A hypothesis is that strength enhancement with additive modification may be a function of the additive concentration and soil composition. In particular, Buncombe County soil had the lowest plasticity (PI = 4) while Guilford and Johnston County soils had PI values that were twice as high (PI = 9 and 8, respectively). Such variable performance in concrete has not been observed, ostensibly because such mixtures are composed of relatively inert aggregates with less specific surface area and reactivity. In the case of soil-cement applications, the surface area is higher and reactive clay minerals could exert greater influence. Kroyer et al. (2003) observes that clay minerals may accelerate cement hydration and therefore, possibly, strength gain. This could mean that a certain fraction of clay is analogous to adding a certain amount of chemical additive. Daniels et al. (2009) suggests that too much of an additive can be deleterious and so soils with high PI values may not be ideal candidates for NaCl-modified cement. This assertion

may hold true for CaCl_2 as well, but requires further examination, perhaps by studying a given soil's cation exchange capacity (CEC) relative to its reactivity to cement and $\text{NaCl}/\text{CaCl}_2$ (e.g., as a function of UC strength).

CONCLUSIONS

As with concrete, chemical additives can be used to improve the performance of cement-modified subgrade soils. The data reported herein suggest that NaCl or CaCl_2 can be used to provide strength increases in samples that are cured at relatively low temperatures. However, the results vary with soil type, and both increased and decreased unconfined compressive (UC) strengths were observed. For example, one local soil (Johnston County, NC) mixed with 6% Portland cement and 1.5% sodium chloride (by volume in molding moisture content) resulted in an increase in UC strength from 1748 to 2303 kPa when cured at 10°C for 7 days. Another local soil (Buncombe County, NC) responded negatively to NaCl addition. The same trend is observed in Guilford County soil which sees strength gain with CaCl_2 additive, while modification is deleterious to UC strength in Buncombe and Johnston Counties. Guilford County also exhibited that there is a potential for an optimum dosage of NaCl and CaCl_2 and that beyond that quantity chemical additive may reduce strength in comparison to the optimum dosage. Clay content and the overall composition are postulated as controls on additive efficacy, a hypothesis which requires further examination.

ACKNOWLEDGMENTS

The authors appreciate the support of the North Carolina Department of Transportation. The opinions and findings are those of the authors and do not constitute a recommendation, guidance or a specification from NCDOT.

REFERENCES

- Daniels, J.L. and Janardhanam, R. (2007). "Cold-weather subgrade stabilization" *Soil Improvement*, (GSP 172), ASCE, Reston/VA: 1-10.
- Daniels, J.L., Janardhanam, R., Starnes, J., DeBlasis, N. and Miles, K (2009). "Cold-weather concreting technology for ground modification" *Contemporary topics in ground modification, problem soils, and geo-support*, (GSP 187) ASCE, Reston/VA 273-280.
- Dodson, V.H. (1990) *Concrete Admixtures*. New York: Van Nostrand Reinhold.
- Korhonen, C.J. (2002) "Off the shelf anti-freeze admixtures" Technical Report TR-02-7, U.S. Army CRREL.
- Korhonen, C.J. (2004) "Extending the season for concrete construction and repair. Phase I: Establishing the technology" Technical Report TR-04-2, U.S. Army CRREL.
- Kroyer, H., Lindgreen, H., Jakobsen, H.J. and Skibsted, J. (2003). "Hydration of Portland cement in the presence of clay minerals studied by ^{29}Si and ^{27}Al MAS NMR spectroscopy" *Advances in Cement Research*, Vol. 15., No. 3, pp. 103-112.

- Ramachandran, V.S. (1984) *Concrete Admixtures Handbook: Properties, Science, and Technology*. Park Ridge, New Jersey: Noyes Publications.
- Rollings, Raymond S, Marian P Rollings, and James Martel. (2002) *Chemical Stabilization Technology For Cold Weather*. Hanover: Cold Regions Research and Engineering Laboratory, 2002.
- Uppot, J.O, Mishra, S.K., and Kalidindi, A. (2008) "Calcium Chloride Activated Road Construction with Soil Cement". International Conference, Transportation Planning and Implementation, Dec. 3-8, 2008, Mumbai, India

TUBE SUCTION TEST FOR EVALUATING MOISTURE SUSCEPTIBILITY RESULTING FROM CALCIUM CHLORIDE

Shaogang Lei¹, John L. Daniels², M. ASCE, P.E., Benjamin F. Bowers³

¹ Associate Professor, State Key Laboratory for GeoMechanics and Deep Underground Engineering, China University of Mining and Technology, Xuzhou, Jiangsu Province, 221008, China.

² Associate Professor, Department of Civil and Environmental Engineering, University of North Carolina Charlotte, NC 28223, USA

³ Ph.D. Student, Department of Civil and Environmental Engineering, University of Tennessee-Knoxville, Knoxville, TN 37996, USA

ABSTRACT: Electrolytic additives can be used to accelerate strength gain in cement-modified soils. However, one of the consequences of adding electrolytic additives, such as calcium chloride (CaCl_2), is the potential to increase moisture susceptibility. Moisture susceptibility affects the strength of the material and its ability to withstand repeated freeze-thaw cycling. In order to evaluate the moisture susceptibility of soil-cement as a function of calcium chloride, different dosages were tested, i.e. 0% control, 5% and 10% of cement weight, with three different soil types. Samples were subjected to tube suction testing, a method which essentially measures capillary rise in soils and aggregates. The data indicate that calcium chloride has a dosage-dependent influence on the extent of capillary rise. It was also found that different soil types exhibit varying suction behavior. In terms of application of this research, moisture susceptibility analysis should be undertaken to assess whether proposed electrolytic chemical additives are appropriate for a given soil type.

Keywords: Tube suction test, soil strength, moisture susceptibility, electrolyte additive

INTRODUCTION

Many electrolytic additives have been used to improve the properties of soil shear strength. Examples of these additives are as follows: Calcium chloride (CaCl_2), sodium chloride (NaCl) and sodium nitrate (NaNO_3) (Jenkins 2007, Sinn 2002, Tamadher et al. 2007). One of the more common electrolyte additives is calcium chloride. Calcium chloride has been added to improve soil strength and accelerate the curing of soil cement under cold weather conditions (Rollings et al., 2002). Calcium chloride exists as a solid compound and can be dissolved into calcium and chloride

ions in water. In addition, it easily hydrates with available liquid or vapor phase water molecules. Calcium chloride is commonly in the form of a dihydrate ($\text{CaCl}_2 \cdot 2\text{H}_2\text{O}$) or hexahydrate ($\text{CaCl}_2 \cdot 6\text{H}_2\text{O}$). Hence, one of the primary consequences of adding CaCl_2 additive to soils is moisture retention and absorption. This means that the additive may alter the moisture susceptibility of the aggregate depending on the soil type. The moisture susceptibility is thought to directly affect the strength of the material and its ability to withstand repeated freeze-thaw cycling. Previous research shows that moisture susceptibility has caused fatigue and stripping of soil-cement materials. For example, Jenkins (2007) indicated that moisture susceptibility is a primary cause of distress in hot mix asphalt pavements. It is therefore important to study the impact of electrolytic additives on the water susceptibility of soil aggregate in the presence of water.

The dielectric value (DV) of air and water is 1 and 81, respectively (Stoffregen et al. 2002). Therefore varying moisture contents in soil will result in different dielectric values. This relationship also infers that the measure of DV can be used to calculate the water content in the soil. In this study, the moisture susceptibility is assessed by tube suction test (TST) based on this principle. The TST was developed for investigating the moisture susceptibility of base coarse materials (Scullion and Saarenketo 1996).

The TST provides an indication of the potential for capillary rise in the stabilized material as well as the state of moisture within the matrix. Tube suction test results allow for analysis of the extent to which water absorption is expected to lead to breakdown (i.e. stripping) of the matrix. Specifically, measurements of the dielectric value (which in turn is a measure of the moisture content), can be correlated to the arrangement of water molecules in and around mix components (Scullion and Saarenketo 1996). In this study, three different dosages of calcium chloride are evaluated to investigate the impact of the additive on moisture susceptibility.

MATERIALS AND METHODS

Three soils were sampled from Johnston County, Buncombe County, and Guilford County in North Carolina, USA. Table 1 provides soil characterization and AASHTO classification for each of these soils. For TST testing, a compaction mold is used for sample preparation with a 4.5 kg. (10 lb.) hammer, as well as porous stones, a soil membrane, filter papers, plastic sheets, sieved soil (#4 Sieve), cement, and a percometer. The mold is 6 inches in diameter, and 7 inches high. Deionized water was needed to avoid the effects of ions in tap water. Calcium chloride solution with a concentration of 38% was used as the chemical additive. This solution was diluted and mixed with soil-cement mixtures so that two levels of CaCl_2 were achieved, 5% and 10% (dry mass of CaCl_2 / dry mass of cement). A percometer (Adek LLC) is used for the simultaneous and non-destructive "in-situ" measurement of the dielectric value and specific conductivity of the samples.

The procedure of the TST was based primarily on the Technical Report written by Bogdan, Barbu, and Scullion (2006). The first task was to mix the soil, cement, CaCl_2 and deionized water (at optimal moisture content of each type of soil). Two duplicate samples were made for each County using the standard compaction method. In this

experiment, the specimen was compacted in four layers at 25 hits per layer using the 4.5 kg (10 lb) hammer at a height of 45.7 cm (18 in).

After compaction, the weight and the dielectric value of each sample are measured. Both the samples and porous stones are then stored in a 60 °C chamber to dry for 48 hours. They are then placed in a room temperature environment to cool for 2 hours. The initial dielectric value is measured before wrapping the sample and porous stone together with the membrane, shown in Figure 1. The samples are then placed in a flat-bottomed stainless steel pan, filled with deionized water. The water depth should come up to approximately 6.35 mm. (0.25 in.) above the top of the lower porous stone. Five dielectric value readings are taken on the top surface of the sample, daily for 10 to 20 days. The readings are taken at the same time each day if possible. Finally, curves of the dielectric values are drawn to determine the moisture susceptibility of the mixture.

Table 1. Soil location and selected properties

No.	Location	Liquid Limit	Plasticity Index	% Passing #200 Sieve	AASHTO ID	Optimum Moisture Content (%)	Maximum Dry Unit Weight (kN/m ³)
1	Buncombe, I-40, near Asheville, NC	33	4	32	A-2-4	16	17.4
2	Guilford, I-40, near Greensboro	37	9	46	A-4	14	17.6
3	Johnston, U.S. 70, near Clayton, NC	35	8	40	A-4	18	17.0

To compare the moisture difference as a result of CaCl₂, three groups of tests were completed. Control samples (0% CaCl₂) were created along with samples at 5% and 10% CaCl₂ by weight of cement. In total, 18 samples were made and tested for this study.



FIG.1. Illustration of the tube suction test using percometer

RESULTS AND DISCUSSION

The results of the control tube suction tests (0% CaCl_2) along with the 5% and 10% CaCl_2 additive are shown in Figures 2, 3, and 4. With respect to the control values, it was found that the Guilford County samples have the highest DV. This indicates that Guilford County soil exhibits stronger water absorption than the Johnston and Buncombe County soils. Johnston County soil was found to be the least susceptible to water. The rate of the increase in DV for each county is also found to vary significantly. The DV curves of Buncombe and Guilford samples become stable after 1 day, but 10 days are required for the Johnston County soil to stabilize. The DV of Johnston and Buncombe County remained stable throughout testing, but Guilford County DV began to drop slightly after 300 hours. This also indicates that the Guilford County soil is more sensitive than the other two soil types. Such sensitivity is likely driven by the higher clay content and finer pore size that gives rise to greater capillary rise in soils.

Samples modified with calcium chloride experienced a similar rate of increase in DV curves as with the unmodified soil. However, the final DV of the Buncombe County and Johnston County samples was much higher due to presence of calcium chloride. Guilford County soil at the 5% concentration yielded the same suction

capacity as the control samples, but exceeded 40 DV (i.e., maximum reading for Percometer) when the dosage of calcium chloride was 10%. The addition of CaCl₂ appears to influence capillary rise in a manner analogous to increased plasticity or smaller pore diameter.

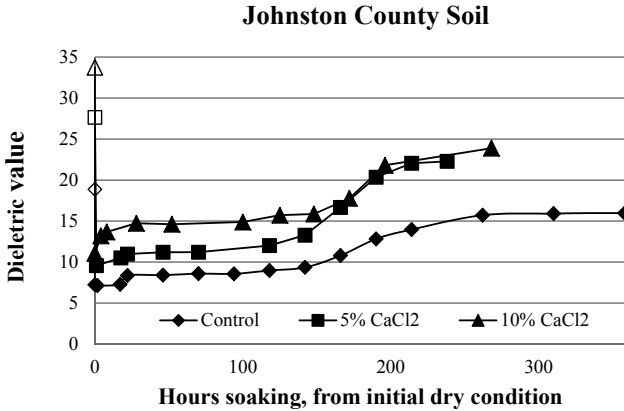


FIG. 2. Johnston County soil average dielectric values for control, 5%, and 10% CaCl₂. Note: Symbols with no fill indicate initial DV reading

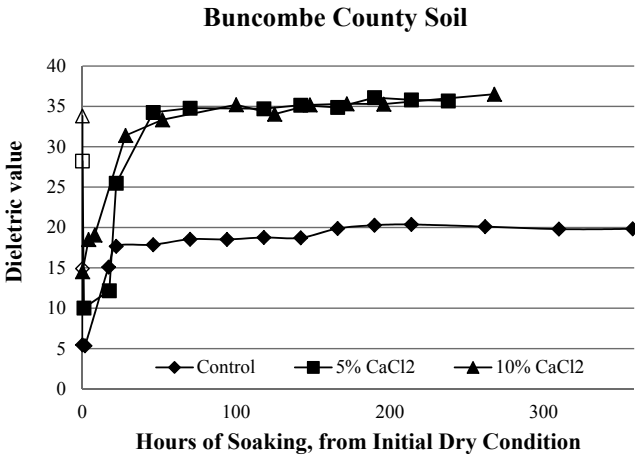


FIG. 3. Buncombe County soil average dielectric values for control, 5%, and 10% CaCl₂. Note: Symbols with no fill indicate initial DV reading

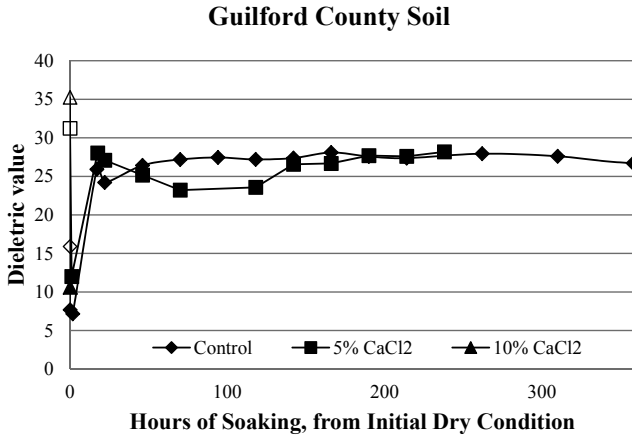


FIG. 4. Guilford County soil dielectric values for control, 5%, and 10% CaCl₂.
 Note: Symbols with no fill indicate initial DV reading

Table 2. Average DV and electric conductivity (EC) given in (μS/cm) at both initial state and final state (10 days in water) for each county at varying CaCl₂ concentrations

Type	Status	Johnston		Buncombe		Guilford	
		DV	EC	DV	EC	DV	EC
0%	Initial	19	19	15	56	16	86
	Final	14	7	20	99	27	290
5%	Initial	28	596	28	722	31	708
	Final	22	112	36	1084	28	3085
10%	Initial	34	427	34	1007	35	974
	Final	24	241	37	1579	>40	4856

Table 2 shows that the initial DV and EC of Johnston County soil is much higher than the final reading, which was measured after 10 days in water. This indicates that the Johnston County soil is not very susceptible to water. In contrast, the initial DV and EC of Buncombe and Guilford County samples were lower than the final values, indicating that these samples draw more water than their optimum water content.

It is clear that the initial DV increases with the addition of CaCl₂. Higher dosages of calcium chloride also yield a higher EC. After 10 days of suction in deionized water the DV of Johnston and Buncombe County soils with calcium chloride are higher than their respective control samples. There is, however, a modest deviation between the 5% and 10% DV.

CONCLUSIONS

Based on the foregoing analyses, it can be concluded that calcium chloride influences the water suction capacity of soil-cement mixes depending on dosage. Guilford County soil was found to be more susceptible to water than Johnston and Buncombe soil in all cases, as it attracts more water than is used at compaction through capillary action. For Johnston and Buncombe County soils, the addition of calcium chloride causes a clear rise in dielectric values indicating that the soil samples are more susceptible to moisture. Guilford County soil showed that the addition of 5% calcium chloride makes very little difference compared to the control. However, at 10% calcium chloride the water suction capacity of Guilford County soil increases greatly. To minimize the impact of CaCl_2 on the water suction capacity for Johnston and Buncombe soils, the CaCl_2 must be less than 5%. For Guilford soil inclusion of CaCl_2 additive must be less than 10%.

This study has found that different soil types have different levels of suction, as well as different responses to CaCl_2 addition. The tube suction test is found to be a suitable method for analysis of the water suction capacity of different soils mixed with electrolyte additives. It is recommended that moisture susceptibility analysis be undertaken to determine whether proposed electrolytic chemical additives are appropriate for specific soil types.

REFERENCES

- Abood, T T, Kasa, A B, Chik, Z B (2007). Stabilisation of silty clay soil using chloride compounds. *Journal of Engineering Science and Technology*.
Journal of Engineering Materials and Technology Quarterly, (2) 1:102-110.
- Bogdan G B, Scullion T (2006). Repeatability and reproducibility study for tube suction test. Texas Transportation Institute, FHWA/TX-06/54114-01-1, 2006.
- Jenkins, J.(2007). *Pavement Interactive*,
http://pavementinteractive.org/index.php?title=Moisture_Susceptibility, Last accessed (10/21/11)
- Rollings, R S, Rollings, M P, Martel. J. (2002) *Chemical Stabilization Technology For Cold Weather*. Hanover: U.S Army ColdRegions Research and Engineering Laboratory.
- Scullion, T. and T. Saarenketo (1996), Using Suction and Dielectric Measurements as Performance Indicators for Aggregate Base Materials, Transportation Research Record 1577, TRB, National Research Council, Washington, D.C.
- Sinn, D. (2002). "Soil Stabilization with Calcium Chloride Filter Cake and Class C Fly Ash." MS thesis, Texas A & M Univ. College Station, Texas.
- Stoffregen, H, Yaramanci, U, Zenker, T (2002). Accuracy of soil water content measurements using ground penetrating radar: comparison of ground penetrating radar and lysimeter data. *Journal of Hydrology*, (267):201–206.
- Tex-113-E, Laboratory Compaction Characteristics and Moisture Density Relationship of Base Materials.

CRITICAL LOAD OF SUBSOIL CONSIDERING POISSON'S RATIO

Chuang Yu¹, Xiaoqing Cai², Liangliang Tang³

¹Associate Professor, Ph.D, College of Architecture and Civil Engineering, Wenzhou University, Zhejiang Wenzhou, China, 325035; geoyuchuang@hotmail.com

²Lecturer, Master, College of Chemistry and Materials Engineering, Wenzhou University, Zhejiang Wenzhou, China, 325035; cxq@wzu.edu.cn

³Bachelor, College of Architecture and Civil Engineering, Wenzhou University, Zhejiang Wenzhou, China, 325035; tll@wzu.edu.cn

ABSTRACT: Considering the different Poisson's ratios of subsoil, this paper derived the calculating formula for the critical edge load under the strip foundation, analyzed and discussed the steps of the calculating formula, carried out the maximum depth for the plastic zone reached and bearing capacity factors. With various Poisson's ratio of subsoil, the bearing capacity factors are dependent on internal friction angle and Poisson's ratio. On the case of the constant friction angle, the bearing capacity factors' values and bearing capacity increase with the increasing of Poisson's ratio. Compared with the engineering examples, it demonstrated the accuracy and reasonableness of the presented calculation approach.

INTRODUCTION

Bearing capacity of the foundation is the ability to bear the load for the foundations, which is the main content in the building ground and the design of the engineering survey. At present, the two of main methods of bearing capacity are calculated by theory and determined by the load test and other in-situ test methods (Liu, 2005). In the process of measuring the bearing capacity, the former adopted the critical edge load to as the bearing capacity of foundation, which appeared to be too conservative and its value was often higher than the actual measured results. This conclusion was confirmed by the view put forward in the 15th International Soil Mechanics and Geotechnical Engineering Conference about that for some problems, the progress of the recent years doesn't validate the correctness of the traditional, such as the Terzaghi's bearing capacity which often overestimates the bearing capacity of the shallow foundation(Zhang, 2007). Although the latter that adopted in situ testing methods was more accurate, it would be more complicated considering the relatively large interference factors, more test time and funding and amendments to the nature of the soil according to the need of the different sizes and depths of the foundation.

Available critical edge load formulas obtained through the theoretical formula are derived using the theory of the elasticity. Calculating the soil at any point M suffered additional principal stress and gravity stress under the strip footing load, we often tend to behave gravity stress as hydrostatic stress that at the same depth, the stress are equal in all directions. Through this way, it concluded a formula of the critical edge load by assuming the static earth pressure coefficient of soil $K_0=1$ in the limit equilibrium zone, which is the conventional

method presented by Craig (1995). However, in fact, the coefficient of the static earth pressure $K_0 \neq 1$, that is, the direction of the additional major and minor principal stress in the point M are not consistent with the direction of the gravity stress, but this two kinds of stresses cannot be a simple superposition. Considering the different Poisson's ratio of soil's effect on the critical edge load in the premise of $K_0 \neq 1$, this paper derived the exact calculating formula of the bearing capacity and the expression of the depth the plastic zone reached, verify the accuracy and reliability of the this expression by comparing with the known literature (Jaky, 1944).

EFFECT OF POISSON'S RATIO ON CRITICAL EDGE LOAD

Assuming the depth of the strip foundation is D , we often divide the load located in the bottom horizontal surface of the strip foundation, which includes the uniformly distributed load in the substrate p and the gravity stress within embedment depth D on both sides of foundation D , into an infinite uniform load γD and uniformly distributed load within the base ($p - \gamma D$) when calculating the principal stress at point M in the depth of z department under the basement. At this point, the principal stress produced by the weight effect of soil at the point M is $\gamma(D+z)$. Considering the calculation of the foundation settlement in the actual engineering is often based on the additional stress suffered under the following of the center of the basis, this paper also considers the distribution of the stress under the following of the center of the basis in order to derive easily. When the depth of the foundation is D , the principal stress at point M under the center of the strip foundation (assuming the lateral pressure coefficient of soil $K_0=1$) is

$$\sigma_1 = \frac{p - \gamma D}{\pi} (2\alpha \pm \sin 2\alpha) + \gamma(D+z) \quad (1)$$

$$\sigma_{cx} = \sigma_{cy} = K_0 \sigma_{cz} \quad (2)$$

$$K_0 = \nu / (1 - \nu) \quad (3)$$

Where p is applied load at the foundation bottom, D is embedded depth, z is depth, α is load angle, ν is poisson's ratio.

According to the coefficient of the static earth pressure K_0 , many scholars created a series of empirical formulas (Schmidt, 1996, Massarch, 1979, CUI, 1998), but here the value of the coefficient of the static earth pressure is as equation (3) shows. In the equation (3), ν stands for Poisson's ratio of soil, which will change according to the soil type, density and other factors. Here the Poisson's ratio of soil μ is assumed as a constant.

Therefore, the equation (1) can be rewritten:

$$\sigma_1 = \frac{p - \gamma D}{\pi} (2\alpha + \sin 2\alpha) + \gamma(D+z) \quad (4)$$

$$\sigma_3 = \frac{p - \gamma D}{\pi} (2\alpha - \sin 2\alpha) + \frac{\mu}{1 - \mu} \gamma(D+z) \quad (5)$$

If the point M reaches the limit equilibrium state, that is, point M is on the boundary of the plastic zone. Based on the strength theory formula, the principal stress at point M meets the following relations.

$$\sin \varphi = \frac{\frac{1}{2}(\sigma_1 - \sigma_3)}{\frac{1}{2}(\sigma_1 + \sigma_3) + c \cot \varphi} \quad (6)$$

Where φ is internal friction of the soil, c is soil cohesion.

Put equation (4), (5) into equation (6), then the depth of the plastic zone of foundation is obtained.

$$z = \frac{p - \gamma D}{\gamma \pi} \frac{2(1 - \mu)(2\alpha \sin \varphi - \sin 2\alpha)}{1 - 2\mu - \sin \varphi} + \frac{c \cot \varphi}{\gamma} \frac{2(1 - \mu) \sin \varphi}{1 - 2\mu - \sin \varphi} - D \quad (7)$$

Equation (7) is the expression of the soil boundary line of the plastic zone.

When calculating the maximum of the depth z_{\max} of the plastic zone of the foundation under the function of the uniformly distributed load in the bar p , we can derivative α to the equation (7), and make this derivative equal to zero.

$$2\alpha = \frac{\pi}{2} - \varphi \quad (8)$$

Put equation (8) into equation (7), we can obtain the expression the maximum depth of the plastic zone of the foundation:

$$z_{\max} = \frac{p - \gamma D}{\gamma \pi} \frac{2(1 - \mu) \sin \varphi}{1 - 2\mu - \sin \varphi} \left(\frac{\pi}{2} - \varphi - \cot \varphi \right) + \frac{c \cot \varphi}{\gamma} \frac{2(1 - \mu) \sin \varphi}{1 - 2\mu - \sin \varphi} - D \quad (9)$$

Meanwhile, we can also obtain the expression of the uniformly distributed load in the substrate p on the basis of equation (9):

$$p = \frac{\pi(\sin \varphi + 2\mu - 1)}{2(1 - \mu) \sin \varphi (\cot \varphi + \varphi - \frac{\pi}{2})} \gamma z_{\max} + \frac{2(1 - \mu) \sin \varphi (\cot \varphi + \varphi - \frac{\pi}{2}) + \pi(\sin \varphi + 2\mu - 1)}{2(1 - \mu) \sin \varphi (\cot \varphi + \varphi - \frac{\pi}{2})} \gamma D + \frac{\pi \cot \varphi}{\cot \varphi + \varphi - \frac{\pi}{2}} c \quad (10)$$

The equation (10) is the basic formula to calculate the critical edge load and critical load.

Order $z_{\max} = 0$ by substituting equation (10) to obtain the formula of the base pressure, the critical edge load p_{cr} , is

$$p_{cr} = \frac{2(1 - \mu) \sin \varphi (\cot \varphi + \varphi - \frac{\pi}{2}) + \pi(\sin \varphi + 2\mu - 1)}{2(1 - \mu) \sin \varphi (\cot \varphi + \varphi - \frac{\pi}{2})} \lambda D + \frac{\pi \cot \varphi}{\cot \varphi + \varphi - \frac{\pi}{2}} c \quad (11)$$

$$\text{Order } p_{cr} = N_q \gamma D + N_c c \tag{12}$$

$$\text{Where } N_q = \frac{2(1 - \mu) \sin \varphi (\cot \varphi + \varphi - \frac{\pi}{2}) + \pi (\sin \varphi + 2\mu - 1)}{2(1 - \mu) \sin \varphi (\cot \varphi + \varphi - \frac{\pi}{2})} \tag{13}$$

$$N_c = \frac{\pi \cot \varphi}{\cot \varphi + \varphi - \frac{\pi}{2}} \tag{14}$$

If the depth of the plastic zone allowed to carry out in the foundation $z_{\max} = B/4$ (B is the width of the base), we substitute it into equation (15), similarly, we can obtain the simplified expression of the corresponding critical load $p_{1/4}$

$$p_{1/4} = N_r \gamma B + N_q \gamma D + N_c c \tag{15}$$

$$\text{Where } N_r = \frac{\pi (\sin \varphi + 2\mu - 1)}{8(1 - \mu) \sin \varphi (\cot \varphi + \varphi - \frac{\pi}{2})} \tag{16}$$

Other symbols are the same in the equations (13) , (14).

N_q N_r N_c are called the capacity factors which are only related to the internal friction angle and Poisson’s ratio of soil. Under the different Poisson’s ratios of soil, the values of N_q N_r N_c change with the internal friction angle as shown follows.

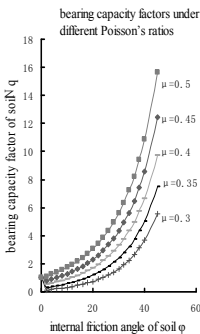


Fig. 1 N_q

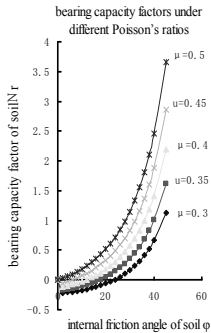


Fig. 2 N_r

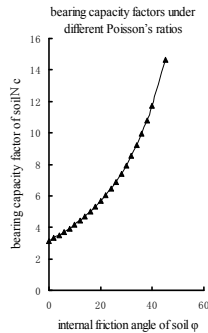


Fig. 3 N_c

Fig. 1, Fig. 2, Fig.3 stand for the variation curve of the values of N_q , N_r and N_c with the change of the angle of internal friction under the different Poisson’s ratio of soil.

Fig. 1 shows that the bearing capacity factor N_q increased with the Poisson’s ratio μ increasing , and got the maximum at $\mu=0.5$, but the trend remained constant.

Fig.2 shows that the bearing capacity factor N_r increased with the Poisson’s ratio μ increasing, and got the maximum at $\mu=0.5$, but the trend remained constant.

Fig.3 shows that the bearing capacity factor N_c was only related with the internal friction angle ϕ , and N_c would be larger with the increased internal friction angle ϕ .

Description: In the application of the equation (12), (15), we need to pay attention to the following points:

- 1) All formulas are derived based on the strip foundation, and the solution to the strip foundation involves the problem of solving the elastic plane strain. It is safer to apply the presented results to the rectangular, square, circular foundation.
- 2) All formulas are derived based on concentrated load or uniformly distributed load based on the strip foundation. Therefore, if there is a significantly eccentric or inclined load in the actual project, we need to modify or re-derived the formula above.
- 3) Poisson's ratio μ is kept constant on computing the lateral pressure coefficient of soil K_0 . Nevertheless, the actual soil is anisotropic in the vertical, and Poisson's ratio μ has changed since the soil transitioned from the elastic zone to the plastic zone. Therefore, it has some differences to consider that Poisson's ratio μ is a constant in calculating with the actual situation.

CONCLUSIONS

This paper considered the different Poisson's ratio and derived the expression of the critical edge load, edge load and the depth the plastic zone reached, which are much closer to the actual situation. In addition, we also obtained the bearing capacity coefficient changing with the Poisson's ratio of soil, but its value was only related with the internal friction angle and Poisson's ratio. When the internal friction angle is constant, with the increase of Poisson's ratio, the bearing capacity factor increases gradually, so does the theoretical bearing capacity of foundation. Therefore, the consideration of appropriate Poisson's ratio in the actual engineering projects to some extent solves the over-conservative situation of calculating the bearing capacity of subsoil.

ACKNOWLEDGEMENTS

The authors appreciate the support of the National Natural Science Foundation of China (Grant No.41002091), the project support by Wenzhou S&T Project of China (Grant No. H20100047), Natural Science Foundation of Zhejiang Province (Grant No. Y1110087)

REFERENCES

- Craig R F.(1995). "Soil mechanics". *Chapman & Hall*:296-299.
- Cui J Y, Song J F. (1998). "Analysis of Foundation's Critical Edge Load", *Engineering Mechanics*, Vol.15(4):96-100.
- Jaky J.(1944). "The Coefficient of Earth Pressure at Rest". *Journal of the Society of Hungarian Architects and Engineers*, Vol.21(3):211-221.
- Liu Z R, Liu C Y, Liang B.(2005). "Soil Mechanics". *Shanghai: Tongji University Press.*(in Chinese).
- Massarch K R. (1979). "Lateral Earth Pressure in Normally Consolidated Clay". *Proceeding of the 7th European Conference on SMFE*. II: 245-249.
- Schmidt B.(1996). "Discussion on Earth Pressure at Rest Related to Stress History". *Canadian Geotechnical Journal*, Vol.13(4):396-398.
- Zhang M, Zhou H L, Gao W S.(2007). "A Number of Synthesis on Theory and Practice in Foundation Design of Architecture Foundation". *The 10th Soil Mechanics and Geotechnical Engineering Conference Proceedings*. Beijing: Science Press, 12-31.

HEAT TRANSFER CAPACITY OF HEAT EXCHANGER PILES IN SOFT CLAY

Chuang Yu¹, Xiaoqing Cai² and Linyou Pan³

¹Associate Professor, Doctor, College of Architecture and Civil Engineering, Wenzhou University, Zhejiang Wenzhou, China, 325035; ac-yc@wzu.edu.cn

²Lecturer, Master, College of Chemistry and Materials Engineering, Wenzhou University, Zhejiang Wenzhou, China, 325035; cxq@wzu.edu.cn

³Professor, Doctor, College of Architecture and Civil Engineering, Wenzhou University, Zhejiang Wenzhou, China, 325035; ply51204@yahoo.com.cn

ABSTRACT: The heat exchanger pile (HEP) is a new type of pile system that combines conventional piles with ground source heat pumps. It has its own characteristics, advantages, and application status, as presented in this paper with its design model and layout pattern explored in detail and its heat transfer capacity calculation discussed with a focus on soft clay ground in coastal regions. The calculations shown in this paper were applied to a six-story residential building in Shanghai. In general, HEP is significantly more cost-effective and environmentally-friendly than a traditional foundation pile.

INTRODUCTION

Geothermal energy is abundant, clean, and renewable; and has a great potential to use with broad application prospects (HARSH, 2007). However, with current available technology, exploring deep geothermal resources is difficult and cost prohibitive, but the exploration and use of shallow geothermal resources are not that difficult as compared to the deep geothermal resource exploration and have become an available method of using ground heat energy (SANNER, 2001).

The heat exchanger pile (HEP) technology is a pile system that combines the conventional foundation piles and ground source heat pumps. It can both provide the mechanical function of the conventional foundation and achieve the heat exchange of shallow geothermal resources through the interaction of piles and the ground. Therefore, it can play the dual role as both the foundation piles and ground source heat pumps, with a cost effective use of construction land.

HEP CONCEPT

The pile foundation is widely used in coastal regions with soft clay of the Quaternary sedimentary soil. High water content and low bearing capacity make local residential buildings generally adopt the pile foundation. While connecting with the pipe surface, HEP achieves the geothermal energy exchange with upper structures through a tube heat exchanger embedded inside, which is filled with an energy exchanger fluid, such as water or water mixed with antifreeze, etc. According to the different patterns of the heat exchanger buried under the pile, the heat exchanger can be divided into the U-tube, tube, and single tube (HAMADA, 2007). The U-tube system can also be sub-divided into single U-tube, double U-tube, and multiple U-tube heat exchanger piles, respectively. Figure 1 and Figure 2 show the diagram and cross-section of a single U-tube heat exchanger pile. Currently in China, the engineering cases that adopt the heat exchanger pile system mostly use the single U-tube heat exchanger pile. Experimental studies showed that the heat capacity of the single-tube within single pile per unit length was increased by 20% -25% more than the double-tube within single pile (Gong, 2002).

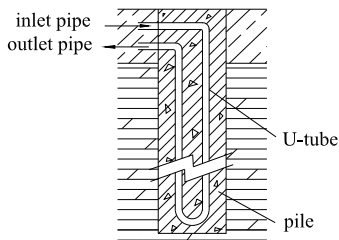


Figure 1. Diagram of HEP

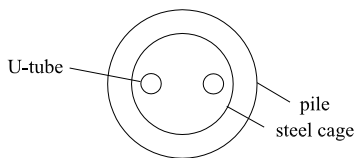


Figure 2. Cross-section of HEP

HEAT TRANSFER CAPACITY OF HEP

Although the HEP design can be compared to other forms of ground-source heat pump pipes, it has its own special characteristics. First of all, once the pile size and length are selected, the number of piles for pipes is also determined. That is, we cannot increase the number of piles according to the change of the hot and cold load. When the hot and cold load provided from the heat exchanger piles can not meet the necessary requirements, we have to consider other forms of pipes or increase the cooling towers and boilers, and other supportive measures.

We also need to take the heat balance issues of the ground heat exchanger into account when designing a HEP system. For the larger gap in the case of hot and cold load, we can select a smaller load value as the basis for determining the length of pipe. But for a relatively large load, we could choose support measures to solve them. Being similar to other forms of heat pump systems, soil's geothermal characteristics are equally important in HEP as in other systems. We need to measure the parameters of the soil composition, soil temperature, thermal conductivity, heat capacity, water quality characteristics, and the flow direction and speed. Each of these parameters has an important impact on the optimization of the entire system.

HEP is a closed loop combined ground source heat pump system that uses underground heat in soils. When winter heating, the fluid in the heat exchanger of HEP crosses the inside and outside layers of thermal resistance of the pile, followed by crossing the soil, pile wall, reinforced concrete of pile, U-tube wall, etc., collects heat from the underground and takes the heat to the interior through the system. While summer cooling, the system reverses the operation and takes the heat away from the room, again crossing U-tube wall, reinforced concrete of pile, pile wall, soil mass, and other related entities, transferring the heat to the earth. Therefore, the heat exchanger piles achieve the heat transferring through the U-tube's heating hot and cold process.

It is generally assumed that when the distance between piles is more than 6 times the length of a pile diameter, the impact of pile interaction can be ignored. We can also often neglect the impact of inter-piles when calculating the heat exchange capacity. For the winter and summer conditions, the engineering technical specifications of ground source heat pump system (GB50366, 2005) shows the heating capacity and cooling capacity of U-tube Q_c and Q_c' as:

$$Q_c = \frac{L_c(t_{max} - t_{\infty})}{R_f + R_{pe} + R_b + R_s \times F_C + R_{sp}(1 - F_C)} \quad (1)$$

$$Q_c' = \frac{L_c(t_{\infty} - t_{min})}{R_f + R_{pe} + R_b + R_s \times F_C + R_{sp}(1 - F_C)} \quad (2)$$

$$F_C = T_{c1} / T_{c2} \quad (3)$$

where: F_C is the heating (cooling) run share; T_{c1} is the operating hours of water source heat pump in a cooling season per month and determined in the hottest month's operating; T_{c2} is the number of hours in the heating season per month and determined in the coldest month's hours; L_c is the length of the U-tube; t_{max} is the design average temperature of heat transfer medium in HEP heat exchanger in the winter; t_{min} is the design average temperature of heat transfer medium in HEP heat exchanger in the summer; t_{∞} is the initial temperature of the regional rock and soil. R_f is the heat transfer resistance between the heat transfer medium and the U-tube wall; R_{pe} is the thermal resistance of U-tube wall; R_b is the thermal resistance of pile's reinforced concrete of the heat exchange piles; and R_s is the thermal resistance considering heat exchange from the pile wall to infinity, also called thermal resistance of the stratum. R_{sp} is the additional thermal resistance caused by continuous pulse load.

FU (2002) made a more detailed description on the values of the five major resistances of R_f , R_{pe} , R_b , R_s , R_{sp} , and analyzed the HEP heat transferring. The author suggested that, in the situation of actual heat transferring, the thermal conductivity of reinforced concrete and soil can be treated as same and the additional thermal resistance caused by the continuous pulse load can often be ignored.

The heat exchange tubes should be designed to ensure the water balance in the pipe system. Any local failure in the system should not affect the normal operation of the whole system.

CASE STUDY OF HEP

A 6-story residential building with a total construction area of 2025 m^2 is located in Shanghai. Its cooling load indicator is 60 W/m^2 for the residential living space (Zhu, 1995). The bathroom and kitchen areas are not air-conditioned, so the air-conditioned area is equivalent to the living area. The living space of unit A is 87 m^2 , with an air-conditioned load of 5220 W ; unit B's living space is 79 m^2 , with an air-conditioned load of 4740 W ; unit C's living space is 78 m^2 , with an air-conditioned load of 4680 W . The heat exchanger of HEP for the residential building should bear a load of $14640 \times 6 = 87840 \text{ W}$. The buried pipes are designed with PVC (polyvinyl chloride). The calculation shows that the heat exchange capacity of the pipe pile is about 35.2 W/m .

The shallow soil in Shanghai is the Quaternary deposits with the geological condition from the surface down in the order of filling soil, clay, mud clay, silty clay, mud silty clay, mud clay, mud clay with silt, and other folders. However in this paper, the values adopted in the heat transfer calculation refer to the ones of the soft clay with the corresponding parameters similar to the soil in Shanghai. The main calculated parameters are shown in Figure 3:

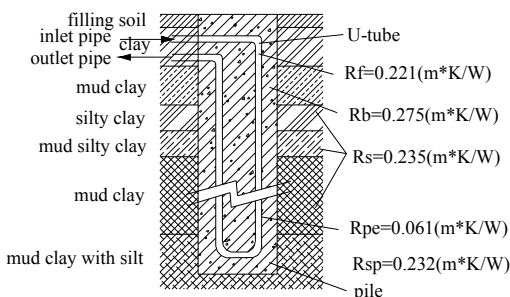


Figure 3. Thermal resistances' values of heat exchanger piles in ground

The meaning of parameters in the figure can be explained as follows. t_{max} is the design average temperature of heat transfer medium in the heat exchanger of HEP in the winter, usually 37°C ; t_{min} is the average temperature of heat transfer medium in the heat exchanger of HEP in the summer, usually -2 to 5°C , here 2°C ; t_∞ is the initial temperature of the regional rock and soil of HEP, usually 15°C ; and the inner diameter of U-tube d_i here is 40 mm . According to $K = Nu_p \lambda_p / l$, we can conclude convective heat transfer coefficient $K = 36.14 \text{ W/m}^2 \cdot \text{K}$. Here, Nu_p is the Nusselt coefficient and l is the unit length of the tube. As a single U-tube, thermal conductivity λ_p is taken as $0.4 \text{ [W/(m} \cdot \text{K)]}$; the U-tube's diameter d_0 and U-tube's equivalent diameter d_e are taken 50 mm and 70 mm respectively; λ_b is the thermal conductivity of reinforced concrete which can be up to $1.54 \text{ [W/(m} \cdot \text{K)]}$; and d_b is the diameter of the pile which is taken as 1 m . The average thermal conductivity of soil λ_s , and thermal diffusivity of soil are taken as $1.8 \text{ [W/(m} \cdot \text{K)]}$ and $7 \times 10^{-7} \text{ m}^2/\text{s}$, respectively. The HEP' radius r_b is taken as 0.5 m and running time τ and r_p are taken as 8 h .

The winter heating and summer cooling capacity obtained by the heat exchange capacity formula are 55.1W/m and 32.5W/m, respectively, which is close to the summer heat exchange capacity of pipe piles 35.2 W/m obtained from the literature (ZHU,1995). The result is consistent with experimental data obtained from the same literature. It can be seen that in this case the calculation results are consistent with the observed status and the calculation process can be used in the future as useful reference for engineering.

CONCLUSIONS

The HEP system combines conventional piles and ground source heat pumps, providing an innovative method that is economical, environment-friendly, and energy-saving. The calculation theory of heat transfer for HEP described in this article focuses on the soft clay's feature in Shanghai, which analyzes the heat exchange capacity of a residential building and verifies the application feasibility of HEP. It concludes that the related theoretically calculated results fit quite well with the data from real constructions, from which it has a guiding role in promoting the use of HEP in coastal soft clay regions. Since most researches studying HEP are still in the theoretical stage, the construction and application of HEP have to be further verified.

ACKNOWLEDGEMENTS

The authors appreciate the support of the National Natural Science Foundation of China (Grant No.41002091), Zhejiang Natural Science Foundation Project (Y1110087).

REFERENCES

- Fu X.Z. (2002). "Building energy-saving technology analysis in hot summer and cold winter areas". *Beijing: China Construction Industry Pres.* (in Chinese)
- GB50366. (2005). "Ground source heat pump system engineering technical specification". (in Chinese)
- Gong yu-lie, Zhao Jun, etc. (2002). "Experimental Research and Application of shallow piles buried heat exchanger". *National HVAC & R 2002 Annual Conference Proceedings.*
- Hamada, Y., Saitoh, H., Nakamura, M., Kubota, H., Ochiuji, K. (2007). "Field performance of an energy pile system for space heating". *Energy and Buildings*,39:517-524
- Harsh, G, Sukanta, R. (2007). "Geothermal energy: An alternative resource for the 21st century". *Amsterdam. The Netherlands*, Boston: Elsevier.
- Sanner B. (2001). "Some history of shallow geothermal energy use". *Quarterly Bulletin*, 22(2).
- Zhu Z. H., Fu X.Z. (1995). "Yangtze River Delta, residential heating and cooling energy system energy pile geothermal heat pump system". *Residential Technology*, 5: 41-42. (in Chinese)

AN EMPIRICAL STUDY ON THE ESTIMATION OF SOIL PROPERTIES OF LOESS GROUND AFTER DYNAMIC COMPACTION

Si-hai Luo¹, Yang Wang², Xiao-qing Pang³, Tong-fa Deng⁴

¹ Professor, Jiangxi University of Science and Technology, Ganzhou, Jiangxi, China, drsoil@163.com

² Master degree student, Jiangxi University of Science and Technology, Ganzhou, Jiangxi, China, wy19866@sina.com

³ Professor, Jiangxi University of Science and Technology, Ganzhou, Jiangxi, China, pxqecit@163.com

⁴ Lecturer, Jiangxi University of Science and Technology, Jiangxi Ganzhou 341000, China; dbdtf@163.com

ABSTRACT: Using dimensional analysis, the dimensional equations for the estimation of soil properties after dynamic compaction (DC) in loess ground are established. Based on these equations and field data obtained from previous practices of DC, the equations are fitted relating soil properties after DC with construction parameters, soil properties before tamping, and even with the surficial deformation during tamping. Finally, the equations are verified by several project examples, and the results indicate that the calculated results agree well with the field measured results. These equations provide a practical way for the prediction of the soil properties after DC for loess.

INTRODUCTION

Estimating soil properties after dynamic compaction (DC) represents an important research topic in the application of this ground improvement technique. Some progress has been made in the past years. Mayne et al. (1984) have drawn scatter diagrams to show the relationship between energy of tamping on a unit area and some soil parameters, such as the pressuremeter limit pressure and pressuremeter modulus. By applying the results of BEM, Qian et al. (1986, 1987) obtained a diagram relating the penetration per blow and tamping energy per unit area of hammer bottom. Lukas (1980, 1981) presented the limit values of some soil properties which can be reached by DC. Lo et al. (1990) also made contribution by presenting equations to calculate the average ground pressuremeter modulus ratio and the average limit pressure ratio. Based on the Biot theory, Zhou (1998) further proposed a method to compute the modulus of compressibility and seepage coefficient from the data obtained from the trial tamping. Luo (2008) worked out a method for estimating the improvement in sands by taking advantage of previous model tests and the quasi-static method. Kong et al. (1999) proposed a single-valued back analysis method by which the modulus of deformation of tamped ground can be deduced using a curve relating the calculated settlement and modulus of deformation. However, these research findings are not widely recognized, nor are they incorporated into design specifications. The current design of DC can only estimate the improvement depth quantitatively, yet there has been no generally accepted

equation to empirically estimate the soil properties after tamping. It is important, therefore, to improve the design and calculation method for DC.

In this paper, using dimensional analysis, the dimensional equations for estimating of soil properties of loess after DC will be established. Based on the field data obtained from previous engineering practices of DC, the fitted equations are established. The equation can be used to predict the soil properties of loess after tamping through construction parameters, soil properties before tamping, the surficial deformation during tamping, and provide a practical way for DC design in loess.

EMPIRICAL EQUATIONS RELATING SOIL PROPERTIES BEFORE AND AFTER DC

The Dimensional Equations

The soil properties after tamping are the dry bulk density γ'_d , modulus of compressibility E'_s , ground bearing capacity f'_s , and the soil properties before tamping are dry bulk density γ_d , modulus of compressibility E_s , ground bearing capacity f_s , water content ω , void ratio e . The construction parameters are average tamping energy E_{av} , tamping pass P , diameter of hammer D , the empirical equations which relate the soil properties after tamping with the construction parameters and the soil properties before tamping could be established as follows:

$$F(E_{av}, P, D, \gamma_d, \omega, \gamma'_d) = 0 \quad (1)$$

$$F(E_{av}, P, D, \gamma_d, E_s, E'_s) = 0 \quad (2)$$

$$F(E_{av}, P, D, \gamma_d, E_s, f_s, f'_s) = 0 \quad (3)$$

Through dimensional analysis, the empirical Equations 1, 2 and 3 can be transformed into:

$$F(\pi_1, \pi_7, \pi_8, \pi_9) = 0 \quad (4)$$

$$F(\pi_2, \pi_8, \pi_9, \pi_{10}) = 0 \quad (5)$$

$$F(\pi_3, \pi_8, \pi_9, \pi_{10}, \pi_{11}) = 0 \quad (6)$$

where:

$$\pi_1 = \frac{\gamma'_d D^2}{E_{av}} \quad \pi_2 = \frac{E'_s D}{E_{av}} \quad \pi_3 = \frac{f'_s D}{E_{av}} \quad \pi_7 = \omega \quad \pi_8 = P \quad \pi_9 = \frac{\gamma_d D^2}{E_{av}} \quad \pi_{10} = \frac{E_s D}{E_{av}} \quad \pi_{11} = \frac{f_s D}{E_{av}}$$

Empirical Equations for Estimating Soil properties After Tamping

Using data collected from 23 sets of previous engineering practices (see the references, when soil parameters are used, the weighted average of the parameters within effective reinforcement depth is adopted), the values of dimensionless quantities in the Equations 4, 5 and 6 are obtained. After the multiple regression analysis by means of the MATLAB software, the fitted equations have been established, which can be applied to predict soil properties after tamping with reference to soil properties before tamping and construction parameters.

$$\pi_1 = -0.0004 - 0.0325\pi_7 + 0.001\pi_8 + 1.2063\pi_9 \tag{7}$$

$$\pi_2 = -0.001 - 0.0005\pi_8 + 0.3371\pi_9 + 0.6394\pi_{10} \tag{8}$$

$$\pi_3 = 0.0069 - 0.0028\pi_8 + 3.2615\pi_9 + 3.4172\pi_{10} + 0.6503\pi_{11} \tag{9}$$

Substituting the dimensionless quantities into the previous equations, Equations 7, 8, and 9 can be transformed into:

$$\gamma'_d = \left[0.0004 - 0.0325\omega + 0.001P + 1.2036 \frac{\gamma_d D^2}{E_{av}} \right] \frac{E_{av}}{D^2} \tag{10}$$

$$E'_s = \left[-0.001 - 0.0005P + 0.3371 \frac{\gamma_d D^2}{E_{av}} + 0.06394 \frac{E_s D}{E_{av}} \right] \frac{E_{av}}{D} \tag{11}$$

$$f'_s = \left[0.0069 - 0.0028P + 3.2615 \frac{\gamma_d D^2}{E_{av}} + 3.4172 \frac{E_s D}{E_{av}} + 0.6503 \frac{f_s D}{E_{av}} \right] \frac{E_{av}}{D} \tag{12}$$

EMPIRICAL EQUATIONS RELATING SOIL PROPERTIES AFTER DC WITH CONSTRUCTION PARAMETERS, SOIL PROPERTIES BEFORE TAMPING AND SURFICIAL DEFORMATION DURING TAMPING

The Dimensional Equations

Suppose the dry bulk density, modulus of compressibility, and ground bearing capacity after tamping are γ'_d , E'_s and f'_s respectively, and the soil properties before tamping are dry bulk density γ_d , modulus of compressibility E_s , ground bearing capacity f_s , water content ω , void ratio e , and the construction parameters are average tamping energy E_{av} , tamping pass P , diameter of hammer D , and the weight of hammer W . The equations, which relate the soil properties after tamping with soil properties before tamping, construction parameters, as well as the surficial deformation during tamping, could be written as:

$$F(E_{av}, S_e, D, W, P, \gamma_d, \gamma'_d) = 0 \tag{13}$$

$$F(E_{av}, S_e, D, W, P, E_s, E'_s) = 0 \quad (14)$$

$$F(e, \omega, f_s, \gamma_d, S_e, E_s, f'_s) = 0 \quad (15)$$

Equations 13, 14 and 15 can be transformed into the following dimensional equations through dimensional analysis:

$$F(\pi_4, \pi_{17}, \pi_{12}, \pi_8, \pi_{18}) = 0 \quad (16)$$

$$F(\pi_5, \pi_{17}, \pi_{12}, \pi_8, \pi_{13}) = 0 \quad (17)$$

$$F(\pi_6, \pi_{14}, \pi_7, \pi_{15}, \pi_{16}) = 0 \quad (18)$$

where $\pi_4 = \gamma_d' D^3 / W$, $\pi_5 = E_s' D^2 / W$, $\pi_6 = f_s' / E_s$, $\pi_{12} = E_{av} D / (W)$, $\pi_{13} = E_s D^2 / W$, $\pi_{14} = e$, $\pi_{15} = f_s / E_s$, $\pi_{16} = \gamma_d S_e / E_s$, $\pi_{17} = S_e / D$, $\pi_{18} = \gamma_d D^3 / W$, and the other variables are the same as before.

Empirical Equations for Estimating Soil Properties After Tamping

On the basis of the data collected from 15 sets of previous practices (see references, when soil parameters are used the weighted average of the parameters within effective reinforcement depth is adopted), the values of dimensionless quantities in the Equations 16 -18 can be obtained. After the multiple regression analysis by means of the MATLAB software, the fitted equations have been established, which can be used to predict soil properties with reference to ground properties before tamping, the construction parameters and the surficial deformation during tamping.

$$\pi_4 = 0.1148 - 0.0340\pi_{17} + 0.0002\pi_{12} - 0.0168\pi_8 + 1.0707\pi_{18} \quad (19)$$

$$\pi_5 = 0.4560 + 0.059\pi_{17} + 0.0011\pi_{12} - 0.0749\pi_8 + 0.6096\pi_{13} \quad (20)$$

$$\pi_6 = -3.137 - 2.324\pi_{14} + 46.367\pi_7 + 0.908\pi_{15} + 4.980\pi_{16} \quad (21)$$

Then substituting the dimensionless quantities into the previous equations, Equations 19, 20, and 21 can be transformed into:

$$\gamma_d' = [0.1148 - 0.0340 \frac{S_e}{D} + 0.0002 \frac{E_{av} D}{W} - 0.0168 P + 1.0707 \frac{\gamma_d D^3}{W}] \frac{W}{D^3} \quad (22)$$

$$E_s' = [0.4560 + 0.059 \frac{S_e}{D} + 0.0011 \frac{E_{av} D}{W} - 0.0749 P + 0.6096 \frac{E_s D^2}{W}] \frac{W}{D^2} \quad (23)$$

$$f_s' = [-3.137 - 2.324e + 46.367\omega + 0.908 \frac{f_s}{E_s} + 4.980 \frac{\gamma_s S_e}{E_s}] E_s \quad (24)$$

COMPARISON AND VERIFICATION OF THE EQUATIONS

Comparison Between Equation Results and Measurement Value

The estimated value obtained in every fitted equation (γ_d', E_s', f_s') by using the data collected from actual engineering practice is T' and the value obtained from actual measurement is set as T , then:

$$\beta = T'/T \tag{25}$$

Where β is the ratio of the actual measurement to the actual engineering practice. The calculated ratio range of different dimensional equations is presented in Table 1.

Table 1. β Range in Different Equations

Equation	(10)	(11)	(12)	(22)	(23)	(24)
β	0.90~1.11	0.66~1.39	0.73~1.34	0.95~1.05	0.74~1.41	0.72~1.21
Percentage of β Between 0.8~1.2	100%	78%	84%	100%	80%	88%

From Table 1, it can be seen that the ratio range of measurement and estimation of dry bulk density after tamping is from 0.90 to 1.11 with reference to the soil properties before tamping and construction parameter, and the ratio range is from 0.95 to 1.05 if surficial deformation during tamping had been considered. In terms of modulus of compressibility after tamping, the ratio range is from 0.66 to 1.39 when the soil properties before tamping and construction parameter are considered, and the ratio range is from 0.74 to 1.41 if the surficial deformation during tamping had been taken into account. In terms of ground bearing capacity after tamping, the ratio range is from 0.73 to 1.34 when the ground properties before tamping and construction parameter had been considered, and the ratio ranges from 0.72 to 1.21 when the surficial deformation during tamping had been taken into account. The fact that the ratio of measurement and estimation ranging from 0.8 to 1.2 occupies more than 78%, as shown in Table 1, shows that the fitted equations can fit well with the measured results.

Equation Verification

In this part, the fitted equations and the ratio coefficient will be applied to estimate the engineering projects which have not been involved in the establishment of fitted equation in order to further verify its feasibility. The results are presented in Tables 2, 3, and 4.

Table 2. The Fitted results of the Dry Bulk Density after Tamping and Comparison with Measured Results

Equation	Beltway in Xi'an (Li, 2009)		A Project (Xu, 2004)		Pu Cheng power plant (Editing Group of Collection of Foundation Treatment Experience 1996)		A Highway (Li, 1998)	
	Est.	β	Est.	β	Est.	β	Est.	β
(10)	15.0	13.5~16.6	16.3	14.7~18.1	16.0	14.4~17.8		
(22)					16.2	15.4~17.0	14.2	15.1~16.7
Measured	14.3		16.0		16.5		15.4	

Table 3. The Fitted Results of Modulus of Compressibility after Tamping and Comparison with Measured Results

Equation	Freight Terminal Warehouse (Hu, 2010)		Pu Cheng power plant (Editing Group of Collection of Foundation Treatment Experience 1996)	
	Est.	β Range	Est.	β Range
(11)	9.3	6.1~12.9	22.0	14.52~30.6
(23)			25.0	18.5~35.2
Measured	9.6		23.2	

Table 4. The Fitted Results of Ground Bearing Capacity after Tamping and Comparison with Measured Results

Equation	Chang Shan thermal power plant (Editing Group of Collection of Foundation Treatment Experience 1996)		Pu Cheng power plant (Editing Group of Collection of Foundation Treatment Experience 1996)	
	Est.	β Range	Est.	β Range
(12)	244	173~328	325	233~441
(24)			327	235~395
Measured	227		300	

As Tables 2, 3 and 4 show, the dry bulk density after tamping, modulus of compressibility and ground bearing capacity can be calculated through the fitted equations in the present study. The measured values fall exactly between the upper and lower limit of estimation, and is close to the calculated values in general by adopting the fitted equations. All of these manifest that it is feasible and practical to estimate the soil properties after tamping with the fitted equations in most of the engineering projects.

CONCLUSIONS

This study has established equations for estimating soil properties after tamping based on soil properties before tamping, construction parameters and surficial deformation during tamping, which lead to the following conclusions:

1. Taking the construction parameters and soil properties before tamping as parameters, the Equations 10, 11, and 12, for estimating dry bulk density, modulus of compressibility and ground bearing capacity of loess after tamping respectively, have been established.
2. Taking the surficial deformation during tamping into consideration, Equations 22, 23 and 24 have been further established.
3. The fact that the ratio of measured and estimated values, β , range from 0.8 to 1.2 for more than 80% of the cases shows that the fitted equations can be used to reliably predict the measured results.

ACKNOWLEDGMENTS

The research is supported by the following funds: National Natural Science Foundation (Project Grant No.: 50869002), Jiangxi Province Natural Science Foundation (Project Grant No.: 2008GZC003), Science and Technology project of Jiangxi Department of Education (Project Grant No.: [2007] 210)

REFERENCES

- Chen, P. (2009). "The Research on Dynamic Compaction in a Collapsible Loess Area in some Transformer Substation." *Shanxi Architecture*, China, 35(15),104-105.
- Ding, Z.H., Feng, Z.Z. (2006). "Application of High-energy Dynamic Compaction in the Collapsible Loess Areas." *West-China Exploration Engineering*, China, 12.
- Dong, J.M., Jin, S.B. (2008). "Application of Dynamic Compaction in the Collapsible Loess in Longxi." *China Science and technology information*, China, 18,62-65.
- Editing Group of Collection of Foundation Treatment Experience. (1996). "Collection of Foundation Treatment Experience." *China Electric Power Press*. Beijing, China.
- Gou, B.Q., Fang, Y. (2009). "Construction Technology of Dynamic Compaction Processing Refilled Loess Foundation." *Shanxi Architecture*, China, 35(27),119-121.
- He, L.S., Ma, X.W. (2008). "8000kn.m Energy Dynamic Compaction Experiment for Collapsible Loess in Dongzhuyuan, Gansu." *Geotechnical Engineering World*, China, 11(9),48-50.
- He, Y., Zhang, W.J., Kang, Y.N. et al. (2009). "The Research on Dynamic Compaction in a Collapsible Loess Area in Dongzhuyuan, Gansu." *Geotechnical Engineering World*, China, 12(7), 61-68.
- Hu, S.Q., Shi, J.F. (2010). "Application of Dynamic Consolidation Method for the Treatment of Collapsible Loess Foundation." *Journal of Baoding University*, China, 23(3),94-95.

- Kong, L.W. (1999). "Back Calculation of Modulus of Deformation and Bearing Capacity for Foundation after Dynamic Consolidation." *Chinese Journal of Geotechnical Engineering*, China,21(2), 153-157.
- Li, B.H. (2005). "Practice on Deeper Consolidation of Foundation with Increased Dynamic Compaction of 8000 kN-m and Related Discussions." *Building Construction*, China, 27(11), 17-18.
- Li, J., Cui, G.M. (2009). "Zhao Jun, Experimental Study on Reinforcing Collapsible Loess Foundation of Earth Dam with Dynamic Compaction Method." *Hena Science*, China, 24(1),111-114.
- Li, Z.H. (2010). "Application of Dynamic Compaction Technology to Reinforcing Collapsible Loess Sub grade." *Railway Engineering*, China, 2, 82-83.
- Li, Z.P. (1998). "A Study on the Application of Dynamic Compaction of High-grade Highway in the Collapsible Loess Areas." *Inner Mongolia Highway and Transportation*, China, 3,3-6.
- Lo, K.W., Ooi, P.L., Lee, S.L. (1990a). "Unified Approach to Ground Improvement by Heavy Tamping." *Journal of Geotechnical Engineering*, ASCE, 116(3),514-527.
- Lo, K.W., Ooi, P.L., Lee, S.L. (1990b). "Dynamic Replacement and Mixing of Organic Soil with Sand Charges." *Journal of Geotechnical Engineering*, ASCE, 116(10),1463-1482.
- Lukas, R.G. (1980). "Densification of Loose Deposits by Pounding." *Journal of the Geotechnical Engineering*, ASCE, 106(4),435-446.
- Lukas, R.G. (1981). "Dynamic Compaction Engineering Consideration." *Grouting/Soil Improvement and Geosynthetics*, 941-947.
- Luo, S.H. (1999). "Computation of the Improvement of Soft Ground Treated by Dynamic Compaction and Dynamic Replacement." *Zhenjiang University, Hangzhou*. China.
- Luo, S.H. (2008). "Quasi-static Analysis on the Estimation of Effect of Dynamic Compaction in the Non-cohesive Soil." *Chinese Journal of Geotechnical Engineering*, China,30(4),480-486.
- Mayne, P.W. and Jones, J.S. (1984). "Ground Response to Dynamic Compaction." *Journal of Geotechnical Engineering*, ASCE, 110(6),757-774.
- Niu X.S., Jiang, Y.J. (2001). "Dynamic Compaction Treatment on the Base of Loess Embankment with Wet Subsidence in the Sanmenxia-Lingbao Expressway." *Journal of the Railway engineering society*, China, 4,34-37.
- Pang, H.C. (2008). "On the test and Effect Evaluation of the Dynamic Consolidation Method in Strengthening the Loess Filling-in and Excavation Roadbeds." *Shanxi Architecture*, China, 34(25),287-288.
- Qian, J.H.,Qian, X.D., et al. (1986). "Theory and Practice of Dynamic Consolidation." *Chinese Journal of Geotechnical Engineering*, China, 8(6), 1-17.
- Qian, J.H., Shuai, F.S. (1987). "On the Application of BEM in Ground Dynamic Compaction." *Science China Series A*, China, (3),329-336.
- Shen, M.P. (2009). "Application of Heavy-tamping Method in Dealing with Deep Layer Collapsible Loess Dam Foundation ." *Ningxia Engineering Technology*, China, 18(3),265-268.

- Su, B. (2001). "Treatment on 46,000 m² Foundation of Chemical Fiber Project of SINOPEC Luoyang Petrochemical Complex with Dynamic Consolidation." *Chinese Journal of Geotechnical Engineering*, China, 23(2), 221-226.
- Wang, J.W., Li Y.Z. (2007). "Application of Dynamic Compaction Method on Collapsible Loess Subgrade." *Soil Engineering and Foundation*, China, 21(3), 7-9.
- Wang, J., Zhang, X.H. (2004). "Effect Analysis of Collapsibility Loess Foundation Treatment with Dynamic Compaction." *Electric Power Survey and Design*, China, 03, 18-21.
- Wang, T.H. (2005). "Foundation Treatment of Capital Engineering Projects in China." *Industrial Construction Press*, Beijing, China.
- Xu, C.Y. (2004). "Practice on Treatment of Collapsible Loess Foundation by Dynamic Consolidation Method." *Ningxia Engineering and Technology*, China, 3(1), 18-23
- Xu, Y. (2007). "Ground Base Treatment by Strong Ramming and Analysis of Engineering Example." *Construction and design for project*, China, 8, 50-53.
- Yang, G.R. (2006). "Experimental Research on Heavy Tamping of Collapsible Loess Foundation of Airport." *Engineering Construction*, China, 38(5), 10-14.
- Ye, K.Z., Liao, Z.J. (2005). "Engineering Practice for Handling Collapsible Loess by Heavy Tamping Method." *Subgrade Engineering*, China, 3, 54-56.
- Zeng, B.G., Jin, Y.H. (2007). "An Application Research on High Energy Strong Rammer in Dealing with Collapsed Loess." *Shanxi Architecture*, China, 143, 44-46.
- Zhan, J.L., Shui, W.H., He, L.J. et al. (2010). "12000 kN-m Energy Dynamic Compaction Experiment for Collapsible Loess." *Industrial Construction*, China, 40(6), 93-96.
- Zhou, L.Z. (1998). "A Study on the Theory of Mild Clay Ground Dynamic Compaction and Construction Technology and its Application in the Airport." *Logistic Engineering University*, China.
- Zhou, C.Y. (2007). "Application of Tamping in the Collapsibility Loess Subgrade Settlement." *Technology and economy in areas of communication*, China, 8, 13-15.
- Zuo, M.L., Zhu, S.S. (1990). "Ground Dynamic Compaction." *China Railway Press*, Beijing, China.

THEORETICAL BACKGROUND OF AXIS-RADIATE INFINITE ELEMENT WITH ITS APPLICATIONS IN FOUNDATION ANALYSIS

Hongyang Xie¹, Yang Huang¹, Jinquan Yin¹

¹ College of Civil Engineering and Architecture, Nanchang Hangkong University, Nanchang, China; xiehongyang486@163.com

ABSTRACT: An axis-radiate infinite element and a radiate damping matrix applicable to 3D curved boundary are developed to simulate the infinite layered foundation under a rigid base layer. Within the infinite element, the coordinate and displacement of any point are expressed by those of the nodes located on the artificial boundary, and concise mapping functions can easily express the attenuation character of the displacement field. By coupling finite/infinite elements, the elastic recovery capacity and radiation damping of the infinite layered foundation can be easily simulated. In the numerical calculation, the infinite element mesh is performed only on the artificial boundary and the general solution is not needed. Results of examples show high accuracy and efficiency.

INTRODUCTION

Since Cheung (1965) first analyzed square plates on elastic foundations by the semi-analytical and semi-numerical method, numerical analyses for the compatibility of the foundation and upper layer has gained more and more attention. In 1973, Ungless 1973 first presented the concept of infinite element (Ungless 1973). For static problems, the infinite foundation can be simulated by coupling finite and infinite elements. In the dynamic problems an artificial viscous boundary (Lysmer 1969) is usually adopted to simulate the radiate damping effect of the infinite foundation. Deeks (1994) developed a viscous elastic boundary capable of simulating both the radiate damping and recovery capacity, but is limited for the plane surface boundary.

In this study, the model of 3D axis-radiate 8-node infinite element is presented. The model can simulate the elastic recovery capacity of the infinite layered foundation underlying a rigid base. A new radiate damping matrix is developed to simulate the radiate damping effect of the 3D curved surface boundary.

MAPPING FUNCTION FOR 1D CASE

Zienkiewicz (1983) presented a type of coordinate mapping function, which maps the finite zone in the local coordinate system to an infinite zone in the global coordinate

system. For the 1D case, a point x_0 in the global coordinate system is selected as the mapping pole, and two other points $x_1, x_2=2x_1-x_0$ are selected to fulfill the mapping. Let the local coordinate ζ direct to the infinity, the coordinate mapping from the local to the global coordinate system is expressed as equation (1):

$$x = \sum_{i=1}^2 N_i^1 x_i \tag{1}$$

where N_i^1 is the mapping function as shown in equation (2):

$$\begin{cases} N_1^1 = -2\zeta / (1-\zeta) \\ N_2^1 = (1+\zeta) / (1-\zeta) \end{cases} \tag{2}$$

Thus the local coordinate $\zeta = -1, 0$ and $+1$ correspond to the global coordinate $x = x_1, x_2$ and ∞ , respectively (FIG. 1).

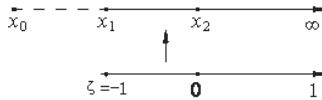


FIG. 1. Two-point coordinate mapping for 1D case

In the mapping as shown in FIG 1, x_1 and x_2 are not mutually independent. In substance, let the pole be the origin of the global coordinate system (i.e., $x_0=0$), only one point x_1 is needed to implement the coordinate mapping from the local to the global coordinate system. The coordinate mapping is shown in equation (3).

$$x = \frac{2}{1-\zeta} x_1 = N^1 x_1 \tag{3}$$

where N^1 is the mapping function. The local coordinate $\zeta = -1, 0$ and $+1$ correspond to the global coordinate $x = x_1, 2x_1$ and ∞ , respectively (FIG. 2).

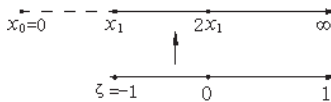


FIG. 2. One-point coordinate mapping for 1D case

Comparing to equation (1), equation (3) has some advantages: the mapping pole is the origin of the global coordinate system, and only one point x_1 on the artificial boundary is needed.

3D AXIS-RADIATE INFINITE ELEMENT

The infinite layered foundation is divided into two subfields by an artificial cylindrical boundary whose symmetric axis is set as the z -axis of the global coordinate system. The subfield inside the boundary is meshed by 3D 20-node isoparametric elements, and the subfield outside the boundary is meshed by 3D axis-radiate 8-node infinite elements. All the 8 nodes of the infinite elements are on the artificial boundary, and the radiate pole is the z -axis. The ζ -axis in the local coordinate system maps the infinite direction (FIG. 3). The coordinate mapping is shown in equation (4).

$$x = \sum_{i=1}^8 N_i x_i, \quad y = \sum_{i=1}^8 N_i y_i, \quad z = \sum_{i=1}^8 N_i^z z_i \tag{4}$$

where

$$\begin{cases} N_i = \frac{(1 + \xi_i \xi)(1 + \eta_i \eta)(\xi_i \xi + \eta_i \eta - 1)}{2(1 - \zeta)} & (i = 1, 3, 5, 7) \\ N_i = \frac{(1 + \eta_i \eta)(\xi^2 - 1)}{1 - \zeta} & (i = 2, 6) \\ N_i = \frac{(1 + \xi_i \xi)(\eta^2 - 1)}{1 - \zeta} & (i = 4, 8) \end{cases} \tag{5}$$

$$\begin{cases} N_i^z = \frac{(1 + \xi_i \xi)(1 + \eta_i \eta)(\xi_i \xi + \eta_i \eta - 1)}{4} & (i = 1, 3, 5, 7) \\ N_i^z = \frac{(1 + \eta_i \eta)(\xi^2 - 1)}{2} & (i = 2, 6) \\ N_i^z = \frac{(1 + \xi_i \xi)(\eta^2 - 1)}{2} & (i = 4, 8) \end{cases} \tag{6}$$

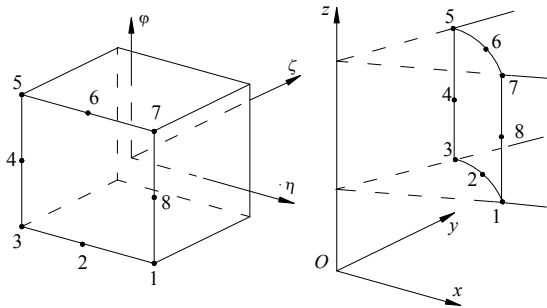


FIG. 3. 3D axis-radiate 8-node infinite element

The mapping functions ensure the coordinate mapping is a continuous transformation. When $\zeta = -1$, the face determined by equation (4) is the same as that determined by the adjacent 3D 20-node isoparametric element. When $\zeta \rightarrow 1$, the determined face tends to the infinity.

As all the nodes of the infinite elements are on the artificial cylindrical boundary, there is an approximate relationship as shown in equation (7).

$$\frac{r_0}{r} \approx \frac{1-\zeta}{2} \tag{7}$$

where r_0 is the radius of the artificial cylindrical boundary, and r is the distance from the point outside the boundary to the z -axis of the global coordinate system.

Assume that along the ζ direction, the displacement field begins to attenuate from the artificial boundary, and the attenuation pole is the the z -axis, the displacement attenuation function can be selected as

$$f(\zeta) = \frac{1-\zeta}{2} \tag{8}$$

Thus the displacement of any point within the infinite element can be determined by

$$u = \sum_{i=1}^8 W_i u_i, \quad v = \sum_{i=1}^8 W_i v_i, \quad w = \sum_{i=1}^8 W_i w_i \tag{9}$$

And the corresponding matrix form is

$$\{\delta\} = [u \quad v \quad w]^T = \begin{bmatrix} W_1 & 0 & 0 & \dots & W_8 & 0 & 0 \\ 0 & W_1 & 0 & \dots & 0 & W_8 & 0 \\ 0 & 0 & W_1 & \dots & 0 & 0 & W_8 \end{bmatrix} \begin{Bmatrix} u_1 \\ v_1 \\ w_1 \\ \vdots \\ u_8 \\ v_8 \\ w_8 \end{Bmatrix} = [W] \{\delta\}^e \tag{10}$$

where $[W]$ is the displacement function matrix of the point-radiate infinite element and W_i is the displacement function:

$$\begin{cases} W_i = \frac{(1+\xi_i \zeta)(1+\eta_i \eta)(\xi_i \xi + \eta_i \eta - 1)}{4} \left(\frac{1-\zeta}{2}\right) & (i=1,3,5,7) \\ W_i = \frac{(1+\eta_i \eta)(\xi^2 - 1)}{2} \left(\frac{1-\zeta}{2}\right) & (i=2,6) \\ W_i = \frac{(1+\xi_i \zeta)(\eta^2 - 1)}{2} \left(\frac{1-\zeta}{2}\right) & (i=4,8) \end{cases} \tag{11}$$

Obviously when $\zeta \rightarrow 1$, the displacements tend to be zero. According to (9), the strain matrix can be determined as

$$[B] = [B_1 \quad B_2 \quad \dots \quad B_8] \tag{12}$$

where

$$[B_i] = \begin{bmatrix} \frac{\partial W_i}{\partial x} & 0 & 0 & \frac{\partial W_i}{\partial y} & 0 & \frac{\partial W_i}{\partial z} \\ 0 & \frac{\partial W_i}{\partial y} & 0 & \frac{\partial W_i}{\partial x} & \frac{\partial W_i}{\partial z} & 0 \\ 0 & 0 & \frac{\partial W_i}{\partial z} & 0 & \frac{\partial W_i}{\partial y} & \frac{\partial W_i}{\partial x} \end{bmatrix}^T \tag{13}$$

The differential coefficients in (13) can be determined as

$$\begin{Bmatrix} \frac{\partial W_i}{\partial x} \\ \frac{\partial W_i}{\partial y} \\ \frac{\partial W_i}{\partial z} \end{Bmatrix} = \begin{bmatrix} \frac{\partial x}{\partial \xi} & \frac{\partial y}{\partial \xi} & \frac{\partial z}{\partial \xi} \\ \frac{\partial x}{\partial \eta} & \frac{\partial y}{\partial \eta} & \frac{\partial z}{\partial \eta} \\ \frac{\partial x}{\partial \zeta} & \frac{\partial y}{\partial \zeta} & \frac{\partial z}{\partial \zeta} \end{bmatrix}^{-1} \begin{Bmatrix} \frac{\partial W_i}{\partial \xi} \\ \frac{\partial W_i}{\partial \eta} \\ \frac{\partial W_i}{\partial \zeta} \end{Bmatrix} = [J]^{-1} \begin{Bmatrix} \frac{\partial W_i}{\partial \xi} \\ \frac{\partial W_i}{\partial \eta} \\ \frac{\partial W_i}{\partial \zeta} \end{Bmatrix} \tag{14}$$

And the stiffness matrix of the infinite element can be determined as

$$[k] = \iiint_V [B]^T [D] [B] dV \tag{15}$$

where $[D]$ is the elastic matrix for 3D elastic problem.

Radiate damping matrix

The radiate damping effect can be simulated by setting a viscous boundary. Lysmer (1969) noticed that on the boundary, if the stress and the velocity of any point satisfy (16), the boundary can be seen as a viscous boundary which reflects little wave energy.

$$\begin{cases} \sigma = \alpha \rho v_p V_n \\ \tau = \beta \rho v_s V_t \end{cases} \tag{16}$$

In equation (16), σ and τ are the normal and tangential stresses, respectively. V_n and V_t are the normal and tangential velocities of the discussed point, respectively. ρ is the density. v_p and v_s are the velocities of the P wave and the S wave, respectively. α and β are dimensionless factors. When both α and β are assigned to the value of 1.0, the

responding viscous boundary is called a standard viscous boundary.

At the point $M(x,y,z)$ on the boundary, take an infinitesimal area dS , then the cast areas on the xy , yz and zx planes are dS_{xy} , dS_{yz} and dS_{zx} respectively. Note that the unit normal line is $\vec{n} = n_1\vec{i} + n_2\vec{j} + n_3\vec{k}$, then

$$\begin{cases} n_1 = \cos(\vec{x}, \vec{n}) = \frac{dS_{yz}}{dS} \text{sign}(x) \\ n_2 = \cos(\vec{y}, \vec{n}) = \frac{dS_{zx}}{dS} \text{sign}(y) \\ n_3 = \cos(\vec{z}, \vec{n}) = \frac{dS_{xy}}{dS} \text{sign}(z) \end{cases} \quad (17)$$

where sign is the symbolic function. The velocity of point M is

$$\vec{V} = \dot{u}\vec{i} + \dot{v}\vec{j} + \dot{w}\vec{k} \quad (18)$$

Thus the normal velocity is

$$\begin{aligned} \vec{V}_n &= (\vec{V} \cdot \vec{n})\vec{n} = (n_1\dot{u} + n_2\dot{v} + n_3\dot{w})\vec{n} \\ &= (n_1^2\dot{u} + n_1n_2\dot{v} + n_1n_3\dot{w})\vec{i} + (n_1n_2\dot{u} + n_2^2\dot{v} + n_2n_3\dot{w})\vec{j} + (n_1n_3\dot{u} + n_2n_3\dot{v} + n_3^2\dot{w})\vec{k} \end{aligned} \quad (19)$$

And the normal damping stress is

$$\vec{p}_n = \rho v_p \vec{V}_n \quad (20)$$

The tangential velocity of point M is

$$\begin{aligned} \vec{V}_t &= \vec{V} - \vec{V}_n = [(1 - n_1^2)\dot{u} - n_1n_2\dot{v} - n_1n_3\dot{w}]\vec{i} \\ &\quad + [-n_1n_2\dot{u} + (1 - n_2^2)\dot{v} - n_2n_3\dot{w}]\vec{j} + [-n_1n_3\dot{u} - n_2n_3\dot{v} + (1 - n_3^2)\dot{w}]\vec{k} \end{aligned} \quad (21)$$

The tangential damping stress is

$$\vec{p}_t = \rho v_s \vec{V}_t \quad (22)$$

The resultant damping stress is

$$\vec{p} = \vec{p}_n + \vec{p}_t = [p] \{\delta\} \quad (23)$$

Where

$$[p] = \rho \begin{bmatrix} (v_p - v_s)n_1^2 + v_s & n_1n_2(v_p - v_s) & n_1n_3(v_p - v_s) \\ n_1n_2(v_p - v_s) & (v_p - v_s)n_2^2 + v_s & n_2n_3(v_p - v_s) \\ n_1n_3(v_p - v_s) & n_2n_3(v_p - v_s) & (v_p - v_s)n_3^2 + v_s \end{bmatrix} \quad (24)$$

As (23) determines the damping stress at any point on the boundary, the equivalent node force $\{P_d\}^e$ can be calculated as

$$\{P_d\}^e = \iint_S [W]^T [p][W] dS \{\delta\}^e \quad (25)$$

where $[W]$ is the displacement function matrix on the boundary, it can be determined by (11) and letting $\zeta = -1$. Thus the radiate damping matrix $[c]$ is obtained.

$$[c] = \iint_S [W]^T [p][W] dS \quad (26)$$

NUMERICAL ANALYSES FOR LAYERED FOUNDATION

Example 1: A static analysis for a foundation composed of two layers underlying a rigid base. For the upper layer, the thickness $h_1 = 5\text{m}$, the elastic modulus $E_1 = 30\text{Mpa}$, and the poisons ratio $\mu_1 = 0.25$. For the lower layer, $h_2 = 5\text{m}$, $E_2 = 50\text{MPa}$, and $\mu_2 = 0.3$. The foundation is subjected to squarely distributed load. The magnitude of the load is 10kPa , and distributed area is $8 \times 8\text{m}^2$.

Due to the symmetry of the problem, only one quadrant of the foundation is taken into account for the calculation. An artificial cylindrical boundary with a radius of 8m is selected. The element mesh is shown in FIG. 4. The part inside the boundary is meshed by 20 3D 20-node elements, and the boundary is meshed by 8 axis-radiate infinite elements.

The ground settlement along the x -axis is shown in FIG. 5. For comparison, the results by FEM with free boundary and fixed boundary are also shown in the figure. It can be seen that the ground settlement calculated by the presented approach is greater than that by FEM with fixed boundary, but smaller than that by FEM with free boundary.

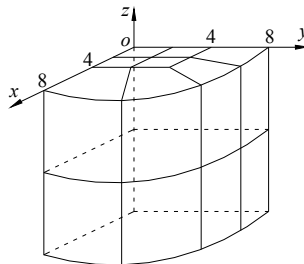


FIG. 4. Element mesh for example 1

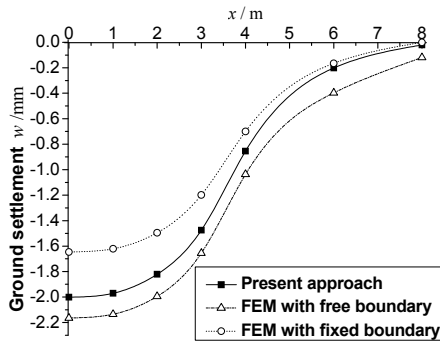


FIG. 5. Ground settlement of example 1

Example 2: The dynamic response of a foundation composed of 2 layers subjected to unit harmonic force. For the upper layer, the thickness $h_1 = 3\text{m}$, the elastic modulus $E_1 = 30\text{Mpa}$, the poisson ratio $\mu_1 = 0.25$, and the soil density $\rho_1 = 1700\text{kg/m}^3$. For the lower layer, $h_2 = 3\text{m}$, $E_2 = 50\text{Mpa}$, $\mu_2 = 0.3$, and $\rho_2 = 1700\text{kg/m}^3$. The peak value of the harmonic force is 1.0 N, the excitation frequency is 20 Hz, and the total excitation time is 3 periodic times, i.e.

$$P(t) = \begin{cases} -\sin(125.6637t) & t < 0.15\text{s} \\ 0 & t \geq 0.15\text{s} \end{cases}$$

The radius of the artificial boundary is 8m. Similar to example 1, only one quadrant of the foundation is taken into account for the calculation. The time-domain deflection responses of the foundation surface are shown in FIG. 6, where r is the distance from the harmonic force.

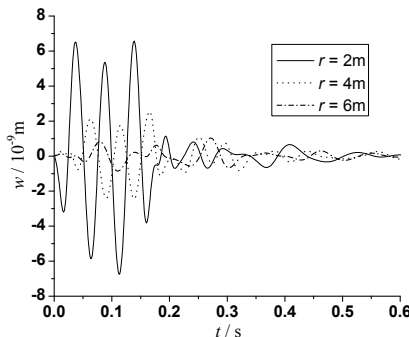


FIG. 6. Vertical displacement response for example 2

CONCLUSION

The model of the 3D axis-radiate infinite element and a new type of radiate damping matrix are developed. By coupling finite and axis-radiate infinite elements, the numerical analyses of layered foundation are conducted. Results of examples show good accuracy and efficiency.

REFERENCES

- Cheung, Y. K. and Zienkiewicz, O. C. (1965). "Plates and tanks on elastic foundation-an application of the finite element method." *International Journal of Solids and structures*, Vol. 1: 529-551.
- Deeks, A. J. And Randolph, M. F. (1994). "Axisymmetric Time-domain Transmitting Boundaries." *Journal of Engineering Mechanics*, Vol. 120: 25-42.
- Lysmer, L. and Kuhlemeyer, R. L. (1969). "Finite dynamic model for infinite media." *Journal of the Engineering Mechanics Division, ASCE EM4*, Vol. 95: 759-877.
- Ungless, R. L. (1973). "An infinite finite element." M.A.Sc. University of British Columbia, Vancouver, British Columbia.
- Zienkiewicz, O. C., Emson, C. and Bettess, P. (1983). "A novel boundary infinite element." *International Journal for Numerical Methods in Engineering*, Vol. 19: 393-404.

INFLUENCE OF FEATURES OF NATURAL SOFT CLAY ON EMBANKMENT BEHAVIOR

Jian-Hua Wang¹, Minna Karstunen² and Zhen-Yu Yin¹

¹Department of Civil Engineering, Shanghai Jiao Tong University, 800 Dong Chuan Road, 200240, Shanghai, PR China; wjh417@sjtu.edu.cn, zhenyu.yin@sjtu.edu.cn

²Department of Civil Engineering, University of Strathclyde, John Anderson Building, 107 Rottenrow, Glasgow G4 0NG, UK; minna.karstunen@strath.ac.uk

ABSTRACT: This paper aims to investigate the influence of different features of natural soft clays, namely anisotropy, destructuration, on modeling the long-term behavior of embankments. The newly developed elasto-viscoplastic model is used for this purpose. The parameters determined from conventional triaxial and oedometer tests are employed for simulations, with additional parameters required representing different soil features. The finite element predictions by using the model coupled with Biot's consolidation theory compare the results for settlement, horizontal displacement and excess pore pressures. All simulations demonstrate that all three features influence significantly the predictions.

INTRODUCTION

The stress-strain behavior of soft soils is very complex. As different fundamental features of natural soil behavior, such as viscosity, anisotropy and destructuration, influence the soil response to foundation loading. Thus, design and construction of embankments on soft soil deposits is still a challenge. Karstunen and Yin (2010) simulated a test embankment on Murro clay in Finland by using a newly developed elasto-viscoplastic model by Yin and Karstunen (2008). Comparisons between simulations and measurements validate the model's predictive ability. However, the influence of viscosity, anisotropy and destructuration on the behavior of embankments has not been discussed.

In this paper, constitutive models and the Murro test embankment are briefly described. Finite element analyses were carried out, using the same finite element mesh for all analyses. The model predictions are then compared to investigate the effect of soil features on the embankment behavior.

CONSTITUTIVE MODELS

Yin and Karstunen (2008) developed a elasto-viscoplastic model, called

EVP-SCLAY1S accounting for soil viscosity, anisotropy and destructuration. The model is based on the overstress theory of Perzyna (1966) and elasto-plastic model S-CLAY1S (Karstunen et al. 2005). Constitutive equations can be found in Yin and Karstunen (2008). Two key equations concerning the anisotropy of yield surface and the destructuration are as follows:

$$d\alpha_d = \omega \left[\left(\frac{3\sigma_d}{4p'} - \alpha_d \right) \left(d\varepsilon_v^{vp} \right) + \omega_d \left(\frac{\sigma_d}{3p'} - \alpha_d \right) d\varepsilon_d^{vp} \right] \quad (1)$$

$$d\chi = -\xi \cdot \chi \cdot \left(d\varepsilon_v^{vp} \right) + \xi_d \cdot d\varepsilon_d^{vp} \quad (2)$$

where α_0 is the initial inclination of yield surface, ω controls the rate at which the components of the deviatoric fabric tensor head toward their current target values, and ω_d controls the relative effect of viscoplastic deviatoric strains in rotating the yield and loading surfaces, χ_0 is the initial amount of bonding, ξ controls the absolute rate of destructuration and ξ_d controls the relative effect of viscoplastic deviatoric strains in destroying the bonds.

The model was implemented into 2D Plaxis v.8 as a user defined model. By switching on/off certain parameters, the model reduces to as EVP-SCLAY1 ($\chi_0 = \xi = \xi_d = 0$) and ultimately to EVP-MCC ($\alpha_0 = \omega = \omega_d = 0$ and $\chi_0 = \xi = \xi_d = 0$). By using the coupled consolidation analysis based on Biot's theory provided in Plaxis with the proposed model, consolidation analyses of boundary value problem can be carried out.

MURRO TEST EMBANKMENT

The geometry of the Murro test embankment is shown in Figure 1. The boundary conditions and details for finite element mesh can be found in Karstunen and Yin (2010). The embankment loading was reproduced by increasing the unit weight of the elements of the embankment fill within 2 days. For the embankment fill, a simple linear elastic-perfectly plastic Mohr Coulomb model was adopted. The typical values of model parameters, as proposed by Karstunen et al. (2005) are summarized as: Young's modulus $E = 40000 \text{ kN/m}^2$, Poisson's ratio $\nu' = 0.35$, critical state friction angle $\phi'_c = 40^\circ$, dilation angle $\psi = 0^\circ$ and unit weight $\gamma = 19.6 \text{ kN/m}^3$.

Karstunen and Yin (2010) presented parameters determination for foundation soils from conventional triaxial and oedometer tests when simulating Murro test embankment by using EVP-SCLAY1S. The selected values of parameters were adopted in this paper (see Table 1). Simulations by using EVP-SCLAY1 were carried out by setting $\chi_0 = \xi = \xi_d = 0$ and keeping other parameters the same as EVP-SCLAY1S. Simulations by using EVP-MCC assumed additionally that $\alpha_0 = \omega = \omega_d = 0$ and $\chi_0 = \xi = \xi_d = 0$ keeping other parameters the same as EVP-SCLAY1S. In order to investigate the effect of viscosity, an additional prediction by EVP-SCLAY1S was made with values of fluidity μ 10 times bigger than that listed in Table 1 for each layer. The results for this case are referred to as "low viscosity".

Table 1. Values of parameters of EVP-SCLAY1S model for Murro clay

Depth (m)	M	K ₀	e ₀	κ	λ _i	υ'	POP(kPa)	N	μ
0.0-1.6	1.70	1.25	1.57	0.01	0.18	0.30	60	25	1.0x10 ⁻¹²
1.6-3.0	1.70	0.34	1.81	0.024	0.18	0.30	0.0	11	3.0x10 ⁻¹²
3.0-6.7	1.65	0.35	2.45	0.041	0.25	0.30	0.0	20	1.0x10 ⁻⁹
6.7-10.0	1.50	0.40	2.16	0.024	0.21	0.30	0.0	9	8.0x10 ⁻⁹
10.0-15.0	1.45	0.42	1.76	0.024	0.21	0.30	0.0	25	5.0x10 ⁻¹⁰
15.0-23.0	1.40	0.43	1.53	0.02	0.15	0.30	0.0	12	1.0x10 ⁻⁸
Depth (m)	α ₀	ω _d	ω	γ ₀	ξ	ξ _d	k _v (m/s)	k _h (m/s)	c _k
0.0-1.6	0.69	1.00	45	2.5	10	0.3	1.8 x10 ⁻⁷	2.3 x10 ⁻⁷	0.43
1.6-3.0	0.69	1.00	25	6	10	0.3	5.6x10 ⁻⁹	7.3 x10 ⁻⁹	0.65
3.0-6.7	0.66	1.02	20	6	10	0.3	4.5 x10 ⁻⁹	6.0 x10 ⁻⁹	0.69
6.7-10.0	0.58	1.00	20	6	10	0.3	2.9 x10 ⁻⁹	3.8 x10 ⁻⁹	0.49
10.0-15.0	0.56	0.98	25	4	10	0.3	1.5 x10 ⁻⁹	2.0 x10 ⁻⁹	0.44
15.0-23.0	0.54	0.95	30	6	10	0.3	6.0 x10 ⁻¹⁰	8.0 x10 ⁻¹⁰	0.45

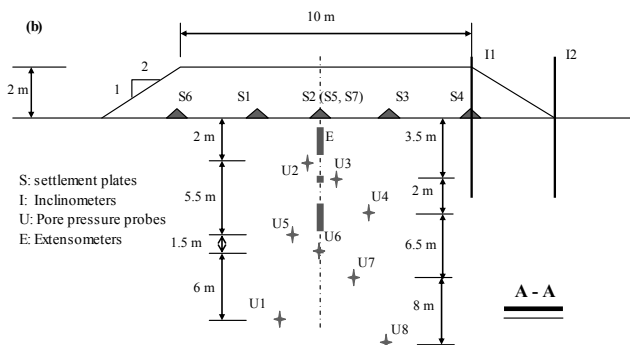


FIG. 1. Cross section of Murro test embankment with details of instrumentation

INFLUENCE OF SOIL FEATURES ON THE EMBANKMENT BEHAVIOR

Settlements

Figure 2 shows the surface settlements under the centerline of the embankment predicted by models with different considerations of soil behavior. Major differences were found between the predictions by different models after 10 days of construction, especially during later stages of consolidation. Comparing the predicted settlements by EVP-SCLAY1 with that by EVP-MCC, it is clear that the incorporation of soil anisotropy results in bigger settlement than in the isotropic case. Accounting for initial bonding and destructuration (by EVP-SCLAY1S) further increases the predicted settlement significantly. The predicted settlement with low viscosity model is larger than the one predicted by the standard viscosity during the early consolidation stage, but converges to the same level during creep. It means that the higher viscosity delays deformations occurring.

Horizontal displacements

Figure 3 presents the predicted horizontal displacements corresponding to inclinometer I1 (see Fig. 1) by all models. At the end of the construction (labeled “immediately after the construction” in figures) the predicted displacements by all models are almost the same. At 3201 days after the construction, the model EVP-MCC predicted the smallest displacements. The consideration of anisotropy increases slightly the displacements. The model considering initial bonding and debonding process predicted much bigger displacements than other models. The predicted displacements with lower viscosity at the end of construction are much larger than the predictions by other models corresponding to the larger settlements, but at 3201 days after the construction return to the same level as the ones with high viscosity model, corresponding to the same level of settlements.

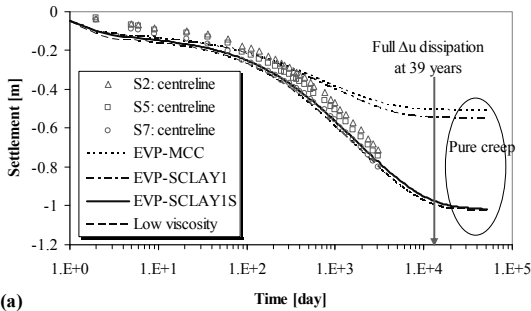


FIG 2. Settlements underneath the embankment at the centerline

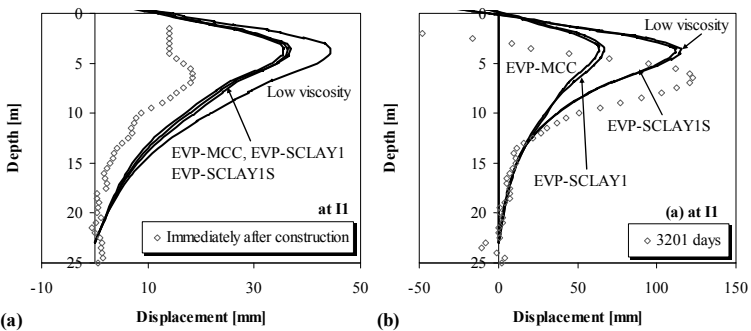


FIG 3. Horizontal displacements at I1: (a) immediately after construction, and (b) 3201 days after construction

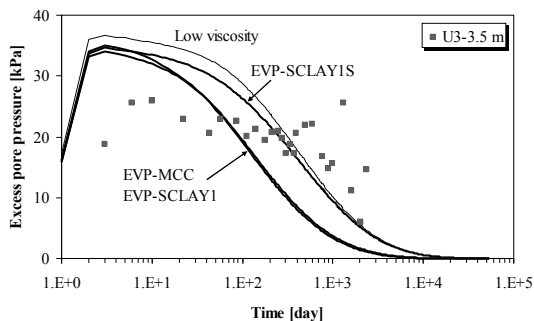


FIG. 4. Excess pore pressures at U3 (3.5 m depth and 0.5 m from centerline)

Excess pore pressure

Figure 4 shows the model predictions for excess pore pressure in the foundation soil under centerline at a depth of 3.5 m. All model predictions are rather similar during the construction and the subsequent consolidation. As expected, all numerical simulations show excess pore pressures gradually dissipating with time. The predicted excess pore pressure with low viscosity is much higher during the consolidation than that with high viscosity, while the anisotropy and destructuration have only a slight influence generated during construction and during the early stage of consolidation. The models without considering bonds predicted faster dissipation of excess pore pressure.

CONCLUSIONS

The behavior of Murro embankment on soft clay was modeled using different constitutive models coupled with Biot's consolidation theory. The results of the finite element analyses are presented for settlements, horizontal displacements and excess pore pressures. The comparisons between predictions by different models were used to investigate the influence of different soil features (i.e., viscosity, anisotropy and destructuration) on the embankment behavior.

REFERENCES

- Karstunen, M., Krenn, H., Wheeler, S. J., Koskinen, M., and Zentar, R. (2005). "The effect of anisotropy and destructuration on the behavior of Murro test embankment." *ASCE International Journal of Geomechanics*, 5(2), 87–97.
- Karstunen, M., and Yin Z. Y. (2010). "Modelling time-dependent behaviour of Murro test embankment." *Géotechnique*, 60(10): 735-749.
- Perzyna, P. (1966). "Fundamental problems in viscoplasticity." *Adv. Appl. Mech.*, 9, 244–377.
- Wheeler, S. J., Näätänen, A., Karstunen, M., and Lojander, M. (2003). "An anisotropic elasto-plastic model for soft clays." *Canadian Geotechnical Journal*, 40, 403–418.
- Yin, Z. Y., and Hicher P. Y. (2008). "Identifying parameters controlling soil delayed

behavior from laboratory and in situ pressuremeter testing.” *International Journal for Numerical and Analytical Methods in Geomechanics*, 32(12), 1515-1535.

Yin, Z. Y., and Karstunen M. (2008). “Influence of anisotropy, destructuration and viscosity on the behavior of an embankment on soft clay.” *12th International Conference of International Association for Computer Methods and Advances in Geomechanics (IACMAG)*, Goa, India, 4728-4735.

INFLUENCE OF FRACTURE FILLING ON MECHANICAL BEHAVIOR OF LOESS

Mingjing Jiang¹, Haijun Hu², Jianbing Peng³, and Xinxin Wang⁴

¹Professor, Department of Geotechnical Engineering, Tongji University, Shanghai, 200092, China; mingjing.jiang@tongji.edu.cn

²Ph.D Candidate, Department of Geotechnical Engineering, Tongji University, Shanghai, 200092, China; hu.hai-jun@163.com

³Dean, School of Geological Engineering and Surveying, Chang'an University, Xi'an, Shanxi, 710054, China; dicexy_1@chd.edu.cn

⁴Master Candidate, Department of Geotechnical Engineering, Tongji University, Shanghai, 200092, China; wangtian753214@163.com

ABSTRACT: Natural loess and natural loess with filling at ground fissures in Jingyang, Shanxi province, China, were experimentally studied to investigate the effect of crack filling on the mechanical behavior of loess and the crack development by conventional triaxial compression test (CTC), reduced triaxial compression test (RTC) and reduced triaxial extension test (RTE) under constant water content condition. The tests were carried out at the consolidation pressure near in-situ stress. Different failure types were observed in the tests. In the CTC test, each soil demonstrates strain-hardening behaviour and shear failure plane is the interface between loess and filling for the natural loess with filling sample. In RTC test, each soil behaves strain-softening. Shear failure planes are conjugate planes for the loess sample and shear failure plane is the interface between loess and filling for the natural loess with filling sample. In RTE test, rupture is observed and the failure surface does not cross the filling for natural loess with filling, that is, the failure surface lies in loess totally. The shear strength of loess with filling is almost the same as that of loess.

INTRODUCTION

A large number of ground fissures have been found in loess in China, especially in the Shanxi Province (Wang et al. 1989; Peng et al. 1992; Li et al.2000; Zhao et al.2009). Mechanical and physical properties of soils around ground fissure have been studied (Lu et al. 2009; Hu et al 2009). Lu et al. (2009) experimentally studied loess with filling by conventional triaxial compression tests and found that stress-strain relation changes from strain-softening to strain-hardening with the increase of consolidation pressure. The shear band often appears at the interface between loess and filling for the sample with the inclination angle of filling $\alpha=60^\circ$ under low consolidation pressure and the

deformation of sample is affected by the filling. Jiang et al. (2011*a, b*) carried out consolidated undrained triaxial tests on saturated loess, saturated loess with filling and saturated filling around ground fissure. The test results indicate that the difference between the shear strength of loess and that of loess with filling is very small and the saturated loess is more likely to behave strain-softening than saturated filling because of the larger void ratio. Hu et al. (2009) examined the physical and mechanical properties of the loess samples with different distances from ground fissures and found that their properties are quite different in space. However, the mechanical characteristics of loess and loess with filling under various stress paths, which will be met in construction and human activity in the near future, have not been studied. During engineering construction, the soil within influence range would encounter different stress paths (Lamber 1967; Lamber and Marr 1979; Cai 2008). For loading engineering such as building or road construction, soil behavior in conventional triaxial compression test (CTC) can represent the behavior of soil in-situ. For unloading engineering such as exaction and metro tunnel construction, the reduced triaxial compression test (RTC), in which the confining pressure decreases and axial stress is constant, is one of the representative tests that can simulate the mechanical behavior of soil in-situ (Weng et al.2008; Malandraki and Toll 2000). Therefore, one motivation of this study is to experimentally study the effect of crack filling on the mechanical behavior of soil sheared along the RTC stress path and compare the mechanical behavior of soils under the CTC stress path and that under the RTC stress path.

The formation mechanism of crack has been studied mainly from geological view and the studies show that the tension stress in horizontal direction is always the cause of cracks (Wang and Chen 1989; Peng et al. 1992, 2007). Sun et al. (2009) studied the ground fissures from the viewpoint of soil mechanics. They experimentally studied the uniaxial tensile strength of undisturbed and disturbed loess samples collected from ground fissure area, obtained that the tensile strength decreases with the increase of water content, and concluded that the cracks often form when the tensile strength is less than the in-situ tensile stress after rainfall. However, the effect of crack filling on the formation of new crack or development of old crack at moderate depth has not been explored because the apparatus they used cannot apply confining pressure. In this study, a triaxial apparatus is developed to carry out the RTE test, in which the confining pressure is constant and axial stress decreases. The RTE carried out on the loess sample and loess with filling sample of which axial direction is horizontal direction in situ, can simulate the crack formation and development of old crack due to tension stress in horizontal direction. Therefore, experimentally studying the effect of crack filling on propagation of crack under the RTE stress path is another purpose of this paper.

The soils in this area are unsaturated soils with low degree of saturation, and thus the excessive pore-air pressure dissipates instantaneously while the excessive pore-water pressure developed dissipates over time in the fast construction situation. Therefore, constant water content tests rather than constant suction tests are adopted, which are generally adopted by other researchers (Rahardjo et al. 2003; Thu et al. 2006).

SPECIMEN PREPARATION AND CHARACTERISTICS OF THE TESTED SOILS

Sampling location and preparation of specimens

The soils used in this research are natural loess and natural loess with filling at ground fissures in Jingyang, China. Blocks of samples were collected by the cutting method after stepped exploratory trenches had been excavated. Fig.1 presents the cross section of geology, the distribution of fissures and the sampling location. The big dark region in bottom left of the map is big crack filling, which may forms after earthquake. Other fissures form due to tension stress in horizontal direction after the formation of the big crack filing. These fissures are nearly vertical, and the width of fissures is about 1mm-200mm and decreases with depth. Loess sample containing fracture filling was collected at f12 (fissure 12) in depth of 10.5 m. The loess is Q_3 loess (Malan loess) and the color is yellow. Filling about 5-7 mm in width exists in the sample of loess as illustrated in Fig.2.

Natural loess specimens and natural loess with filling specimens were prepared for the triaxial test. And the angle between the plane of filling in loess and the end plane of specimen is 45° for triaxial samples of loess with filling. Conventionally, the direction in which stress reduced is horizontal during excavation and construction of tunnel. The sampling direction is shown in Fig.3. For the CTC and the RTC samples, the sampling direction is nearly vertical. For the RTE samples, the sampling direction is horizontal. This can ensure the direction in which stress reduced is almost the same for the RTC test and the RTE test. During the specimen preparation, the initial water content of each specimen was measured. After preparation, the specimen was wrapped up in the plastic film and placed in the moist chamber. The water content of the specimen was adjusted to 15% by air-drying the specimen or adding water to the specimen after its initial water content was known. Then the specimen was wrapped up in the plastic film again and stayed in the moist chamber for more than two days in order to ensure that the water distributes evenly in the sample. Many researchers (Zhang et al. 2006; Yang et al.2010) adopt this method to obtain the loess sample with specific water content.

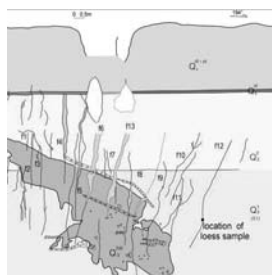


FIG. 1. Sampling location, geological profile and distribution of fissures

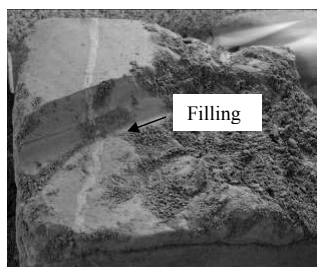


FIG. 2. Collected sample

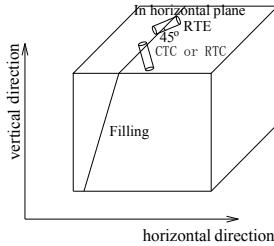


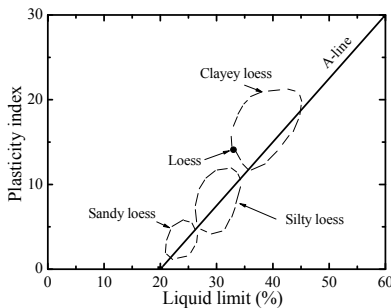
FIG. 3. Sampling direction

Physical properties of the tested soils

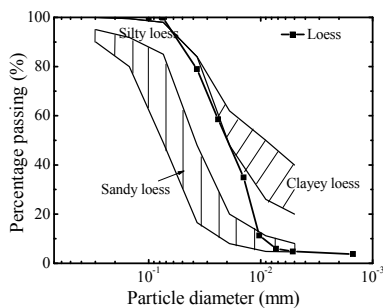
Table 1 presents the physical properties of natural loess. In comparison to loess types defined by Gibbs & Holland (1960) based on plasticity index and liquid limit shown in Fig.4 (a), the loess falls into the category of clayey loess. Compared with loess types defined by Gibbs & Holland (1960) using the grain size distribution shown in Fig.4 (b), the loess falls into clayey loess or almost silty loess. The filling has more clay component than the loess.

Table 1 Physical Property of Loess and Filling

Soil	Natural Moisture Content /%	Natural Density /($\text{g}\cdot\text{cm}^{-3}$)	Void Ratio	Sand >0.05mm /%	Silt 0.05-0.005mm/%	Clay <0.005mm /%	Liquid Limit w_L /%	Plastic Limit w_p /%
Loess	16.9	1.52	1.07	12.1	83.1	4.8	33	18.9
Filling	-	-	-	19.1	61.4	19.5	-	-



(a) Plasticity property of loess



(b) Grain size distribution curve

FIG. 4. Comparison to loess types defined by Gibbs et al. (1960)

TESTING EQUIPMENT AND TESTING PROGRAM

Testing equipment

Figs.5 shows the GDS triaxial testing system which was used to carry out CTC and RTC tests. The working principle of GDS triaxial testing system is introduced in detail in another paper (Menzies 1988). The GDS triaxial apparatus can carry out a single continuous linear total stress path in p - q space. In CTC and RTC tests, in order to keep air pressure at atmosphere pressure during shearing, one copper plate with nine holes and 2mm in thickness was put at each end of sample to exhaust air pressure due to compression of sample during shearing.

Fig. 6 shows the apparatus for RTE test, which is improved based on the stress-control dynamic triaxial apparatus. The top base can apply upward force in vertical direction and the connection between the base and sample was improved. The base and sample are glued together through glue and organic glass plate. Therefore it can transfer tension force to the sample, and carry out uniaxial tension test and RTE test. The axial stress is reduced step by step through stress control method during test process.

During shearing, the maximum saturation of samples does not reach 85% and pore air is continuous (Fredlund et al. 1993), so constant water can be ensured in the tests. The weight of specimen was measured before and after test and the difference is always less than 0.3g (Δw is about 0.2%), which indicates the constant water content ensured.

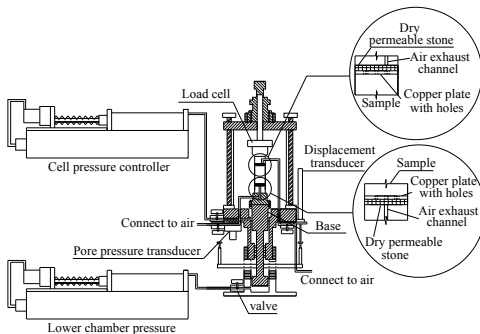


FIG. 5. Schematic diagram of GDS triaxial apparatus

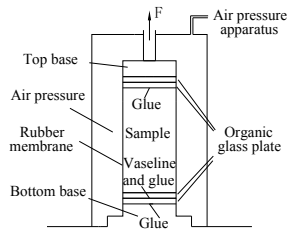


FIG. 6. The improved apparatus for reduced triaxial extension test

Testing program

As shown in Fig.7, firstly the sample was consolidated at confining pressure 200kPa and then the shear test was carried out according to CTC, RTC and RTE stress path. These three stress paths tests are carried out on the loess sample and the loess with filling sample.

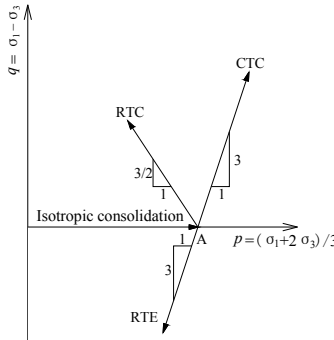


FIG. 7. Three stress paths in triaxial tests

TEST RESULTS AND DISCUSSION

Shear strength and stress-strain behavior

Fig.8 presents the results of stress-strain curves in triaxial tests. Table 2 lists the ultimate strength $(\sigma_1 - \sigma_3)_f$, deviatoric stress at yield point, the secant modulus at 50% shear strength (E_{50}) and the axial strain at yield point. The ultimate strength $(\sigma_1 - \sigma_3)_f$ is defined as the peak deviatoric stress or the deviatoric stress at the axial strain $\epsilon_1 = 15\%$ and the yield stress is defined as the deviatoric stress at the turn point of stress-strain curve in $\log(\sigma_1 - \sigma_3) - \epsilon_1$ space. In the CTC test, both soils demonstrate strain-hardening behaviour and the ultimate strength of loess with filling is higher than that of loess. In RTC test, both soils demonstrate strain-softening behaviour and the shear strength of loess with filling is almost the same as that of loess. In the RTE test, rupture is observed in the test for both soils and the shear strength of loess with filling is almost the same as that of loess. The strength in the RTC test is almost the same as that in the RTE test. From the above discussion, the shear strength of filling is larger than that of loess totally. The failure in the RTC stress path occurs very abruptly and the deformation is very small before failure.

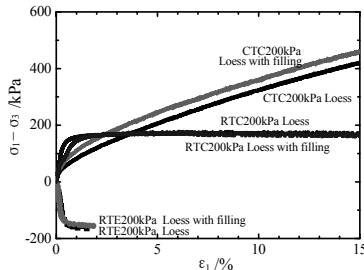


FIG. 8. Stress-strain curves in triaxial tests

Table 2 Results from the three stress paths

Tests		Ultimate strength	Deviatoric stress at yield point	E_{50}	Axial strain at yield point
Natural Loess	CTC200kPa	420kPa	33 kPa	4MPa	0.16%
	RTC200kPa	177 kPa	134 kPa	44 MPa	0.34%
	RTE200kPa	164 kPa	122 kPa	36 MPa	0.35%
Natural Loess with filling	CTC200kPa	462 kPa	43 kPa	5 MPa	0.13%
	RTC200kPa	177 kPa	129 kPa	20 MPa	0.71%
	RTE200kPa	155 kPa	117 kPa	46 MPa	0.24%

Failure type

Fig.9 presents the photos of samples after failure. In the CTC and RTC tests, the failure planes of loess with filling are the interfaces between loess and filling, so the weak planes are the interfaces between loess and filling. In the RTE test, the failure plane of loess with filling does not cross filling, which indicates the shear strength of filling is larger than that of loess. Therefore, it can be concluded that the new crack will form in loess and the propagation of old crack may develop along the interface between loess and filling.

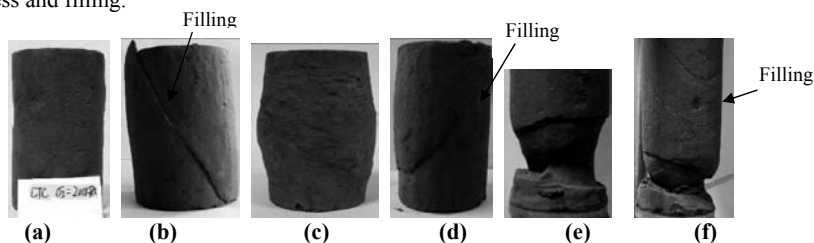
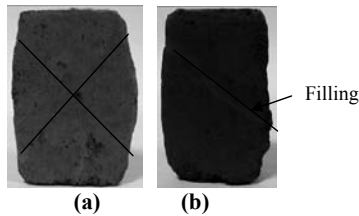
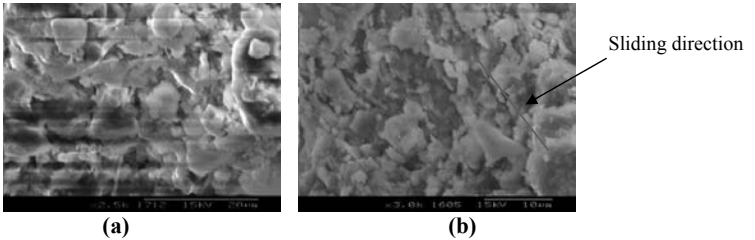


FIG. 9. Failure types of : (a) loess in CTC test (b) loess with filling in CTC test (c) loess in RTC test (d) loess with filling in RTC test (e) loess in RTE test (f) loess with filling in RTE test

Fig.10 presents the section of loess sample and that of loess with filling sample after failure in the RTC test. The failure plane of loess sample is conjugate plane, while the failure plane of loess with filling sample is a single plane along interface of loess and filling. Fig.11 shows the micro-structure of soils at two positions in the sample of loess with filling after RTC200kPa test, which is obtained by the scanning electronic microscope (SEM) test. One is the filling located at the interface between loess and filling, the other is loess located at some distance from the interface in the sample. The plane of the SEM observation is parallel to the shear band plane for filling while it is parallel to end plane of the sample for loess. The particles of filling at the interface between loess and filling are smaller than those of loess. The major axes of the particles of filling are prone to be parallel to the sliding direction of the shear plane, while the major axes of particles of loess distribute homogeneously in space.



**FIG. 10. Section of samples after failure: (a) loess in RTC test
(b) loess with filling in RTC test**



**FIG. 11. SEM photos of the loess with filling sample after RTC200kPa test:
(a) the loess (b) the filling at interface between loess and filling**

CONCLUSIONS

This paper presents an experimental study of natural loess and natural loess with filling under three stress paths. The main conclusions are as follows:

(1) In the CTC test, both soils demonstrate strain-hardening behaviour. In the RTC test, both soils behave strain-softening. In the RTE test, rupture is observed for each soil at failure. The shear strength of filling is larger than that of loess totally.

(2) In the CTC and RTC tests, the failure planes of loess with filling are the interfaces between loess and filling. In the RTE test, the failure plane of loess with filling does not cross filling, which lies in loess completely. The weak region is loess or interface between loess and filling.

(3) The failure in the RTC stress path test occurs very abruptly and the deformation is very small before failure. Hence, the RTC stress path test rather than the CTC test should be used to decide the mechanical parameter of the soil in order to ensure safety in the unloading condition. In addition, the shear band always appears at the interface between loess and filling in the RTC stress path or the CTC stress path test, which indicates corresponding measures should be sought in this area before construction.

(4) New cracks form within loess or at the old crack along the interface between loess and filling.

ACKNOWLEDGMENTS

The authors would like to express their gratitude to Mr. Tang Fuyuan and Ms. Li Hong for their assistance in the tests, Mr. Wu Xiaofeng for his suggestion in the tests and Dr. Liu Fang, Mr. Yang Qijun, Mr. Shen Zhifu, Mr. Su Jiaying for their help in the process of preparing this paper. This research was financially supported by China National Funds for Distinguished Young Scientists (Grant No. 51025932), the National Natural Science Foundation of China (Grant No. 10972158 and No. 41130753), and the Land and Natural Resources of China (Grant No. 1212010914013). These supports are greatly appreciated. In addition, the authors would like to thank the reviewers for their valuable comments which have improved the quality of this paper.

REFERENCES

- Cai, M. (2008). "Influence of stress path on tunnel excavation response - Numerical tool selection and modeling strategy." *Tunnelling and Underground Space Technology*, Vol. 23(6): 618-628.
- Fredlund, D.G. and Rahardjo, H. (1993). *Soil Mechanics for Unsaturated Soils*. New York: John Wiley and sons.
- Gibbs, H.J. and Holland, W.Y. (1960). "Petrographic and engineering properties of loess." *United States Department of the Interior Bureau of Reclamation, Engineering Monograph*, 28:1-37.
- Hu, Z.P., Zhao, Z.R., Zhu, Q.D. and Ma, Y.P. (2009). "Experimental study on physical mechanic property of loess near ground fissure in Xi'an." *Journal of Earth Sciences and Environment*, Vol. 31(1): 85-88. (in Chinese).
- Huang, Q.B., Peng, J.B., Fan, H.W., Yang, P.M. and Men, Y.M. (2009). "Metro tunnel hazards induced by active ground fissures in Xi'an and relevant control measures." *Chinese Journal of Geotechnical Engineering*, Vol. 31(5):781-788. (in Chinese).
- Jiang, M.J., Hu, H.J., Peng, J.B., and Leroueil, S. (2011a). "Experimental study of two saturated natural soils and their saturated remoulded soils under three consolidated undrained stress paths." *Frontiers of Architecture and Civil Engineering in China*, Vol. 5(2): 225-238.
- Jiang, M.J., Hu, H.J., Peng, J.B. and Wang, X.X. (2011b). "Properties of Loess and Fillings about Ground Fissures in Jingyang, China" *In 14th Asian Regional Conference on Soil Mechanics and Geotechnical Engineering*, Hong Kong, China:115.
- Lamber, T.W. (1967). "Stress path method." *Journal of the soil mechanics and foundations division*, Vol. 93(6):309-331.
- Lamber, T.W. and Marr, W.A. (1979). "Stress path method: Second edition." *Journal of geotechnical engineering division*, Vol. 105(6):727-738.
- Malandraki, V., and Toll, D. (2000). "Drained probing triaxial tests on a weakly bonded artificial soil." *Geotechnique*, Vol. 50(2): 141-151.
- Li, Y.L., Jing, C.Y. and Xiao, M.H. (2000). "Origin of ground fissures in the Shanxi Graben system, Northern China." *Eng. Geol.*, Vol. 55(4): 267-275.
- Lu, Q.Z., Ge, X.R., Peng, J.B. and Feng, L.B. (2009). "Failure characteristics of fissured loess under triaxial compression condition." *Rock and soil mechanics*, Vol.

- 30(12): 3689-3694. (in Chinese).
- Menzies, B.K. (1988). "A computer controlled hydraulic triaxial testing system." In advanced triaxial testing of soil and rock, ASTM STP 977. Edited by Donaghe, R.T., Chaney, R.C., and Silver, M.L. American Society for Testing and Materials, Philadelphia. pp. 82–94.
- Peng, J.B., Zhang, J. and Su, S.R. (1992). Active faults and geo-hazards in Weihe Basin. Xi'an: Northwest University Press. (in Chinese).
- Peng, J.B., Fan, W., Li, X.A., Wang, Q.L., Feng, X.J., Zhang, J., Li, X.S., Lu, Q.Z., Huang, Q.B., Ma, R.Y. and Lu, Y.D. (2007). "Several key problems in the mechanism of ground fissures in Fenwei Basin." *Journal of Engineering Geology*, Vol. 15(4): 433-440. (in Chinese).
- Wang, J.M. and Chen, S.Q. (1989). "An approach to the ground rift and its cause for Jingyang." *Journal of Soil and Water Conservation*, Vol. 3(1): 31-36. (in Chinese)
- Weng, M.C., Jeng, F.S., Hsieh, Y.M., and Huang, T.H. (2008). "A simple model for stress-induced anisotropic softening of weak sandstones." *International Journal of Rock Mechanics & Mining Sciences*, Vol. 45(2): 155-166.
- Yang, L.G., Luo, Y.S., Li Y. and Wang Z.J. (2010). "Research on effect of initial stress conditions on dynamic strength of compacted loess." *Rock and Soil Mechanics*, Vol. 31(1): 87-91. (in Chinese).
- Zhang, M.H., Xie, Y.L., Liu, B.J. (2006). "Analysis of shear strength characteristics of loess during moistening process." *Rock and Soil Mechanics*, Vol. 27(7): 1195-1200. (in Chinese).
- Zhao, C.Y., Zhang, Q., Ding, X.L., Lu, Z., Yang, C.S. and Qi, X.M. (2009). "Monitoring of land subsidence and ground fissures in Xi'an, China 2005–2006: mapped by SAR interferometry." *Environ. Geol.*, Vol. 58(7):1533–1540.

ONE-DIMENSIONAL CONSOLIDATION OF SOFT GROUND WITH IMPEDED BOUNDARIES UNDER DEPTH-DEPENDENT RAMP LOAD

Jia-cai Liu¹ and Qiang Ma²

¹ College of Transportation Science & Engineering, Nanjing University of Technology, 200 Zhongshan North Road, Nanjing 210009, China; liujchhu@163.com

² College of Transportation Science & Engineering, Nanjing University of Technology, 200 Zhongshan North Road, Nanjing 210009, China; maqiang86@126.com

ABSTRACT: In this paper, the one-dimensional consolidation of soft ground is studied with impeded boundaries under a depth-dependent ramp load. First, an analytical solution is obtained by using the method of separation of variables and orthogonal relations of the infinite series. A computational program is then developed according to the analytical solution. Lastly, examples are analyzed using the developed computational program. The one-dimensional consolidation can be treated as a completely drained boundary when the impeded parameter is greater than 100 and is not affected by the load duration. The effects of impeded boundaries on the average degree of consolidation depend on the variation of the total stress increments

INTRODUCTION

Terzaghi conducted pioneering work on the one-dimensional consolidation theory of saturated soils. Boundary conditions and applied methods of external loads have great influence on the dissipation of the excess pore water pressures. Many researchers (Gray, 1945; Schiffman, 1970; Xie, 1999; Cai, 2004; Liu, 2011) have recognized that partially drained boundaries may be more realistic in most practical consolidation problems because the external load is not applied instantly. Many documents have studied consolidation under a time-dependent load (Alonso, 1974; Cai, 2004), but the corresponding stress increment resulted from the external load within the foundation is always considered to be uniformly distributed along the column depth. In many cases, the total stress varies not only with time, but also with depth. Zhu (1999) presented a mathematical solution for the consolidation analysis of a double-layered soil profile under a depth-dependent ramp loading. Lei (2006) presented a solution for the situation where the stress increase in the ground is arbitrarily distributed along the depth of the vertical drain. However, there are few papers on consolidation problems that consider both impeded boundaries and depth-dependent and time-varying total stress increment. This paper investigates the one-dimensional consolidation of soft ground with impeded

boundaries under a depth-dependent ramp load. An analytical solution is obtained for the consolidation problem and some useful conclusions are presented for engineering practice by example analysis.

MATHEMATICAL MODELLING

The analysis scheme of the one dimensional consolidation of soft ground with impeded boundaries under depth-dependent ramp load is shown in Fig. 1. As shown, h =the thickness of the soft ground; k_v =the vertical coefficient of permeability; m_v =the coefficient of volume compressibility; $c_v=k_v/(m_v \times \gamma_w)$, the coefficient of consolidation; γ_w =the unit weight of water. There are two impeded layers on and under the soft ground, respectively. Impeded layers are used to describe partially drained boundaries, which cannot be compressed but satisfy Darcy's law. L_t , L_b , k_t , and k_b are the thickness and the permeability coefficients of impeded layers on the top and at the bottom, respectively. The z -axis is perpendicular to the surface of the layers with the coordinate origin at the top of the soft ground, pointing downwards in the positive direction. The vertical total stress is depth-dependent and time-varying, and it is assumed to satisfy

$$\sigma(z, t) = \left(\sigma_0 + \frac{\sigma_1 - \sigma_0}{h} z \right) q(t) \quad (1)$$

where $q(t)$ is a function of time. σ_0 and σ_1 are the vertical total stress increases when $q(t)=1$ at $z=0$ and $z=h$ respectively. When t is less than t_c , $q(t)=t/t_c$; otherwise $q(t)=1$. The loading period is t_c .

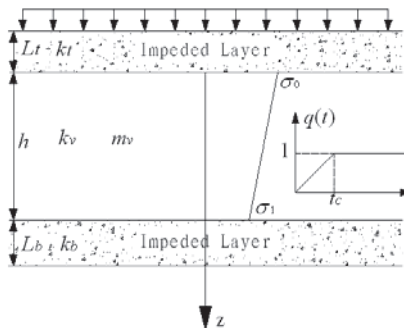


Figure 1. Scheme of the consolidation problem.

All of the assumptions in Terzaghi's basic one dimensional consolidation theory are retained except for the boundaries and vertical total stress. The differential governing equation for the consolidation of the soft ground can be obtained as follows:

$$\frac{\partial u}{\partial t} = c_v \frac{\partial^2 u}{\partial z^2} + \frac{\partial \sigma}{\partial t} \quad (2)$$

where u is the excess pore water pressure in the soft ground, and t and z are the variables of time and space, respectively.

The boundary conditions in the top and bottom of the soft ground are as follows:

$$\begin{cases} \left. \frac{\partial u}{\partial z} \right|_{z=0} = \frac{R_t}{h} u \\ \left. \frac{\partial u}{\partial z} \right|_{z=h} = -\frac{R_b}{h} u \end{cases} \quad (3)$$

where $R_t = k_t \times h / (k_v \times L_t)$, $R_b = k_b \times h / (k_v \times L_b)$.

SOLUTIONS

Using the method of separation of variables, the solution of equation (2) becomes

$$u = \sum_{m=1}^{+\infty} T_m(t) Z_m(z) \quad (4)$$

The general solution for $Z_m(z)$ can be expressed as follow

$$Z_m(z) = \sin(\lambda_m z) + A_m \cos(\lambda_m z) \quad (5)$$

where A_m and λ_m are the coefficients to be found out. Substituting Eq. (5) into Eq. (4), then substituting the result into Eq. (3), A_m and λ_m can be obtained

$$\begin{cases} A_m = \frac{\lambda_m h}{R_t} \\ \left[\lambda_m h - \frac{R_t R_b}{\lambda_m h} \right] \sin(\lambda_m h) = (R_t + R_b) \cos(\lambda_m h) \end{cases} \quad (6)$$

Eq. (2) can be assumed as follows by introducing a Fourier series and substituting Eq. (1) and Eq. (4) into Eq. (2)

$$T'_m(t) = -c_v \lambda_m^2 T_m(t) + \xi_m(t) \quad (7)$$

where $\xi_m(t)$ is the coefficient obtained by the orthogonal relation of $Z_m(z)$

$$\xi_m(t) = \begin{cases} \frac{D_m}{Q_m} \frac{1}{t_c} & t < t_c \\ 0 & t \geq t_c \end{cases} \quad (8)$$

where,

$$\begin{aligned}
 D_m &= \int_0^h Z_m(z) \left[\sigma_0 + \frac{\sigma_1 - \sigma_0}{h} z \right] dz \\
 &= \frac{\sigma_0}{\lambda_m} - \frac{\sigma_1 - \sigma_0}{R_t} \frac{1}{\lambda_m} + \sin(\lambda_m h) \left[\frac{h\sigma_1}{R_t} + \frac{\sigma_1 - \sigma_0}{h} \frac{1}{\lambda_m^2} \right] + \cos(\lambda_m h) \left[\frac{\sigma_1 - \sigma_0}{R_t} \frac{1}{\lambda_m} - \frac{\sigma_1}{\lambda_m} \right] \\
 Q_m &= \int_0^h Z_m^2(z) dz = \frac{h}{2} \left[1 + \left(\frac{\lambda_m h}{R_t} \right)^2 + \frac{1}{R_t} \right] + \frac{1}{4\lambda_m} \left[\left(\frac{\lambda_m h}{R_t} \right)^2 - 1 \right] \sin(2\lambda_m h) - \frac{h}{2R_t} \cos(2\lambda_m h)
 \end{aligned}$$

$T_m(t)$ can be obtained by solving the ordinary differential equation Eq. (7)

$$T_m(t) = \begin{cases} \frac{D_m}{Q_m} \frac{1}{t_c c_v \lambda_m^2} \left[1 - e^{-c_v \lambda_m^2 t} \right] & t < t_c \\ \frac{D_m}{Q_m} \frac{1}{t_c c_v \lambda_m^2} \left[e^{-c_v \lambda_m^2 (t-t_c)} - e^{-c_v \lambda_m^2 t} \right] & t \geq t_c \end{cases} \tag{9}$$

Thus, the solution of excess pore water pressure of the consolidation problem is obtained and can be represented as follows:

$$u = \begin{cases} \sum_{m=1}^{+\infty} [\sin(\lambda_m z) + A_m \cos(\lambda_m z)] \frac{D_m}{Q_m} \frac{1}{t_c c_v \lambda_m^2} \left[1 - e^{-c_v \lambda_m^2 t} \right] & t < t_c \\ \sum_{m=1}^{+\infty} [\sin(\lambda_m z) + A_m \cos(\lambda_m z)] \frac{D_m}{Q_m} \frac{1}{t_c c_v \lambda_m^2} \left[e^{-c_v \lambda_m^2 (t-t_c)} - e^{-c_v \lambda_m^2 t} \right] & t \geq t_c \end{cases} \tag{10}$$

The average degree of consolidation defined according to increment of effective stress can be derived

$$U(t) = \frac{\int_0^h [\sigma(z,t) - u(z,t)] dz}{\int_0^h \left(\sigma_0 + \frac{\sigma_1 - \sigma_0}{h} z \right) dz} = \begin{cases} \frac{t}{t_c} - \sum_{m=1}^{+\infty} \frac{E_m D_m}{Q_m} \frac{1}{t_c c_v \lambda_m^2} \left[1 - e^{-c_v \lambda_m^2 t} \right] & t < t_c \\ 1 - \sum_{m=1}^{+\infty} \frac{E_m D_m}{Q_m} \frac{1}{t_c c_v \lambda_m^2} \left[e^{-c_v \lambda_m^2 (t-t_c)} - e^{-c_v \lambda_m^2 t} \right] & t \geq t_c \end{cases} \tag{11}$$

where, $E_m = \frac{2}{\sigma_1 + \sigma_0} \left[\frac{1}{\lambda_m h} + \frac{\sin(\lambda_m h)}{R_t} - \frac{\cos(\lambda_m h)}{\lambda_m h} \right]$

EXAMPLE AND DISCUSSION

A computational program has been developed based on the analytical solution. To analyze the consolidation characteristics of the soft ground with impeded boundaries under depth-dependent ramp load, a case is studied. Parameters of the consolidation problem are as follows: $k_v=2 \times 10^{-9}$ m/s, $h=10$ m, $m_{v1}=2/3$ MPa⁻¹, $t_c=100$ days.

The boundary conditions become pervious top and impervious bottom (PTIB) when

$R_t = \infty$ and $R_b = 0$. The boundary conditions become pervious top and pervious bottom (PTPB) when $R_t = \infty$ and $R_b = \infty$. These two cases are the special cases studied by Zhu (1999). The comparisons of the average consolidation degree under $\sigma_0 = 100\text{kPa}$ and $\sigma_1 = 50\text{kPa}$ by the present analytical solution and Zhu's solution are shown in Figure 2. Figure 2 shows that there is no difference between the results calculated by the present analytical solution and Zhu's solution.

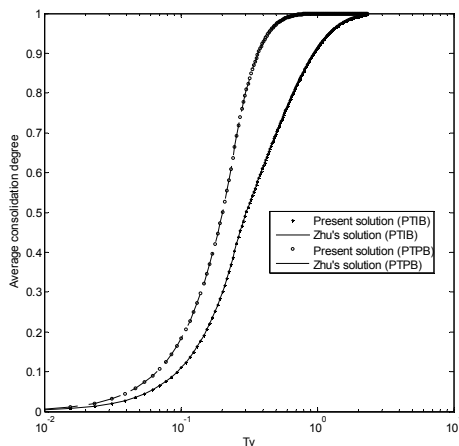


Figure 2. Comparisons of average degree

Fig. 3 shows the curves of the average consolidation degree of $U(t)$ vs. time factor $T_v = c_v t/h^2$ corresponding to different values of R_t and R_b when $\sigma_0 = \sigma_1 = 100\text{kPa}$. It can be seen that the values of R_t and R_b have great influence on the average consolidation degree. When either R_t or R_b remains unchanged, the greater the changed value is, the greater the average consolidation degree will be. The curve of average consolidation degree obtained when $R_t = 100$ almost coincides with the curve obtained when $R_t = \infty$. It corresponds to the completely permeable boundary when $R_t = \infty$. Therefore, this case has similar conclusions with the ones under instantly applied load (Xie, 1999).

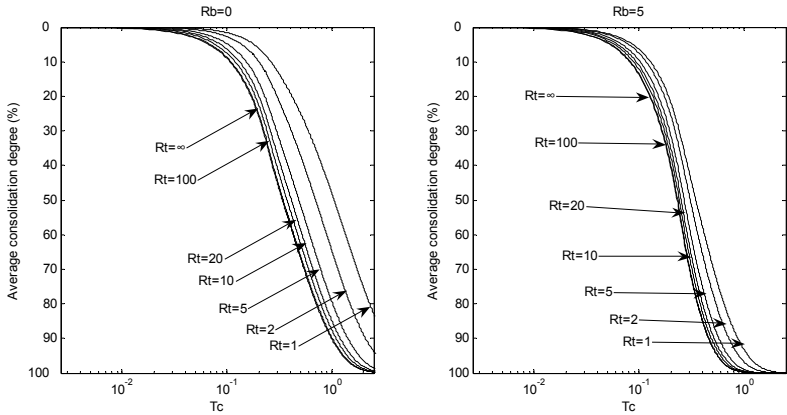


Figure 3. Average consolidation degree vs. T_v curves at different R_t and R_b .

Three types of distribution patterns of total stress increment along depth are often encountered in engineering: 1) rectangular pattern; 2) trapezoidal pattern ($\sigma_0 < \sigma_1$); and 3) inverse trapezoidal pattern ($\sigma_0 > \sigma_1$). Fig. 4 shows the influence of impeded boundaries on average consolidation degree under different types of distribution patterns of total stress increment along depth. The stress distribution is shown in Table 1. It can be seen that the average degree of consolidation of inverse trapezoidal stress pattern is the maximum and that the average degree of consolidation of trapezoidal stress pattern is the minimum. The differences of the average consolidation degree among the three patterns of total stress increment are more obvious with the increase of impeded parameters R_t at the initial stage of consolidation.

Table 1. Total Stress Increment distribution patterns

Stress Increment	Rectangular	Trapezoidal	Inverse Trapezoidal
σ_0 (kPa)	100	100	100
σ_1 (kPa)	100	500	20

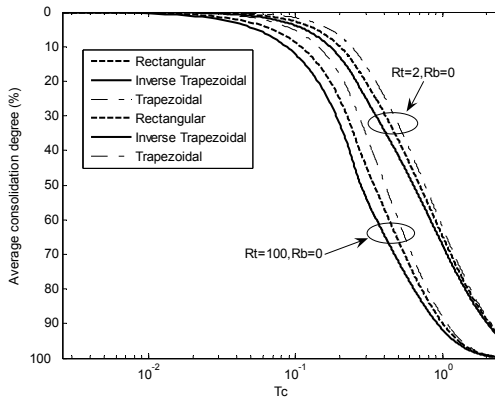


Figure 4. Average consolidation degree of different stress pattern.

CONCLUSIONS

This paper presents the analysis for the consolidation of soft ground with impeded boundaries under a depth-dependent ramp vertical total stress and a variety of solutions are obtained for one dimensional soil consolidation under different boundary conditions. A computational program has been developed based on the analytical solutions. Both the drainage boundary conditions and total stress increment pattern have a great influence on the consolidation process. The differences become more obvious with the increase of impeded parameters R_i at the initial stage of consolidation.

REFERENCES

- Alonso, E.E., Krizek, R.J. (1974). "Randomness of settlement rate under stochastic load." *Journal of the Engineering Mechanics Division, ASCE*, Vol. 100 (6): 1211 - 1226.
- Cai, Y.Q., Liang, X. and Wu, S.M. (2004). "One-dimensional consolidation of layered soils with impeded boundaries under time-dependent loadings." *Applied Mathematics and Mechanics*, Vol. 25 (8): 937-944.
- Gray H. (1945). "Simultaneous consolidation of contiguous layers of unlike compressible soils." *Transactions, ASCE*, 110: 1327 - 1356.
- Lei, G.H., Jiang, C.X. and Shi, J.Y. (2006). "Equal strain solutions of radial and vertical coupled consolidation by vertical drains under arbitrarily distributed ground soil stress increase." *Rock and Soil Mechanics*, Vol. 27 (2): 173 - 178. (in Chinese)
- Liu, J.C., Lei, G.G. and Wang, Y.X. (2011). "One-dimensional consolidation of soft ground considering non-Darcy flows." *Chinese Journal of Geotechnical Engineering*, Vol. 33 (7): 1117-1122. (in Chinese)
- Schiffman, R.L., Stein, J.R. (1970). "One-dimensional consolidation of layered

- systems." *Journal of the Soil Mechanics and Foundation Division, ASCE*, Vol. 96 (4): 1499 - 1504.
- Xie, K.H., Xie, X.Y. and Gao, X. (1999). "Theory of one dimensional consolidation of two-layered soil with partially drained boundaries." *Computers and Geotechnics*, Vol. 24 (4): 265-278.
- Zhu, G.F., and Yin, J.H. (1999). "Consolidation of double soil layers under depth-dependent ramp load." *Géotechnique*, Vol. 49 (3): 415-421.

REMOTE MONITORING AND EARLY WARNING SYSTEM FOR SUBWAY CONSTRUCTION

Mingyang Wang¹, Junhua Xiao² and Xiaoli Rong³

¹Professor, Engineering Institute of Engineering Corps, PLA University of Science & Technology, No.1 Haifuxiang Rd., Nanjing, 210007

²Corresponding author, Associated professor, College of Transportation Science and Engineering, Nanjing University of Technology, No.200 North Zhongshan Rd., Nanjing, 210009; geoxjh@hotmail.com

³Associated professor, Engineering Institute of Engineering Corps, PLA University of Science & Technology, No.1 Haifuxiang Rd., Nanjing, 210007

ABSTRACT : The remote monitoring and early warning system for subway construction is a Browser/Server (B/S) mode application system which is developed based on web page. The system is applied to tracking, monitoring, reporting, early warning and management in whole areas during subway construction, and the emergency or safety risk site can be warned and treated in advance. The system provides lots of facilities such as the spatial information of building, road, construction plant, the conformation of geology and pipelines, and provides available facilities of storage, display, query, statistics and analysis. The system can manage real-time monitoring and early warning, which has been successfully applied in subway construction in Beijing, Nanjing, Nanchang, etc.

INTRODUCTION

Subway construction has a lot of characteristics such as complex environment conditions, difficulty in construction, long duration, which is a high-risk project. As the geotechnical conditions of subway construction is complex and uncertain, the design theory of underground engineering is not perfect, and the new subway engineering usually will be constructed near the ground or underground infrastructures, it will result in serious accident if it is not controlled well.

The remote monitoring and early warning system for subway construction can track, monitor, report, early warn and manage the whole construction process, and it is the most useful tool for safety risk management and emergency decision support in subway construction.

RESEARCH BACKGROUND

In research area, the “Geotechnical Engineering Construction Monitoring Information System (GeoMis)” proposed by Li and Zhu (2002) was used in monitoring tunnels, excavation and slope construction. This system used new thought of engineering visualization technique and Geographic Information System (GIS) to integrate the database management, forecasting analysis and monitoring graphics functions seamlessly. This system had two-way visualization to query and input or output data using the monitoring point map as the center point. But risk warning and control method was not deeply studied; it only had the monitoring function but can’t control risk. Sun (2001) researched in the construction network multimedia monitoring and control management system for shield engineering. He used the technique of graphic data object distributed processing, artificial intelligence scientific method software of artificial neural network forecast, fuzzy logic control and technique of 3D dynamic visual simulation in shield construction.

In application area, there was an information management system named GDMS used in underground construction risk proposed by GeoDATA Company in Italy. This system used techniques of Geographic Information System (GIS) and web page, and was composed by five subsystems such as building condition system, building risk assessment, Tunnel Boring Machine (TBM) data management, monitoring data management and document management system. It had the perfect risk management program and has been applied in St. Petersburg, Rome and Santiago Metro projects (Qian and Rong 2008). But it is too expensive and doesn’t suit for Chinese conditions in some areas such as monitoring tools and construction management. Additionally, in shield construction area, Shanghai Tunnel Engineering Co. Ltd developed Shield Tunneling Intelligent Management System (Zeng and Rong 2010). It uses advanced analysis method in effective management and comprehensive technical support for construction projects at home and abroad.

The PLA University of Science and Technology has developed Safety Risk Management Information System in underground construction, Shield Construct Real-Time Management System, and Civil Engineering Geographic Information System, which have been applied in remote monitoring and early warning of subway construction in Beijing, Nanjing, and Nanchang successfully in recent 3 years (Zeng and Rong 2010).

INTRODUCTION TO THE SYSTEM

The remote monitoring and early warning system for subway construction is a common safety-risk management platform for all parties in subway construction. The modern information technology is adopted to achieve the aims of transmitting engineering information rapidly, analyzing engineering information timely, sharing information, strengthening risk monitoring and control, and improving risk management ability. This system includes several functions such as remote monitoring management, early warning management, monitoring data management, shield data management, safety risk management, GIS map management and mobile

phone message management. The software components of the system are shown in Figure 1.

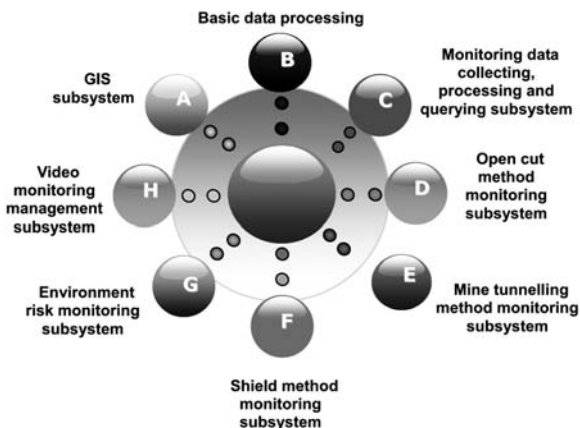


FIG. 1. Software components of remote monitoring and early warning system

DATA MANAGEMENT FUNCTION

Excavation data management

Monitoring data of excavation include ground settlement and horizontal displacement, water level, stress and stratified inclination of soil. Data acquisition can be realized manually or automatically. Variation quantity and rate can be shown through curve graphs and histograms, and the range of controlling value can be marked clearly. The illustration of monitoring data and curves of inclinometry of soil are shown in Table 1 and Figure 2.

Table 1. Monitoring Data in Remote Monitoring System

Measure point	Type	Safety status	Maximum value (mm)	Maximum deformation rate(mm/d)	Warning value (mm)	Warning rate (mm/d)
QD13	Settlement	Normal	-2.32	0.61	15.0	2.0
ZQT26	Inclinometry	Normal	24.18	0.23	30.0	3.0
ZQT25	Inclinometry	Yellow	34.34	-2.71	30.0	3.0
ZQT31	Inclinometry	Yellow	7.74	-3.74	30.0	3.0

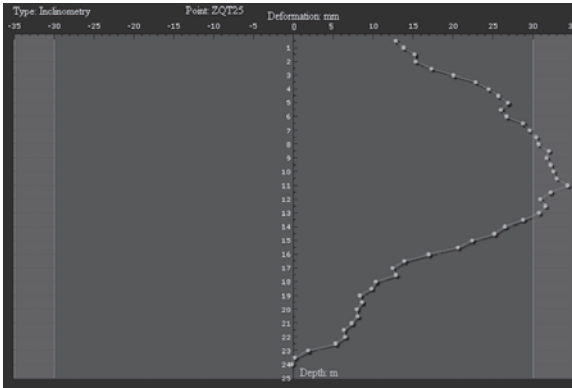


FIG. 2. Curve of soil inclinometry of ZQT25 point

Shield data management

Based on network technology and database technology, construction parameters can be acquired from underground shield computer and transmitted to center server on ground. Mass data of shield construction parameters can be stored dynamically and inquired efficiently through dynamic database technology. Assistant analysis of shield parameters can be realized based on data mining technology. The transmission process of shield data is shown in Figure 3.

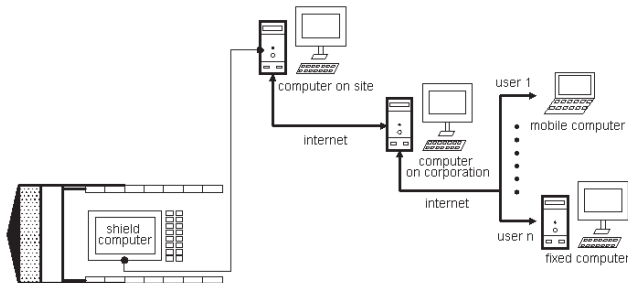


FIG. 3. Data transmission process

The shield real-time monitoring software platform contains following functions:

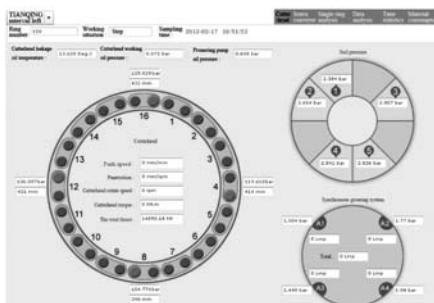
1. Interface display of shield remote monitoring system can be defined by users through mouse clicking and dragging technology.
2. Encryption algorithm is adopted to compress mass data. Compressed data are transmitted to the center server through multiple modes, identified and stored automatically in the center server.

3. Shield parameters, such as materials consumption, efficacy, propulsion ring number and mileage, can be statistical analyzed and inquired in the form of time segment. The result can be outputted through report from.

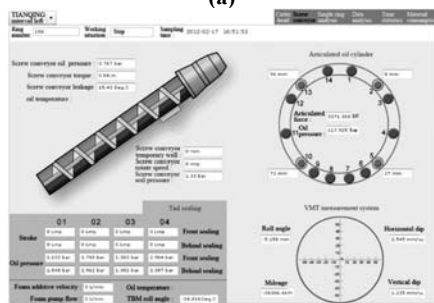
4. Acquiring, statistical analysis and visualization of shield data can be realized based on various conditions.

5. B/S framework is realized based on Rich Internet Applications (RIA) technology, the client can display progress of works, analyze materials consumption, control cost, output and print report, analyze multiple ring, analyze single ring comparatively through browser. It is convenient for overall process analysis of shield construction, safety, cost and quality control of shield construction.

The monitoring interface of Earth Pressure Shield (EPS) construction is shown in Figure 4.



(a)



(b)

FIG. 4. Monitoring interface of Earth Pressure Shield construction

EARLY WARNING FUNCTION

Early warning level management

The system divides early warning into two categories, one is the individual early warning which refers to unusual monitor data or abnormal index, and the other is comprehensive early warning which refers to increase of the possibility of a risk by

the comprehensive risk analysis and real-time evaluation. According to monitoring control index value proposed by the designer, early warning in the construction process includes three levels according to severity: yellow, orange and red early warning.

1. Yellow early warning: the “double-control” indexes (variation quantity and change rate) are over 70% of control values, or one index is over 85% of control value;

2. Orange early warning: the “double control” indexes are over 85% of control values, or one index is over control value;

3. Red early warning: the “double control” indexes are over control value, or there is a sharp change in rate of growth.

For individual early warning, the system can set the standard (threshold), when monitoring data is over the standard, the system will automatically issue individual early warning. Figure 5 shows schematic diagram of individual early warning.

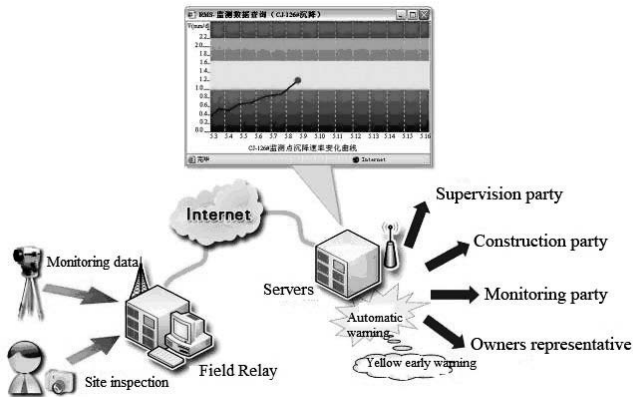


FIG. 5. Schematic diagram of individual early warning

The comprehensive early warning is manually issued based on risk assessment by professional engineers.

Display of early warning in system

Individual early warning contains monitoring or inspection early warning. The monitoring/inspection early warning information can be displayed through the monitoring/inspection early warning list in the system. The comprehensive early warning is issued by evaluating the unsafe status of risk project synthetically from checking, comprehensive analysis and expert judgment according to the information of individual early warning. The display of the comprehensive early warning in the map of a subway line is shown in Figure 6.



FIG. 6. Display of comprehensive early warning

Disposal process of early warning

After individual early warning occurs, the relevant people including construction, supervision and owner parties should input the disposal information into the system. The individual early warning will not eliminate until the monitoring data and inspection indexes turn to normal. For comprehensive early warning, construction party is responsible for giving suggestion on elimination of early warning; supervision party is responsible for the first examination, and the monitoring management center takes the responsibility for final examination. The elimination of the dangerous project of red comprehensive early warning still needs re-examination by chief engineer of owner party.

CONCLUSIONS

This system has been applied in subway construction in Beijing, Nanjing, Nanchang, etc. Based on the system which contains monitoring, early warning, data analysis, decision and management, the safety of the subway construction are ensured.

REFERENCES

- Li, Y.H. and Zhu, H.H.(2002). "Development of monitoring information system software for geotechnical engineering". *Rock and Soil Mechanics*, Vol. 23(1):103-106.
- Qian, Q.H. and Rong, X.L.(2008). "State Issues and Relevant Recommendations for Security Risk Management of China's Underground Engineering". *Chinese Journal of Rock Mechanics and Engineering*, Vol.27(4):649-655.
- Zeng, L.B., Huang, M. and Rong,X.L.(2010)."Research on construction monitoring geology and geography information system for underground engineering". *Rock and Soil Mechanics*, Vol.S1:348-354.
- Zhou, X.S. and Sun.J.(2001)."Multimedia monitor and simulation system in shield tunnel construction". *China Civil Engineering Journal*, Vol. 34(6):50-54.

RESEARCH ON THE INFLUENCE OF THE ROTATION OF PRINCIPLE AXIS OF STRESS TO THE CONSTITUTIVE RELATION SOIL

Yuan-xue Liu¹, Zhong-you Li², Yu Zhang³

¹Director, Chongqing Key Laboratory of Geomechanics & Geoenvironmental Protection; Professor, Department of Architecture and Civil Engineering, Logistical Engineering University, Chongqing 400041; lyuanxue@vip.sina.com

²Ph.D Candidate, Department of Architecture and Civil Engineering, Logistical Engineering University, Chongqing 400041; lizhongyou0726@sina.com

³Graduate, Department of Architecture and Civil Engineering, Logistical Engineering University, Chongqing 400041; zhangyu.zy.cool@163.com

ABSTRACT: The rotation of principal axis of stress is a mechanical problem that must be considered in geotechnical engineering. In light of matrix theory, the characteristic of stress increment that causes the rotation of principal axis of stress is obtained and the arbitrary stress increment is decomposed into the coaxial part and rotary part. A general mode for stress-strain behaviors involving the rotation of the principal axis of stress is presented. Based on the generalization from the increment of stress invariant to the invariant of stress increment, the expression system of elastoplastic theory for complete stress increment is presented. The plastic deformation caused by the rotation of the principal axis of stress can be computed strictly, and it indicates that the influences can be attributed to the shearing deformation and dilatancy caused by the generalized shear of the stress increment.

INTRODUCTION

With the rapid advance of calculator technique and calculation methodology, the research on the constitutive relation of geotechnical materials reached its high tide in 1970's. After the middle 1980's, similar research seemed to decrease. At the same time, the development of measuring instruments for geomaterials brought an unprecedented understanding of the deformation mechanism of soils. The inconsistency about the complexity and the practicability of the constitutive model of soils is increasingly significant with regard to the complication of the soil deformation mechanism. It's still difficult to accurately predict the soils stress-strain characteristic under the complex stress condition and stress path. Some scholars still approach from two aspects: On one hand they try to colligate, predigest and modify the original model that is welcomed by the engineering field to focus on normalization, practicability, and popularization; On the other hand they carry on further research of the stress-strain relation for more

complicated stress conditions and more challenging characteristics of soils, such as loop load, abrupt turn of stress path, the rotation of principal axis of stress, the anisotropic of soils, etc.

The generalized rotation of principal axis of stress of soils contains two types. One type is that three principal values of stress are fixed but the direction of the principal axis of stress changes. This can be described as the rotary movement around the principal axis of stress in general stress-space called pure rotation of the principal axis of stress. The other is that the direction of the principal axis of stress, hydraulic stress, p , and generalized shear stress, q , are invariant but the stress Lode angle ($\theta\sigma$) changes, and the stress path is the circular motion on the π -surface (it is the rotary stress path on the π -surface), and it is called as pure change of stress Lode angle. The relation of p , q , $\theta\sigma$ with three principal values of stress σ_1 , σ_2 , σ_3 is:

$$\begin{cases} p = (\sigma_1 + \sigma_2 + \sigma_3)/3 \\ q = \sqrt{(\sigma_1 - \sigma_2)^2 + (\sigma_1 - \sigma_3)^2 + (\sigma_3 - \sigma_2)^2} / \sqrt{2} \\ \text{tg } \theta_\sigma = (2\sigma_2 - \sigma_1 - \sigma_3) / [\sqrt{3}(\sigma_1 - \sigma_3)] \end{cases} \quad (1)$$

A great deal of geotechnical engineering practice indicates that the pure rotation of principal axis of stress will cause the obvious plastic yield of soil (Wong 1986); In the undrained condition, even the liquefaction of the sandy soils will appear (Shibuya 1986). However, ordinary geomaterial models now can not reflect this property reasonably. The problem of rotation of principal axis of stress exists in many geotechnical engineering problems, such as foundation, slope, etc. There are many loads which often cause the rotation of principal axis of stress, such as earthquake, transportation, wave, building and so on. Thus the rotation of principal axis of stress is a mechanical problem in geotechnical engineering that must be considered. Some geotechnical engineering accidents were caused because this problem had not yet been solved. With regard to the influence the rotation of principal axis of stress may have, many theoretical and experimental outcomes have been achieved. Some representative work is provided and commented on in this manuscript.

THE CONSTITUTIVE MODELS INVOLVING THE ROTATION OF PRINCIPAL AXIS OF STRESS AND THE COMMENTS

To simulate the deformation characteristics of soils involving the rotation of the principal axis of stress, much exploration has been performed, such as a constitutive relation expressed in general stress-space, model based on bounding surface theory or kinematic hardening theory, etc. The influential theories are introduced and reviewed systematically henceforth.

Constitutive Model of Soils in General Stress-space

The essential component of the rotation of the principal axis of stress is that the stress increment contains rotary shear. The principal directions will change with the rotary part, but the principal values will remain constant (Liu Yuan-xue 1998). The plastic

deformation caused by the rotation of the principal axis of stress could not be described by the traditional plastic theory model. The rotation of the principal axis of stress was considered through the change of general stress increment in experiments performed by Matsuoka (1987, 1990). The deformation caused by the rotation of principal axis of stress could then be calculated by experimental formulas. The model can reflect the influence of general two-dimensional stress increments.

Currently the traditional model can always be expressed as stress invariant and strain invariant, or their increment is established so that the influence of the rotation of the principal axis of stress can not be computed. It would be very helpful if the relationship between the general stress increment and strain increment can be established directly. This is very difficult, so help must be sought from the empirical equations and assumptions. There are however experimental errors in the empirical equations which are the foundation of the model, and there are the limitations of soils type and stress condition in these equations. Especially the assumption for the model generalized to three-dimension lacks the scientific basis, which is just the reason that the comparison was not provided for three-dimensional experimental results.

The Kinematic Hardening Model

Anisotropy is apparent in the elastic-plastic deformation of soils. The anisotropy induced by stress of soils (secondary anisotropy) is also significant even if the original anisotropy was ignored. Namely the difference of strain increments caused by the stress increments with the same magnitude and different orientation may be considerable even under the same stress condition. For example under the condition of $\sigma_1 > \sigma_2 = \sigma_3$ and the soils stress state near damage, significant plastic flow will appear if the stress increment, $d\sigma_1 > 0, d\sigma_2 = d\sigma_3 = 0$, is applied. However, negligible plastic flow will occur under the action of stress increment $d\sigma_1 = 0, d\sigma_2 = d\sigma_3 > 0$, and the stress condition of soils trend to be safer.

One essential cause of the plastic yield of soils induced by the rotation of principal axis of stress is the anisotropy of soils. There is also the phenomena of the rotation of principal axis of stress in elastic mechanics, but the elastic stress increment and elastic strain increment exhibit a one-to-one correspondence (size is proportional, orientation of principal axes is conform). The strain increment rotates synchronously with the stress increment. The deformation only relates with the principal values and is independent of the change of principal orientation. However, the deformation of soils is dependent on the stress history. The size and orientation of strain increment not only changes with the size and orientation of stress increment, but is also confined by the size and orientation of stress, so the variation of the strain increment of soils with the rotational stress increment display the hysteretic phenomenon. Thus the plastic yield of soils will be induced by the rotation of principal axis of stress, and the different principal directions of stress and strain will appear. This is due to the anisotropic influence induced by the stress of the soils.

Yield surface is isotropic hardening in traditional plastic mechanics, some models with kinematic hardening yield surface is put forward to consider the anisotropy of soils. In the kinematic hardening model, the center, size and shape of yield surface are changed with stress state. Introducing the kinematic hardening law of yield surface, the

Mobilized Plane model was revised by Nakai (1991). When pure principal axis of stress rotates, namely the position of stress state point in the principal stress space does not change, but the yield surface moves with the rotation of principal axis of stress. Then the soils will be yielded after the yield surface meet the stress state point.

The kinematic hardening theory can be regarded as the remedy to the yield surface theory of the traditional plastic theory, and the fact of anisotropy could be reflected visually. It can be drawn from the work of Nakai (1991) that their key is the moving rule of the yield surface. However, the anisotropy of soils dependent on stress state and stress path. It is a very complex problem, and the moving rule of the yield surface is very difficult to be given once the stress path is very complex, especially in three-dimensional stress space. This may be the reason for this kind models develop slowly.

The Boundary Surface Model

The boundary surface model was put forward by Dafalis (1975), and it was first used to describe the loop load of metallic material. The basic ideas of the model are presented in the following: In the stress space, the moving geometrical boundary of stress point and yield surface are limited by one boundary surface; Within the boundary surface there is usually a yield surface geometric similarity with the bounding surface, thus the yield surface can move with definite rule; In the process of loading, the stress point is always located on the inner or outer surface of the yield surface; The plastic modulus and orientation of exterior normal on the boundary surface are decided by the flow rule of traditional plastic theory; The plastic modulus of the stress point on the yield surface is decided by the plastic modulus of the conjugate stress point on the bounding surface and a simple hypothesis was used to relate the position of yield surface with the boundary surface.

The traditional plastic theories can be divided into three parts: yield surface theory, flow rule and hardening rule. The kinematic hardening theory is an amendment to the yield surface of the traditional plastic theory, and the plastic deformation caused by rotation of principal axis of stress is introduced through the moving of the yield surface with the rotation of the principal axis of stress. The bounding surface model is an amendment to the flow rule. The orientation of plastic flow is the same as the orientation of exterior normal of yield surface in traditional plastic theory. However, the plastic flow relates with the exterior normal orientation of the conjugate stress point on the boundary surface, thus the influence of the rotation of principal axis of stress can be calculated by the boundary surface model which is expressed in the general stress space.

The rule of plastic flow was acquired through a number of hollow torsion shear experiments involving the rotation of principal axis of stress Then a boundary surface model for sandy soils was developed which can reflect the influence of principal axis of stress rotation (Miura(1986)). In this model, the failure surface is chosen as the bounding surface, and the form of yield surface and the failure surface of soils is the same. This model can reflect the deformation characteristics of soils involving the rotation of principal stress axis in two-dimensional stress space.

Obviously, the concept of the bounding surface model is based on the experimental

results and lacks a rigorous theoretical foundation. Thus the application scope of the regulation has to limit to the experimental stress path. It needs to be verified by experiment whether it can be generalized to another stress condition and another stress path or not. Certainly, it is very difficult to search the rule of plastic flow of soils under the condition of a complicated stress state.

To reflect the deformation characteristic of soils involving the rotation of principal stress axis, a lot of efforts have been contributed. But they focus on building up the practical model and the constitutive theory has been seldom studied. The system of constitutive theory of soils involving the rotation of principal axis of stress is built up in this paper, and it sets out from the analyses of stress increment.

DECOMPOSITION OF STRESS INCREMENT

In this paper, the general stress increment is decomposed into two parts by matrix analysis. One part is coaxial with the stress, which can be called coaxial part. The other part is the rotation of principal axis of stress, which is called rotary part.

Decomposition of Two-dimensional Stress Increment

The principal values of two-dimensional (2-D) stress σ is expressed as σ_1, σ_2 , the corresponding unit principal vectors are N_1, N_2 . Then stress σ can be expressed as the following:

$$\sigma = (N_1 \quad N_2) \begin{pmatrix} \sigma_1 & 0 \\ 0 & \sigma_2 \end{pmatrix} \begin{pmatrix} N_1 \\ N_2 \end{pmatrix} = T_1 \Lambda T_1^T \quad (2)$$

When only principal stress value changes, the coaxial part of stress increment $d\sigma_c$ can be got by the differential of equation (2), where the matrix T_1, T_1^T in equation (2) are constant matrix, and just σ_1, σ_2 in the diagonal matrix Λ change. Thus:

$$d\sigma_c = d(T_1 \Lambda T_1^T) = T_1 d\Lambda T_1^T = T_1 \begin{pmatrix} d\sigma_1 & 0 \\ 0 & d\sigma_2 \end{pmatrix} T_1^T \quad (3)$$

The above equation indicates that the negative diagonal elements of coaxial part of stress increment are zero, and the positive diagonal elements are the principal values increment.

When the principal orientation of stress changes, the diagonal matrix Λ in equation (1) is constant, and the matrix T_1, T_1^T in equation (2) changes, the rotary part of stress increment $d\sigma_r$ is obtained by the differential of Eq. (2):

$$d\sigma_r = d(T_1 \wedge T_1^T) = dT_1 \wedge T_1^T + T_1 \wedge dT_1^T = T_1 \begin{pmatrix} 0 & d\theta(\sigma_1 - \sigma_2) \\ d\theta(\sigma_1 - \sigma_2) & 0 \end{pmatrix} T_1^T \quad (4)$$

where $d\theta$ is the rotation angle increment of principal axis of stress.

When the last equation indicates that the positive diagonal elements of $d\sigma_r$ are zero and the negative diagonal elements are equal, its value is equal to the arithmetic product of the difference of principal values and the rotation angle increment of principal axis of stress.

Then arbitrary 2-D stress increment $d\sigma$ can be decomposed into the sum of coaxial part $d\sigma_c$ and rotary part $d\sigma_r$, namely:

$$d\sigma = d\sigma_c + d\sigma_r = T_1 \begin{pmatrix} d\sigma_1 & 0 \\ 0 & d\sigma_2 \end{pmatrix} T_1^T + T_1 \begin{pmatrix} 0 & d\theta(\sigma_1 - \sigma_2) \\ d\theta(\sigma_1 - \sigma_2) & 0 \end{pmatrix} T_1^T \quad (5)$$

Decomposition of Three-dimension Stress Increment

Considering the same argument, the three-dimensional (3-D) general stress increment can be decomposed as:

$$\sigma = \begin{pmatrix} N_1 & N_2 & N_3 \end{pmatrix} \begin{pmatrix} \sigma_1 & 0 & 0 \\ 0 & \sigma_2 & 0 \\ 0 & 0 & \sigma_3 \end{pmatrix} \begin{pmatrix} N_1 \\ N_2 \\ N_3 \end{pmatrix} = T \Lambda_1 T^T \quad (6)$$

where $\sigma_1, \sigma_2,$ and σ_3 are principal values, $N_1, N_2,$ and N_3 are the corresponding principal vectors.

Arbitrary stress increase $d\sigma$ is transferred to principal stress space, and can be expressed as:

$$T^T d\sigma T = \begin{pmatrix} M_1 & A_1 & C_1 \\ A_1 & M_2 & B_1 \\ C_1 & B_1 & M_3 \end{pmatrix} \quad (7)$$

Then the coaxial part of the stress increment $d\sigma_c$, and the rotary parts of the stress increment $d\sigma_{r1}, d\sigma_{r2}, d\sigma_{r3}$ can be obtained:

$$d\sigma_c = T \begin{pmatrix} M_1 & 0 & 0 \\ 0 & M_2 & 0 \\ 0 & 0 & M_3 \end{pmatrix} T^T \quad M_1 = d\sigma_1 \quad M_2 = d\sigma_2 \quad M_3 = d\sigma_3 \quad (8)$$

$$d\sigma_{r1} = T \begin{pmatrix} 0 & A_1 & 0 \\ A_1 & 0 & 0 \\ 0 & 0 & 0 \end{pmatrix} T^T \quad A_1 = d\theta_1(\sigma_1 - \sigma_2) \quad (9)$$

$$d\sigma_{r2} = T \begin{pmatrix} 0 & 0 & 0 \\ 0 & 0 & B_1 \\ 0 & B_1 & 0 \end{pmatrix} T^T \quad B_1 = d\theta_2(\sigma_2 - \sigma_3) \quad (10)$$

$$\mathbf{d}\sigma_{r3} = T \begin{pmatrix} 0 & 0 & C_1 \\ 0 & 0 & 0 \\ C_1 & 0 & 0 \end{pmatrix} T^T \quad C_1 = d\theta_3(\sigma_1 - \sigma_3) \quad (11)$$

$$\mathbf{d}\sigma = \mathbf{d}\sigma_c + \mathbf{d}\sigma_r = \mathbf{d}\sigma_c + \mathbf{d}\sigma_{r1} + \mathbf{d}\sigma_{r2} + \mathbf{d}\sigma_{r3} \quad (12)$$

where $\mathbf{d}\theta_1$, $\mathbf{d}\theta_2$, and $\mathbf{d}\theta_3$ indicate the rotary angle increment around the corresponding principal axis of stress caused by the rotary stress increment $\mathbf{d}\sigma_{r1}$, $\mathbf{d}\sigma_{r2}$, $\mathbf{d}\sigma_{r3}$ respectively.

The decomposition of the stress increment indicates that the rotary part of the stress increment $\mathbf{d}\sigma_r$ is a transitional quantity, and could not cause the change of stress invariant σ_i . The yield surface in the traditional constitutive model is always the only function of the stress invariant, so it can not calculate the plastic deformation of soils caused by the rotation of principal axis of stress.

A General Mode of Stress-strain Behavior Which Contains the Influence of the Rotation of Principal Axis of Stress

Based on the elastoplastic theory, the strain increment can be decomposed into two parts, the elastic part and plastic part, and take no account of elastoplastic coupling. The elastic part $d\epsilon^e$ can be calculated by the Generalized Hooke's law. Plastic strain can be decomposed into the coaxial part $d\epsilon_c^p$ induced by the coaxial part of stress increment $d\sigma_c^p$, and the rotary part $d\epsilon_r^p$ resulted in by the rotary parts of stress increments $d\sigma_r^p$:

$$d\epsilon = d\epsilon^e + d\epsilon^p = d\epsilon^e + d\epsilon_c^p + d\epsilon_{r1}^p + d\epsilon_{r2}^p + d\epsilon_{r3}^p \quad (13)$$

On the assumption that the elastic deformation of soils satisfies the Generalized Hooke's law, then the increment of elastic strain would be:

$$\begin{pmatrix} d\epsilon_{11}^e \\ d\epsilon_{22}^e \\ d\epsilon_{33}^e \\ d\epsilon_{12}^e \\ d\epsilon_{13}^e \\ d\epsilon_{23}^e \end{pmatrix} = \frac{1}{E} \begin{pmatrix} 1 & -\mu & -\mu & 0 & 0 & 0 \\ -\mu & 1 & -\mu & 0 & 0 & 0 \\ -\mu & -\mu & 1 & 0 & 0 & 0 \\ 0 & 0 & 0 & A & 0 & 0 \\ 0 & 0 & 0 & 0 & A & 0 \\ 0 & 0 & 0 & 0 & 0 & A \end{pmatrix} \begin{pmatrix} d\sigma_1 \\ d\sigma_2 \\ d\sigma_3 \\ d\theta_1(\sigma_1 - \sigma_2) \\ d\theta_3(\sigma_1 - \sigma_3) \\ d\theta_2(\sigma_2 - \sigma_3) \end{pmatrix} \quad (14)$$

$G = E/A \quad A = 2(1 + \mu)$

where E is elastic modulus, and μ is Poisson's ratio.

In the general stress space, the increment of elastic strain would be:

$$d\boldsymbol{\varepsilon}^e = T \begin{pmatrix} d\varepsilon_{11}^e & d\varepsilon_{12}^e & d\varepsilon_{13}^e \\ d\varepsilon_{12}^e & d\varepsilon_{22}^e & d\varepsilon_{23}^e \\ d\varepsilon_{13}^e & d\varepsilon_{23}^e & d\varepsilon_{33}^e \end{pmatrix} T^T \tag{15}$$

In the next segment, the coaxial part $d\boldsymbol{\varepsilon}_c^p$ and the rotary parts $d\boldsymbol{\varepsilon}_r^p$ will be computed by a new way.

THE COMPLETE STRESS INCREMENT FORMULATION FOR THE ELASTOPLASTIC STRESS-STRAIN RELATION OF SOIL

The mean stress p , the generalized shear stress q , the volumetric strain ε_v , and the generalized shear strain ε_s could be defined as:

$$p = \sigma_{ii} / 3, \quad q = \sqrt{\frac{3}{2} S_{ij} S_{ij}}, \quad S_{ij} = \sigma_{ij} - p \delta_{ij} \tag{16}$$

$$\varepsilon_v = \varepsilon_{ii}, \quad \varepsilon_s = \sqrt{\frac{2}{3} e_{ij} e_{ij}}, \quad e_{ij} = \varepsilon_{ij} - \varepsilon_v \delta_{ij} / 3 \tag{17}$$

The elastic deformation is always supposed to satisfy the generalized Hook’s Law. Thus the hard core of the elastoplastic model is the plastic stress strain relation. The stress-strain relation of soil is usually expressed on the p - q plane, and the plastic constitutive relation could be put forward as:

$$\begin{cases} d\varepsilon_v^p = Adp + Bdq \\ d\varepsilon_s^p = Cdp + Ddq \end{cases} \tag{18}$$

where $d\varepsilon_v^p$ is the increment of plastic volumetric strain, $d\varepsilon_s^p$ is the increment of generalized plastic shear strain, dp, dq are the increment of mean stress and that of generalized shear stress, and A, B, C, D are the corresponding plastic coefficients.

Obviously, the influence of the change of the stress Lode’s angle and the rotation of principal axis of stress to the stress-strain relation could not be computed by the above expression because it is formulated by the stress invariants and the stress Lode’s angle is ignored. A new idea is present herein: the stress strain relation is put forward by the invariant of stress increment and strain increment instead of the increment of stress invariant and strain invariant:

$$\begin{cases} d\varepsilon_v^{p'} = Adp' + Bdq' \\ d\varepsilon_s^{p'} = Cdp' + Ddq' \end{cases} \tag{19}$$

where

$$dp' = d\sigma_{ii} / 3, \quad dq' = \sqrt{\frac{3}{2} dS_{ij} dS_{ij}}, \quad dS_{ij} = d\sigma_{ij} - dp' \delta_{ij} \quad (20)$$

$$d\varepsilon_v^p = d\varepsilon_{ii}^p, \quad d\varepsilon_s^p = \sqrt{\frac{2}{3} de_{ij}^p de_{ij}^p}, \quad de_{ij}^p = d\varepsilon_{ij}^p - d\varepsilon_v^p \delta_{ij} / 3 \quad (21)$$

The following shows that the influence of the change of the Lode's angle and the rotation of principal axis of stress can be calculated by this new method.

The calculation method of plastic yield which is caused by rotary part in the stress increment is in accordance to the calculation of influence of pure stress Lode angle.

Plastic Yield Caused by the Rotary Part of Stress Increment

The stress increment caused by the stress rotation around the third principal stress axis is $d\sigma_{r1}$ in Eq. (9), the stress increment invariant of it corresponded to:

$$\begin{cases} dp' = 0 \\ dq' = \sqrt{3} |\sigma_1 - \sigma_2| d\theta_1 \end{cases} \quad (22)$$

Then, the plastic yield caused by the $d\sigma_{r1}$ is:

$$\begin{cases} d\varepsilon_{vr1}^p = Adp' + Bdq' = Bdq' = n_2 B_0 \sqrt{3} |\sigma_1 - \sigma_2| d\theta_1 \\ d\varepsilon_{sr1}^p = Cdp' + Ddq' = Ddq' = n_2 D_0 \sqrt{3} |\sigma_1 - \sigma_2| d\theta_1 \end{cases} \quad (23)$$

Where

$$n_2 = \frac{(\sin \phi - \sin \phi_{m0})(3p - q \sin \theta_\sigma)}{3p \sin \phi \cos \theta_\sigma}, \quad \sin \phi_{m0} = \frac{\sqrt{3}q \cos \theta_\sigma}{3p - q \sin \theta_\sigma} \quad (24)$$

From Eq.(23), we can know that the influence of the rotation of principal axis of stress to the stress-strain relation can be attributed to the shearing deformation and dilatancy which is caused by the generalized shear part of stress increment. It also is a expressive form for dilatancy of soils, so plastic flow on the orientation of stress axes is like the expression of Rowe stress ratio- dilatancy:

$$\begin{cases} \frac{d\varepsilon_{11r1}^p}{d\varepsilon_{22r1}^p} = R \sigma_1 / \sigma_2 \\ \frac{d\varepsilon_{33r1}^p}{d\varepsilon_{11r1}^p} = 0.3 \sigma_3 / (R\sigma_1) \\ R = \operatorname{tg}^2(45^\circ + \phi/2) \end{cases} \quad (25)$$

where 0.3 in the equation comes from the experimental results when the pure principal

axis of stress rotate and $d\varepsilon_{vr1}^p = d\varepsilon_{11r1}^p + d\varepsilon_{22r1}^p + d\varepsilon_{33r1}^p$

Each plastic strain increment \that can be found from the two equations above is:

$$\left\{ \begin{aligned} d\varepsilon_{11r1}^p &= E_{r1}^1 |d\theta_1| \quad d\varepsilon_{22r1}^p = E_{r1}^2 |d\theta_1| \quad d\varepsilon_{33r1}^p = E_{r1}^3 |d\theta_1| \quad d\varepsilon_{12}^p = E_{r1}^4 |d\theta_1| \\ E_{r1}^1 &= R\sigma_1 k_{f1} \quad E_{r1}^2 = \sigma_2 k_{f1} \quad E_{r1}^3 = 0.3\sigma_3 k_{f1} \\ k_{f1} &= \frac{n_2 B_0 \sqrt{3} |\sigma_1 - \sigma_2|}{(R\sigma_1 + \sigma_2 + 0.3\sigma_3)} \\ E_{r1}^4 &= \sqrt{(9D_0^2 + 2B_0^2)(\sigma_1 - \sigma_2)^2 n_2^2 - 2(E_{r1}^2 + E_{r1}^2 + E_{r1}^2)} \end{aligned} \right. \quad (26)$$

In the general stress space, plastic strain increment $d\varepsilon_{r1}^p$ caused by the $d\sigma_{r1}$ is:

$$d\varepsilon_{r1}^p = T \begin{pmatrix} d\varepsilon_{11r1}^p & d\varepsilon_{12}^p & 0 \\ d\varepsilon_{12}^p & d\varepsilon_{22r1}^p & 0 \\ 0 & 0 & d\varepsilon_{33r1}^p \end{pmatrix} T^T \quad (27)$$

With the same method, the plastic strain increment $d\varepsilon_{r2}^p$, $d\varepsilon_{r3}^p$ caused by the $d\sigma_{r2}$, $d\sigma_{r3}$ can be found by using the following:

$$\left\{ \begin{aligned} d\varepsilon_{11r2}^p &= E_{r2}^1 |d\theta_2| \quad d\varepsilon_{22r2}^p = E_{r2}^2 |d\theta_2| \quad d\varepsilon_{33r2}^p = E_{r2}^3 |d\theta_2| \quad d\varepsilon_{23}^p = E_{r2}^4 |d\theta_2| \\ E_{r2}^1 &= R\sigma_1 k_{f2} \quad E_{r2}^2 = \sigma_2 k_{f2} \quad E_{r2}^3 = 0.3\sigma_3 k_{f2} \\ k_{f2} &= \frac{n_2 B_0 \sqrt{3} |\sigma_2 - \sigma_3|}{(0.3\sigma_1 + R\sigma_2 + \sigma_3)} \\ E_{r2}^4 &= \sqrt{(9D_0^2 + 2B_0^2)(\sigma_1 - \sigma_2)^2 n_2^2 - 2(E_{r2}^2 + E_{r2}^2 + E_{r2}^2)} \end{aligned} \right. \quad (28)$$

$$\left\{ \begin{aligned} d\varepsilon_{11r3}^p &= E_{r3}^1 |d\theta_3| \quad d\varepsilon_{22r3}^p = E_{r3}^2 |d\theta_3| \quad d\varepsilon_{33r3}^p = E_{r3}^3 |d\theta_3| \quad d\varepsilon_{13}^p = E_{r3}^4 |d\theta_3| \\ E_{r3}^1 &= R\sigma_1 k_{f3} \quad E_{r3}^2 = 0.3\sigma_2 k_{f3} \quad E_{r3}^3 = \sigma_3 k_{f3} \\ k_{f3} &= \frac{n_2 B_0 \sqrt{3} |\sigma_1 - \sigma_3|}{(R\sigma_1 + 0.3\sigma_2 + \sigma_3)} \\ E_{r3}^4 &= \sqrt{(9D_0^2 + 2B_0^2)(\sigma_1 - \sigma_3)^2 n_2^2 - 2(E_{r3}^2 + E_{r3}^2 + E_{r3}^2)} \end{aligned} \right. \quad (29)$$

In general stress space, $d\varepsilon_{r2}^p$, $d\varepsilon_{r3}^p$ are:

$$d\varepsilon_{r2}^p = T \begin{pmatrix} d\varepsilon_{11r2}^p & 0 & 0 \\ 0 & d\varepsilon_{22r2}^p & d\varepsilon_{23}^p \\ 0 & d\varepsilon_{23}^p & d\varepsilon_{33r2}^p \end{pmatrix} T^T \quad (30)$$

$$d\varepsilon_{r3}^p = T \begin{pmatrix} d\varepsilon_{1r3}^p & 0 & d\varepsilon_{13}^p \\ 0 & d\varepsilon_{22r3}^p & 0 \\ d\varepsilon_{13}^p & 0 & d\varepsilon_{33r3}^p \end{pmatrix} T^T \tag{31}$$

Forecast and Verification to the Model

Many experiments and studies have been conducted regarding the problem of the rotation of pure principal axis of stress. Regularity of the stress-strain curve for normal consolidated soils is quite accordant under the rotation of pure principal axis of stress. Fig.1 shows the predicted result of stress-strain curve for a normal consolidated Chongqing soils. From the comparison, we can find that the predicted result of the theory and the experimental result of Miura (1986) are very similar at the regularity. It also indicates that this theory can preferably reflect the constitutive character of soils deformation under the condition of the rotation of principal axis of stress, and it validates this theory indirectly.

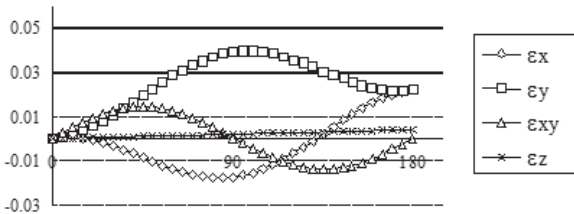


FIG. 1. Theoretical prediction of the relation between each stress parts and the rotation angle under the pure rotation of principal stress axis

CONCLUSIONS

(1) The characteristic of stress increment that cause the rotation of principal axis of stress are obtained based on the matrix analysis, and any stress increment can be decomposed into two parts: One part is coaxial with the stress, it can be called the coaxial part; another part is the rotation of principal axis of stress, it can be called rotary part. The reason that the plastic yield caused by the rotation of principal axis of stress can not be computed by traditional plastic potential theory is that its yield surface is only a function of invariant, which could not consider the influence of the rotation of principal axis of stress. A general mode is put forward for stress-strain behavior, which contains the influence of the rotation of principal axis of stress.

(2) An expression method of elasto-plastic theory for the total stress increment is put forward by the invariant of stress increment instead of the stress invariant, and it can calculate the influence of all kinds of stress increments. From this, the plastic yield caused by the rotation of principal axis of stress can be calculated. Analyses of this theory indicate that the influence of the rotation of principal axis of stress to the

deformation of soils can be attributable to the shearing deformation and dilatancy, which are caused by the generalized shear part of stress increment. The predicted result is verified by the experiment of soils deformation under the pure rotation of principal axis of stress.

ACKNOWLEDGMENTS

We gratefully acknowledge the support from National Natural Science Foundation of China (50979112), and Science and Technology Commission of Chongqing.

REFERENCES

- Dafalias Y F, Popov E P. (1975). "A Model of Non-Linearly Hardening Materials for Complex Loadings." *Acta Mechanica*, Vol. 21(3):173-192.
- Liu Yuan-xue, Zheng Ying-ren, Chen Zheng-han. (1998). "The general stress strain relation of soils involving the rotation of principal stress axes." *Applied Mathematics and Mechanics*, Vol. 19(5): 407-413.
- Matsuoka H, Sakakihara K. (1987). "A Constitutive Model for Sands and Clays Evaluating Principal Stress Rotation." *Soils and Foundations*, Vol. 27(4):73-88.
- Matsuoka H, Suzuki Y. (1990). "A Constitutive Model for Soils Evaluating Principal Stress Rotation and Its Application to Some Deformation Problems." *Soils and Foundations*, Vol. 30(1): 142-154.
- Miura K, Shosuke, Miura S. (1986). "Deformation Prediction for Anisotropic Sand during the Rotation of Principal Stresses Axes." *Soils and Foundations*, Vol. 26(3): 42-56.
- Nakai T, Hoshikawa T. (1991). "Kinematic Hardening Models for Clay in Three-Dimensional Stresses." *Computer Methods and Advances in Geomechanics*: 655-660.
- Shibuya S, Hight D W. (1986). "Patterns of Cyclic Principal Stress Rotation and Liquefaction." *2nd Int. Symp. On Numerical Models in Geotechnics*, Ghent: 265-268.
- Wong R K S, Arthur J R F. (1986). "Sand Sheared by Stresses with Cyclic Variations in Direction." *Geotechnique*, Vol. 36(2): 215-226.

SETTLEMENT ANALYSIS OF EMBEDDED FOUNDATION RESTING ON ELASTIC SOIL

Guoxiong Mei¹, Meijuan Xu²

¹Dean, College of Civil Engineering and Architecture, Nanchang Hangkong University, No. 696, Fenghenan Avenue, Nanchang, Jiangxi 330063, China; meiguox@163.com

²Director, Nanjing Communications Institute of Technology, Nanjing, Jiangsu 211188, China; xumeijuanj@163.com

ABSTRACT: The paper first analyzes the embedment depth effect including Gibson effect, trench effect, side-wall contact effect, retaining wall effect and floating foundation effect. A new settlement calculation model for embedded foundation resting on elastic soil is presented. According to the present model, Groth & Chapman, a solution can be used to calculate the settlement of the rectangular embedded foundation. In conclusion, the influences of parameters including the ratio of depth to length α , ratio of length to width β , compensation ratio χ and Poisson's ratio ν on the reduction coefficient of embedded foundation are discussed in detail and some valuable conclusions are made for engineering practice.

INTRODUCTION

Embedded foundations are widely used. For settlement analysis of embedded foundation resting on elastic soil, the floating foundation effect is considered in Chinese textbook and manual (i.e. using the load $q - \gamma D$ to substitute the load q , then adapt the settlement analysis of no embedded foundation to calculate the settlement of embedded foundation); the trench effect is considered in foreign textbook and manual (i.e. use chart of Janbu, et al to calculate the settlement of embedded foundation). Gazetas, et al (1985) first analyzed the embedment depth effect, including Gibson effect, trench effect and side-wall contact effect, and then proposed the calculation equation of embedded foundation by fitting available analytical and numerical result. The paper first analyzes the embedment depth effect including Gibson effect, trench effect, side-wall contact effect, retaining wall effect and floating foundation effect. Subsequently, a new settlement calculation model for embedded foundation resting on elastic soil is presented. According to the present model, Groth & Chapman solution can be used to calculate the settlement of the rectangular embedded foundation. The reduction coefficients of embedment depth effect are discussed in the end and some valuable conclusions are made for engineering practice.

SETTLEMENT ANALYSIS OF EMBEDDED FOUNDATION

In order to determine how to calculate the settlement of embedded foundation, we discuss and analyze the embedment depth effects first, and then present a simple settlement calculation method for embedded foundation.

Embedment depth effects

An embedded foundation has the following five effects in comparison with a surface footing, shown in Fig. 1 (Gazetas et al., 1985; Budhu, 2010): (a). Soil stiffness generally increases with depth, so the footing loads will be transmitted to a stiffer soil than the surface soil. This can result in smaller settlement. This is called the modulus increment effect or Gibson effect. (b). Normal stresses from the soil above the footing level have been shown (Eden, 1974; Gazetas and Stoke, 1991) to reduce the settlement by providing increased confinement on the deforming half-space. This is called the trench effect, shown in Fig. 1a. (c). Part of the load on the footing may also be transmitted through the side walls depending on the amount of shear resistance mobilized at the soil-wall interface. The accommodation of part of the load by side resistance reduces the vertical settlement. This has been called the side wall-contact effect, shown in Fig. 1b. (d). The actual buried footing soon will fill in the excavated soil body and stop the ambient soil body from the movement towards the excavation part. This has been called the retaining wall effect, shown in Fig. 1c. (e). As common knowledge, the foundation floating effect is another important effect. Using $q - \gamma D$ to replace q in the computation can consider the floating foundation effect conveniently, where q is foundation pressure, γ is soil unit weight and D is the embedment depth.

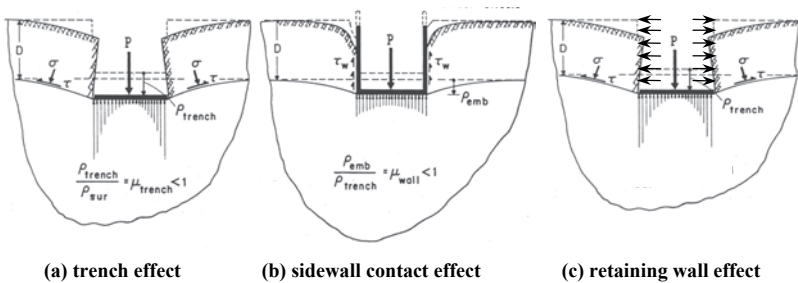


FIG. 1. Embedded foundation: schematic diagram of trench, sidewall contact and retaining wall effects

Settlement calculation method

Based on an improved further qualitative understanding of five effects of embedment depth and the assumptions as follow: (a). The modulus increment effect or Gibson effect is neglected; (b). The trench effect, the side wall-contact effect and the retaining wall effect produced by the actual embedded foundation are the same as those

produced by the same size “foundation” made of soil which has the same properties as the ambient soil.

Therefore, the problem of the settlement calculation of embedded foundation can be simplified as the problem of loading beneath the surface of a homogenous soil layer, shown as Fig. 2. Especially, Groth & Chapman obtained the solution of distributed loading on a rectangular area beneath the surface of a semi-infinite soil layer. So we can use Groth & Chapman solution to calculate the settlement of rectangular foundation with embedment depth.

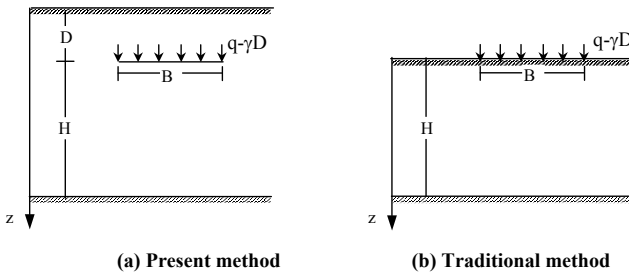


FIG. 2. Schematic illustration of Embedded Foundation

For distributed loading q on a rectangular area beneath the surface of a semi-infinite mass, the vertical displacement ρ_{emb} of the corner of a rectangular is given by (Groth & Chapman, 1969):

$$\rho_{emb} = qBI_{corner} / E \tag{1}$$

where the influence factor I_{corner} is given by

$$I_{corner} = K_0 \left[K_1 \left\{ \beta \ln \left(\frac{1 + \sqrt{1 + \beta^2}}{\beta} \right) + \ln(1 + \sqrt{1 + \beta^2}) \right\} + K_2 \left[\ln \left(\frac{\beta + t}{\sqrt{1 + 4\alpha^2 \beta^2}} \right) + \beta \ln \left(\frac{1 + t}{\beta s} \right) - 2\alpha\beta \tan^{-1} \left(\frac{1}{2\alpha\beta} \right) + 4\alpha\beta \tan^{-1} \left(\frac{(1-s)(\beta s - t)}{2\alpha} \right) \right] + 2\alpha\beta K_1 \tan^{-1} \left(\frac{1}{2\alpha} \right) + \frac{8\alpha^4 \beta t}{s^2(1 + 4\alpha^2 t^2)} \left\{ 2 + \frac{1}{4\alpha^2} - \frac{1}{t^2} \right\} \right] \tag{2}$$

$$K_0 = \frac{1 + \nu}{8\pi(1 - \nu)}; \quad K_1 = 3 - 4\nu; \quad s = \sqrt{1 + 4\alpha^2}$$

Where: $\beta = L / B$; $\alpha = D / L$; $t = \sqrt{1 + \beta^2(1 + 4\alpha^2)}$

$$K_2 = 5 - 12\nu + 8\nu^2$$

where ν is Poisson’s ratio of soil, E is Young’s modulus of soil, D is embedment depth of foundation, L is the length of rectangle foundation, B is the width of rectangle foundation.

To determine values inside or outside a rectangular or irregularly shaped area we can simply divide the region into a number of rectangles, determine $\delta\rho_{emb}$ at the corner of the various rectangles and, making use of the principle of superposition, add or subtract the individual effects. For example, for the L-shaped building in Fig. 3 the settlements at the corner E can be found by adding the effects of the rectangles DABE, BCFE and HGDE; the settlement at the external point J can be found by subtracting the effects of the rectangle HEFJ from that of the rectangle GACJ.

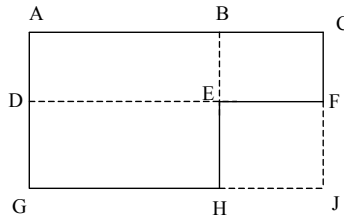


FIG. 3. Division of rectangular loaded areas

REDUCTION COEFFICIENT OF EMBEDDED FOUNDATION

In order to analyze the influence of the embedded foundation on the settlement, take a rectangular foundation as an example, and make a definition of reduction coefficient of embedded foundation first, and then analyze the influence of parameters α , β , χ and ν on the reduction coefficient of embedded foundation.

Definition of reduction coefficient

The reduction coefficient μ_{emb} of embedded foundation can be used as a reduction or correction factor to apply to the settlement calculated for the equivalent surface footing, this equivalent surface footing being taken as resting on a layer of depth equal to the depth of material below the foundation level of the actual buried footing (Fig. 2). The floating foundation effect is also considered, that is, use the load stress $q - \gamma D$ to replace load stress q in the computation. Take the corner settlement foundation with semi-infinite soil layer depth as an example.

$$\mu_{emb} = \rho_{emb} / \rho_{sur} \tag{3}$$

where ρ_{emb} is the settlement of the corner of a rectangular embedded foundation, ρ_{sur} is the settlement of the corner of a rectangular surface foundation. ρ_{emb} can be computed by Groth & Chapman solution (1969).

$$\rho_{emb} = (\chi - 1)\gamma DBI_{corner} / E \tag{4}$$

where $\chi = q / \gamma D$.

ρ_{sur} can be computed by Giroud solution (1968)

$$\rho_{sur} = qB(1-v^2)I_s / E \tag{5}$$

where

$$I_s = \frac{2}{\pi} [\ln(\beta + \sqrt{1+\beta^2}) + \beta \ln(\frac{1+\sqrt{1+\beta^2}}{\beta})] \tag{6}$$

Substituting the equation (4) and the equation (5) into the equation (3), the equation (3) can be changed:

$$\mu_{emb} = (\chi - 1)I_{corner} / [\chi(1-v^2)I_s] \tag{7}$$

Influencing factors of reduction coefficient μ_{emb} have the parameters α , β , χ and v . In the following section, the influence of the parameters α , β , χ and v on reduction coefficient μ_{emb} is discussed. To simplify the analysis, only one parameter is changed at one time in the following section. Unless otherwise stated, the parameters α , β , χ and v have the values of $\alpha=0.5$; $\beta=1.0$; $\chi=10$; $v=0.3$.

Influence of the parameter α on the reduction coefficient μ_{emb}

The influence of the parameter α is analyzed by defining the parameter α as $\alpha=0.1, 0.25, 0.5, 0.75, 1, 2, 3, 5, 7, 10, 15, 20, 50,$ and 100 . The reduction coefficients μ_{emb} for different the parameter α are plotted in Fig. 4. Two conclusions can be made: (a). The larger the parameter α , the smaller the reduction coefficients μ_{emb} ; (b). When the parameter α is less than 3, the larger parameter α makes the reduction coefficients μ_{emb} decrease more significantly, that is, the embedment depth less than 3 times of the width of the rectangular foundation greatly reduces the settlement of embedded foundation.

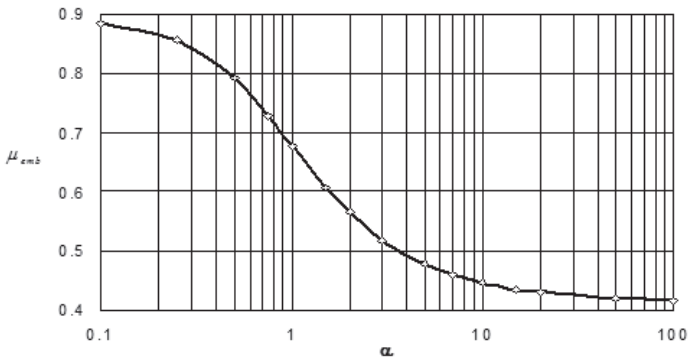


FIG. 4. Influence of the parameter α on the reduce coefficient of embedment effect

Influence of the parameter β on the reduction coefficient μ_{emb}

The influence of the parameter β is analyzed by defining the parameter β as $\beta=1, 3, 5,$

7, 10, 15, 20, and 25. The reduction coefficients μ_{emb} for different the parameter β are plotted in Fig. 5. Two conclusions can be made: (a). The larger the parameter β , the smaller the reduction coefficients μ_{emb} ; (b). When the parameter β is less than 5, the larger parameter β makes the reduction coefficients μ_{emb} decrease more significantly, that is, the length of the rectangular less than 5 times of the width of the rectangular foundation greatly reduces the settlement of embedded foundation and when $\beta > 10$, the rectangular foundation can be considered as a strip foundation.

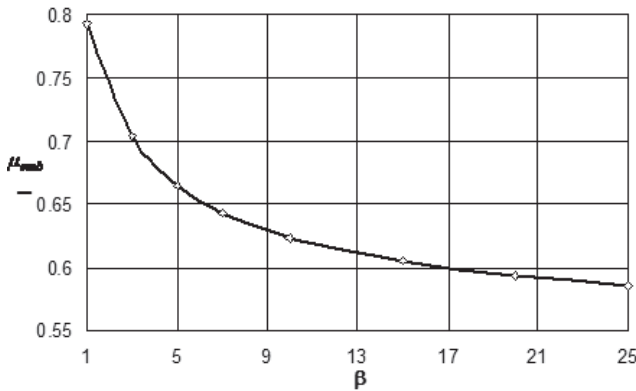


FIG. 5. Influence of the parameter β on the reduce coefficient of embedment effect

Influence of the parameter χ on the reduction coefficient μ_{emb}

The influence of the parameter χ is analyzed by defining the parameter χ as $\chi=0.5, 1, 3, 5, 7, 10, 15, 20, 30,$ and 50 . The reduction coefficients μ_{emb} for different the parameter χ are plotted in Fig. 6. Three conclusions can be made: (a). The larger the parameter χ , the larger the reduction coefficients μ_{emb} ; (b). When the parameter χ is less than 5, the larger parameter χ makes the reduction coefficients μ_{emb} increase more significantly, that is, the embedment depth corresponding the vertical excavation swelling stress larger than 1/5 times of foundation pressure is greatly reduces the settlement of embedded foundation; when the parameter χ is larger than 10, the larger parameter χ makes the reduction coefficients μ_{emb} increase less significantly, that is, the embedment depth corresponding to the vertical excavation swelling stress less than 1/10 times of foundation pressure rgreatly reduces the settlement of embedded foundation.(c). When the parameter χ is less than 1, the reduction coefficients μ_{emb} is less than 0.0, which is due to the vertical excavation swelling stress larger than the foundation pressure and $\rho_{emb} < 0.0$.

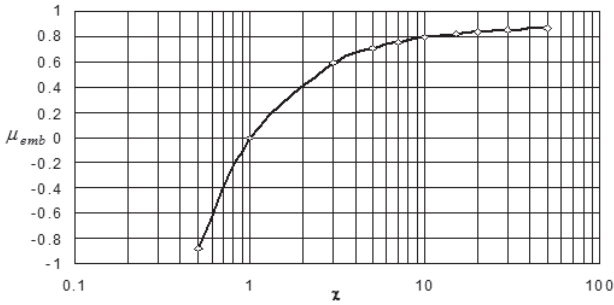


FIG. 6. Influence of the parameter χ on the reduce coefficient of embedment effect

Influence of the parameter ν on the reduction coefficient μ_{emb}

The influence of the parameter ν is analyzed by defining the parameter ν as $\nu = 0.00, 0.05, 0.10, 0.15, 0.20, 0.25, 0.30, 0.35, 0.40, 0.45,$ and 0.50 . The reduction coefficients μ_{emb} for different the parameter ν are plotted in Fig. 7. Two conclusions can be made: (a). Poisson ratio ν has a larger influence on the reduction coefficients μ_{emb} ; and the larger Poisson ratio ν , the larger reduction coefficients μ_{emb} ; (b). The influence of Poisson ratio on the reduction coefficients μ_{emb} can be best fitting with linear regression line: $\mu_{emb} = 0.3054\nu + 0.7038$ and the error of fitting $R^2 = 0.9963$.

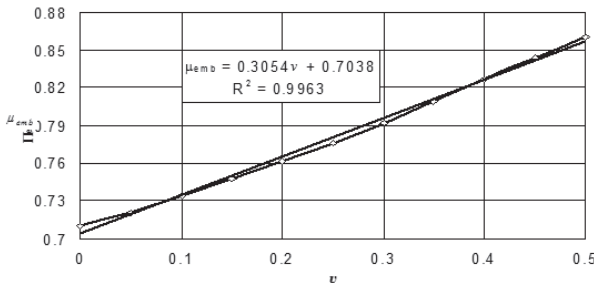


FIG. 7. Influence of the parameter ν on the reduce coefficient of embedment effect

CONCLUSION

The paper analyzed the embedment depth effect including Gibson effect, trench effect, side-wall contact effect and floating foundation effect, and proposed retaining wall effect. A new settlement calculation model for embedded foundation resting on elastic soil is presented. According to the present model, Groth & Chapman solution can be used to calculate the settlement of the rectangular embedded foundation resting on

elastic soil. The reduction coefficients of embedment depth effect are discussed in detail and some valuable conclusions are made for engineering practice.

ACKNOWLEDGMENTS

Financial supports from Fok Ying Hung Education Foundation (91076), from Construction Foundation of JiangSu province (JS200416) are gratefully acknowledged.

REFERENCES

- Craig, R. F. (1997). Soil mechanics, London, New York, Chapman & Hall, 6th ed.
- Bowles, Joseph E. (1996). Foundation analysis and design, New York: McGraw-Hill, 5th Edition.
- Eden, S. M. (1974). "Influence of shape and embedment on dynamic foundation response." Ph.D. Thesis, University of Massachusetts
- Gazetas, G., Tassoulas, J. L., Dobry, R. and O'rourke, M. J. (1985). "Elastic settlement of arbitrarily shaped foundations embedded in half-space." *Geotechnique*, 35, 339-346.
- Gazetas, G., and Stokoe, K. H. (1991). "Free vibration of embedded foundations: theory versus experiment." *J. Geotech. Eng.*, 117(9), 1363-1381
- Groth, N. N. & Chapman, C. R., (1969). "Computer evaluation of deformations due to subsurface loads in a semi-infinite elastic medium." B. E. Thesis, Univ. of Sydney, Australia.
- Giroud, J. P. (1972). "Settlement of rectangular foundation on soil layer." *Journal of the soil mechanics and foundations division*, 98, 149-154.
- Muni Budhu, (2010). Soil mechanics and foundations, John Wiley & Sons, Inc., 3rd Edition

STUDY ON MECHANISM OF EXPANSIVE SOIL SLOPE FAILURE AND NUMERICAL SIMULATION

Ting-hao Lu^{1,2}, Jun-hua Wu³, Song Yang⁴, Guo-xiong Mei^{3,5}

¹ Key Laboratory of Ministry of Education for Geomechanics and Embankment Engineering, Hohai University, Xi-Kang Road 1#, Nanjing 210098, China

² Geotechnical Research Institute, Hohai University, Xi-Kang Road 1#, Nanjing 210098, China

³ College of Civil Engineering and Architecture, Nanchang Hangkong University, Nanchang 330063, China

⁴ College of Hydraulic and Architectural Engineering, Yunnan Agricultural University, Kunming 650201, China

⁵ College of Transportation Engineering, Nanjing University of Technology, Nanjing 210009, China

ABSTRACT: Swell-shrinking, crack development, and over-consolidation are the characteristics of expansive soil, and it is an over-consolidation soil undergoing dry-wet cycles. Therefore, there are some faults to analyze expansive soil slope stability adopting the traditional strength criterion and calculation methods. In this paper, the Bilinear Strain-Hardening/Softening Ubiquitous-Joint (BSHSUJ) model in FLAC^{3D} is adopted to analyze the slope stability combined with strength reduction method. Results showed that the BSHSUJ model can be used to analyze the expansive soil slope stability considering cracks and soil softening. The area of major plastic shear strain expanded gradually from the slope base and top to the middle and was linked totally. The developing process of concentrated area of plastic shear strain is the forming process of shear zone actually. The characteristic of expansive soil landslide as progressive development can be simulated well. The numerical analysis simulates the progressive failure of expansive soil slope clearly and the application for slope stability by FLAC^{3D} is feasible.

Key words: expansive soil; crack; FLAC^{3D}; slope stability; strength reduction method

INTRODUCTION

Swell-shrinking, crack development and over-consolidation are the main characteristics of expansive soil which contains hydrophilic minerals (e.g., montmorillonite, glimmerton). Expansive soil has been found in more than 20 provinces in China with a wide distribution, and its damage to projects could not be neglected. For example, the middle route of South-to-North Water Diversion will

pass through the areas of expansive soil with more than 300 kilometers. The slope stability of expansive soil is important to the projects for normal operation. So it is necessary to study the slope stability of expansive soil (LI, 1992; BAO, 2004).

The researches on expansive soil slope at present could be grouped as stability analysis (HUANG et al., 2002), strengthening methods (ZHANG, 2006; YING, 2007), and numerical simulation (LI et al., 2001; YIN et al., 2002; WU et al., 2008) etc. The characteristics of expansive soil slope can be seen as follows: cracks develop on soil surface; the soil has the properties of shear dilation and softening; the characteristics of landslide show a progressive and tractive development (SHEN, 2000). Skempton (1964), Bjerrum (1967) and Bishop (1971) had studied the mechanism of strength loss under long-term loading and the choice of strength parameters in slope stability respectively. The influences on strength (LIU, 2008) and seepage (CHEN et al., 2006) by cracks were mainly focused in analysis of slope stability considering cracks. As we know, expansive soil undergoing dry-wet cycles is an over-consolidation soil. At the beginning of shearing, the anti-shear capacity increases rapidly with the increasing of shearing deformation and reaches to a peak. Then the anti-shear capacity reduces due to softening and reaches to the residual strength finally. In the process of stability analysis, not only the macroscopic strength of soil should be determined according to the degree of crack development, but also the active degree of anti-shear capacity should be considering during the process of shearing. So there are some faults to analyze expansive soil slope stability adopting the traditional strength criterion and calculation methods. Accordingly, the Bilinear Strain-Hardening/Softening Ubiquitous-Joint model in FLAC^{3D} is adopted to analyze the slope stability combined with strength reduction method.

FLAC^{3D} is a three-dimensional explicit finite-difference program for engineering mechanics computation. The basis for this program is the well-established numerical formulation used by our two-dimensional program FLAC. FLAC^{3D} extends the analysis capability of FLAC into three dimensions, simulating the behavior of three-dimensional structures built of soil, rock or other materials that undergo plastic flow when their yield limits are reached. Materials are represented by polyhedral elements within a three-dimensional grid that is adjusted by the user to fit the shape of the object to be modeled. Each element behaves according to a prescribed linear or nonlinear stress/strain law in response to applied forces or boundary restraints. The material can yield, flow, and the grid can deform (in large-strain mode) and move with the material that is represented. The explicit, Lagrangian, calculation scheme and the mixed-discretization zoning technique used in FLAC^{3D} ensure that plastic collapse and flow are modeled very accurately. Because no matrices are formed, large three-dimensional calculations can be made without excessive memory requirements. The drawbacks of the explicit formulation (i.e., small timestep limitation and the question of required damping) are overcome by automatic inertia scaling and automatic damping that does not influence the mode of failure. FLAC^{3D} offers an ideal analysis tool for solution of three-dimensional problems in geotechnical engineering.

CONSTITUTIVE MODELS

The Bilinear Strain-Hardening/Softening Ubiquitous-Joint (BSHSUJ) model in FLAC^{3D} can be used to account for the presence of an orientation of weakness (e.g., crack), as well as the cohesion, friction, dilation and tensile strength may harden or soften after the onset of plastic yield. In Mohr-Coulomb (MC) model, those properties are assumed to remain constant. However, the cohesion, friction and dilation as piecewise-linear functions of a hardening parameter can be defined to measure the plastic shear strain. A piecewise-linear softening law for the tensile strength can also be prescribed in terms of another hardening parameter measuring the plastic tensile strain. The program measures the total plastic shear and tensile strains by incrementing the hardening parameters at each step, and causes the model properties to conform to the user-defined functions. The hardening parameters are incremented if plastic flow has taken place, and the parameters of cohesion, friction, dilation and tensile strength are adjusted for the soil and the crack.

Incremental Elastic Law

The incremental expression of Hooke's law in terms of the generalized stress increments has the form as follows:

$$\Delta\sigma_{ij} = \lambda\Delta\theta\delta_{ij} + 2G\Delta\varepsilon_{ij} \quad (1)$$

where σ_{ij} is stress, kPa ; ε_{ij} is strain; $\lambda = \frac{E\mu}{(1+\mu)(1-2\mu)}$ is Lamé coefficient; δ_{ij} is

Kronecker delta; $\theta = \varepsilon_{xx} + \varepsilon_{yy} + \varepsilon_{zz}$ is volumetric strain; $G = \frac{E}{2(1+\mu)}$ is shear modulus; μ is

Poisson's ratio; E is Young's modulus.

Failure Criterion

The criterion for failure in the soil used in this model is sketched in the principal stress plane (seen in FIG. 1). Note that the compressive stresses are negative in FLAC^{3D} and, by convention $\sigma_1 \leq \sigma_2 \leq \sigma_3$. The failure envelope is defined by two Mohr-Coulomb failure criteria: $f_1^s = 0$ and $f_2^s = 0$ for segments A-B and B-C respectively and a tension failure criterion $f^s = 0$ for segment C-D. The shear failure criterion has the general form $f^s = 0$. The criterion is characterized by a cohesion c_2 , and a friction angle φ_2 , for segment A-B, and by a cohesion c_1 , and a friction angle φ_1 , for segment B-C. The tensile failure criterion is specified by means of the tensile strength, σ_t (positive value); thus we have:

$$f^s = \sigma_1 - \sigma_3 N_\varphi + 2c\sqrt{N_\varphi} \quad (2)$$

$$f' = \sigma_3 - \sigma' \tag{3}$$

where c is cohesion, kPa ; σ_3 is minimum principal stress, kPa ; σ_1 is maximum principal stress, kPa ; σ' is tensile strength, kPa ; $N_\varphi = (1 + \sin\varphi)/(1 - \sin\varphi)$, φ is internal friction angle, degree.

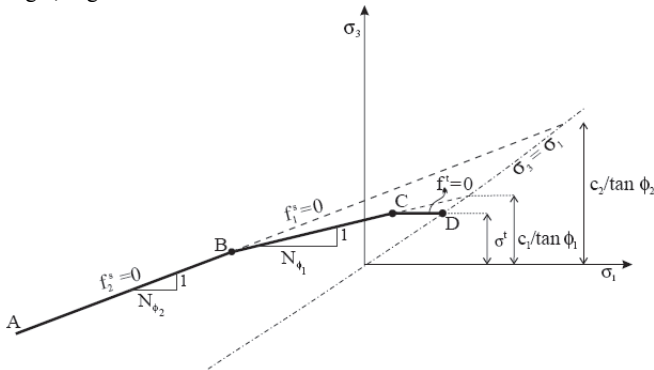


FIG. 1. Soil failure criterion

The stresses, corrected for plastic flow in the soil, are resolved into components parallel and perpendicular to the crack, and tested for failure of crack. The failure criterion is represented in FIG. 2 and corresponds to two Mohr-Coulomb failure criteria: $f_2^s = 0$ for segment A-B, $f_1^s = 0$ for segment B-C; and a tension failure criterion $f^s = 0$ for segment C-D. Each shear criterion has the general form $f^s = 0$, and is characterized by a cohesion and a friction angle c_j, φ_j equal to c_{j2}, φ_{j2} along segment A-B, and c_{j1}, φ_{j1} along B-C. The tensile criterion is specified by means of the tensile strength, σ'_j (positive value). Thus, we have:

$$f^s = \tau + \sigma_{33} \tan \varphi_w - c_w \tag{4}$$

$$f^s = \sigma_{33} - \sigma'_w \tag{5}$$

where c is cohesion, kPa ; σ_{33} is normal stress on the crack, kPa ; τ is tangential stress on the crack, kPa ; σ'_w is tensile strength of crack, kPa ; φ_w is internal friction angle of crack, degree.

For the crack, the formula is:

$$\Delta \kappa_w^f = \Delta \varepsilon_{33}^{pr} \tag{9}$$

where $\Delta \varepsilon_{33}^{pr}$ is plastic tensile strain increment of crack.

Potential Function and Flow Rule

Considering the softening property, the potential function for shear yielding is g_m^s which corresponds to the non-associated flow rule, and the potential function for tensile yielding is g_m^t which corresponds to the associated flow rule. The expressions are shown as follows:

$$g_m^s = \sigma_1 - \sigma_3 N_\psi \tag{10}$$

$$g_m^t = \sigma_3 \tag{11}$$

where $N_\psi = (1 + \sin \psi) / (1 - \sin \psi)$, ψ is dilation angle, degree.

The potential function for shear yielding on crack is g_w^s which corresponds to the non-associated flow rule, and the potential function for tensile yielding on crack is g_w^t which corresponds to the associated flow rule. The expressions are shown as follows:

$$g_w^s = \tau + \sigma_{33} \tan \psi \tag{12}$$

$$g_w^t = \sigma_{33} \tag{13}$$

STRAIN LOCALIZATION AND STABILITY JUDGMENT

Strain localization can be defined as that the strain concentrates on a local scale when soil begins to fail. Softening happens due to stress concentration for strain softening soil. This will lead to stress redistribution in soil, which may cause softening and large strain in large scale in soil, and shear zone will be formed finally. In FLAC^{3D}, the change of maximum shear strain rate is recorded to represent the forming process of shear zone.

Theoretically, the unbalanced force should be zero when a static equilibrium state is achieved in slope everywhere. A plastic flow state is achieved when the unbalanced force is a nonzero constant. Although the unbalanced force cannot be zero by using numerical methods usually, a slope can achieve a static equilibrium when the unbalanced force is much less than the initial force (e.g., lower by five orders of magnitude). In FLAC^{3D}, the method to track the maximum unbalanced force at grid node is adopted to judge the state of slope (i.e., static equilibrium or plastic flow).

USER-DEFINED FUNCTIONS FOR SOIL PARAMETERS

User-defined functions for zone yielding parameters can be determined by back-analysis of the post-failure behavior of soil. We can define the cohesion, friction, dilation and tensile strength variance as a function of the plastic shear strain. Hardening and softening behaviors for the cohesion, friction and dilation in terms of the shear parameter $\Delta\varepsilon^p$ are provided in 'table' as fish language in FLAC^{3D}. Each table contains pairs of values: one for the parameter, and one for corresponding property value. It is assumed that the property varies linearly between two consecutive parameter entries in the table. Softening of the tensile strength is described in a similar manner using the parameter $\Delta\varepsilon^p$.

SLOPE STABILITY ANALYSES

Based on the theory above, the slope stability analyses have been carried out by MC model and BSHSUI model respectively combined with strength reduction method. The calculating model is shown in FIG. 3 and the soil parameters are listed in Table 1. The x-displacement at $x=0m$ and $x=70m$ are fixed. The x-displacement and z-displacement at $z=0m$ are fixed too. Here, the soil parameters (e.g., cohesion, friction angle, dilation angle, tensile strength etc.) are the brittle functions of hardening parameters. That means the values of soil parameters decrease from peak to residual when the values of hardening parameters are equal to 0.002.

Table 1. Strength Parameters of Soil

Strength parameters	Cohesion	Friect.	Dilation	Tensile	Youngs	Poissons	Unit	
		angle	angle	strength	Modul.	ratio	Wt.	
	<i>/kPa</i>	<i>°</i>	<i>°</i>	<i>/kPa</i>	<i>/kPa</i>	<i>/</i>	<i>/kN·m⁻³</i>	
Soil	peak	20	20	10	10	8180	0.36	20
	residual	4	10	5	0	8180	0.36	20
Crack	peak	10	20	0	0	\	\	\
	residual	0	10	0	0	\	\	\

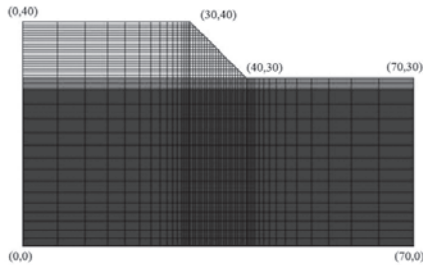
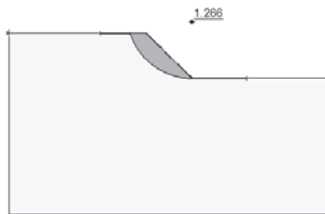


FIG. 3. The Finite Difference Mesh

Results Respect to SLOPE/W and MC-Model in FLAC3D

The calculating parameters are adopted with soil peak strength and kept constant. The safety factor is 1.266 obtained by the software SLOPE/W in GeoStudio2004, and 1.325 obtained by FLAC^{3D} adopting strength reduction method. It is clearly seen that the slope is stable without considering the soil softening and the slip shape in FIG. 4 are very similar. Moreover, compared with the result of limit equilibrium method, the strength reduction method applied in FLAC^{3D} can be useful to analyze the slope stability and obtain the safety factor.



(a) with SLOPE/W



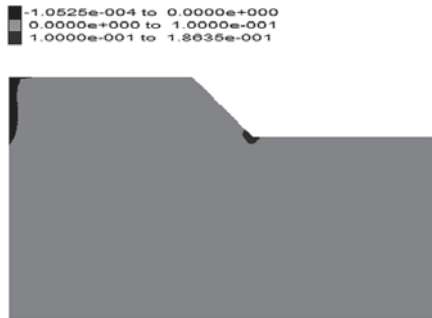
(b) with FLAC^{3D} (plastic shear strain)

FIG. 4. The Slip Shape with Peak Strength

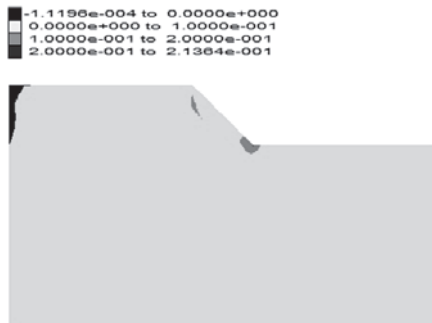
Results Respect to BSHSUJ Model

Simulation of Gradual Landslide

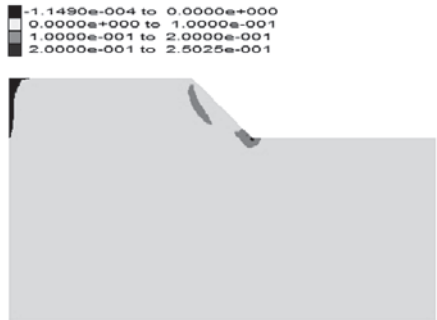
The dip angle (intersection angle between crack plane and horizontal plane) of crack plane is 20 degree and the soil characteristic of softening is taken into account meanwhile in BSHSUJ model. The results of the distribution and variation of plastic shear strain are shown in FIG. 5. The concentrated area of plastic shear strain appeared on slope base at 700 time step (FIG. 5-(a)). With time step increasing, the concentrated area of plastic shear strain also appeared on slope top at 770 time step (FIG. 5-(b)). The concentrated area of plastic shear strain expanded gradually from the slope base and top to the middle of slope at 850 time step (FIG. 5-(c)). At 950 time step, the concentrated area of plastic shear strain was linked totally and an obvious shear zone was formed (FIG. 5-(d)). The developing process of concentrated area of plastic shear strain is the forming process of shear zone. The simulation results reflected the forming process of gradual landslide clearly.



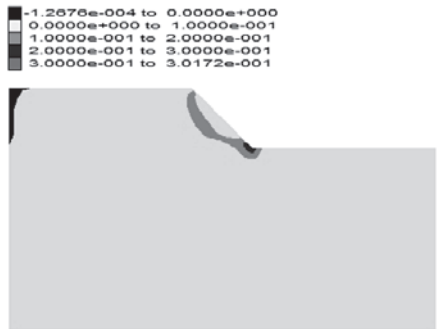
(a) 700 time step



(b) 770 time step



(c) 850 time step



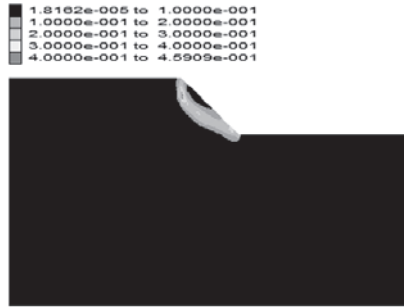
(d) 950 time step

FIG. 5. Distribution and Variation of Plastic Shear Strain.

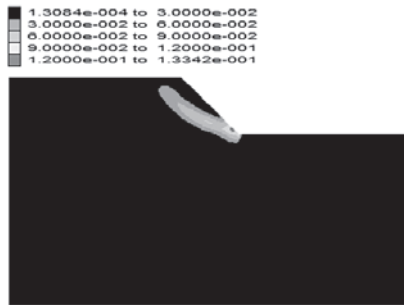
Calculation Results

Based on the strength reduction method, the slope stability analysis was carried out adopting BSHSUJ model. The dip angle of crack surface is still 20 degree. Two schemes were conducted as follows: one is of considering cracks and soil softening; another is of considering cracks only. The distribution of plastic shear strain was shown in FIG. 6. Numerical results indicate that the safety factor considering cracks only is 1.242, while the safety factor considering cracks and soil softening is 0.568. It can be seen that the slope is overall stable considering cracks only and the maximum plastic shear strain is 0.133. The area of plastic shear strain is located in deeper place and does not go through the whole slope. With regard to the slope considering cracks and soil softening, slope failure happens and the maximum plastic shear strain is

0.459. The area of plastic shear strain is located in shallower place and goes through the whole slope. The shallow slide appears clearly with the use of BSHSUJ model considering cracks and soil softening, and it is similar to actual landslide of expansive soil slope.



(a) including cracks and soil softening



(b) including cracks only

FIG. 6. The Slip Shape with BSHSUJ Model (Plastic Shear Strain)

CONCLUSIONS

(1) Compared with the results by limit equilibrium method, it is feasible to analyze slope stability by FLAC^{3D} combined with strength reduction method. The safety factor and potential location of slip surface can be obtained accurately.

(2) The functional relationship between strength and softening parameters (plastic shear strain) is established. The simulation of soil softening is achieved and the slope behavior after soil initial failure is obtained.

(3) The BSHSUJ model can be used to analyze the slope stability considering cracks and soil softening. The characteristic of expansive soil landslide can be

simulated well. In this study, plastic shear strain is adopted to represent the slope deformation at different time. The concentrated area of plastic shear strain appeared on slope base at the beginning and also appeared on slope top afterwards. With time step increasing, the concentrated area of plastic shear strain expanded gradually from the slope base and top to the middle of slope and was linked totally. An obvious shear zone was formed finally. The developing process of concentrated area of plastic shear strain is the forming process of shear zone. The simulation results reflected the forming process of gradual landslide clearly.

ACKNOWLEDGEMENTS

This work is supported by the National Science and Technology Ministry of China under its 11th Five-Year Plan (No. 2006BAB04A10), National Natural Science Foundation of China (No. 51008117) and the project of enterprise and public institution entrusted by Jiangxi Transportation Research Institute (No. 2011-11-056). All opinions, findings and conclusions in this work represent the views of the authors only.

REFERENCES

- Bao C.G. (2004). Characters of Unsaturated Soil and The Stability of Expansive Soil Slope. *Chinese Journal of Geotechnical Engineering*, Vol. 26(1): 1-15.
- Bishop A. W. (1971). The influences of progressive failure in the choice of the method of stability analysis. *Geotechnique*, Vol. 21(2):168-172.
- Bjerrum C. (1967). Progressive failure in slopes of over consolidated plastic clay and clay shales. *SMFE, ASCE*, Vol. 93(5):3-49.
- Chen T.L., Deng G., Chen S.S. et al. (2006). Effects of fissures on stability of unsaturated soil slope. *Chinese Journal of Geotechnical Engineering*, Vol. 28(2): 210-215.
- FLAC (Fast Lagrangian Analysis of Continua., version 5.0) (2005). Itasca Consulting Group, Inc..
- Huang R.Q. and QI G.Q. (2002). The Effect of Unsaturated Soil Suction on Slope Stability. *Journal of Engineering Geology*, Vol. 10(4): 343-348.
- Li S.L. (1992). Studies on the Engineering Geology of Expansive Soil in China. *Jiangsu Science and Technology Publishing House*.
- Li Z.P. and Zhang M. (2001). Effects of Rain Infiltration on Transient Safety of Unsaturated Soil Slope. *China Civil Engineering Journal*, Vol. 34(5):57-61.
- Shen Z.J. (2000). Theoretical Soil Mechanics. *Beijing: China WaterPower Press*.
- Skempton A. W. (1964). Long-term stability of clay slopes. *Geotechnique*, Vol. 14(2):77-102.
- Liu H.Q. (2008). Study on analysis method and influencing factors of expansive soil slope stability. *Nanjing, HoHai University*.
- Wu J.H., Yuan J.P. and Lu T.H. (2008). Stability Analysis of Unsaturated Expansive Soil Slope. *Rock and Soil Mechanics*, Vol. 29(S):363-367.

- Ying X.D. (2007). Study on Stabilizing Effect to Expansive Soft Slope by Manual Bored Concrete Piles. *Jiangsu Construction*, Vol. 6:20-22.
- Yin K.L., Wang Y. and Tang Z.H. (2002). Mechanism and Dynamic Simulation of Landslide by Precipitation. *Geological Science and Technology Information*, Vol. 21(1): 75-78.
- Zhang K.J. (2006). Study on Failure Mechanism and Treatment Technology of Expansive Soil Slope in Landscape Area. *Jiangsu Construction*, Vol. 4:44-47.

TIME EFFECT ON BEARING CAPACITY OF JACKED PILES USING THE BACK-ANALYSIS METHOD

Tong-fa Deng¹, Zhong-fang Zhao², and Yong Gui³

¹ Lecturer, Jiangxi University of Science and Technology, Ganzhou, Jiangxi 341000, China, dbdtf@163.com

² Lecturer, Jiangxi University of Science and Technology, Ganzhou, Jiangxi 341000, China, zhongfangcn@163.com

³ Lecturer, College of Applied Science, Jiangxi University of Science and Technology, Ganzhou, Jiangxi 341000, China, 594008657@qq.com

ABSTRACT: The mechanism of the time effect on pile capacity can be interpreted as thixotropic recovery and soil consolidation around the pile. Based on the final installation or jacking force and subsequent reload or re-jacking force, the final load capacity of the pile can be estimated. A parametric inversion was conducted to determine the increasing load capacity curve of the jacked pile, which can be used to estimate the increasing load capacity curve of other piles installed in the same subsurface conditions. The results of this paper are instructive and constructive to the design and construction of jacked piles.

KEYWORDS: statically pressed pile (jacked pile); back-analysis; load capacity; recompression; time effect

INTRODUCTION

Jacked piles produce less noise and vibration, allow lower strength concrete, and/or require less reinforcement compared to driven piles due to their lower driving stresses. The jacked pile does not produce spoil as compared with the cast-in-place bored pile. In addition, the precast jacked pile is of higher quality than the cast-in-place bored pile. The jacking force or penetration resistance of the jacked pile is also known during the installation and it can be used to estimate the ultimate bearing capacity of the pile. The above-mentioned advantages of the jacked pile have increased its popularity in coastal areas and soft soil regions in densely populated cities.

When a jacked pile penetrates into the soil, the surrounding soil will be disturbed and remolded. The destruction of original soil structure will alter the stress state and engineering properties of the soil around the pile. After the pile penetrates into the soil, excess pore water pressure gradually dissipates. With the process of soil consolidation, the effective stress will increase thus increasing the shear strength of the soil around the pile. In addition to the soil consolidation, there is thixotropic recovery. Therefore, the soil consolidation and thixotropic recovery will form a stiff soil layer around the pile with an increased shear strength. The stiff layer soil will deform together with the pile

under a vertical load. The pile and the stiff layer of clay act together, thus increasing the bearing capacity of the pile. Such a change is the result of the thixotropic recovery and soil consolidation.

During the final stage of the penetration, the pile driving pressure can be easily determined. A jacked pile driver can be moved back to re-load the pile periodically during the project. The field measurements can be used as described in this article to determine the capacity growth curve parameters and estimate the time-dependent ultimate capacity of the jacked piles on site.

BACK-ANALYSIS OF TIME EFFECT ON THE JACKED PILE BEARING CAPACITY

The Growth Curve of Bearing Capacity

Based on the static load tests where the piles were penetrated into the soil at different time intervals, Li and Liu (1992) obtained an empirical formula showing a hyperbolic increase of the pile bearing capacity. After conducting a pile-soil interface shear test, Zhang and Dung (2002) believed that the increase of pile-soil friction and the soil thixotropic recovery basically followed the same trend, both in accordance with the hyperbolic growth law. Zhang et al. (2002) also studied the time effect on the jacked pile bearing capacity and found experimentally that the re-penetration test and static load test results followed the hyperbolic curves. Therefore, the growth curve of the jacked pile bearing capacity can be expressed in the following formula:

$$\eta_{ur} = \frac{t}{a + bt} \quad (1)$$

where η_{ur} represents the increase in jacked pile bearing capacity relative to the initial installation capacity (%); t represents the time elapse after the pile is set (days); and a , b represents the constants.

Thus, the ultimate load capacity of the jacked pile at different time can be determined by the following formula:

$$Q_{ur} = Q_0(1 + \eta_{ur}) \quad (2)$$

where Q_{ur} represents the ultimate bearing capacity (kN) and Q_0 represents the ultimate piling force (kN) during installation (time = 0)

Determination of Back-Analyzed Target Function

The parametric inversion of the growth curve of the jacked pile bearing capacity by an optimization method is to determine necessary parameters. After the parametric inversion, the time-dependent growth curve of the jacked pile bearing capacity can be worked out and be used to calculate the bearing capacity. The calculated capacity should be close to that measured in field. When Eq. (1) is substituted into Eq. (2), the following formula can be obtained:

$$\frac{Q_0}{Q_{ur} - Q_0} = \frac{a}{t} + b \quad (3)$$

Letting $\frac{Q_0}{Q_{ut} - Q_0} = S$ and $\frac{1}{t} = T$, thus,

$$S_i = aT_i + b \tag{4}$$

In actual projects, due to the effects of the thixotropic recovery and the consolidation of the surrounding soil, the load capacity of the jacked pile increases. Therefore, Eq. (1) is a monotone increasing function. In this equation, when $t \rightarrow \infty$, $\eta_{ut} = 1 / b$ (they are positive values). In this way, the target function is as follows:

$$\left. \begin{aligned} F(x) &= \sum_{i=1}^N [S_i(x) - S_i^*]^2 \\ \text{s.t. } x &> 0 \end{aligned} \right\} \tag{5}$$

where x are the parameters, and $x = [a \quad b]^T$; $S_i(x)$ is to the calculated ultimate bearing capacity after the pile is re-pressed i th times; S_i^* is the measured ultimate bearing capacity after it is re-pressed i th times; N is the number of times the pile is re-pressed, $N = \sum_{i=1}^m n_i$; m is the number of the piles; and n_i is the number of times the i th pile is re-pressed.

ENGINEERING EXAMPLE

Based on the statistics from the tests cited in the literature (e.g., Zhang et al. 2003; Wang 2003), the measured initial installation pressed force and re-pressed force can be shown in Tables 1 and 2.

Table 1. Initial Installation Pressed Force and Re-pressed Force of Test Piles in Fill

Tested piles	Initial installation Force (kN)	Interval Time (day)	Re-pressed Force (kN)
1 [#]	451	0.6	853
		2.7	984
		4.0	1066
		5.8	1115
		0.22	680
2 [#]	447	0.98	848
		3.84	976
		7.70	1154
		1.53	840
		2.83	978
3 [#]	476	4.75	1053
		7.64	1129

Table 2. Initial Installation Pressed Force and Re-pressed Force of Test Piles in Thick Soft Clay

Tested Piles	Initial installation Force (kN)	Interval Time (day)	Re-pressed Force (kN)
1 [#]	647.8	7.2	1194.4
		14.8	1393.1
		25.0	1598.5
		60.1	1897.5
		90.0	2003.4
		182.9	2195.8
2 [#]	684.2	7.2	1253.2
		14.8	1499.7
		25.0	1696.0
		60.1	2003.4
		90.0	2095.9
		182.9	2243.9
3 [#]	639.0	7.2	1098.3
		14.8	1254.2
		25.0	1499.6
		60.1	1902.2
		90.0	2109.5
		182.9	2265.6

The parametric inversion here was a linear least square problem with constraints. Matlab was used to determine these parameters. Using the data in Tables 1 and 2, different final pressed force, different re-pressed force at different time, the growth curve of the relevant bearing capacity can be obtained. The comparisons between the growth curve and the measured scatter data are shown in Figures 1 and 2. The comparisons show satisfactory results.

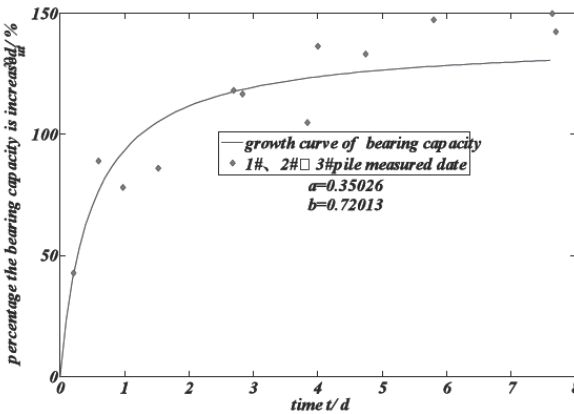


FIG. 1. Growth Curve of the Jacked Pile Bearing Capacity in Fill

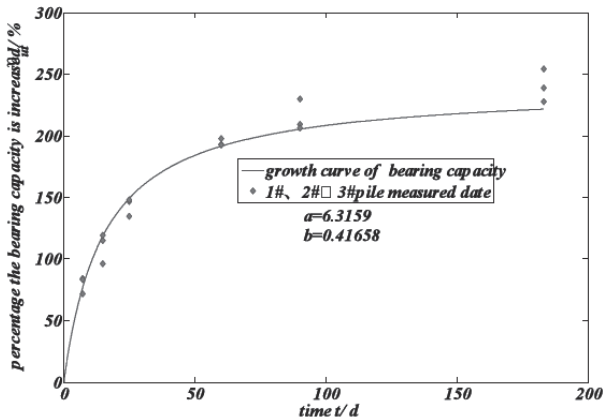


FIG. 2. Growth Curve of the Jacked Pile Bearing Capacity in Thick Soft Clay

In order to test and verify the feasibility of determining the jacked pile bearing capacity by means of back-analysis, a pile installation project in silty clay in Ganzhou, Jiangxi Province was selected as an example. The parametric inversion was conducted for two groups of measured final pressed force and re-pressed force (See Table 3). Its relevant growth curve of the bearing capacity is shown in Figure 3. Then this growth curve was applied to No. 3 pile, resulting in the test results shown in Figure 4. Figure 4 shows that it is feasible and applicable to determine the growth curve of the bearing capacity based on a back-analysis method using fewer piles and then determine the growth of the bearing capacity of other piles.

Table 3. Initial Installation Pressed Force and Re-pressed Force of Test Piles

Tested Piles	Initial installation Force /KN	The Interval Time /d	Re-pressed Force /KN
1 [#]	598	1	1235
		2	1332
		3	1385
		7	1422
		14	1446
2 [#]	671	1	1428
		2	1445
		3	1512
		7	1565
		14	1589
3 [#]	724	3	1625
		14	1695

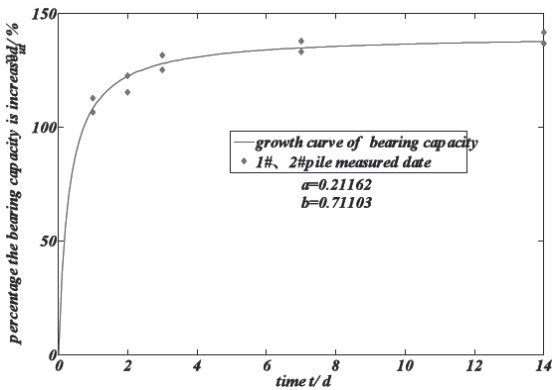


FIG. 3. Growth Curve of the Jacked Pile Bearing Capacity

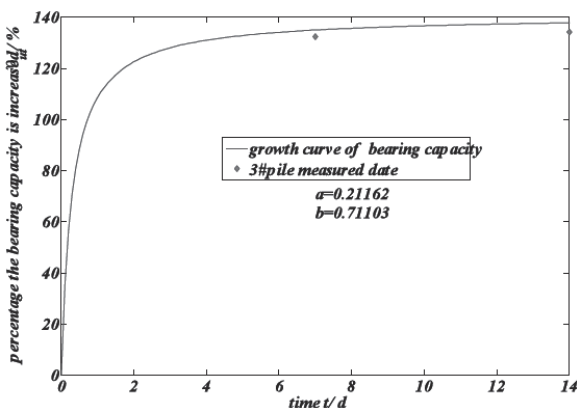


FIG. 4. Verification of the Jacked Pile Bearing Capacity

Due to the differences in the length, diameter, size of the pile and the soil where the pile stands, it may not be so accurate to deduce the growth curve of the bearing capacity of the jacked pile under other soil conditions using the statistics in one specific field. In addition, although in the same field, the soil condition can be totally different. The measured data may be scatter. The growth of bearing capacity may not significantly follow a specific rule. However, this back-analysis method is constructive as to the estimation of the bearing capacity growth under the same condition.

CONCLUSIONS

- (1) The measured reload data from the above three groups of piles demonstrate that the jacked pile bearing capacity is time dependent. The time effect results from the thixotropic recovery and soil reconsolidation.
- (2) The analysis suggests that the growth curve for the increase in the bearing capacity can be approximated by a hyperbolic function, and the parameters deduced from the parametric inversion can be used to estimate the growth curve of other piles of similar diameter and length at the same site.

REFERENCES

- Deng, X.Z. (2006). "The Study On Jacking Pressure And Bearing Capacity Of Jacked-IN Pil. " *A dissertation submitted to Southeast University in conformity with the requirements for the degree of Doetor of Philosophy*. China.
- Guo, J.J., He, J.P., and Shi J.Y. (2010). "Laboratory Strain-Holding Tests Of Setup Of Jached-In Piles In Cohesive Soil." *Industrial Construction.*, China, Vol. 40(5).
- Guo, J.J. and Shi, J.Y. (2009). "Laboratory Strain Holding Tests Of Set-Up Of Jacked-In Piles In Sand." *Industrial Construction .*, China, Vol.39(7).
- Li, X. and Liu J.L. (1992). "Time Effect of Bearing Capacity of Driven Pile in

- Saturated Soft Soil." *Chinese Journal of Geotechnical Engineering*, China, Vol.14(4): 9-16.
- Lu, Q., Sun, X.D., and Zhang, J.X. (2011). "Experimental Study on Sliding Friction between Pile and Soil in Tianjin Binhai New Area." *Bulletin of science and technology*, China, Vol.27(1).
- Rong, S.H. and Wang, X.Q. (2003). "Bearing Capacity Increasing After Construction Of Static Pressure Precast Concrete Pile On Soft Clay." *Mineral Resources And Geology*, China, Vol.17(98).
- Sun, X.D, Song, K.X., and Zhang, J. (2010). "Study On Sliding Friction And Time Effect Between Jacked Pile And Soil." *Journal of Hebei University of Engineering (Natural Science Edition)*, China, Vol.27(1).
- Wang, J.T. and Zhang, M.Y. (2011). "Time Effect of Bearing Capacity Of Jacked Piles Based On Spherical Cavity Expansion Theory." *Sichuan Building Science*. China.
- Wang, S.P. (2003). "Study on time effect of PHC open-ended pile in deep soft soil." *Chinese Journal of Geotechnical Engineering*, China, Vol.25(2):239-241.
- Xiang, Y.F. (2007). "Study Of sinking resistance and compaction effect of Static Press Pile." *A dissertation submitted to Tongji University in conformity with the requirements for the degree of Doctor of Philosophy*. China,
- Zhang, M.Y. and Deng, A.F. (2002). "Experimental Study on Sliding Friction between Pile and Soil." *Rock and Soil Mechanics*, China, Vol.23(2): 246-249.
- Zang, M.Y., Liu, J.W., Zhang, Z.M, and Yu, X.X. (2003). "Optimum design method of jacked piles based on interval re-pressed test". *Chinese Journal of Geotechnical Engineering*, China, Vol.25(2):239-241.
- Zhang, M.Y., Shi, W., and Wang, C.G. et al. (2002). "Time Effect on the Ultimate Bearing Capacity of Static Pressed Pile." *Chinese Journal of Geotechnical Engineering*, China, Vol.21 (Supp 2): 2601-2604.